Technical Report No. 32-663

Ranger Block III Attitude Control System

Will Turk

JET PROPULSION LABORATORY
CALIFORNIA INSTITUTE OF TECHNOLOGY
PASADENA, CALIFORNIA

November 15, 1964

ERRATA dated 4-15-65 inserted

ERRATA FOR JPL TECHNICAL REPORT NO. 32-663

Page 5: 1. Table 1, bottom set of data: change 2.5 to 2.8 in column 3; change 2.75 to 3.08 in column 4; and change 2.25 to 2.52 in column 5.

2. Eq. (14), last line: should read $\dot{\theta}_{max_{UL}} = -7.78$ mrad/sec

Page 6: In the paragraph following Eq. (19), θ should read $\dot{\theta} = 3$ deg/sec.

Page 7: 1. In the paragraph below Fig. 7, θ should read $\dot{\theta} = 0.919$ mrad/sec

2. In Fig. 8, on the vertical ordinate lines, delete the tick marks for 0.919 and -0.919; these two numbers relate specifically to the upper and lower total rate deadband lines, respectively. Also, insert $\pm$ before 52.4 mrad/sec.

Page 8: 1. After Eq. (23), and following the words "and where", the 3rd line down should have W changed to $\dot{W}$.

2. In Eq. (32) and (35), change θ to $\dot{\theta}$.

Page 9: 1. Right-hand column, 17th line down: change $(\theta)^2$ to $(\dot{\theta})^2$.

2. In the top of Fig. 9: $\dot{\theta}_i$ should read $\dot{\theta}_0$

Page 10: 1. Left-hand column, lines 3, 4, 5 from the top: change θ to $\dot{\theta}$; line 7 from the top should read:

$$t_{on} = \frac{\dot{\theta}_1 - \dot{\theta}_0}{\ddot{\theta}} + \frac{\dot{\theta}_2 - \dot{\theta}_1}{\ddot{\theta}}$$

2. Right-hand column, 2nd paragraph, line 4: change θ to $\dot{\theta}$.

Page 11: In Fig. 11, the preset hinge angle designates the angle between the spacecraft roll axis and the *RF* axis of the antenna.

Page 12: In Fig. 13, for the ordinate call-out: θ should read $\dot{\theta}$.

Page 13: Right-hand column, paragraph following Table 4, line 5: change θ to $\dot{\theta}$.

Page 14: 1. Fig. 15: after 17.5, add mrad.

2. Fig. 16: for the *Ranger* 6 and 7 system, delete the vertical lines connecting the gas system to K_G and to K_{sensor}; all *S*'s should be lower case.

Page 20: Fig. 25: the right-hand t_2 should read t_0.

Page 22: 1. Eq. (118): change θ^2 to $\dot{\theta}^2$.

2. Table 6, column 2, 4th and 5th groups of data: change θ to $\dot{\theta}$.

3. Fig. 27: should read "theoretical" curve, within the graph.

Page 23: Table 7, column 1, 3rd group of data: change all θ to $\dot{\theta}$.

Page 27: Left-hand column, Section III-B.-1.-c.: change mrad/sec to meters/sec

Page 31: Eq. (136): change θ to $\dot{\theta}$.

Page 32: Fig. 36: the abscissa call-out should read "TIME, sec"

Page 34: Right-hand column, Eq. (144): change 0.053 to 0.0525

Page 35: Table 11, column 3: the notation E-3 denotes 10^{-3}

Page 36: 1. Tables 12 and 13, columns 3 and 7: the notation E-3 denotes 10^{-3}

2. Left-hand column, paragraph 3, should read: . . . the 3-σ standard deviation is $\sqrt{3}L$.

Page 38: Fig. 43: the top and bottom abscissa call-outs are expressed in "deg".

Page 44: 1. Left hand column, line 16 from the top: delete the dot from q_i.

2. Eq. (A-2): θ^2 should be $\dot{\theta}^2$; $(\theta + \phi_3)^2$ should be $(\dot{\theta} + \dot{\phi}_3)^2$

3. Fig. A-2: change V_0 to r_0; b_4 = distance between B and C_4; b_3 = distance between B and C_3.

Page 46: 1. Fig. A-3: l_1 = distance between C_1 and A_1; r_1 = distance between C_1 and O; h = distance between line $C_1 - C_2$ and O; r_0 = distance between A_0 and O; r_2 = distance between C_2 and O; l_2 = distance between A_2 and C_2.

2. In the legend for Fig. A-3, right-hand column: change all $\simeq$ signs to read as "minus" signs.

Page 47: Left-hand column, line 9 from top: delete the dot over z.

Page 50: Eq. (A-54): the denominator of the term in brackets should be $M_0 (l_1 + d_1) (\lambda^2 + l_1^2)$

Page 51: Fig. A-5: within the graph, change j to J.

Page 61: 1. Fig. B-5, lower right-hand box: should read $5 \times 10^{-3} (s + 323)$

2. Fig. B-6, 2nd box at top: change K_t to K_T; in the lowest box, change R_t to R_T; on the upper left-hand horizontal line of this Fig. B-6, change e_t to e_T

Page 63: 1. Left-hand column, Eq. (B-24): should be $\dot{\beta}$

2. Fig. B-10, 1st low set of two boxes: change to read $5 \times 10^{-3} (s + 323)$

Page 64: Fig. B-12: the locus originating at the pole at -1000 is a straight line ending at the zero at -320.

Page 70: Fig. C-3: should show two poles at the origin.

Page 71: 1. Fig. C-5, for β, deg: delete 0.5, and change 1 to -5.

2. Fig. C-4, for β, deg: change -15 to $+5$.

Page 72: Fig. C-6: should show two poles at the origin.

Page 74: Fig. C-10: within the graph, insert j before 298 rad/sec.

Page 76: 1. Fig. C-12: change F_y to F_z.

2. Right-hand column, lines 9 and 11 from top of column: change the last y to subscript y for the preceding parenthetical expressions.

Page 77: Fig. C-13: change F_y to F_z.

Page 78: Fig. C-14: change 0.1 to 0.05 for ϕ_2 and ϕ_1.

Page 84: Fig. C-23: change F_y to F_z.

Page 85: Fig. C-24 and 25: change F_y to F_z, respectively.

Page 86: Fig. C-26: change F_y to F_z.

Page 87: Fig. C-27: change F_y to F_z.

Page 88: Fig. C-28 and 29: change F_y to F_z, respectively.

Page 89: Fig. C-30 and 31: change F_y to F_z, respectively.

Page 90: Fig. C-32: change F_y to F_z.

Page 100: 1. Fig. D-4: delete the $-\varepsilon_Y$ and its arrow; insert $-\varepsilon_Y$ and arrows as being the angle between ω_p and the lowest dashed arrow.

2. Fig. D-5: lowest arrow pointing southeast should be designated x; ε_{11} = angle between x_1 and x.

Page 106: Eq. (D-68): the 3rd line down within the 2nd group of three components should read: $-(\Delta\theta_p + \delta\theta_p + \delta_p)$

Page 110: Eq. (D-99) should read $\rho = \frac{\delta}{l}$

Page 111: The revised Fig. D-11 is presented below.

Page 112: Fig. D-12: the axis pointing toward the lower left of the diagram should be labeled $-y$.

Page 116: Table D-3: in column 4, line 21 from top, should be $\dot{\theta}_p$; in column 5, line 18, should be $\dot{\theta}_R \sin \theta_p$.

Page 118: Fig. D-17: the angle between y and $\overline{V}$ should read α_2.

Page 128: Fig. E-7: in the upper-right and lower-right portions of the graph, add the word "deg" for the numbers 1.25 and 1, respectively.

Page 131: Fig. F-1: the 2nd to last box on the right should read $1/Z_T$; the last box on the right should read Z_0.

Page 133: Eq. (F-12): within the basic denominator, 0.6 should read 0.3.

Page 134: Eq. (F-17): within the basic denominator, 0.6 should read 0.3.

Page 135: Eq. (F-18): within the basic denominator, 0.6 should read 0.3.

Page 143: Fig. G-6: within the graph, 0.005 should read 0.035.

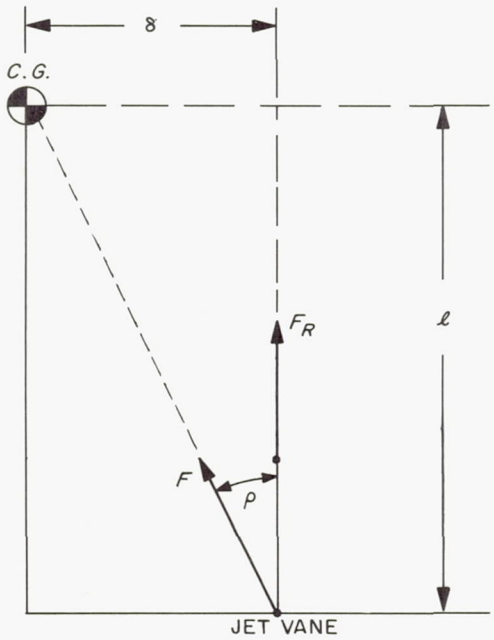

Fig. D-11. Center-of-gravity offset

Technical Report No. 32-663

Ranger Block III Attitude Control System

Will Turk

R. G. Forney, Chief
Spacecraft Control Section

JET PROPULSION LABORATORY
CALIFORNIA INSTITUTE OF TECHNOLOGY
PASADENA, CALIFORNIA

November 15, 1964

Prepared Under Contract No. NAS 7-100
National Aeronautics & Space Administration

CONTENTS

CONTENTS (Cont'd)

TABLES

FIGURES

FIGURES (Cont'd)

FIGURES (Cont'd)

FIGURES (Cont'd)

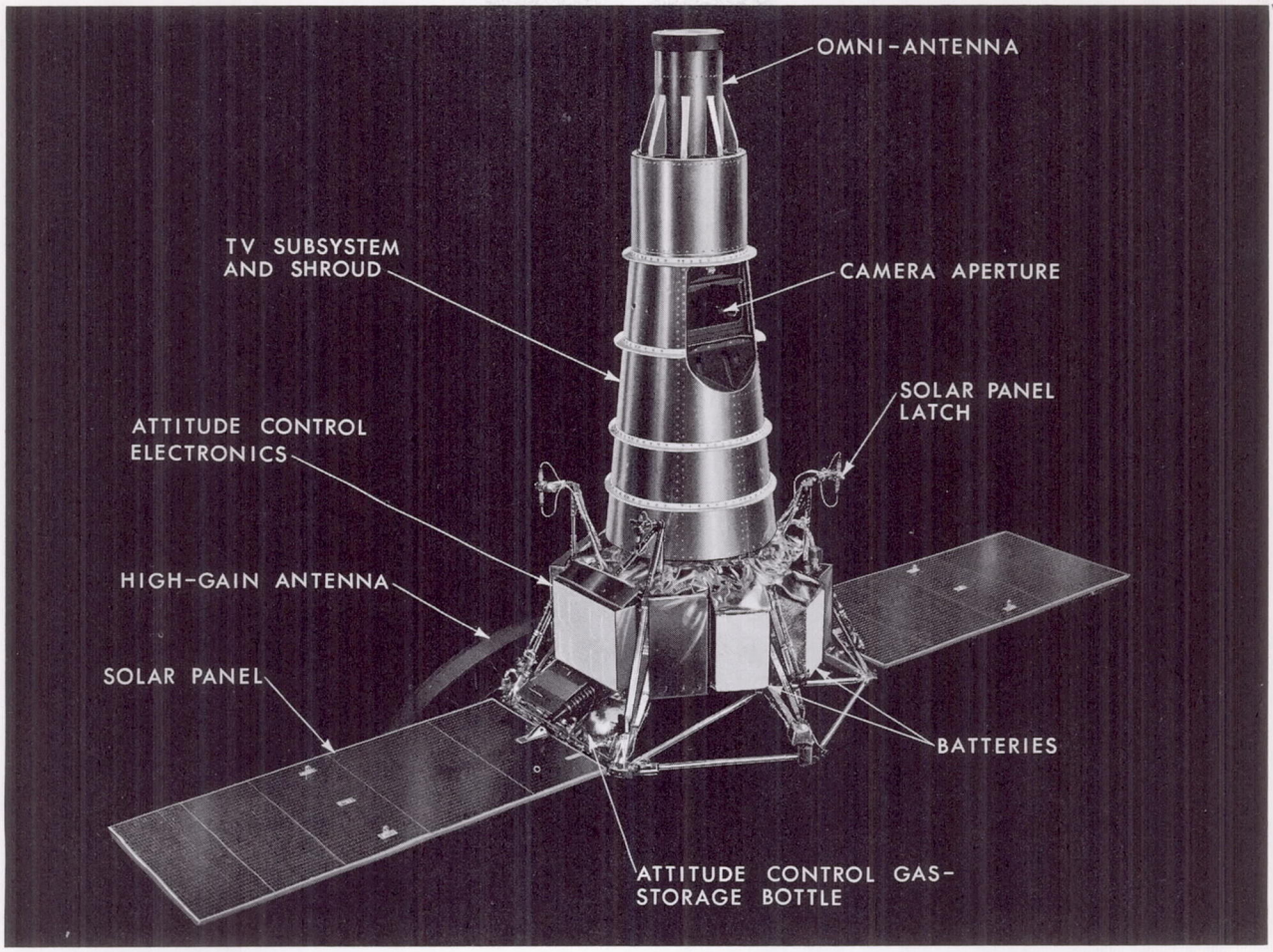

***Ranger* spacecraft, Block III configuration**

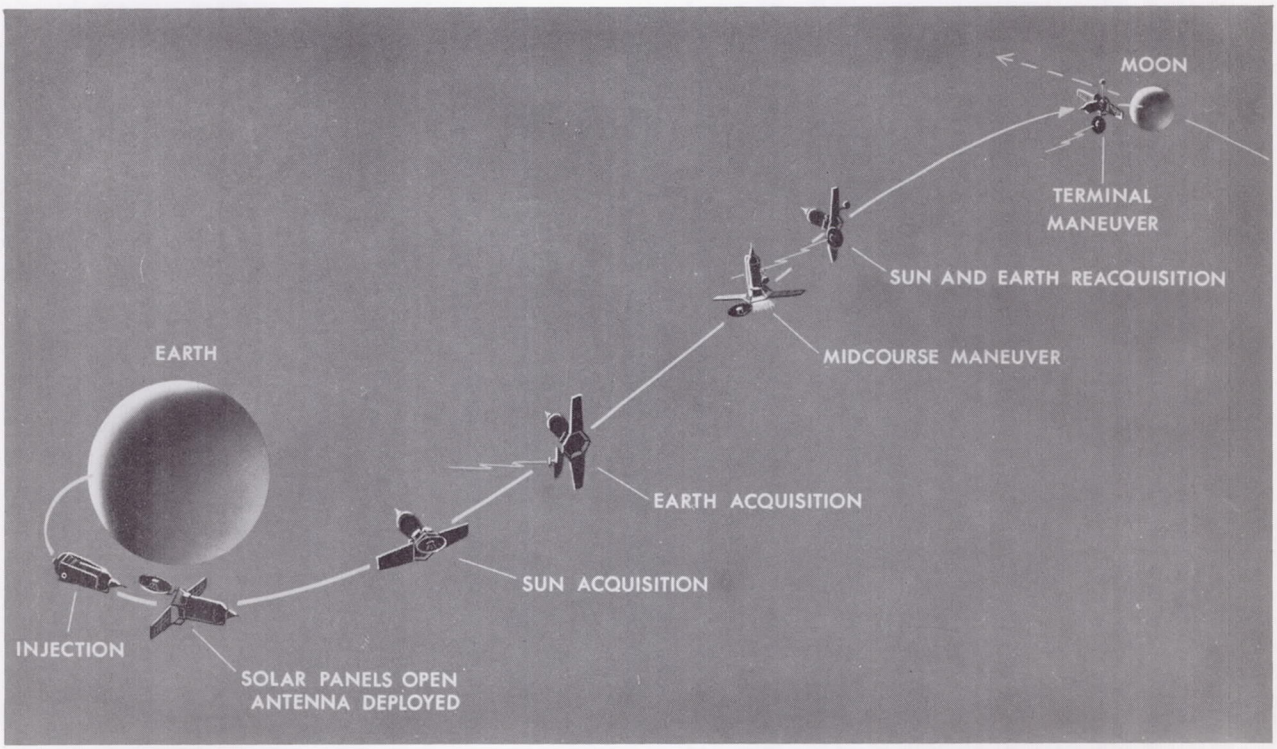

Spacecraft trajectory

FIGURES (Cont'd)

PREFACE

The *Ranger* program was established in 1959 to investigate the surface of the Moon through the use of several scientific experiments. The program was separated into three missions, each having a primary objective. *Ranger* Block I (*RA* 1, 2) served as an interplanetary vehicle which evaluated the basic systems of the spacecraft; Block II (*RA* 3, 4, 5), which was the first lunar mission, carried a gamma-ray instrument, a television (TV) camera, and a seismometer capsule. The Block III (*RA* 6, 7, 8, 9) effort is purely a photographic mission designed to obtain high-resolution close-up pictures of the lunar surface.

The function of the *Ranger* Block III attitude control system is to stabilize and control the *Ranger* vehicle orientation from second-stage separation until lunar encounter.

The *Ranger* system utilizes an *Atlas* booster for its first stage, an *Agena* B second stage, and the JPL *Ranger* spacecraft. The basic configuration of the Block III (*Ranger* 6 through 9) consists of a hexagonal frame composed of electronic packages; two erectable solar-power panels, a television experiment, and a movable parabolic high-gain communications antenna. The spacecraft configuration is shown on the adjacent page.

The spacecraft trajectory, approximately 68 hrs, is also shown on the adjacent page. The spacecraft is initially confined within a shroud for environmental protection during the launch phase. The shroud is ejected following the *Atlas* sustainer burn-out. At the conclusion of the first *Agena* burn, the spacecraft is in a coasting or parking orbit. A second ignition and burn of the *Agena*, concluding in spacecraft injection into an impact trajectory with the Moon, is followed by the separation of the spacecraft from the *Agena* B.

After separation, the spacecraft's Sun and Earth acquisition sequence is initiated. The attitude control system is activated, the solar panels are erected, and the high-gain antenna is rotated to a preset hinge angle. Sun sensors provide position errors which control the attitude control jets and provide for pointing the roll axis of the vehicle towards the Sun, thus placing the solar cells in such a position so that they have the maximum illumination. The solar power system is now in operation. The spacecraft is next commanded to turn about the roll axis until the high-

PREFACE (Cont'd)

gain antenna beam lies in the plane defined by the spacecraft roll axis and the Earth. The Earth sensor provides the roll and hinge angle control for the antenna actuator by measuring the error signal and feeding it back so that the antenna rotates about the hinge axis, orientating the propagation axis normal to the Earth, establishing the high-gain communication link. The vehicle is then in the cruise phase.

After approximately 16 hrs in the cruise phase, the required trajectory corrections (if needed) are transmitted to the spacecraft. The result of the midcourse maneuver is the reorientation of the spacecraft by commanding the proper turns to accomplish the trajectory correction. Following this maneuver, the Sun and Earth are re-acquired. Upon the approach to the lunar surface, the terminal maneuver is performed to align the television cameras for high resolution pictures of the Moon.

ACKNOWLEDGEMENT

In mid-1963, general requirements to complete a Report containing the complete history and description of the *Ranger* Block III attitude control system were established by Mr. R. Forney, Chief of the Spacecraft Control Section of the Jet Propulsion Laboratory (JPL). Several discussions with Mr. Forney, Mr. S. Szirmay (Group Supervisor in the Spacecraft Control Section), and Mr. R. Hill (Attitude-Control Project Engineer on the *Ranger* program) helped to set the specific approach of the Report as one that would discuss the analyses conducted, in order to formulate the *Ranger* Block III attitude-control system configuration.

Special acknowledgement is made to Mr. H. K. Bouvier, Mr. A. E. Cherniack, Mr. J. Dahlgren, and Mr. H. Nakano for their critical analyses, contributions, and many suggestions in helping to prepare this comprehensive document. Also, an extensive list of responsible personnel contributing significantly to this Report may be found in Appendix I; this listing of supplemental documents, for the most part, is not generally available for off-Laboratory distribution. Additional acknowledgement is made to Mr. F. Ray, of the Technical Reports Department, for his services as Editor of the entire Report.

This Report was compiled while the writer (Mr. W. Turk), a senior research engineer at the Northrop Space Laboratory (Hawthorne, California), was a JPL contractor-in-residence for the *Ranger* Block III mission, serving as part of the flight-analysis team of the Guidance and Control division for the *Ranger* 6 and 7 missions during the past year.

ABSTRACT

This Report describes the attitude control system designed to orientate, stabilize, and maneuver the *Ranger* spacecraft in its mission to obtain the first detailed close-up television (TV) pictures of the Moon's surface. The system is capable of three-axis orientation, midcourse trajectory correction, and terminal orientation for picture-taking. The attitude control system is composed of several subsystems: the inertial sensors to sense the rates and positions about each axis and to serve in a trajectory correction and orientation during terminal; the celestial sensors to provide for the Sun and Earth reference coordinates for the three-axis position stabilization; and, the gas jet system to provide the torque control for the spacecraft. Each of the modes of spacecraft attitude control operation is discussed in detail. A complete analysis of the gas system requirements, spacecraft dynamic effects, and midcourse autopilot control, as well as the maneuver error analyses, is included in this Report. Added in the appendices is a discussion of the subsystem concept, design, and development.

I. INTRODUCTION

The specific mission of the *Ranger* Block III spacecraft is to obtain high-resolution close-up television (TV) pictures of the Moon's surface. To do so, requires precise control of the vehicle about its center of mass during the flight from the Earth launch site to the lunar surface. The ability to maintain the orientation of the spacecraft about the desired trajectory and also provide for the correction of injection errors is the function of the attitude control system. The performance requirements are derived from the over-all mission requirements and objectives for the spacecraft.

This Report is a comprehensive study of the analytical description of the attitude control system. The text of material is divided into two main sections, i.e., Spacecraft Orientation and Stabilization, and Trajectory Corrections. The Report describes and analyzes the various modes of operation of the attitude control system.

Two basic requirements imposed on the spacecraft's control system are (1) to provide for the solar-power generation to the vehicle by orientating the solar panels in such a way that the energy-producing elements are normal to the Sun, and (2) to position the directional antenna so that it is pointing toward the center of the Earth. Celestial sensors, mounted on both the solar panels and antenna arm, therefore act as the control elements in the feedback loops of the pitch, yaw, and roll axes and measure the angular displacement errors. Gyroscopes, mounted about each axis, measure and correct for the rate of

change of the spacecraft's position. The correcting torques are applied by the ejection of cold gas from an internally pressurized gas supply.

If the injection into the desired trajectory were accomplished perfectly, there would be no need for any other requirements of the attitude control system; however, a perfect trajectory is a difficult objective to attain, and to correct for the errors a maneuver must be made. The flight duration for the lunar trip is approximately 68 hrs; after about 16 hrs, the midcourse maneuver is commanded. The maneuver allows for a combination of a roll and pitch turn, and a change in the spacecraft's velocity. Furthermore, the thrusting of the midcourse correction rockets generally produces an overturning moment generated by the misalignment of the thrust vector with respect to the spacecraft center of mass. To correct for this, an autopilot loop is included in the attitude control system to overcome these moments. Stabilizing torques are supplied by jet deflection vanes acting on the propelling stream of the midcourse motor. The maneuver is conducted under both celestial and inertial control. The roll turn is made after Earth lock is disengaged; it is provided by a gyro command. After the roll turn, the Sun lock is broken and the pitch turn is commanded. The velocity increment is then added to the spacecraft's velocity vector. Communication at this time is carried on by the spacecraft's omnidirectional antenna. Re-acquisition of the celestial bodies follows the maneuver and is identical to the sequence followed during the initial acquisition.

Finally, the terminal maneuver is commanded to align and maintain the optical axis of the TV cameras parallel to the expected lunar-impact velocity vector of the vehicle. To do so, a combination pitch-yaw-pitch turn is commanded. Earth lock is maintained at this time by maintaining the communications antenna pointed toward the Earth. A functional mechanization of the *Ranger* Block III attitude control system is shown in Fig. 1.

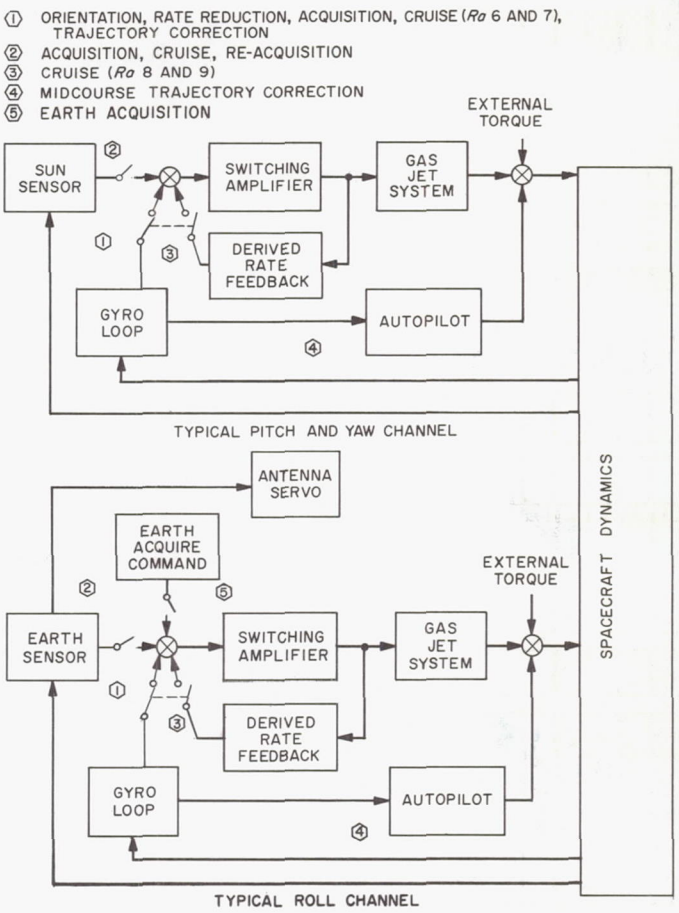

Fig. 1. *Ranger* attitude control system, general block diagram

II. SPACECRAFT ORIENTATION AND STABILIZATION

A. Discussion

Following the separation from the *Agena* booster, the *Ranger* spacecraft attitude control system is required to perform a pre-programed set of events. The vehicle is in an unstable mode of flight following its injection into the intended trajectory since control about the pitch, yaw, and roll axes is not commanded until a Sun acquisition command, some 60 min after launch. At the command for Sun acquisition, the gas-jet system is turned on, the primary and secondary Sun sensors activated, and the communications antenna slewed-out to a pre-set angle. The attitude control system is required to reduce first the initial tumbling rates created by the separation torques and then to acquire the Sun with the use of photoconductive sensors to provide for pitch and yaw position control. Rate control for the pitch and yaw axes is obtained from two single-axis integrating rate gyros, mounted about each axis. Roll control at this time is derived purely from the gyro mounted about the roll sensitive axis. Error signals, as measured by the rate and position sensors, are summed in their respective channels to operate gas-jet valve-switching amplifiers which provide an *on-off type* control torque. The high-gain directional antenna must be rotated, from its stowed position beneath the spacecraft bus about a hinge axis which is perpendicular to the roll axis and parallel to the pitch axis of the spacecraft, to one of eight pre-set angles. The choice of the particular angle is dependent upon the trajectory relationships between the Earth, Moon, and Sun; the angle is selected so that it is very close to the expected Earth acquisition angle.

At launch plus 3½ hrs, the command for Earth acquisition is made. The dc power is instantly applied to the Earth sensor, the secondary Sun sensors are turned off, and a roll search is initiated. The roll search commands the spacecraft to rotate at a constant velocity in a clockwise direction about the Sun (roll) axis. The Earth sensor, mounted colinearly with the antenna, tracks and acquires the Earth, thus providing roll-position control, and the antenna hinge servo maintains the communications antenna pointed toward the Earth. Earth acquisition is completed within a 30-min duration.

The *Ranger* spacecraft is now under three-axis control in the Sun-Earth coordinate reference system. This phase of the *Ranger* mission is considered to be the cruise mode. During the cruise, which is of 60-hr duration, stabilization of the spacecraft is obtained by control torques provided by a cold gas-mass expulsion system operating in an *on-off* fashion as mentioned above. Pairs of gas-jet nozzles are precisely mounted about the three spacecraft axes (operating from a dual gas source) and provide the corrective torquing. A position limit cycle is established with the switching-amplifier deadband. The rate feedback signal provides the proper damping. If some unexpected noncatastrophic event takes place, the cruise attitude control mode provides for the automatic re-acquisition of the Sun and Earth.

B. Orientation Requirements and Constraints

The trajectory constraints imposed on and by the attitude control system have a gross effect on the spacecraft trajectory and launch window. The trajectory constraints for the orientation phase are the following:

1. The spacecraft must be in the sunlight for 1 hr prior to Earth acquisition, and continuously thereafter.

2. The illuminated portion of the Earth, as seen from the spacecraft, must be within the bounds of the angular range from 32 to 148 deg relative to the probe-Sun line at the time of the Earth acquisition command. This corresponds to an Earth-probe-Sun (EPS) angle constraint of 40 to 135 deg at a distance of 64,000 km. The Earth-light incident on the spacecraft sensors at the start of the Earth acquisition must be greater than 0.7 ft-candles.

3. The Earth-light incident at the spacecraft must be between 0.06 and 40 ft-candles from the Earth acquisition to the end of the mission.

4. The high-gain antenna must be pointed within 5 deg of the Earth receiving station. Transmission and reception are received through the omni-antenna until approximately 4 hrs after launch when the high-gain antenna becomes active.

If the lower EPS angle and the incident light constraint, given in (2) above, are exceeded, the Earth sensor may track reflections from the spacecraft, lose Earth lock, and drive the antenna outward to an angle such that a subsequent acquisition is impossible. Under these conditions, a mission success depends upon the successful execution of the roll override command, RTC-1 (Real Time Command No. 1).

C. Separation and Initial Tumbling Rate Reduction

1. Pitch and Yaw Channels

Upon separation of the *Ranger* spacecraft from the *Agena* B, a maximum random tumbling motion may be imparted to the vehicle with rates of 52.4 mrad/sec. This tumbling rate represents a maximum moment of momentum of 32.5 ft-lb/sec.

The rate reduction is not initiated until the Sun acquisition command is given. As mentioned previously, the gyros are constantly sensing the error signals in rate about the three orthogonal axes. Upon the reception of the Sun acquisition command, the switching amplifiers are turned on. The gyro signals activate the gas system so that corrective torques reduce the angular velocity. The Sun sensors, mounted on two solar panels extending from the spacecraft, are also turned on at this instant. These sensors measure the difference of the light energy absorbed from the Sun and relay this measurement as a position signal. Since the maximum error signal available is sufficiently below that of the maximum gyro output, the rate signal controls the firing of the gas jets during tumbling. The Sun sensors are subject to saturating behavior and do not operate in their characteristic linear region until the error signal is reduced sufficiently. At that time, rate and position control is available to further eliminate the error signals. A block diagram of the *Ranger* spacecraft attitude control system is shown in Fig. 2; a single-axis representation is illustrated.

a. Initial rate reduction. The behavior of the attitude control system during the Sun acquisition mode is based on reducing first the initial rate and then acquiring the Sun. The analysis which follows is conducted under the following assumptions:

1. That thrust of the gas jets is constant.
2. That position and rate sensor dynamics are neglected.
3. That no external disturbance torques act upon the vehicle.

The differential equation that characterizes system behavior is:

$$\varepsilon(t) = K_S \theta_i(t) + K_G \dot{\theta}_i(t) \tag{1}$$

where

$\varepsilon(t)$ = error signal, actuating switching amplifier

K_S = position sensor gain

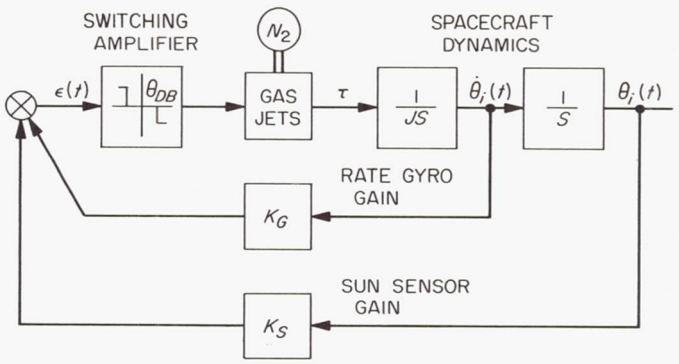

Fig. 2. Single axis pitch or yaw control loop

K_G = rate sensor gain

θ_i = vehicle angular position

$\dot{\theta}_i$ = vehicle angular rate

i = notation for pitch (p) or (y) yaw

Both spacecraft position and rate are sensed by a Sun sensor and rate gyro, respectively. The signals from these sensing elements are then mixed, and together they control the switching action of the *on-off type* amplifier which in turn operates the gas jets, applying a corrective torque to the vehicle.

The rate-reduction analysis is studied by the use of the phase-plane diagram. The switching lines which describe the characteristics of the systems behavior [Eq. (1)] may be obtained by separating Eq. (1) into a linear and saturated region. The analysis follows below.

In the linear region:

$$\varepsilon(t) = (K_S)\,\theta(t) + (K_G)\,\dot{\theta}(t) \tag{2}$$

Dividing both sides by K_S,

$$\frac{\varepsilon(t)}{K_S} = \theta(t) + \left(\frac{K_G}{K_S}\right)\dot{\theta}(t) \tag{3}$$

The deadband of the switching amplifier is represented by

$$-\varepsilon_{DB} \leqq \varepsilon(t) \leqq +\varepsilon_{DB} \tag{4}$$

Therefore, the position deadband is given by

$$\pm\theta_{DB} = \frac{\pm\varepsilon_{DB}}{K_S} \tag{5}$$

where

θ_{DB} = position deadband

ε_{DB} = switching amplifier electrical deadband

If Eq. (5) is substituted into Eq. (3) along with the substitution of the rate to position gain by

$$\tau_G = \frac{K_G}{K_S} \tag{6}$$

then, the equation of the system switching line in the linear region is

$$\pm\theta_{DB} = \theta(t) + \tau_G \dot{\theta}(t) \tag{7}$$

In the saturated region:

When the Sun sensor output saturates,

$$\varepsilon_S = K_S \theta_{S_s} \tag{8}$$

where

ε_S = Sun sensor saturated output

θ_{S_s} = Sun sensor saturated displacement

Therefore, the maximum position signal is

$$\theta(t) = \theta_{S_s} \tag{9}$$

Substituting Eq. (9) back into Eq. (7) yields

$$\pm\theta_{DB} = \theta_{S_s} + \tau_G \dot{\theta}(t) \tag{10}$$

Since the position deadband is a fixed value, as are the rate to position gain and the sensor saturation level, then Eq. (10) may be rewritten as

$$\dot{\theta}(t) = \frac{(\pm\theta_{DB} - \theta_{S_s})}{\tau_G} \tag{11}$$

which represents the velocity switching lines in the phase plane.

The phase trajectories are determined by integrating the identity

$$\ddot{\theta} = \dot{\theta}\frac{d\dot{\theta}}{d\theta} = \alpha \tag{12}$$

which yields

$$\tfrac{1}{2}(\dot{\theta}^2 - \dot{\theta}_o^2) = \pm\alpha(\theta - \theta_o) \tag{13}$$

Equation (13) represents a parabolic trajectory in the phase plane since the acceleration due to the gas jets (and hence the torque) is constant.

The analysis is now extended by numerically solving the switching line and phase trajectory equations. The subsystem parameters are given in Table 1.

Table 1. Phase-plane switching-line parameters, pitch and yaw

Parameter	Description	Nominal	Maximum	Minimum
K_S	Sun sensor scale factor	−18.5 v/deg ±10%	16.65 v/deg	20.45 v/deg
τ_G	Rate to position gain	3.18 sec ±10%	3.5 sec	2.86 sec
θ_{S_s}	Sun sensor saturation	±17.5 mrad ±7%	18.73 mrad	16.27 mrad
θ_{DB}	Switching amplifier deadband	±2.5 mrad ±10%	2.75 mrad	2.25 mrad

b. Phase plane of the initial rate reduction. The expression which describes the control of the gas jets is given in Eq. (11). Here it states mathematically that the switching amplifier-control voltage is a function of the position and rate sensors and their respective gain constants. Based upon this equation, the switching lines are derived and shown in Fig. 3.

Maximum acquisition rate—upper limit:

$$\dot{\theta} = -\frac{\theta_{S_s}}{\tau_G} - \frac{\theta_{DB}}{\tau_G}$$

$$= -\frac{18.73\,\text{mrad}}{2.86\,\text{sec}} - \frac{3.5\,\text{mrad}}{2.86\,\text{sec}}$$

$$= -(6.55 + 1.23)\,\text{mrad/sec}$$

$$\dot{\theta}_{max_{UL}} = --7.78\,\text{mrad/sec} \tag{14}$$

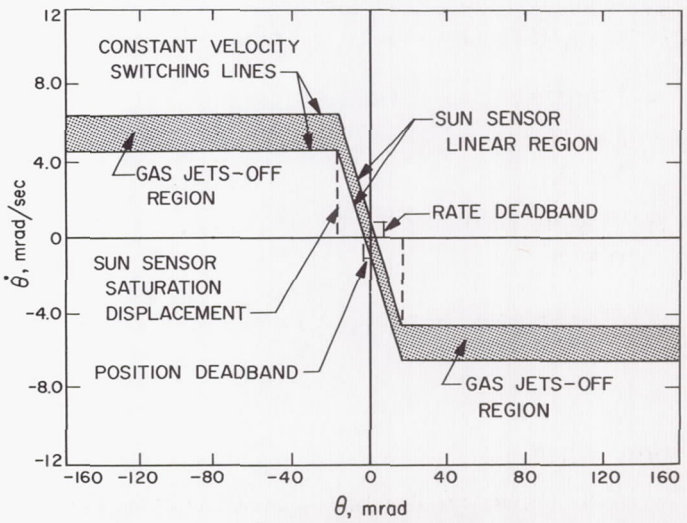

Fig. 3. Phase plane for the pitch and yaw channel

Nominal acquisition rate:

$$\dot{\theta} = \frac{-\theta_{S_8}}{\tau_G}$$

$$= \frac{-17.5 \text{ mrad}}{3.18 \text{ sec}}$$

$$\dot{\theta}_{nom} = -5.51 \text{ mrad/sec} \tag{15}$$

Minimum acquisition rate—lower limit:

$$\dot{\theta} = -\frac{\theta_{S_8}}{\tau_G} + \frac{\theta_{DB}}{\tau_G}$$

$$= -\frac{16.27 \text{ mrad}}{3.52 \text{ sec}} + \frac{3.08 \text{ mrad}}{3.52 \text{ sec}}$$

$$= -(4.62 - 0.875) \text{ mrad/sec}$$

$$\dot{\theta}_{min_{LL}} = -3.75 \text{ mrad/sec} \tag{16}$$

The rate deadband is determined for the system by setting the angular displacement to zero.

Rate deadband:

$$\dot{\theta} = \pm\frac{\theta_{DB}}{\tau_G}$$

$$= \pm\frac{2.8 \text{ mrad}}{3.18 \text{ sec}}$$

$$\dot{\theta}_{DB} = \pm 0.88 \text{ mrad/sec} \tag{17}$$

The maximum and minimum acquisition rate is therefore obtained by combining Eq. (15) and (17).

$$\dot{\theta}_{max} = \dot{\theta}_{nom} + \dot{\theta}_{DB}$$

$$= 5.51 \text{ mrad/sec} + 0.88 \text{ mrad/sec}$$

$$\dot{\theta}_{max} = 6.39 \text{ mrad/sec} \tag{18}$$

$$\dot{\theta}_{min} = \dot{\theta}_{nom} - \dot{\theta}_{DB}$$

$$= 5.51 \text{ mrad/sec} - 0.88 \text{ mrad/sec}$$

$$\dot{\theta}_{min} = 4.63 \text{ mrad/sec} \tag{19}$$

The specified maximum *Agena* separation velocity that is tolerable is given as $\theta = 3$ deg/sec $= 52.4$ mrad/sec about each axis. This velocity constraint, together with the spacecraft switching lines, is shown in Fig. 4.

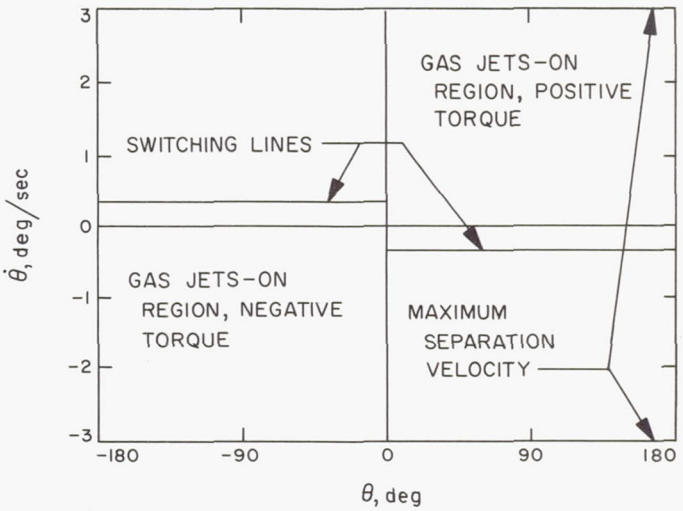

Fig. 4. Phase plane showing the maximum separation velocity

The equation of the spacecraft's trajectory assuming zero initial conditions and an acceleration constant of $\alpha = 0.6$ mrad/sec^2 yields from Eq. (13)

$$\theta = \frac{1}{2}\left(\frac{\dot{\theta}^2}{\alpha}\right)$$

$$= 0.835\dot{\theta}^2 \tag{20}$$

As an example of the spacecraft's trajectory during the initial rate reduction period, we can assume that the vehicle is tumbling at a rate of 2 deg/sec with a displacement of $\theta = -90$ mrad. The trajectory is shown in Fig. 5, point A. As it is shown, the trajectory intersects the upper switching line and then coasts in toward the origin. If the displacement is now chosen as $\theta = +90$ mrad, the switching occurs at the lower line as indicated by the trajectory emanating from point B.

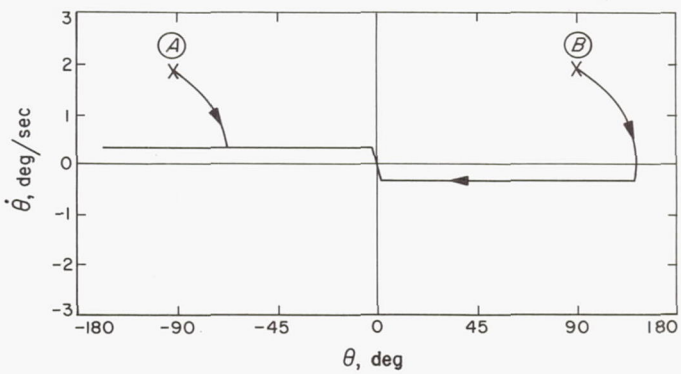

Fig. 5. Typical trajectories for the pitch and yaw initial rate reduction

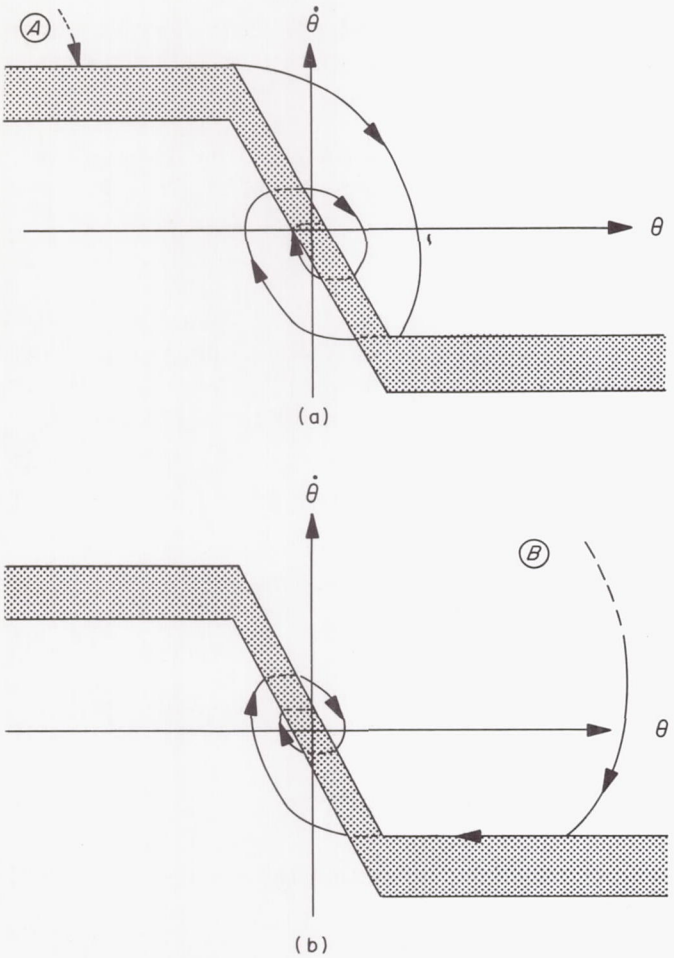

Fig. 6. General phase plane diagrams of initial rate reduction and acquisition from both the upper and lower switching lines

A blowup of the origin shows the switching lines and also indicates the acquisition trajectories, Fig. 6.

If the rate were negative, the trajectories would lie in the bottom portion of the phase plane and follow the identical type of loci. The controlled portion of flight, i.e., outside of the switching-line deadband, is indicated in Fig. 4.

2. Roll Mode

The block diagram of the roll mode during the separation rate reduction is similar to that of pitch and yaw; however, there is no position control prior to Earth acquisition. Fig. 7 shows a block diagram of the roll channel.

During the rate reduction phase of the spacecraft orientation and stabilization, the vehicle is controlled in roll

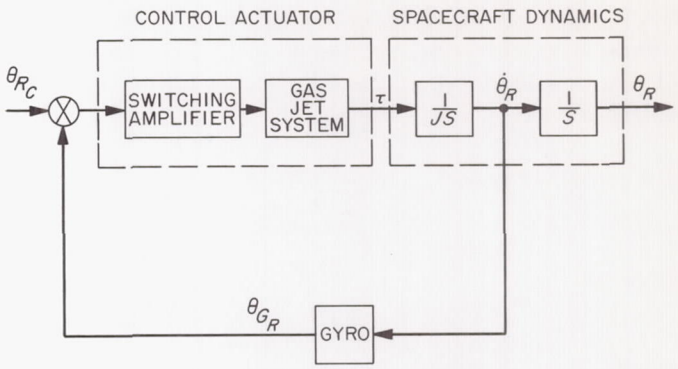

Fig. 7. Roll channel block diagram, initial rate reduction

by the integrating rate gyro. Therefore, the initial conditions in roll are such that the gas jets are on until the vehicle rates are reduced to the rate deadband which is $\theta = 0.919$ mrad/sec. The phase plane for the roll mode is shown in Fig. 8.

If the initial conditions in roll were given by some rate and displacement at points A or B, the roll correcting torques would be applied to the spacecraft by the gas jets until the trajectory of rate and position intersected the rate deadband. At this time, the spacecraft rate would remain constant and the gas jets turned off. If the vehicle is initially within the rate deadband, the gas system will not be turned on since there would be no error signal.

3. Gas Requirements for Initial Rate Reduction

The gas required in order to eliminate the angular rates produced by the separation torques is determined

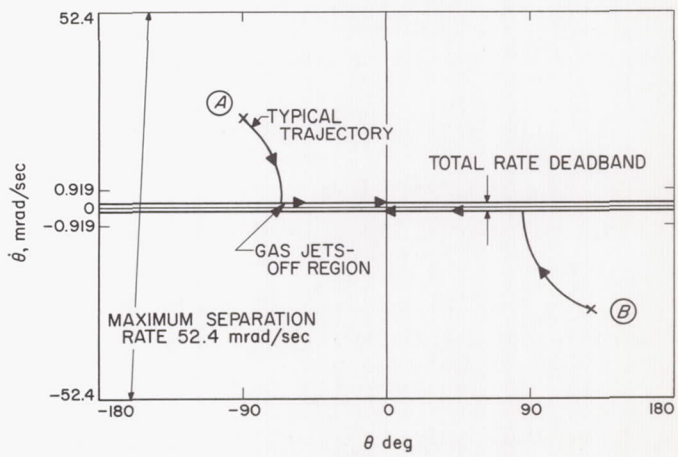

Fig. 8. Typical trajectories for the roll initial-rate reduction

by a worst case analysis of a single axis. The gas consumption calculations are based upon the computation of the gas jet-on time, i.e., the elapsed time that the valves are on.

Therefore, since

$$\tau = I\alpha \tag{21}$$

and also

$$\tau = FL \tag{22}$$

where

$$F = \dot{W} I_{sp} \tag{23}$$

and where

τ = torque due to gas expulsion

F = force due to gas expulsion

W = gas weight flow rate

I_{sp} = specific impulse of the gas

L = lever arm of the gas jets

then, by substituting Eq. (22) and (23) into (21),

$$I\alpha = FL = \dot{W} I_{sp} L \tag{24}$$

and, rewriting yields

$$\dot{W} = \frac{I\alpha}{I_{sp}L} \frac{\text{lb}}{\text{sec}} \tag{25}$$

The above expression represents the rate of flow of the gas during the jet firing. The amount of gas expended is given by the expression

$$W = \frac{I\alpha}{I_{sp}L} t_{on} \text{ (lb)} \tag{26}$$

As given by Eq. (11), the saturated sensor rate deadband is

$$\dot{\theta}_s = \frac{(\theta_{DB} - \theta_s)}{\tau_G} \tag{27}$$

The rate may also be defined by the equation

$$\dot{\theta}_s = \pm\alpha t_{on} + \dot{\theta}_o \tag{28}$$

which is rewritten as the total change in rate

$$\Delta\dot{\theta} = (\dot{\theta}_s - \dot{\theta}_o) = \pm\alpha t_{on} \tag{29}$$

Finally, the total *on* time during deceleration is given by

$$t_{on} = \frac{\Delta\dot{\theta}}{\alpha} \text{ (sec)} \tag{30}$$

Equations (25), (26), and (30) define the amount of gas required during any control period that the gas valves are open.

Some typical values are computed for the pitch, yaw, and roll initial rate reduction based upon the *Ranger* 6 parameters, Table 2.

Pitch and yaw channel:

$$\dot{\theta}_S = \frac{-17.5 \text{ mrad} + 2.8 \text{ mrad}}{3.2 \text{ sec}} = -4.6 \text{ mrad/sec} \tag{31}$$

$$\theta = 52.4 \text{ mrad/sec} - 4.6 \text{ mrad/sec} = 47.8 \text{ mrad/sec} \tag{32}$$

$$t_{on} = \frac{47.8 \text{ mrad/sec}}{0.6 \text{ mrad/sec}^2} = 80 \text{ sec} \tag{33}$$

Roll channel:

$$\dot{\theta}_S = \frac{-17.5 \text{ mrad} + 5.0 \text{ mrad}}{5.45 \text{ sec}} = -2.29 \text{ mrad/sec} \tag{34}$$

$$\theta = 52.4 \text{ mrad/sec} - 2.3 \text{ mrad/sec} = 51 \text{ mrad/sec} \tag{35}$$

$$t_{on} = \frac{51 \text{ mrad/sec}}{0.6 \text{ mrad/sec}^2} = 85 \text{ sec} \tag{36}$$

If we assume a continuous gas discharge

$$I_{sp} = I_c = 70 \text{ sec} \tag{37}$$

then from Eq. (26),

$$W = \frac{I\alpha}{I_{sp}L} t_{on} \tag{38}$$

Table 2. Some typical *Ranger* 6 parameters

Moments of Inertia:		I_{xx} = 92 slug-ft^2 I_{yy} = 113 slug-ft^2 I_{zz} = 60 slug-ft^2
Gas Jet Moment Arms:		L_P = 2.42 ft L_Y = 1.83 ft L_R = 2.19 ft
Gas Jet Specific Impulse:	Continuous Discharge Hysteresis System Derived Rate	I_c = 70 sec I_h = 45 sec I_D = 35 sec
Acceleration Constant:	Full-Gas System Half-Gas System	α = 0.6 mrad/sec^2 α = 0.3 mrad/sec^2
Rate to Position Gain:	Pitch and Yaw Roll	τ_G = 3.2 sec τ_G = 5.45 sec
Sun Sensor Saturation:	All Axes	θ_{S_s} = 17.5 mrad
Switching Amplifier Deadband:	Pitch and Yaw Roll	θ_{DB} = ±2.8 mrad θ_{DB} = ±5.0 mrad
Limit Cycle Rate Increment:	Hysteresis Derived Rate	θ_h = ±60 μrad/sec θ_D = ±18 μrad/sec

so

$$W_{pitch} = \frac{92 \text{ slug-ft}^2 (0.6 \text{ mrad/sec}^2)}{70 \text{ sec } (2.42 \text{ ft})} 80 \text{ sec}$$

$$= 2.61 \times 10^{-2} \text{ lb} \quad (39)$$

$$W_{yaw} = \frac{113 \text{ slug-ft}^2 (0.6 \text{ mrad/sec}^2)}{70 \text{ sec } (1.83 \text{ ft})} 80 \text{ sec}$$

$$= 4.24 \times 10^{-2} \text{ lb} \quad (40)$$

$$W_{roll} = \frac{60 \text{ slug-ft}^2 (0.6 \text{ mrad/sec}^2)}{70 \text{ sec } (2.20 \text{ ft})} 85 \text{ sec}$$

$$= 1.98 \times 10^{-2} \text{ lb} \quad (41)$$

The total gas required for the initial rate reduction is

$$W = 8.93 \times 10^{-2} \text{ lb} \quad (42)$$

D. Acquisition Phase

The orientation of the vehicle prior to the Sun and Earth acquisition is random due to the vehicle tumbling arbitrarily in space. After the initial separation rates are eliminated, the vehicle is prepared to follow a predetermined sequence of events in order to establish the reference coordinate system desired. To do so, the Sun and the Earth must be sought. Two sensing systems are required: (1) the Sun sensor must have a 4-π steradian field of view, since its position in space is unknown and a complete rotation of the spacecraft might be desired, and (2) after acquiring the Sun, the Earth sensor is required to locate the Earth. The Earth sensor field of view is constrained to ± 10 deg in hinge angle movement and ± 5 deg in roll angular displacement; the reasons are discussed in Appendix E.

The phase plane diagrams derived in Section II-C, above, described the switching lines basic to the pitch, yaw, and roll channels. The actual acquisition trajectories are derived based on a system acceleration constant of $\alpha = 0.6$ mrad/sec^2. The duration for the acquisition may be established by measuring the total time the gas jets are on.

1. Sun Acquisition

The block diagram describing the Sun acquire mode is identical to that shown in Fig. 2. At the instant the Sun acquire command is accepted by the spacecraft, the Sun sensors located on both sides of the extended solar panels provide the position error signals (assuming that the vehicle is not already pointing directly at the Sun). The pitch and yaw position errors are mixed, respectively, with the gyro signals about both the pitch and yaw axes, and the corrective torques are applied. The orientation of the spacecraft is such that the $-Z$ axis (roll axis) is pointed directly toward or normal to the Sun.

The phase plane trajectories for both the upper and lower switching lines are shown in Fig. 9. The *on* time, as mentioned earlier, is computed from the following equation:

$$t_{on} = \frac{\dot{\theta} - \dot{\theta}_o}{\ddot{\theta}} \quad (43)$$

where

$\dot{\theta}_o$ = initial rate at switching line

$\dot{\theta}$ = instantaneous rate

$\ddot{\theta} = \alpha$ = spacecraft acceleration (0.6 mrad/sec)

The equation of the trajectory (zero initial conditions) is given by Eq. (20) as

$$\theta = 0.835 (\theta)^2$$

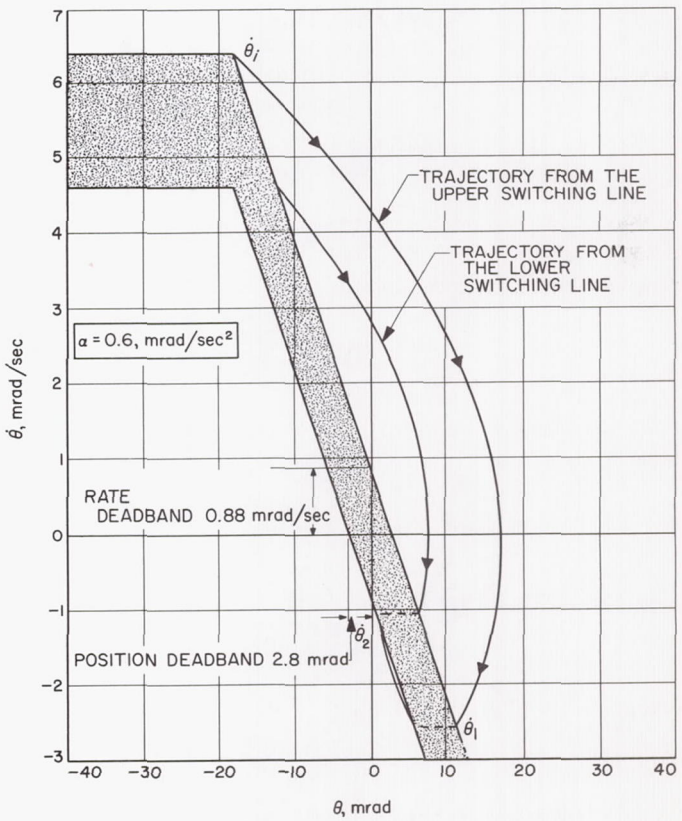

Fig. 9. Pitch and yaw acquisition transients obtained from the upper and lower switching lines

The *on* time is determined by substituting the values obtained from Fig. 9 into Eq. (43). From Fig. 9,

$$\theta_o = 6.39 \text{ mrad/sec}$$

$$\theta_1 = -2.56 \text{ mrad/sec}$$

$$\theta_2 = -1.3 \text{ mrad/sec}$$

and therefore

$$t_{on} = \frac{\theta_o + \theta_1}{\theta} + \frac{\theta_1 + \theta_2}{\theta}$$

Thus,

$$t_{on} = 17.0 \text{ sec} \tag{44}$$

2. Earth Acquisition

To complete the three-axis attitude stabilization, the roll axis must be controlled. As mentioned in Section II-A, above, the Earth sensor is mounted on the same hinged arm that supports the antenna and is, in fact, fixed to the vehicle with respect to motions about the roll axis. The arm supporting the Earth sensor is erected from its nested position to a preset angle with respect to the vehicle's roll axis during the Sun acquisition, as shown in Fig. 10. This hinge angle is physically set by the choice of a position on an eight-tapped voltage divider which is commanded to one of eight antenna angles. These angles, together with the other possible fixed hinge angles,

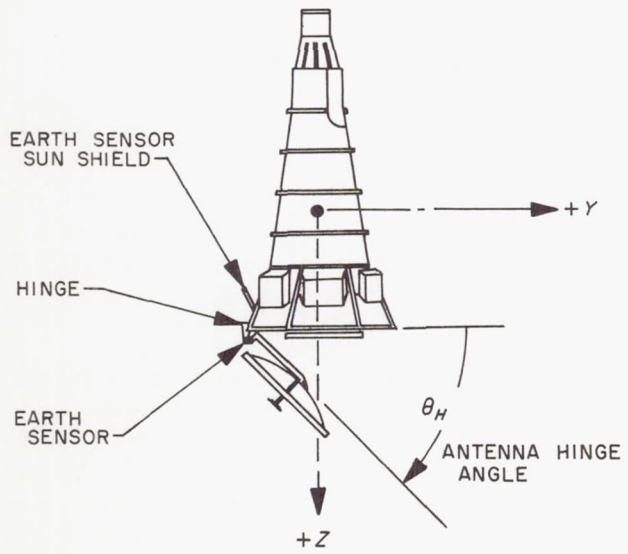

Fig. 10. Spacecraft antenna hinge angle

Table 3. Antenna angles

Angle (deg)	Comments
0	Nested—Launch only
45 135 122 109 97 84 71 58	Eight preset angles; after the last position, the cycle is repeated.
180	Exit—Midcourse only

are listed in Table 3 for a third-quarter of the Moon launch.

If for some reason the angle must be changed, a hinge override, RTC-2 (Real Time Command No. 2), or a CC&S (Central Computer and Sequencer) command for a roll maneuver is executed, and the tap on the voltage divider advances one step. This preset angle is chosen so that the Earth illuminance falls within the field of view of the Earth sensor when the spacecraft is commanded to turn about the roll axis to acquire the Earth. If the launch is attempted during the first quarter of the Moon, the circuit is wired so that the preset angle increment is increasing or opposite to the sequence given in Table 3. The field of view of the Earth sensor is 20 deg in hinge and 10 deg in roll. When the Earth is initially acquired, the error signal from the Earth sensor is used to control both the rotation of the antenna hinge servo and the spacecraft's roll axis until the vehicle is in such a position that the directional antenna is pointed directly toward the Earth, as shown in Fig. 11.

When the Earth acquisition command is given, the roll search generator is switched into the roll channel (which up to that moment has been under pure rate control). The roll search rate is $\theta = -3.78$ mrad/sec and provides for a maximum roll search duration of approximately 30 min. This allows for a complete rotation of the vehicle and is sufficient to acquire the Earth. A block diagram of the Earth acquisition phase is shown in Fig. 12. The phase plane description of this particular acquisition is shown as a sequence of events, Fig. 13. Prior to the command, the roll rate is constant as shown in Fig. 13 (Part A). Figure 13 (Part B) depicts the switching line, biased by the generator providing the search rate. The vehicle follows a parabolic trajectory that will intersect this switching line. When the Earth sensor detects the light of the Earth, the light-intensity signal actuates an Earth acquisition relay. This relay switches-out the roll

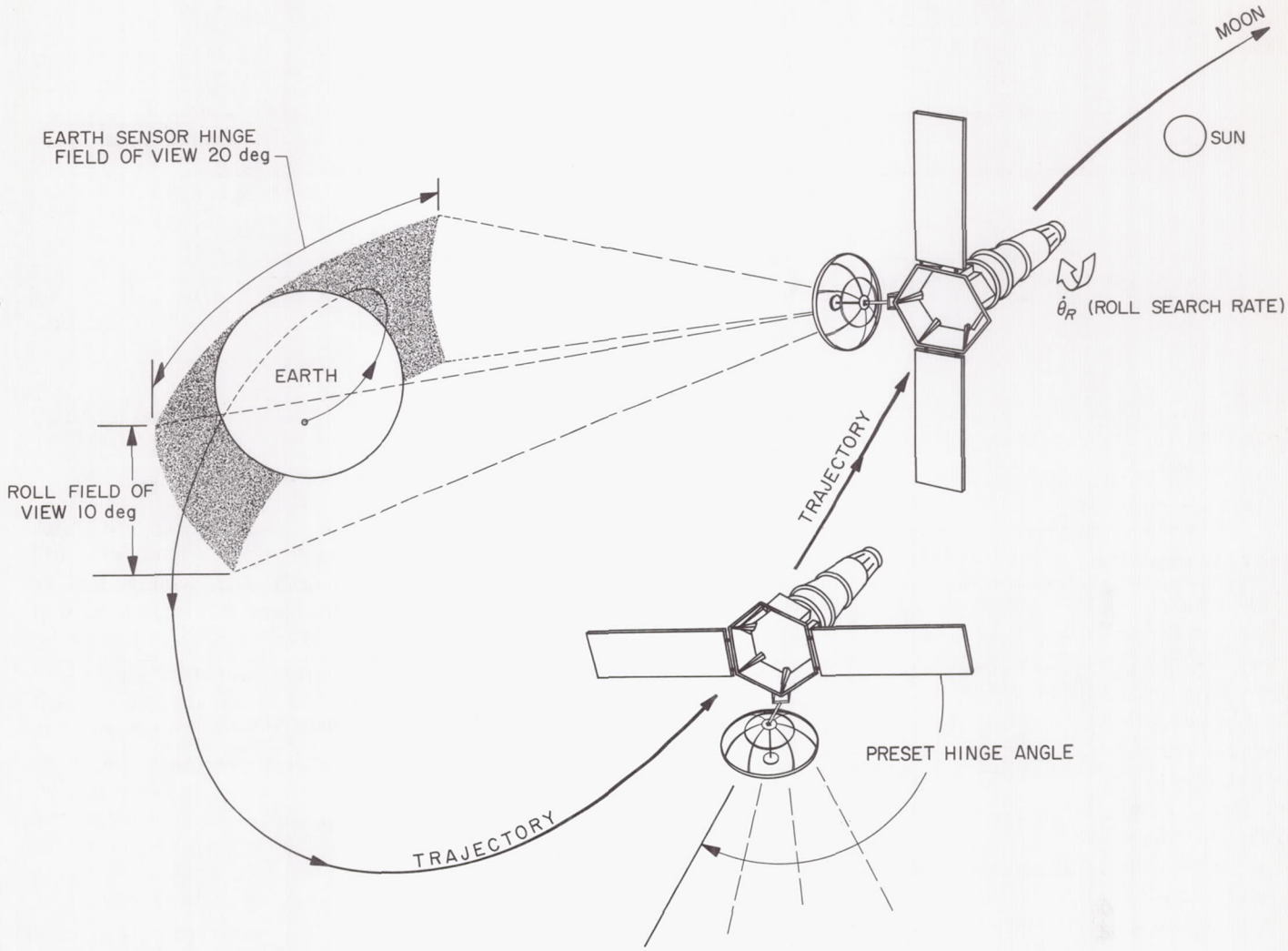

Fig. 11. Earth acquisition

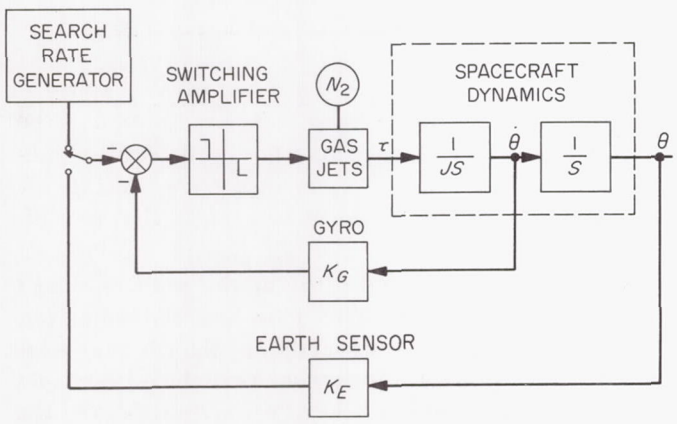

Fig. 12. Block diagram of the Earth acquire mode

search, switches-in the Earth sensor roll-position signal, and switches the hinge control from the preset angle to the hinge output of the Earth sensor. Thus, the preset angle, determined by the voltage divider, and the roll search are disconnected, and the Earth sensor assumes control of the roll and hinge orientation. The acquisition relay also switches-out the secondary Sun sensors.

The action of the hinge override is used primarily prior to launch to select the hinge orientation angle,but if the Earth sensor acquires on the Moon instead of the Earth, as is possible for some trajectories, a roll override (RTC-1) breaks the acquisition of the system about the Moon, and puts the spacecraft back into a roll search. This is accomplished by transferring this relay to the unacquired position and re-initiating roll search until the Earth sensor

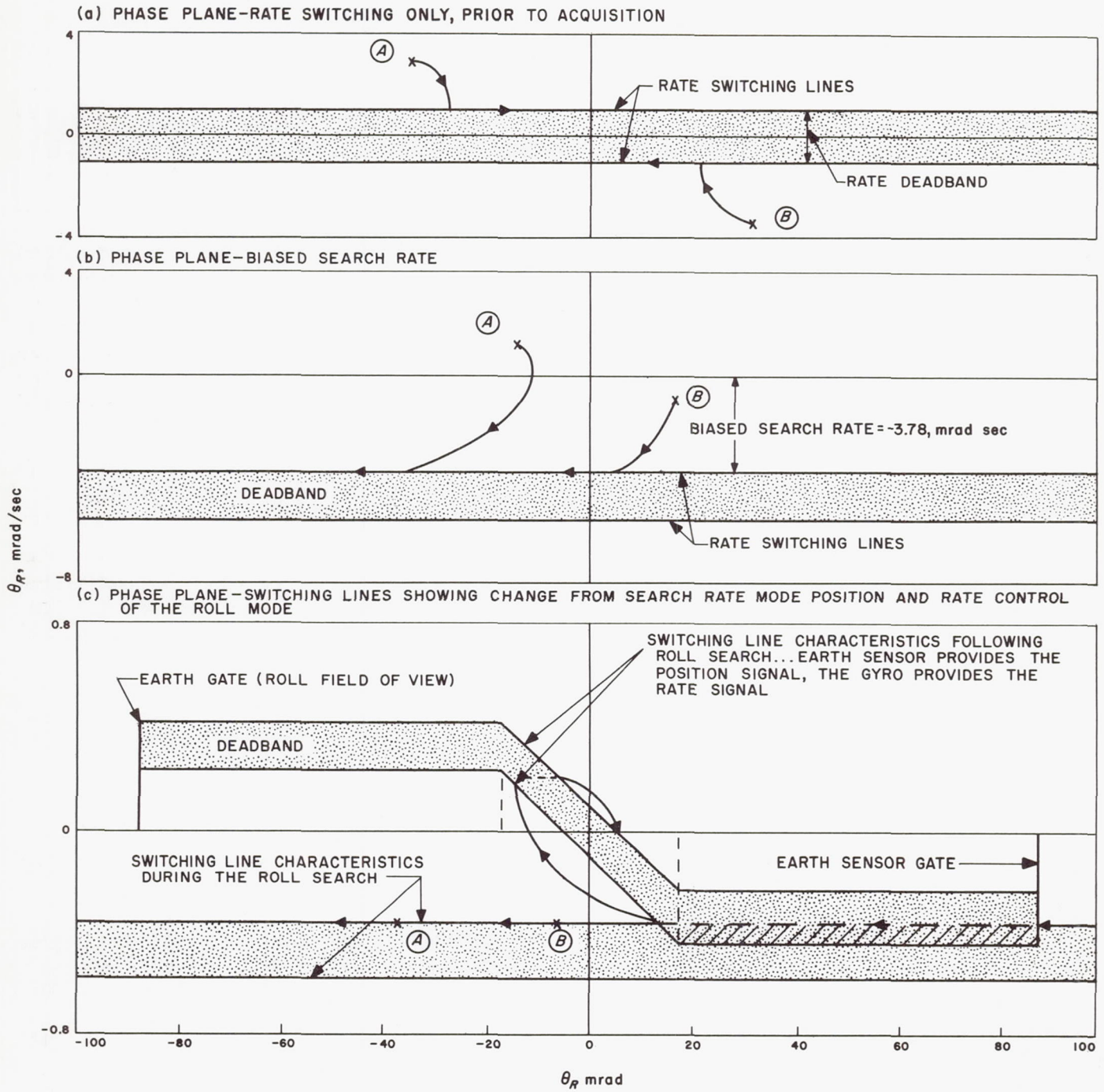

Fig. 13. Phase plane of the Earth acquire (general)

again detects light. The spacecraft then goes through a second acquisition.

Part C of Fig. 13 shows the addition of the switching lines characteristic of the rate and position-controlled roll axis. Acquisition proceeds as in the pitch and yaw modes. The equations which describe this dual control are identical to those described in the pitch and yaw analyses, Eq. (14) through (19). However, the magnitude of the roll scale factor is a function of the distance from the Earth. It is important to note that the scale factor is low when the sensor is close to the Earth, as is the case during the initial Earth acquisition; therefore, the switching lines are shallow. However, during the re-

acquisition following the midcourse maneuver, the switching lines are steeper due to the change in the Earth sensor roll scale factor. Another important point is that the roll deadband is actually electrical and is only physical at terminal maneuver ranges. The nominal value of roll deadband is used in this analysis. Since the Earth cannot be treated as a point source of light during the initial acquisition, compensation is added in terms of adjusting the measured roll position as a function of the distance and Earth-probe-Sun angle, as shown in Fig. 14. This figure was taken from results obtained from an Earth sensor computer simulation which was run for various altitudes and Earth-probe-Sun angles. The phase-plane diagram of the roll acquisition is based on the nominal parameters given in Table 4, and also the phase-plane rate characteristics given below.

Nominal acquisition rate:

$$\dot{\theta} = \pm 3.22 \text{ mrad/sec} \tag{45}$$

Rate deadzone:

$$\dot{\theta}_{DB} = \pm 0.919 \text{ mrad/sec} \tag{46}$$

Maximum acquisition rate:

$$\dot{\theta}_{max} = \pm 4.14 \text{ mrad/sec} \tag{47}$$

Minimum acquisition rate:

$$\dot{\theta}_{min} = \pm 2.3 \text{ mrad/sec} \tag{48}$$

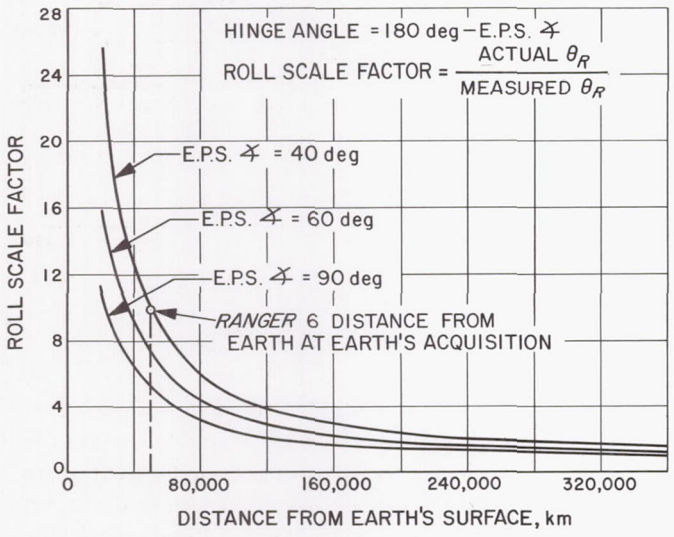

Fig. 14. Earth sensor roll-scale factor vs distance as a function of Earth-probe-Sun angle

Table 4. Roll attitude control parameters, Earth acquisition

Parameter	Description	Nominal
K_E	Earth sensor scale factor	8.0 v/deg ± 10%
τ_G	Rate to position gain	5.45 sec ± 10%
θ_{E_s}	Earth sensor saturation	17.5 mrad ± 10%
θ_{DB}	Roll deadband	5.0 mrad ± 5%

Figure 14 shows the typical trajectory that would be generated in the Earth acquire mode. The *on* time is approximated since the trajectory joggles down the switching line. To take this effect into account, the *on* time for the ideal system, $t_{on} = \theta/\alpha$, is adjusted to account for the nonlinear effects, i.e., minimum *on* time, by including a 50% margin. Therefore, for an acceleration constant of $\alpha = 0.6$ mrad/sec^2,

$$t_{on} = 11.0 \text{ sec} \tag{49}$$

3. Acquisition Phase—Gas Requirements

The acquisition transients are determined by assuming a pulsing hysteresis system (thought to be conservative). The *on* time for the pitch, yaw, and roll modes is measured from Fig. 9 and 15 and is given in Eq. (44) and (49), where

$$\begin{aligned} t_{on} &= 17 \text{ sec (pitch)} \\ t_{on} &= 17 \text{ sec (yaw)} \\ t_{on} &= 11 \text{ sec (roll)} \end{aligned} \tag{50}$$

The gas consumed is determined from Eq. (26) for

$$I_{sp} = 45 \text{ sec} \tag{51}$$

Therefore,

$$W = 0.86 \times 10^{-2} \text{ lb (pitch)} \tag{52}$$

$$W = 1.40 \times 10^{-2} \text{ lb (yaw)} \tag{53}$$

$$W = 0.40 \times 10^{-2} \text{ lb (roll)} \tag{54}$$

and the total gas consumed eliminating the acquisition transients is

$$W = 5.32 \times 10^{-2} \text{ lb} \tag{55}$$

E. Cruise Phase

Following acquisition of the Sun and Earth, the *Ranger* spacecraft is in what is termed the cruise portion of the mission. The cruise phase is characterized by low amplitude limit cycling of the spacecraft about the established

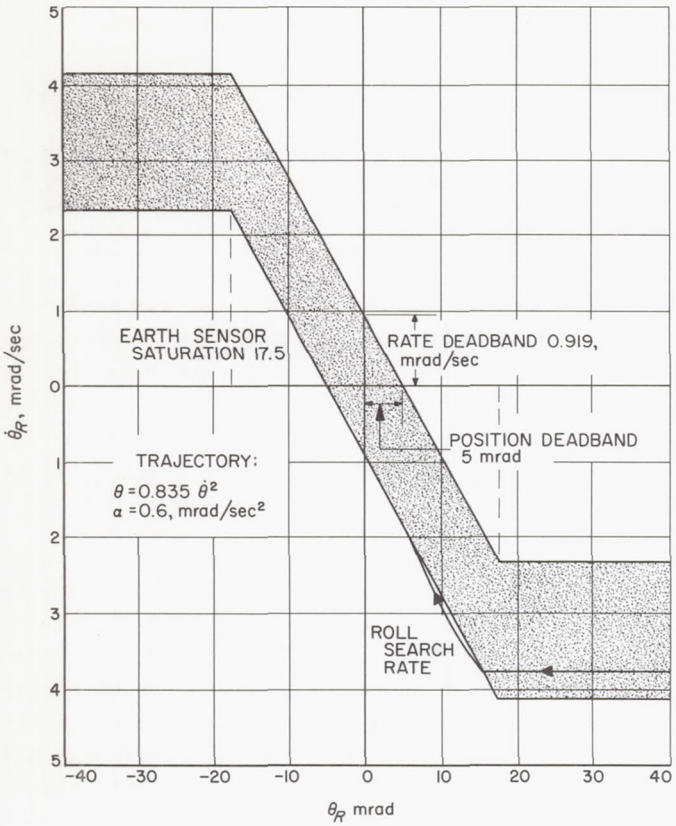

Fig. 15. Roll acquisition

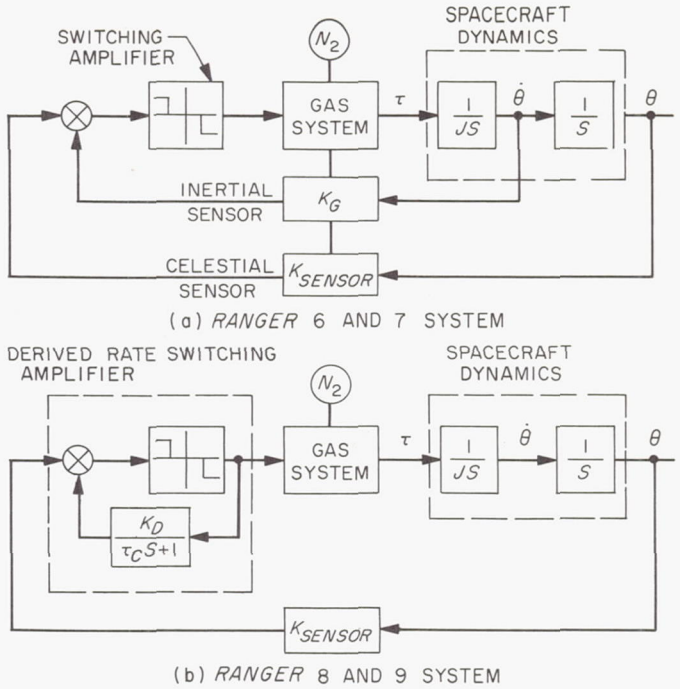

Fig. 16. Cruise attitude control system, *Ranger* Block III

reference trajectory. The Block III effort uses two types of rate control during the cruise as shown in the block diagrams of Fig. 16.

Ranger 6 and 7 use gyros to measure and feed back the rate information. The *Ranger* 8 and 9 attitude control systems use "derived-rate" compensation in the switching amplifier to sense and feed back the effective rate of the vehicle. Both systems use position-error signal information obtained from the Sun and Earth attitude sensors.

During the cruise phase, which lasts for over 60 hrs of the 68-hr flight, the gas jets operate to provide for the stable limit cycle about all of the axes. During this phase of the mission, the amount of gas consumed throughout the control portion is of grave importance. The success of the mission is dependent upon proper orientation of the vehicle for its mission goal of taking TV pictures of the lunar surface.

1. Cruise Phase Attitude Control Requirements and Constraints

The orientation of the spacecraft during the cruise mode of operation must be such that the vehicle power system and communications are always operating in the most efficient manner. To do so, the following conditions must be met:

1. An establishment of the reference directions toward the Earth and Sun to an accuracy of ±17.0 mrad.
2. A limit cycle size in pitch and yaw of ±2.8 mrad in position; and for roll, ±5.0 mrad in position.
3. A re-establishment of the spacecraft directions following a noncatastrophic disturbance of the normal spacecraft orientation.
4. A lifetime extending a minimum of 68 hrs from launch.

2. Derived Rate Compensation

The derived rate switching amplifier is incorporated into the *Ranger* 8 and 9 cruise control system in order to improve the reliability of the system. The gyro is switched out during the cruise phase and the derived rate compensation, as shown in Fig. 16–Part (b), is fed back around the switching amplifier to stabilize the loop. The action of the circuitry is such that when the Sun sensor output reaches the deadband level of the switching amplifier, it is turned on for a 20-msec minimum *on* time. At this instant, the derived-rate capacitor voltage builds up as a ramp function. At the end of the

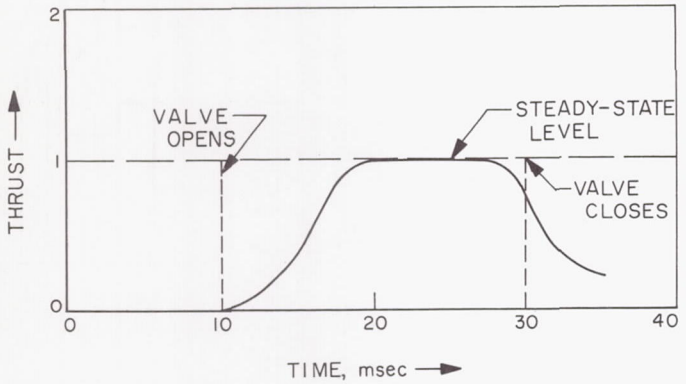

Fig. 17. Jet valve thrust vs time

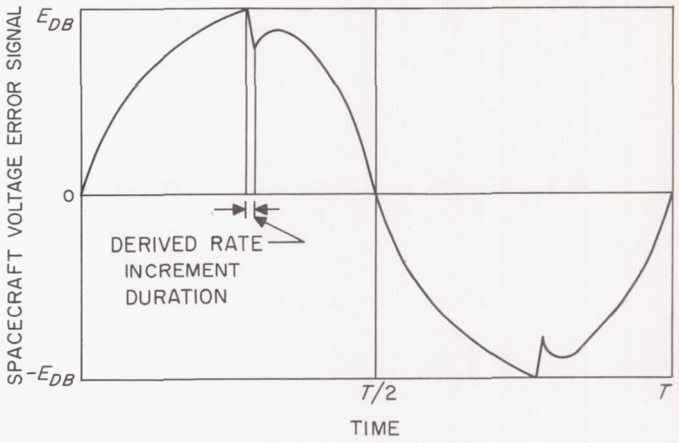

Fig. 18. Derived rate effect on the voltage error signal

20 msec, the voltage is large enough to turn the amplifier off and keep it turned off. During the 20-msec period, an impulse is imparted to the vehicle equivalent to 30 msec of gas jet actuation; this 30 msec corresponds to a change in spacecraft rate in the order of 12 to 24 μrad/sec and is due to a delay associated with the jet valves. Figure 17 shows a plot of the jet-valve thrust vs time.

The thrust is zero until after the 10-msec period when the electrical signal is turned on. This is the time it takes to establish the current in the inductive coil of the valve. The poppet begins to move and the valve opens; then the thrust builds up toward its steady-state value. By that time, the electrical input is off, but there is again a delay due to the inductance of the valve and the inertia of the poppet. The valve then begins to close. Hence, the thrust is constant until that time. After the valve closes, there is gas stored in the nozzle, on the output side of the valve. This tail-off process delivers a residual amount of momentum to the spacecraft. Therefore, the equivalent thrusting time is approximately 30 msec, i.e., for a 20-msec actuation time. For example, the desired rate increment is $\Delta\dot{\theta} = 18 \pm 6$ μrad/sec; if $\dot{\theta} = \pm 9$ μrad/sec, the trajectory hardly moves away from the switching line. There is no reason why the switching amplifier should not turn on again, except that we are now biased off to an equivalent position corresponding to something less than the switching amplifier deadband; this is the derived rate increment as shown in Fig. 18.

Now the system is designed so that there is enough gain in the passive feedback loop, such that the bias voltage is in a direction greater than the noise. Hence, a single pulse gives enough voltage on the capacitor so that the noise in the system will not turn the gas jets on for a second time. This is a very important consideration in setting up the derived rate system because the double-pulsing doubles the velocity increment. As we double the velocity increment, the gas consumption increases by a factor of four, and the gas supply is rapidly depleted. Since the spacecraft changes position slowly and since both the Sun sensor voltage starts decreasing and the capacitor voltage comes down exponentially, the resultant voltage at the input to the amplifier might decay such that the switching amplifier could turn on again. If the derived-rate time constant is too short and the voltage leaks off too fast, this situation corresponds to the voltage signal returning to the switching line which then is turned on again based upon the sum of the associated characteristic signals.

3. Derived Rate Parameters

The derived rate parameters for the *Ranger* pitch, yaw, and roll cruise-attitude control system are chosen as a function of their relationship with the various spacecraft parameters. The primary criterion for their selection is based upon the effect of noise coupling into the switching amplifier. This is due to the fact that a possible noise pulse could cause a double pulse from the switching amplifier, thereby doubling the limit cycle-rate increment.

A block diagram of the switching amplifier with derived rate is shown in Fig. 19.

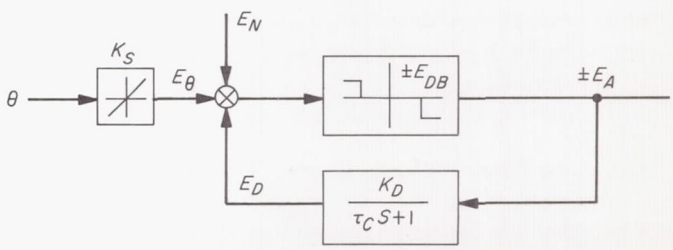

Fig. 19. Derived rate amplifier block diagram

Two problems are emphasized in the following analysis: (1) prevent the noise from turning on the jets after the minimum *on* time pulse, and (2) prevent the decaying derived-rate signal from turning on the jets before the position error is reduced sufficiently. Thus, the solution for establishing a criterion for limit-cycle operation during the cruise is based on the analysis of the above stated problems.

a. Pitch and yaw cruise constraints. Assuming that the initial conditions are zero, the output of the feedback network shown in Fig. 19 is given as

$$E_D = -K_D E_A (1 - e^{-\Delta t/\tau_c}) \tag{56}$$

where

Δt = minimum *on* time

τ_c = charge time constant

If the *on* time is much smaller that the time constant ($\Delta t << \tau_c$), then the exponential may be expanded and approximated by neglecting the higher order terms,

$$1 - e^{-\Delta t/\tau_c} = + \frac{\Delta t}{\tau_c} + \frac{\Delta t^2}{\tau_c^2 2!} + \frac{\Delta t^3}{\tau_c^3 3!} + - - -$$

$$\simeq \frac{\Delta t}{\tau_c} \tag{57}$$

The magnitude of the output, E_D, is then given by

$$|E_D| = K_D E_A \frac{\Delta t}{\tau_c} \tag{58}$$

and if $E_D > E_N$, where E_N is the noise into the switching amplifier, then

$$K_D E_A > \frac{E_N}{\Delta t} \tau_c \tag{59}$$

Hence, Eq. (59) is the criterion desired in order to insure that the noise signal will not turn the jets on after the minimum *on* time pulse is off.

To cope with the second problem, the following analysis is made. During the decay,

$$E_D = E_{D_i} e^{-t/\tau_D} \tag{60}$$

where

E_{D_i} = initial conditions remaining from the charge-up

τ_D = discharge time constant

From Eq. (58),

$$E_{D_i} = K_D E_A \frac{\Delta t}{\tau_c} \tag{61}$$

and substituting Eq. (61) into (60),

$$E_D = K_D E_A \frac{\Delta t}{\tau_c} e^{-t/\tau_D} \tag{62}$$

Now in order to find the maximum magnitude of E_D, the derivative gives

$$\left| \frac{dE_D}{dt} \right| = \frac{K_D E_A \Delta t}{\tau_C \tau_D} e^{-t/\tau_D} \tag{63}$$

and as time goes to zero

$$\left| \frac{dE_D}{dt} \right|_{max} = \frac{K_D E_A \Delta t}{\tau_C \tau_D} \tag{64}$$

Equation (64) is related to the Sun sensor input by the following expression,

$$\left| \frac{dE_S}{dt} \right| > \left| \frac{dE_D}{dt} \right|_{max} \tag{65}$$

where

E_S = saturated Sun sensor output

and

$$\dot{E}_S = K_S \dot{\theta}_1 \tag{66}$$

where

K_S = Sun sensor scale factor

$\dot{\theta}_1$ = limit cycle rate

Now by equating Eq. (64) and (66), we obtain the inequality

$$K_D E_A < \frac{K_S \dot{\theta}_1}{\Delta t} \tau_C \tau_D \tag{67}$$

Based upon the derived rate mechanization

$$\tau_D = 2\tau_c \tag{68}$$

so that

$$K_D E_A < 2 \frac{K_S \dot{\theta}_1}{\Delta t} \tau_C^2 \tag{69}$$

Table 5. Pitch and yaw system parameters

Parameter	Value	Comment
K_S	18.5 v/deg ±10%	scale factor through null
Δt	20 msec	electrical on time
$\Delta t'$	33 msec effective	multiply by the steady-state acceleration constant α for true limit-cycle rate
E_N	≤30 mv	noise input
α	0.25–0.6 mrad/sec^2	control system must have the capability for control with $\alpha/2$
θ_{DB}	2.5 mrad	pitch and yaw deadband
E_S	16.8 v	Sun sensor saturation

Finally, the range of values that may be chosen for the derived rate amplifier in pitch and yaw is given by

$$\frac{E_N}{\Delta t}\tau_C < K_D E_A < 2\frac{K_S\dot{\theta}_1}{\Delta t}\tau_C^2 \qquad (70)$$

A numerical solution of Eq. (59) and (69) is based upon the parameters in Table 5.

Hence, by substituting the minimum *on* time of 20 msec into Eq. (59), we get

$$K_D E_A > 1.5\,\tau_C\,(\text{v}) \qquad (71)$$
$$> 1.455\,\tau_c\,(\text{mrad})$$

Equation (71) is plotted in Fig. 20 as $K_D E_A$ vs τ_C. The noise input has a range $E_N \leq 30$ mv.

Similarly, Eq. (69) is plotted by first substituting the limit cycle rate by

$$\dot{\theta}_1 = 1/2\alpha\Delta t' \qquad (72)$$

so that

$$K_D E_A < \frac{K_S\alpha\Delta t'}{\Delta t}\tau_C^2 \qquad (73)$$

and then studying the extreme cases based upon the acceleration constants of 0.25 and 0.60 mrad/sec^2. These two cases yield

$$K_D E_A < 0.425\,\tau_C^2\,(\text{v}) \quad \text{(worst case)} \qquad (74)$$
$$< 0.413\,\tau_C^2\,(\text{mrad})$$

and

$$K_D E_A < 1.02\,\tau_C^2\,(\text{v}) \quad \text{(best case)} \qquad (75)$$
$$< 1.05\,\tau_C^2\,(\text{mrad})$$

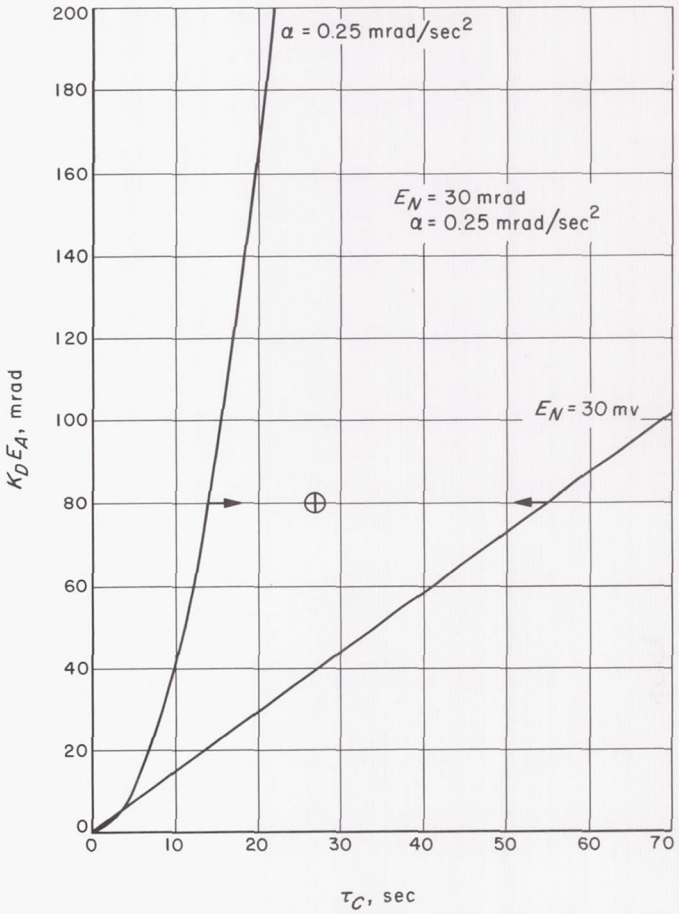

Fig. 20. Derived rate parameters, pitch and yaw

Plotting $K_D E_A$ vs τ_C in Fig. 20 provides the region of acceptable derived-rate parameters.

b. Roll constraints. The computation of the range of parameter values acceptable for the roll cruise-attitude control is similar in method to that just developed for pitch and yaw. However, the addition of the effect of the Earth-probe-Sun angle β, as shown in Fig. 21, provides the only difference in the ensuing solution.

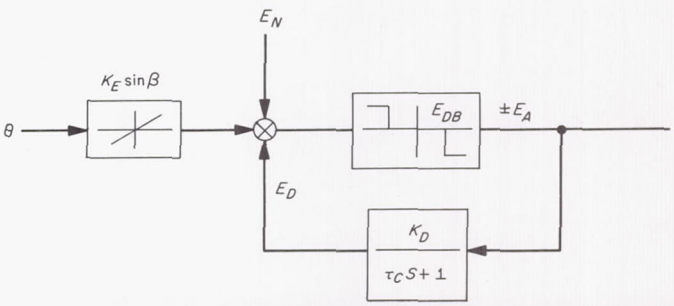

Fig. 21. Roll cruise-system block diagram

Thus, Eq. (59) and (69) are rewritten simply as

$$K_D E_A > \frac{E_N}{\Delta t}\tau_C \tag{76}$$

and

$$K_D E_A < 2\frac{K_E \sin\beta\dot{\theta}_1}{\Delta t}\tau_C^2 \tag{77}$$

where

K_E = Earth sensor scale factor 0.229 v/mrad minimum

β = Earth-probe-Sun angle, 45-deg minimum

Again the numerical solutions are determined by use of the parameters in Table 5 and those given below.

Equation (76) yields

$$K_D E_A > 13.1\,\tau_C \text{ mrad} \tag{78}$$

for $E_N \leq 60$ mrad and substitution into Eq. (77) gives the inequality

$$K_D E_A < 0.146\,\tau_C \tau_D \text{ mrad} \tag{79}$$

assuming that

$$\sin\beta\dot{\theta}_1 = 2.92\,\mu\text{rad/sec}$$

$$\alpha = 0.25\,\text{mrad/sec}^2$$

The results are plotted in Fig. 22 for various values of τ_C.

c. Switching amplifier parameters. The choice of switching amplifier parameters is based upon the selection of $K_D E_A$ from the graphs in Fig. 20 and 22. However, the relationship between the switching amplifier components and this gain selected from the charts must be specified in order to describe fully the derived rate parameters. The switching amplifier is shown in Fig. 23.

The output of the amplifier is given as

$$E_A = K_A \theta_{DB} \tag{80}$$

where

$$K_A = \frac{K_S}{R_S} R_T$$

and R_T is equivalent transresistance of amplifier

K_S = sensor gain (v/mrad)

R_S = input resistance (ohm)

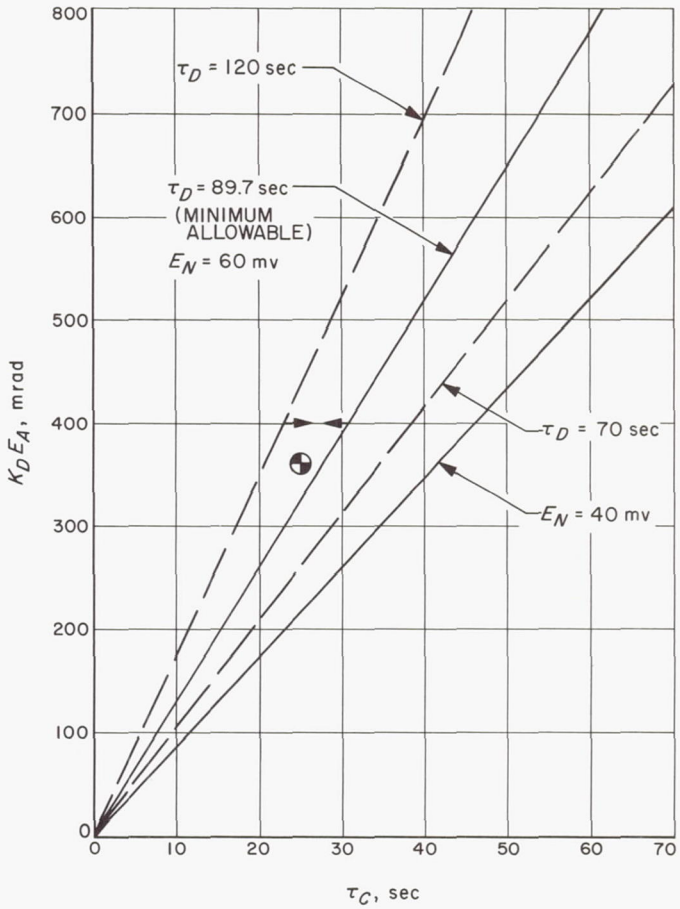

Fig. 22. Derived rate, roll

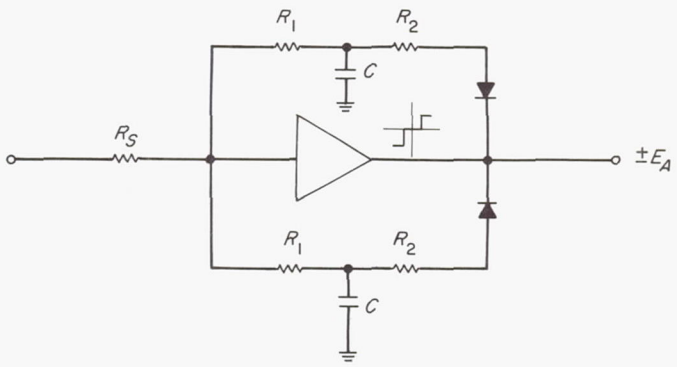

Fig. 23. Switching amplifier network

The time constant of the feedback loop is given by

$$\tau_C = \frac{1}{\frac{1}{R_1} + \frac{1}{R_2}} C \tag{81}$$

where

$$R_1 = R_2$$

so that the charge time constant is

$$\tau_C = \frac{R_1 C}{2} \tag{82}$$

Now the discharge time constant as given by Eq. (68) is

$$\tau_D = R_1 C \tag{83}$$

Finally, if

$$K_D E_A = \frac{E_A}{R_1 + R_2} = \frac{E_A}{2R_1} \quad \frac{\text{v}}{\text{ohm}} \tag{84}$$

then by multiplying by $1/K_A$ and converting Eq. (84) to mrad

$$K_D E_A = \frac{1}{2} \frac{R_S E_A}{R_1 K_S} \tag{85}$$

Therefore, the choice of $K_D E_A$ allows the analyst to pick the appropriate design values for the derived rate-switching amplifier components.

Typically, the *Ranger* derived-rate network might be based upon the following set of parameters:

Pitch and yaw:

$$\begin{aligned} \tau_C &= 27 \text{ sec} \\ \tau_D &= 54 \text{ sec} \\ K_D &= 80 \\ E_N &= 30 \text{ mv} \end{aligned} \tag{86}$$

Roll:

$$\begin{aligned} \tau_C &= 27 \text{ sec} \\ \tau_D &= 54 \text{ sec} \\ K_D &= 360 \\ E_N &= 60 \text{ mv} \\ \beta_{min} &= 45 \text{ deg} \\ \alpha &= 0.25 \text{ mrad/sec}^2 \end{aligned} \tag{87}$$

4. Cruise Gas Requirements

The gas jet system is discussed in detail in Appendix G. The design criteria for the gas system fuel supply were based in part on a conservative estimate of the cruise-phase limit-cycle fuel consumption in which the on-off attitude control system was treated as an uncoupled system with *worst case* initial conditions. The limit-cycle frequency and fuel consumption may be calculated independently for each control channel and the results combined to yield an over-all gas consumption for the cruise phase. A typical plot of the ideal limit cycle is shown in Fig. 24. The time between gas jet firing is found from knowledge of the rate deadband; therefore,

$$\Delta T_1 = -\frac{2\theta_{DB}}{\dot{\theta}} \tag{88}$$

$$\Delta T_2 = \frac{2\theta_{DB}}{\dot{\theta} + \Delta\dot{\theta}} \tag{89}$$

where

θ_{DB} = ½ the deadband in deg

$\Delta\dot{\theta}$ = velocity increment caused by the jet firing for a minimum *on* time Δt

a. Effect of external disturbances. The effect of external torques such as those created by solar pressures are investigated next. It is assumed that the solar torques are large enough to prevent the spacecraft from hitting both sides of the deadband. In order to maintain the pointing error within the deadband, the total torque impulse provided by the gas expulsion must equal the total solar torque impulse; the average velocity will therefore be zero.

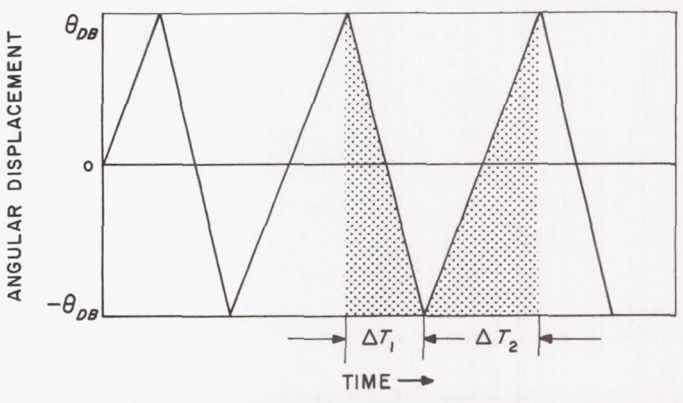

Fig. 24. Cruise attitude-control limit cycle

The expression for the conservation of momentum is given by

$$\tau_c t_c - \tau_s t_s = Iw = 0 \tag{90}$$

where

τ_c = control torque due to jets

t_c = duration of control torque

τ_s = solar torque

t_s = duration of solar torque

and rewriting gives

$$t_c = \frac{\tau_s}{\tau_c} t_s \tag{91}$$

Now, if

$$t_c = t_{on}$$

$$t_s = t_m$$

where

t_{on} = gas system *on* time

t_m = mission time

therefore,

$$t_{on} = \frac{\tau_s}{\tau_c} t_m \tag{92}$$

Now, we also know that the response of the spacecraft to the control torque is

$$\tau_c = I\alpha \tag{93}$$

and the weight of gas is

$$W = \frac{I\alpha}{I_{sp}L} t_{on} \tag{94}$$

By substituting Eq. (93) into (92), and Eq. (92) into (94), then

$$W = \left(\frac{\tau_s}{I_{sp}L}\right) t_m \tag{95}$$

Hence, this is the general expression for gas consumption under influence of solar torque. The equation is true about each of the axes.

The solar torque, which causes the spacecraft trajectory to actuate the gas jets on one side of the deadband and to just touch the other side of the deadband, can be determined with the use of Fig. 25.

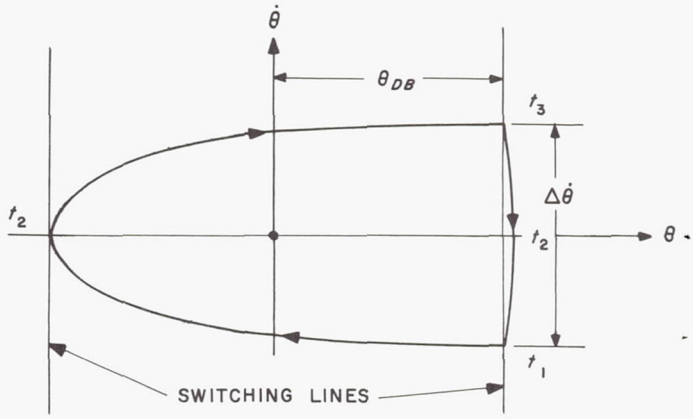

Fig. 25. Solar torque effects on the limit cycle

Since

$$\dot{\theta} = \alpha_s t_s + \dot{\theta}_o \tag{96}$$

then

$$\theta = \frac{\alpha_s t_s^2}{2} + \dot{\theta}_o t_s + \theta_o \tag{97}$$

where

α_s = solar torque acceleration constant

The marginal solar torque is determined by first relating the deadband to the rate increment and solar acceleration constant.

Thus, from Fig. 25, in the region $t_1 \rightarrow t_2$, or $t = t_s/2$, the acceleration constant due to solar pressure is positive and conditions are $\dot{\theta} = 0$, $\dot{\theta}_o = \Delta\dot{\theta}/2$, $\theta_o = +\theta_{DB}$; hence,

$$\dot{\theta} = 0 = \frac{\alpha_s t_s}{2} + \frac{\Delta\dot{\theta}}{2} \tag{98}$$

The position at $t_s/2$ is $\theta = -\theta_{DB}$, so

$$-\theta_{DB} = \frac{\alpha_s t_s}{2} + 0 + \theta_{DB} \tag{99}$$

Equating (98) and (99) and eliminating t_s,

$$\theta_{DB} = \frac{1}{16} \frac{(\Delta\dot{\theta})^2}{\alpha_s} \tag{100}$$

The controlled portion of the limit cycle is given by

$$\Delta\dot{\theta} = \alpha_c \Delta t_c \tag{101}$$

where

α_c = acceleration due to gas-jet torque

Substituting into Eq. (100) and writing in terms of α_s,

$$\alpha_s = \frac{1}{16}\left(\frac{\alpha_c^2 t_c^2}{\theta_{DB}}\right) \tag{102}$$

Finally since

$$\tau_s = I\alpha_s \tag{103}$$

then, substituting Eq. (102) into (103) yields

$$\tau_{s_m} = \frac{I\alpha_c^2 \Delta t^2}{16\theta_{DB}} \tag{104}$$

Therefore, for the marginal case when the torque disturbance is greater than Eq. (104) or is just sufficient to cause the gas jets to fire, Eq. (95) provides the expression for determining the gas consumed.

The relationship of the gas consumed, due to solar torquing and that from the ideal limit cycle, is given below. The frequency of the limit cycle (Fig. 26) is

$$f = \frac{1}{2t_c + 2t_{off}} \tag{105}$$

where

f = frequency

t_c = control time

t_{off} = off time

The number of cycles is given by

$$n = ft_m \tag{106}$$

where

t_m = mission time

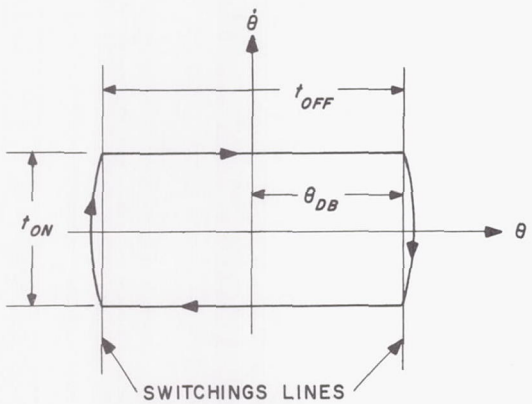

Fig. 26. Limit cycle

Therefore, the total time is

$$t_{on} = 2nt_c \tag{107}$$

where

t_{on} = gas jet *on* time

Substituting Eq. (105) and (106) into (107),

$$t_{on} = 2ft_m t_c = 2\left[\frac{1}{2t_c + 2t_{off}}\right] t_m t_c$$

$$t_{on} = \left[\frac{t_c}{t_c + t_{off}}\right] t_m \tag{108}$$

assuming

$$t_{off} >> t_c$$

Therefore, the *on* time as a function of the control time, *off* time, and mission time for any torque greater than the marginal torque is

$$t_{on} = \left(\frac{t_c}{t_{off}}\right) t_m \tag{109}$$

where

$$t_c = \Delta t \tag{110}$$

and

$$t_{off} = \frac{2\theta_{DB}}{\frac{1}{2}\Delta\dot{\theta}} = \frac{4\theta_{DB}}{\Delta\dot{\theta}} \tag{111}$$

so that

$$t_{on} = \left(\frac{\Delta t}{4\dfrac{\theta_{DB}}{\Delta\dot{\theta}}}\right) t_m$$

or

$$t_{on} = \left(\frac{(\Delta\dot{\theta})^2}{4\alpha\theta_{DB}}\right) t_m \tag{112}$$

This then is the gas jet *on* time for the case when both sides of the deadband are touched. Now Eq. (92) is substituted into (95) yielding

$$W = \left(\frac{\tau_c}{I_{sp}L}\right) t_{on} \tag{113}$$

The *on* time, Eq. (112), is substituted into (113), and then

$$W = \frac{\tau_c}{I_{sp}L}\left(\frac{\Delta\dot{\theta}\,\Delta t}{4\theta_{DB}}\right) t_m$$

which can be rewritten by substituting Eq. (101) for $\Delta\theta$, so then

$$W_I = \frac{I\alpha_c^2 \Delta t^2 t_m}{4 I_{sp} L \theta_{DB}} \tag{114}$$

The above equation expresses the amount of gas consumed due to an ideal limit cycle. A graph, showing the relationship between the gas consumed relative to the ideal limit cycle consumption vs the ratio of unbalance to marginal torque, is drawn in Fig. 27.

The ratio of solar-torque gas consumption to the ideal limit cycle consumption is

$$\frac{W}{W_I} = \frac{1}{4} \tag{115}$$

when torque unbalance equals marginal torque.

The analysis in this section provides the insight desired to enable one to determine the amount of gas required during the cruise phase. A safety factor of 1.5 times the nominal limit cycle consumption was chosen. Therefore, from Fig. 27 and

$$W = 1.5\, W_I \tag{116}$$

the ratio of the unbalance to marginal torque is

$$0 < \frac{\tau}{\tau_m} \leq 6.0 \tag{117}$$

In the region $\tau > 6\tau_m$, the gas consumption increases as the ratio

$$\frac{W}{W_I} = \left(\frac{16\theta_{DB}}{I\Delta\theta^2}\right)\tau \tag{118}$$

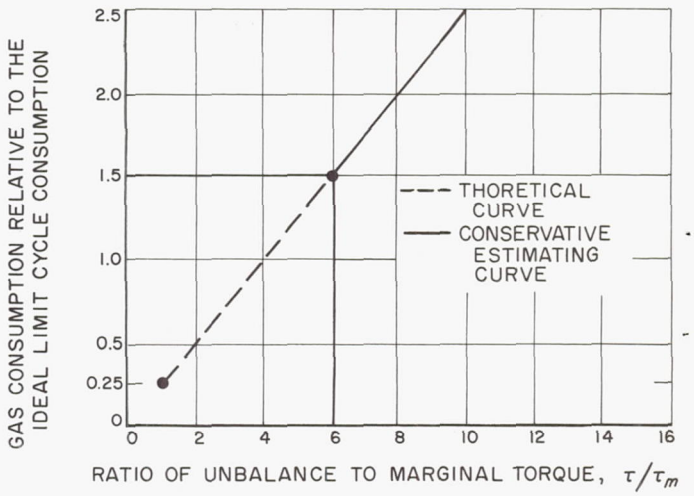

Fig. 27. Normalized gas consumption vs the ratio of unbalance to marginal torque

b. Cruise gas requirement summary. The cruise gas requirements are now computed based on the parameters given in Table 6. Some sample computations are given as follows:

Gas consumption (pitch—continuous I_{sp}):

$$W = \frac{I\alpha_c^2 \Delta t^2}{4 I_{sp} L \theta_{DB}}$$

$$= \frac{(92\ \text{ft-lb-sec}^2)\,(60 \times 10^{-6}\ \text{rad/sec})^2}{4\,(70\ \text{sec})\,(2.42\ \text{ft})\,(2.8 \times 10^{-3}\ \text{rad})}\,(2.4 \times 10^{-5}\ \text{sec})$$

$$W_I = 0.0418\ \text{lb}$$

$$W = 1.5 W_I = 0.063\ \text{lb} \tag{119}$$

Table 6. Summary of some important cruise parameters

Parameter	Symbol	Units	Pitch	Yaw	Roll
Moment of inertia	I	slug-ft^2	92	113	60
Effective moment arm	L	ft	2.42	1.83	2.19
Angular acceleration constant	α	mrad/sec^2	0.6	0.6	0.6
Gas specific impulse	I_{sp}	sec			
continuous	I_c		70	70	70
pulsing	I_p		45	45	45
derived rate	I_D		35	35	35
Limit cycle position deadband	θ_{DB}	mrad	± 2.8	± 2.8	± 5.0
Limit cycle velocity increment	$\Delta\theta$	μrad/sec			
nominal			60 ± 30	60 ± 30	60 ± 30
derived rate			18 ± 6	18 ± 6	18 ± 6
Total mission time	t_m	sec	2.4×10^5	2.4×10^5	2.4×10^5
Agena B separation rates	θ	mrad/sec	52.4	52.4	52.4

Flow rate:

$$\dot{W} = \frac{W}{t_{on}}$$

where

$$t_{on} = \frac{(\Delta\dot{\theta}^2)}{4\alpha\theta_{DB}} t_m$$

$$= \frac{(60 \times 10^{-6}\,\text{rad/sec})^2\,(2.4 \times 10^5\,\text{sec})}{4\,(0.6 \times 10^{-3}\,\text{rad/sec}^2)\,(2.8 \times 10^{-3}\,\text{rad})}$$

$$t_{on} = 128.5\,\text{sec} \qquad (120)$$

Therefore,

$$\dot{W}_I = \frac{0.0418\,\text{lb}}{128.5\,\text{sec}}$$

$$\dot{W}_I = 3.26 \times 10^{-4}\,(\text{lb/sec}) \qquad (121)$$

Marginal torque:

$$\tau_{S_m} = \frac{I\,(\Delta\dot{\theta})^2}{16\theta_{DB}}$$

$$= \frac{(92\,\text{ft-lb-sec}^2)\,(60 \times 10^{-6}\,\text{rad/sec}^2)^2}{16\,(2.8 \times 10^{-3}\,\text{rad})}$$

$$\times\,(1.36 \times 10^7\,\text{dyne-cm}^2/\text{ft-lb})$$

$$= 100\,\text{dyne-cm} \qquad (122)$$

Table 7 summarizes the data, below.

F. Summary of Sub-system Constraints on the Attitude Control System

Up until now, we have approached the problems associated with the attitude control system from the systems viewpoint; however, it is very important to understand how the constraints imposed upon the sub-systems, in turn, create constraints on the attitude control system. The attitude control sub-systems are integrated into the spacecraft body, as shown in Fig. 28. This section will review the sub-system constraints; a more detailed discussion will be covered in the appendices.

1. Sun Sensor

The Sun sensors field of view is completely unobstructed. A single, stable null exists in the pitch and yaw channels in order to point the roll axis at the Sun. There are two types of Sun sensors to provide the 360-deg field of view about the pitch and yaw axes. The primary Sun sensors detect the Sun within a nominal range of 45 deg of the roll axis. The secondary Sun sensors provide for the additional field of view, in particular for the Sun acquisition phase. The additional Sun sensor characteristics are:

Scale factor:	-18.5 v/deg
Saturation level:	± 17.5 mrad $\pm 7\%$
Null offset (mechanical and electrical):	2.7 mrad (3σ)

Table 7. Cruise gas consumption requirements

Parameters	Symbol	Units	Pitch	Yaw	Roll	Total Gas Consumption
Gas weight consumption	W_I	lb				
continuous	W_c		0.0418	0.068	0.0169	
Gas flow rate	$\dot{W}_I$	lb/sec				
continuous	$\dot{W}_{Ic}$		3.26×10^{-4}	5.3×10^{-4}	2.35×10^{-4}	
pulsing	$\dot{W}_{Ip}$		5.00×10^{-4}	8.2×10^{-4}	3.64×10^{-4}	
derived rate	$\dot{W}_{DR}$		6.50×10^{-4}	1.0×10^{-3}	4.7×10^{-4}	
Gas weight consumption (with 1.5 safety factor)		lb				
nominal ($\theta = 60$ μrad/sec)	W		0.063	0.102	0.025	0.189
worst case ($\theta = 90$ μrad/sec)	W		0.152	0.230	0.052	0.434
derived rate	W		0.03			
Marginal torque	τ	dyne-cm				
nominal			100	123	36.5	
worst case			225	276	82.1	
derived rate			37	46	12.0	
Jet on time	t_{on}	sec	128.5	128.5	71.8	

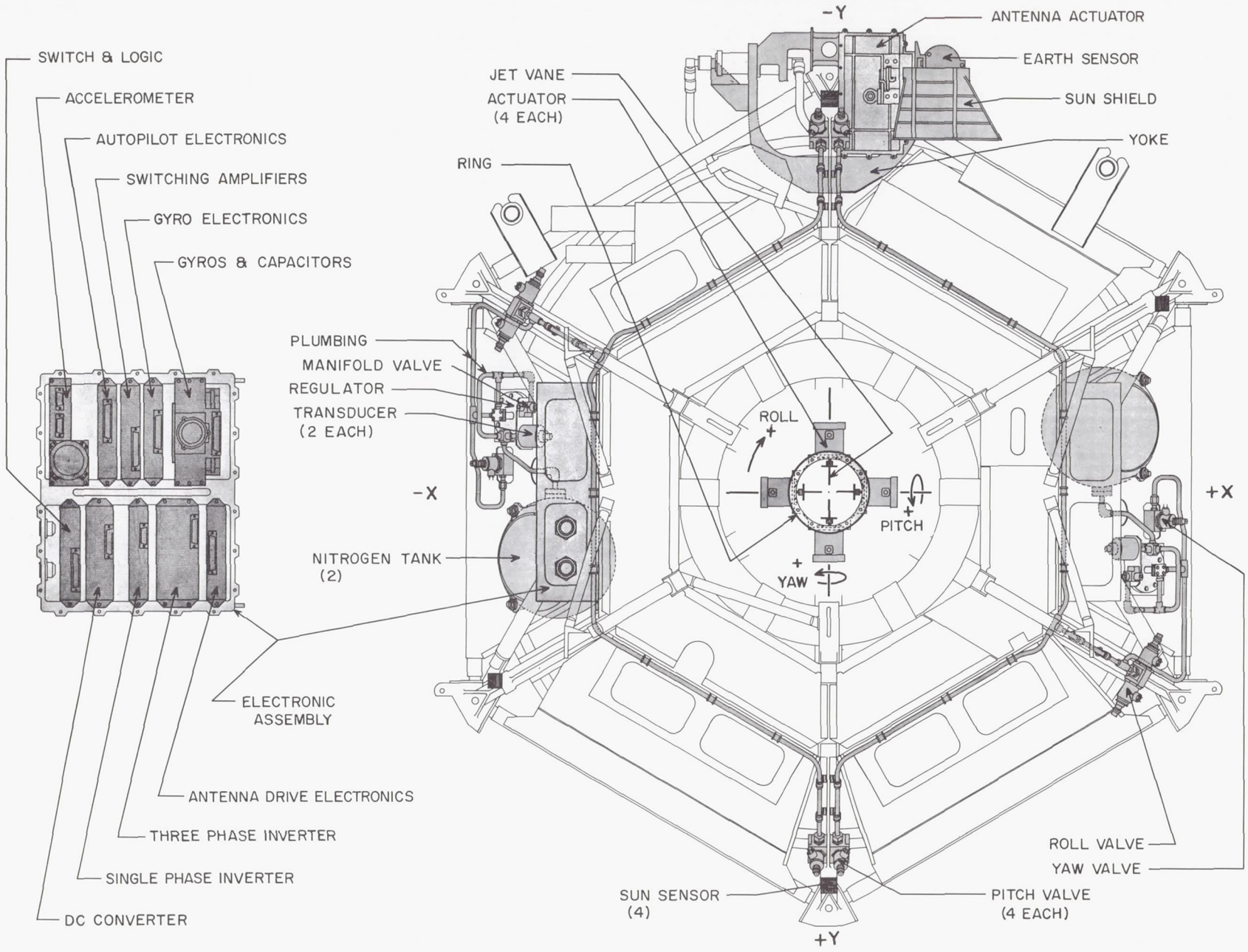

Fig. 28. *Ranger* attitude control configuration

2. Earth Sensor

The Earth sensor provides signals to both the roll control and hinge servo. The Earth sensor characteristics are given below:

Field of view in roll:	±5 deg
Field of view in hinge:	±10 deg
Scale factor in roll:	−8 v/deg
Scale factor in hinge:	2 v/deg
Null offset (mechanical and electrical):	9.73 mrad (3σ)

The sensor saturation level was chosen so that the roll rate in the saturated region of the sensor is close to the roll search rate. Trade-offs were made between the deadband and search rate so as to arrive at a compromise value for each. The gyro mix ratio (rate-to-position gain) was determined by the choice of the maximum acquisition rate that could be tolerated. Tolerances were added in a *worst case* manner, and then the parameters were selected such that acquisition was still possible. The parameters are given below:

Earth sensor saturation:	17.5 mrad
Control acceleration:	0.6 mrad/sec^2
Rate to position gain:	5.45 sec ±10%
Roll search rate:	−3.78 mrad/sec
Switching amplifier deadband:	±5.0 mrad

3. Gyroscopes

Three, single, degree-of-freedom integrating rate gyros are body-fixed about the three mutually perpendicular axes. The gyros have the capability of sensing rate (as will be discussed in Section III-C(1), as well as position displacements. The gyros operate in several different phases of the mission as follows:

1. Rate reduction about all axes.
2. Initial acquisition.
3. Cruise (*Ranger* 6 and 7 only).
4. Midcourse.
5. Re-acquisition.
6. Roll override.
7. Terminal.

The gyro saturation range is 1500-2000 deg/hr.

a. Pitch and yaw modes. The chief constraint on choosing the gyro rate to position gain is the saturation level of the gyro rate measurement. When the Sun's light level saturates the sensor, the spacecraft turning-rate will stabilize to a constant rate, determined primarily by the saturation level of the sensor and the rate to position gain τ_G. Tolerances are applied to the parameters in a manner that will provide an absolute *worst case* condition; the gyro mix ratio is determined to be that value that provides the greatest rate without saturating the gyros. For the pitch and yaw modes, the rate to position gain is $\tau_G = 3.2$ sec.

b. Roll mode. By the identical type of reasoning as given above, the roll rate to position gain is given as $\tau_G = 5.45$ sec.

4. Gas System

The amount of gas stored onboard the spacecraft is chosen by the study of the *worst case* gas requirements expected during the entire mission. Analytical techniques were used to arrive at the figure of $W = 4.18$ lb. A summary of the gas consumed during the mission is given in Appendix G.

a. Pitch, yaw, and roll control-torque acceleration. The control-torque acceleration that was selected was determined for cruise primarily by the minimum impulse capability of the gas valves, in order to minimize gas consumption during the cruise limit-cycle operation. The second constraint on the acceleration constant is the commanded turn sequence which has a minimum acceleration to prevent gyro saturation. The acceleration constant is given as $\alpha = 0.6$ mrad/sec^2.

5. Switching Amplifier

The size of the switching amplifier deadband was found to be noncritical. This is due to a pointing accuracy requirement of 1 deg for the pitch and yaw axes, and also due to a small-sensor null offset. The pitch and yaw deadband is $\theta_{DB} = \pm 2.5$ mrad.

a. Pitch and yaw derived-rate parameters. The parameters of the derived-rate amplifiers used on *Ranger* 8 and 9 are chosen based upon the following criteria:

1. The ability to reacquire from a small disturbance must be significant; e.g., a disturbance not large enough to activate the gyros for automatic acquisition.

2. The derived-rate signal must be large enough that a noise pulse will not cause an extra rate increment in the limit cycle.

3. The rate of decay of the derived-rate signal must be long enough that a noise pulse will not cause an extra rate increment until the position signal is far enough inside the switching deadband to prevent it.

The following derived-rate parameters were chosen for pitch and yaw:

Derived-rate gain: $K_D = 80$ mrad

Derived-rate time constant: $\tau_C = 27$ sec

b. Roll derived-rate parameters. These parameters are picked in the same manner as those in Section II-F-5(a); however, the discussion in Section II-E-3(b) points out that the effect of the Earth-probe-Sun angle must be taken into account as well as the different level of noise. The parameters are:

Derived-rate gain: $K_D = 360$ mrad

Derived-rate time constant: $\tau_C = 27$ sec

6. Hinge Servo

The criteria used to determine the hinge servo parameters were:

1. Under the *worst case* tolerances, the Earth sensor must be capable of supplying a sufficient error signal to operate the hinge-actuator amplifier.
2. Under the *worst case* tolerance situation, the total overshoot from the maximum slewing rate, including the effects of the filter time constants in the Earth sensor, must not cause the minimum hinge-actuator amplifier dead zone to be entirely consumed and the antenna to reverse direction.
3. At the minimum slewing rate, the antenna must arrive at the exit angle before motor ignition.
4. Earth acquisition by the use of overrides must be a certainty in all geometry situations. For example:

Hinge Servo:

Hinge servo slewing rate: $0.4\left(\frac{\text{deg}}{\text{sec}}\right)$ minimum

Hinge servo backlash: 1.5 deg maximum

Antenna exit angle: 180 deg

5. Capability of tracking the Earth continuously during terminal maneuver must be maintained.

III. TRAJECTORY CORRECTIONS

A. Discussion

A midcourse trajectory correction is performed early in the flight to reduce errors introduced by the injection guidance system. This correction is accomplished by means of a small monopropellant motor mounted parallel to the Z-axis of the spacecraft. The attitude control system is required to reorient the spacecraft so that the propulsion unit is aligned with the direction of the required velocity increment.

B. Trajectory Correction Requirements and Constraints

The necessity to perform a midcourse maneuver imposes the following requirements and constraints on the attitude control system.

1. Performance requirements are:

   a. Thrust vector pointing error = 34.68 mrad (3σ)

   b. Proportional shutoff error = 12.45×10^{-3} v

   c. Velocity resolution errors = 0.00525 mrad/sec

2. During *midcourse* correction, the high-gain antenna must be positioned as far as possible away from the rocket exhaust (the antenna is initially stowed beneath the rocket-motor exhaust path) in order to avoid obstructing the correction rocket exhaust. At this time, communications are carried via the omni-antenna.

3. The spacecraft shall be capable of achieving a commanded velocity increment at *midcourse* (for an 810-lb spacecraft) of up to 190 ft/sec. No velocity increment shall be commanded which requires a midcourse motor burn of less than one second.

4. The attitude control system must meet the above requirements when the illuminated Earth as seen from the spacecraft is bounded within the angular range, 43.5 through 137 deg relative to the probe-Sun line. This corresponds to an EPS angle of 46 through 135 deg at a range from Earth of 150,000 km.

If an early midcourse maneuver is deemed necessary in order to reduce excessive injection errors, the following system errors should be considered:

1. Light reflected from the spacecraft will produce a roll position error.

2. The roll limit cycle position error is proportional to cosecant θ_H where θ_H, the antenna hinge angle, is the supplement of the Sun-probe-center of illumination of Earth angle. This error is the dominant source of midcourse system error and increases rapidly as the EPS angle and/or range from the Earth are reduced.

3. The roll-position gain of the Earth sensor decreases with decreasing range from the Earth. This causes a further increase of the roll limit cycle position error.

Additional restraints imposed on the attitude control system are due to the control of the center of gravity (c.g.) during course correction, as follows:

1. The c.g. must lie within 0.25 in. of the predicted position in the X-Y plane.

2. The line of action of the engine must pass within 3/16 in. of the predicted c.g. position in the X-Y plane.

3. Products of inertia shall not exceed 10% of the minimum moment of inertia.

C. Midcourse Maneuver

During the midcourse maneuver, a corrective velocity increment is added to the spacecraft velocity vector in order to eliminate or reduce the initial injection dispersion error in the trajectory. In the first part of the maneuver,

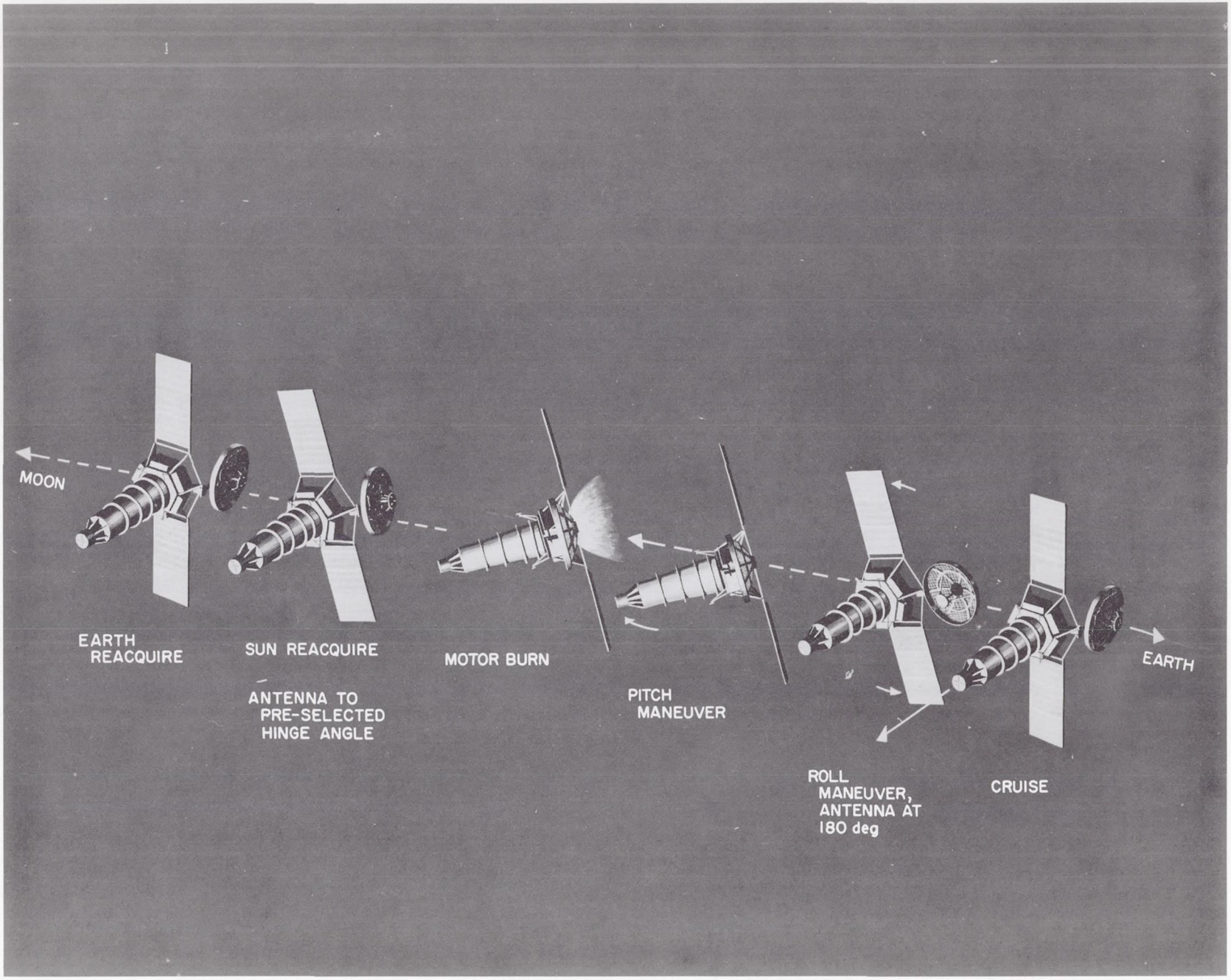

Fig. 29. Midcourse maneuver sequence

the spacecraft is reoriented such that the direction of the midcourse motor thrust will coincide with that of the computed corrective velocity increment. In the second part, the midcourse motor is activated for a specified duration of time at which the required magnitude of the corrective velocity is attained. The maneuver sequence is illustrated in Fig. 29.

The midcourse autopilot controls the spacecraft attitude during the latter part of the maneuver. The basic operation of the autopilot is to stabilize the spacecraft about its center of mass by means of jet vanes which are placed downstream of the midcourse motor exhaust. The attitude error is sensed by the gyros, and the gyro signals, in turn, control the jet vanes. Thus, the autopilot corrects the initial attitude error due to the deadband of the attitude control system, and minimizes the effect of the disturbance torques.

It is intended in this section to analyze the autopilot stability characteristics and discuss the directional uncertainty of the velocity correction due to the autopilot performance. The block diagram of the attitude control system during the midcourse maneuver is given in Fig. 30.

1. Commanded Turns

Prior to the midcourse maneuver, the spacecraft control is a function of the error signals measured by the Sun and Earth sensors and gyros. At the initiation of the first commanded turn in roll, a predetermined set of events takes place within the attitude control system, as follows:

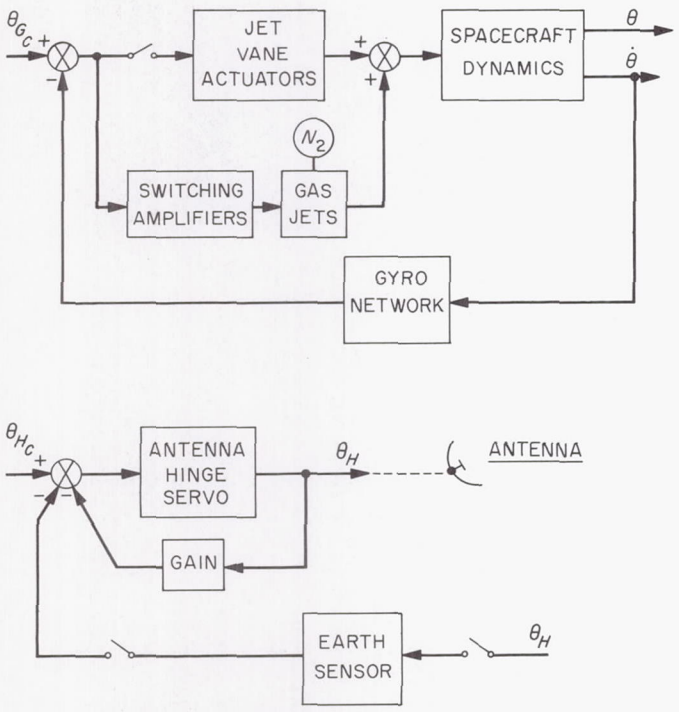

Fig. 30. Attitude control system, midcourse maneuver

1. The Earth sensor is turned off.

2. The nozzle of the midcourse rocket motor points down the +Z direction of the spacecraft. In order to move the antenna away from the exhaust of the rocket motor, it is oriented to the exit position of 180 deg, which is the full-out position. This is accomplished by a relay switching action.

3. Capacitors are switched into the feedback loop of the roll gyro as shown in Fig. 31. The function of these capacitors is to integrate the rate signal and provide for the equivalent position signal.

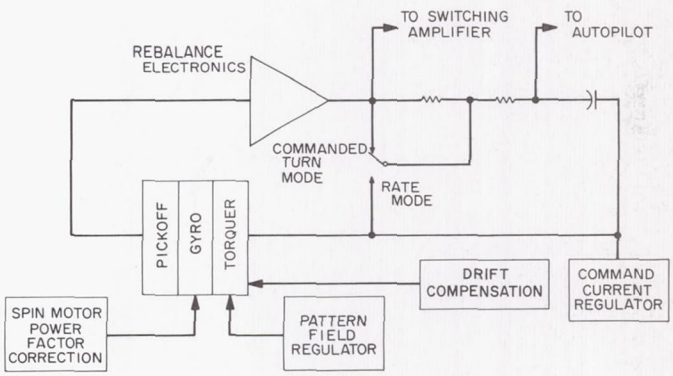

Fig. 31. Gyro commanded-turn configuration

4. A constant current is applied to the gyro torquer to provide the proper magnitude and polarity of the computed corrective turn. The input to the gyro is open at this time. The vehicle rolls in response to the torquer signal which activates the roll switching amplifier and, in turn, provides the thrusting from the gas jets. A block diagram of the attitude control system during the roll turn is given in Fig. 32.

5. After the pre-computed turn duration, the constant current input is switched out, and the normal gyro input is switched-in to again provide rate and position information, so as to reduce the transients about the new roll position and maintain spacecraft stability. The determination of the turn is actually made in the Central Computer and Sequencer (CC&S), where turn angle is defined by the time over which a turn-rate specified magnitude is applied. Thus, a precision (±0.3% deviation from calibration) turn-rate signal must be generated and applied to

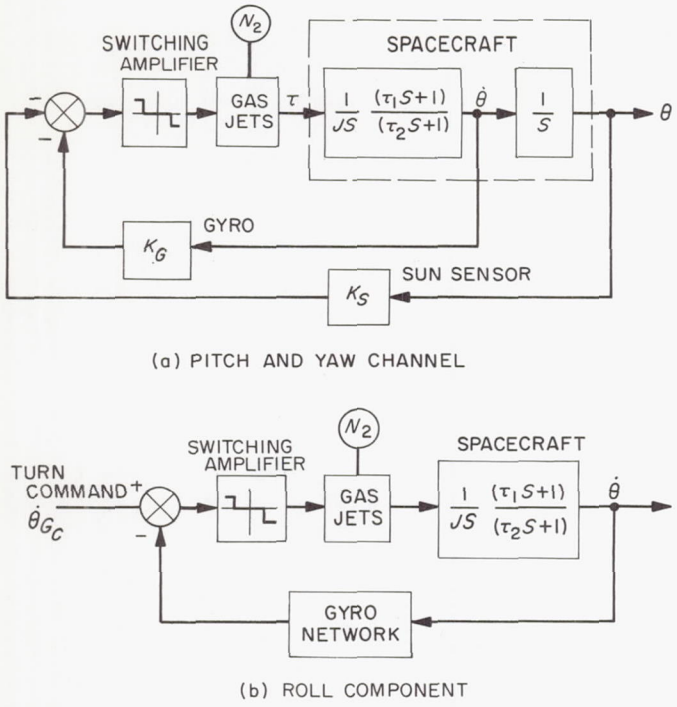

Fig. 32. Attitude-control system block diagram, roll turn

the inertial sensing system from within the attitude control system. The established turn rate is 3.5 mrad/sec ±5%.

Similarly, at the initiation of the pitch turn, the pitch and yaw Sun sensors are switched out of the pitch and yaw switching amplifier inputs and the capacitors are switched into the pitch and yaw gyro loops providing for the rate and position information. A constant current is applied to the pitch gyro torquer for the proper magnitude and polarity of the computed turn. The pitch-turn attitude-control block diagram is shown in Fig. 33. The time constant for pitch, yaw, and roll modes during course correction is $\tau_G = 5.45$ sec.

a. Commanded turns—gas requirements. The gas consumed during the midcourse and terminal maneuvers is computed, based upon an analog computer analysis. A pulsing system is simulated (conservative estimate).

The results from the computer simulation are given in Table 8 for both the full and half-gas system. The table indicates results for a pitch, yaw, and roll turn. The gas consumption is based on the on time of the jets. (A typical analog record is shown in Fig. 36.)

The commanded turns consist of a roll and pitch maneuver at midcourse and pitch-yaw-pitch maneuver in

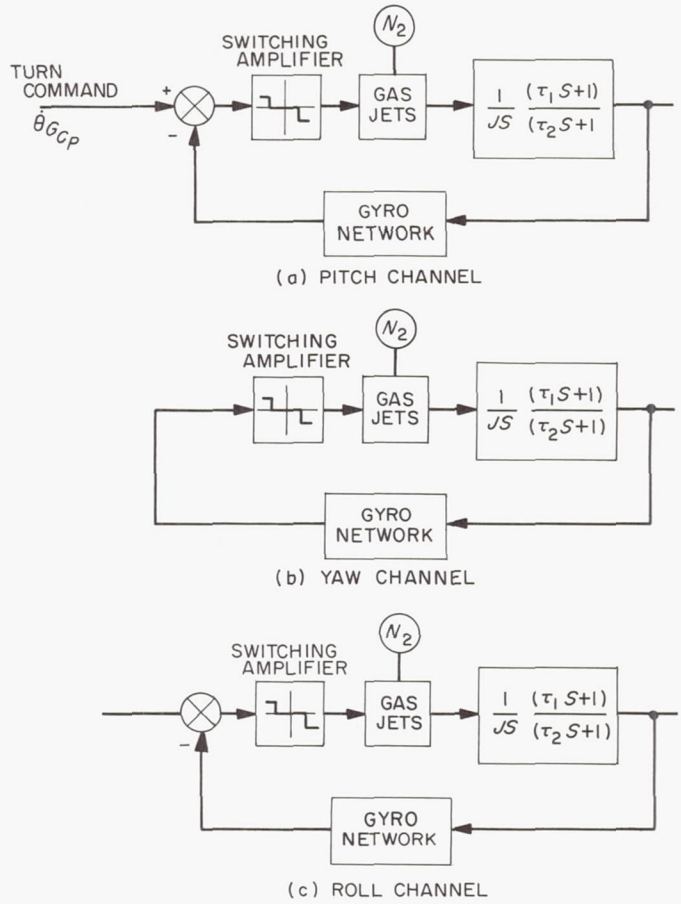

Fig. 33. Attitude-control system block diagram, pitch turn

the terminal mode. The total gas consumed is therefore a function of the turns commanded so that:

$$\textit{Total Gas Consumed} = \text{gas consumed in pitch} \times 3 + \text{gas consumed in yaw} \times 1 + \text{gas consumed in roll} \times 1$$

Therefore,

Full system: $W_T = 9.5 \times 10^{-2}$ lb

Half system: $W_T = 12.2 \times 10^{-2}$ lb

Table 8. Commanded turns, gas on-time

Maneuver	System			
	Full		Half	
	t_{on} (sec)	W (lb)	t_{on} (sec)	W (lb)
Pitch	35	1.78×10^{-2}	90	2.28×10^{-2}
Yaw	35	2.88×10^{-2}	90	3.71×10^{-2}
Roll	35	1.27×10^{-2}	90	1.64×10^{-2}

In addition to using the analog computer to obtain the gas jet *on* time, an analytical representation of the *on* time is described by studying the gyro circuit. The gyro control amplifier is connected to a passive network and to the gyro torquer, as shown in Fig. 34. In the ensuing analysis, it is assumed that the time constants of the gyro capture loop are sufficiently small so that they can be neglected.

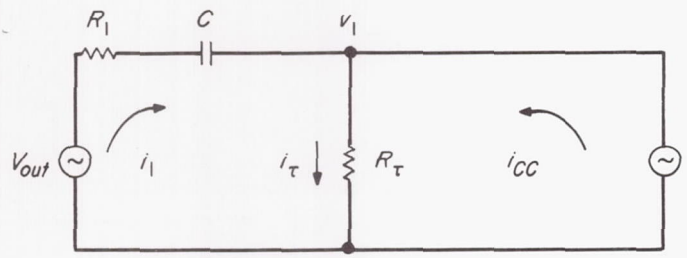

Fig. 34. Gyro network circuit analysis

The parameters are:

v_{out} = gyro amplifier output voltage (switching amplifier input)

i_1 = current out of gyro amplifier

i_τ = gyro torquer current

i_{cc} = command current (assumed constant)

C = angle storage capacitors

R_τ = torque resistance

v_1 = torquer voltage

R_T = pure resistance

The node equations are:

$$(v_{out} - v_1) = \left(\frac{R_1Cs + 1}{Cs}\right) i_1 \tag{123}$$

$$V_1 = R_\tau i_\tau \tag{124}$$

The current is given by

$$i_\tau = i_1 + i_{cc} \tag{125}$$

Substituting Eq. (124) and (125) into (123) and solving v_{out} gives

$$v_{out} = -\left(\frac{R_1Cs + 1}{Cs}\right) i_{cc} + \left(\frac{(R_1 + R_\tau)\,Cs + 1}{Cs}\right) i_\tau \tag{126}$$

Equations further defining the rate gyro are:

$$\dot{\theta}_c = i_{cc}k_\tau \tag{127}$$

and (neglecting any torquer time constants)

$$\dot{\theta}_a = i_\tau k_\tau \tag{128}$$

where

$\dot{\theta}_c$ = command rate

$\dot{\theta}_a$ = actual rate about input axis

k_τ = gyro torquer scale factor

Substituting Eq. (127) and (128) into (126) gives

$$v_{out} = -\left(\frac{R_1Cs + 1}{sCk_\tau}\right)\dot{\theta}_c + \left(\frac{(R_1 + R_\tau)\,Cs + 1}{sCk_\tau}\right)\dot{\theta}_a \tag{129}$$

Rewriting yields

$$v_{out}Ck_\tau = -\,(R_1Cs + 1)\,\theta_c + [(R_1 + R_\tau)\,Cs + 1]\,\theta_a \tag{130}$$

Now we define

$$\tau_1 = R_1C$$

$$\tau_G = (R_1 + R_\tau)\,C \tag{131}$$

Therefore,

$$v_{out}Ck_\tau = -\,(\tau_1 s + 1)\,\theta_c + (\tau_G s + 1)\,\theta_a \tag{132}$$

The switching amplifier will switch when

$$v_{out}Ck_\tau = \pm\theta_{DB} \tag{133}$$

From the time $t = 0$, until that time at which the error into the switching amplifier turns off the jets, we see that

$$\dot{\theta}_c = \omega_c \tag{134}$$

and

$$\theta_c = \omega_c t \tag{135}$$

also

$$\theta_a = \alpha t \tag{136}$$

and

$$\theta_a = 1/2\alpha t^2 \tag{137}$$

The first switch-off occurs at

$$v_{out} C k_\tau = -\theta_{DB} \tag{138}$$

Substituting Eq. (134) through (138) into (132) yields

$$-\theta_{DB} = -\tau_{1c} - \omega_c t + \tau_G \alpha t + 1/2 \alpha t^2 \tag{139}$$

Rewriting in terms of time, we have

$$t^2 + \frac{2}{\alpha}(\tau_G \alpha - \omega_c)\, t + \frac{2}{\alpha}(\theta_{DB} - \tau_1 \omega_c) = 0 \tag{140}$$

Equation (140) describes the time, t_1, between $t = 0$ and the first turn-off of the jet valves during the commanded turn. The *on* time is therefore determined for that increment of time and for each succeeding increment thereafter by solving Eq. (132) with the appropriate conditions. Hence,

$$t_1 = \frac{(\omega_c - \tau_G \alpha) + \sqrt{(\omega_c - \tau_G \alpha)^2 + 2\alpha(\tau_1 \omega_c - \theta_{DB})}}{\alpha} \tag{141}$$

The total *on* time is therefore given by

$$t_{on} = t_1 + t_2 + \cdots + t_N$$

or

$$t_{on} = \sum_{n-1}^{N} (t_n) \tag{142}$$

As an illustration of the above discussion, Fig. 35 shows commanded turn rate vs time. Due to overshoot, there is transient time until the signal settles out to the steady-state rate. Each time the switching amplifier switches, the initial conditions are determined and the *on* or *off* time is computed. The sum of the *on* time can be used for determining gas consumption.

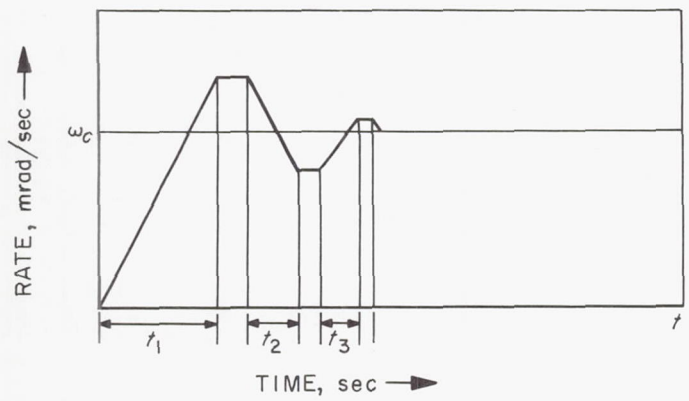

Fig. 35. Illustration of commanded-turn transient

However, further simplifications can be made by realizing that the primary gas usage is involved in the *on* period following the start and stop of the turn. Since the turn-on and turn-off periods require approximately the same amount of gas, then the total gas consumed can be approximately found by adding 25% to the initial gas *on* time and doubling this result to account for both the turn-on and turn-off transients and also $t_2, t_3 \cdots t_N$. Hence,

$$t_{on} \simeq 2.5 t_1 \tag{143}$$

Fig. 36 represents analog computer results indicating a commanded turn with an acceleration constant of 0.6 mrad/sec^2. This strip chart was taken from an analysis of turns as a function of the acceleration constant; the criterion for the turns was the loading of the gyro amplifier.

2. Thrust Phase

Following the roll and pitch turns, the pre-computed velocity increment is added to the spacecraft's velocity by the thrust from the midcourse motor. The velocity increment required to provide for the desired velocity is measured by an integrating accelerometer sensitive along the roll axis. The accelerometer is turned-on at the start of the maneuver and measures the acceleration imparted by the midcourse motor thrust along the nominal thrust line by providing pulses at a rate proportional to the measured acceleration. The pulses are summed by the CC&S; at the instant that they are equivalent to the commanded velocity increment, the shift register in the computer overflows and provides the signal to shut-off the

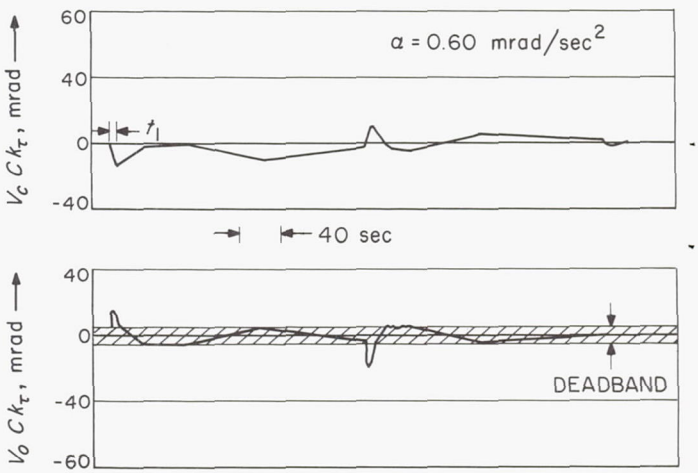

Fig. 36. Commanded turn on time, analog computer results

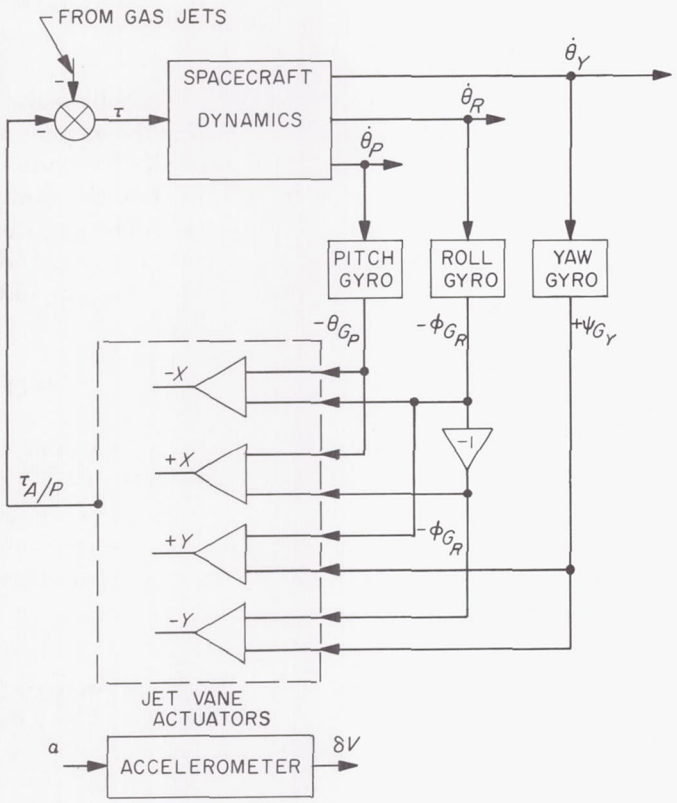

Fig. 37. Attitude control system: thrust phase, midcourse maneuver

midcourse motor. The block diagram of the system during the thrust phase is given in Fig. 37.

a. Jet valve gas expended during midcourse motor firing. After the pitch turn is completed, the midcourse motor ignites, thrusting the vehicle in the desired direction. The burning time for the midcourse motor is 90 sec. The gas jet system remains *on* throughout the thrust phase; however, the torque it exerts on the spacecraft, if any, is negligible compared to the thrust applied by the midcourse motor. Assuming continuous gas discharge, the following gas consumption was computed for the normal and half-gas system (Table 9).

Table 9. Gas consumption, motor-firing period

Mode	System			
	Full		Half	
	t_{on}	W	t_{on}	W
	sec	lb	sec	lb
Pitch	90	2.94×10^{-2}	90	1.47×10^{-2}
Yaw	90	4.77×10^{-2}	90	2.38×10^{-2}
Roll	90	2.10×10^{-2}	90	1.05×10^{-2}
Total		9.8×10^{-2}		4.9×10^{-2}

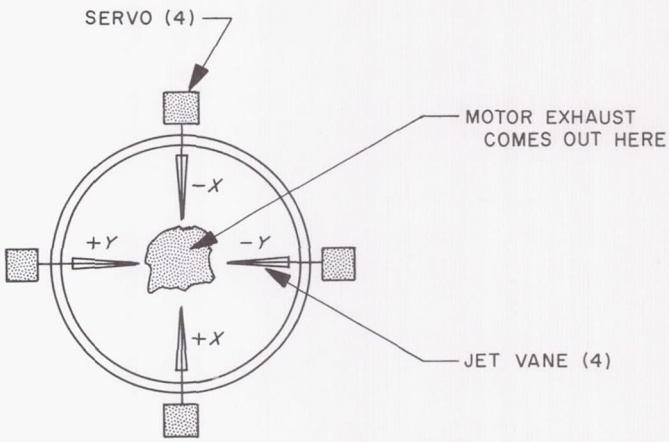

Fig. 38. Autopilot jet vanes

b. Autopilot control. Stability of the spacecraft during the thrust phase of the midcourse maneuver is derived from position and rate control. Two pitch and two yaw vanes extend into the path of the motor exhaust stream, as shown in Fig. 38, and act upon the position error signals. The jet vanes are situated along the axes which are parallel to the pitch and yaw axes. The gyros sense the change in rate and are switched to the input of the autopilot amplifiers at the same instant that the capacitors are switched into the gyro network. Control about pitch, yaw, and roll is dependent upon which of the four vanes are rotated and how their error signals mix. For example, if $+x$ and $-x$ vanes were displaced, the thrust vector component in pitch would be controlled. A combination of the x and y vane deflections provide for control of the thrust vector in the roll sense. It is the purpose of the autopilot to direct the thrust vector through the c.g. of the vehicle.

The jet-vane actuator loop consists of the actuator amplifier, actuator, position feedback potentiometer and appropriate compensations, as shown in Fig. 39. The complete analysis of the jet vane actuator loop and its effects on the autopilot are discussed thoroughly in Appendix B.

3. Midcourse Maneuver Error Analysis

Due to the requirement of the midcourse maneuver, a study of the errors introduced by the attitude control sub-system components during the performance of the turns is important. The residual errors from the attitude control system must be very small in order to satisfactorily reduce the injection guidance errors.

The midcourse maneuver, as described in Sections III-A through C, is a function of several distinct actions

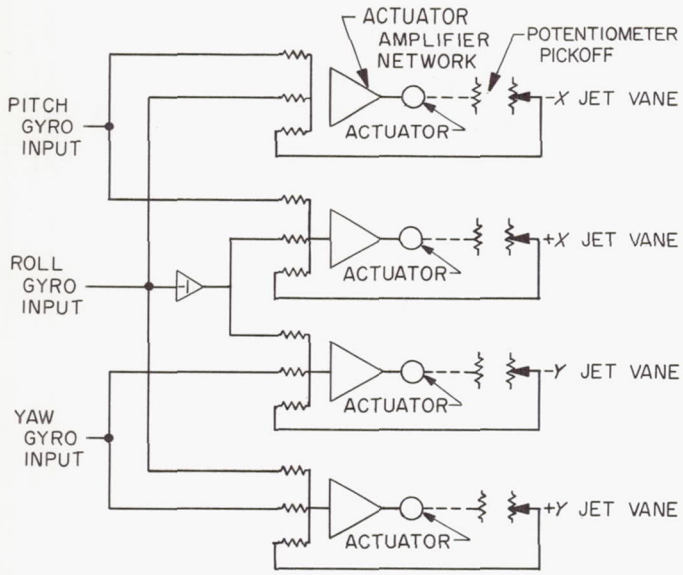

Fig. 39. Jet vane actuator loop

taken by the attitude control system. The error-laden equations are developed fully in Appendix D, and only the results are discussed here. The execution errors, introduced by the maneuvering of the vehicles and secondly by the rocket firing, are of interest. Prior to the maneuver, the spacecraft is in the cruise configuration. The turn commands are sent to the spacecraft and stored in the on-board computer (CC&S). At the roll command, the spacecraft rolls at a constant rate through an angle θ_R. The spacecraft then remains at rest for the remainder of the roll turn period T_R, a fixed interval sufficiently long to allow the maximum roll turn of 90 deg. Following the roll turn, the pitch and yaw axes are switched to inertial control and the pitch turn is performed in a similar manner. The pitch rate $\dot{\theta}_p$, for a duration T_P, pitches the spacecraft by the angular displacement θ_P.

At the completion of the pitch turn, the nominal motor-thrust line is pointed in the correct direction and is parallel to the roll axis. The rocket motor is ignited at the completion of the pitch turn and is turned off when the accelerometer indicates that the commanded velocity increment has been added.

The midcourse-maneuver error analysis is conducted using the parameters listed in Table 10.

The errors due to the sub-system components are enumerated in Table 11, and are related to the maneuver pointing errors derived in Appendix D. Because the velocity vector is added along the roll axis, only pointing errors about the pitch and yaw axes need be considered.

Table 10. Midcourse maneuver parameters

Parameter		Values
Roll turn angle	θ_R	$-90° \leq \theta_R \leq +90°$
Pitch turn angle	θ_P	$-180° \leq \theta_P \leq +180°$
Roll turn rate	$\dot{\theta}_R$	± 3.5 mrad/sec
Pitch turn rate	$\dot{\theta}_P$	± 3.5 mrad/sec
Roll turn period	T_R	570 sec
Pitch turn period	T_P	1020 sec
Earth-probe-Sun angle	β	$45° \leq \beta \leq 135°$
Feedback gain in the pitch gyro-autopilot-jet vane loop	G_{FBP}	4.0
Feedback gain in the yaw gyro-autopilot-jet vane loop	G_{FBY}	4.0
Average acceleration of the spacecraft during the motor burn	V	0.615 m/sec

Infinitesimal approximations are made to simplify the analysis. Tables 12 and 13 list the error sources that contribute to shutoff and resolution errors, respectively, in the maneuver magnitude. The shutoff errors are proportional to the maneuver magnitude, while the resolution errors are independent of the maneuver magnitude. The results from Tables 11 through 13 are:

$$\begin{aligned} \textit{Pointing error} &= 34.68 \text{ mrad} \\ \textit{Shutoff error} &= 1.25\% \\ \textit{Resolution} &= 0.053 \text{ m/sec} \end{aligned} \tag{144}$$

For the rms maneuver of 20 m/sec, the 3-σ shutoff error is 0.249 m/sec.

The assumptions introduced in the analysis of the estimating of the pitch and yaw pointing errors, and the shutoff and resolution magnitude errors, are described below. Each of the error sources is assumed to have a zero mean value, and to be statistically independent of all other sources. As a result of the first assumption, the variance of each individual error source is equal to the mean value of the squared error, and the standard deviation is equal to the root-mean-square (rms) value. As a result of the second assumption, the variance of the final pointing, resolution, or shutoff error, is the sum of the products formed when the square of each individual error standard deviation is multiplied by the square of its coefficient. When each individual product is divided by the sum of the squares and multiplied by 100, the percentage contribution of the individual error source to the variance of the final error under consideration is obtained. If 3-σ values are used instead of the 1-σ standard deviations, the square root of the sum of the squares

Table 11. Pointing error

Error source	Units	3 σ source error	Origin of 3 σ source error number	Pitch coefficient	Yaw coefficient	Maximum coefficient	3 σ error (mrad)	Percent of total variance
Pitch sensor electrical null offset	mrad	0.5	Hardware	-1	0	1	0.50	<0.1
Pitch sensor mechanical null offset	mrad	2.2	Spec. RL-4-420A	-1	0	1	2.20	0.4
Pitch initial dead zone position	mrad	5.0 (1)	Spec. RL-4-420A	1	0	1	5.00	2.1
Pitch switching amplifier null offset	mrad	1.0	Spec. RL-4-420A	-2	0	2	2.00	0.3
Yaw sensor electrical null offset	mrad	0.5	Hardware	0	$-\cos\theta_P - \cot\beta \sin\theta_P$	$\sqrt{2}$	0.71	<0.1
Yaw sensor mechanical null offset	mrad	2.2	Spec. RL-4-420A	0	$-\cos\theta_P - \cot\beta \sin\theta_P$	$\sqrt{2}$	3.11	0.8
Yaw initial dead zone position	mrad	5.0 (1)	Spec. RL-4-420A	0	$\sqrt{\cos^2\theta_P + \cot^2\beta \sin^2\theta_P}$	1	5.00	2.1
Yaw switching amplifier null offset	mrad	1.0	Spec. RL-4-420A	0	$-2\cos\theta_P - \cot\beta \sin\theta_P$	$\sqrt{5}$	2.24	0.4
Roll sensor electrical null offset	mrad	8.0	Spec. RL-4-420A	0	$-\sin\theta_P/\sin\beta$	$\sqrt{2}$	11.31	10.6
Roll sensor mechanical null offset	mrad	1.73	Spec. RL-4-420A	0	$-\sin\theta_P/\sin\beta$	$\sqrt{2}$	2.45	0.5
Roll initial dead zone position	mrad	15.0 (1) (2)	Hardware	0	$\sin\theta_P/\sin\beta$	$\sqrt{2}$	21.21	37.4
Roll switching amplifier null offset	mrad	1.0	Spec. RL-4-420A	0	$-2\sin\theta_P/\sin\beta$	$2\sqrt{2}$	2.83	0.7
Pitch gyro drift	mrad/sec	4.85 E-3	Spec. RL-4-420A	$-T_P$	0	1020	4.95	2.0
Yaw gyro drift	mrad/sec	4.85 E-3	Spec. RL-4-420A	0	$-\sin\theta_P/\dot{\theta}_P - (T_P - \theta_P/\dot{\theta}_P)$	1020	4.95	2.0
Roll gyro drift	mrad/sec	4.85 E-3	Spec. RL-4-420A	0	$-T_R \sin\theta_P - (1 - \cos\theta_P)/\dot{\theta}_P$	925	4.49	1.7
Roll turn calibration	mrad/rad	3.0	Spec. RA345-4-440A	0	$\theta_R \sin\theta_P$	1.57	4.71	1.9
Roll capacitor leakage	mrad	5.0	Spec. RA345-4-440A	0	$-\sin\theta_P$	1	5.00	2.1
Roll turn time resolution	sec	0.867 (1)	Hardware	0	$\dot{\theta}_R \sin\theta_P$	3.5 E-3	3.03	0.8
Pitch turn calibration	mrad/rad	3.0	Spec. RA345-4-440A	θ_P	0	3.14	9.42	7.4
Pitch capacitor leakage	mrad	5.0	Spec. RA345-4-440A	-1	0	1	5.00	2.1
Pitch turn time resolution	sec	0.867 (1)	Hardware	$\dot{\theta}_P$	0	3.5 E-3	3.03	0.8
Yaw gyro misalignment in roll	mrad	1.53	Spec. RL-4-420A	0	$\sin\theta_P$	1	1.53	0.2
Roll gyro misalignment in yaw	mrad	1.53	Spec. RL-4-420A	0	$-(1 - \cos\theta_P)$	2	3.06	0.8
Roll sensor hinge misalignment in yaw	mrad	2.6	Spec. RL-4-420A	0	$\cot\beta \sin\theta_P$	1	2.60	0.6
Roll sensor hinge misalignment in roll	mrad	2.6	Spec. RL-4-420A	0	$-\sin\theta_P$	1	2.60	0.6
C.G. location, angular error in pitch	mrad	5.0	New Estimate	$1 + 1/G_{FBP}$	0	1.25	6.25	3.2
Thrust vector angular error in pitch	mrad	2.8	New Estimate	$-1/G_{FBP}$	0	0.25	0.70	<0.1
C.G. location, angular error in yaw	mrad	5.0	New Estimate	0	$1 + 1/G_{FBY}$	1.25	6.25	3.2
Thrust vector, angular error in yaw	mrad	2.8	New Estimate	0	$-1/G_{FBY}$	0.25	0.70	<0.1
Roll sensor albedo asymmetry	mrad	9.6 (2)	Hardware	0	$-\sin\theta_P/\sin\beta$	$\sqrt{2}$	13.57	15.3
					Total 3 σ pointing error (mrad) =		34.68	100.0

Notes:

(1) These parenthetical numbers (in column three above) have been taken as uniform distributions.

(2) These parenthetical numbers depend on angle, i.e., angular diameter from the Earth, and were calculated for 16 hrs, or approximately 160,000 km.

Table 12. Proportional shut-off error

Error source	Units	3 σ source error	Origin of 3 σ source error number	Error coefficient	Coefficient	3 σ error	Percent of total variance
Accelerometer scale factor	—	2.5 E-3	New estimate	V	V	2.5 E-3V	4.0
Accelerometer null offset	m/sec^2	7.5 E-3	Spec. RA 345-4-440A	$V/\dot{V}$	1.63 V	12.2 E-3V	96.0
					Total 3 σ Proportional Shutoff Error =	12.45 E-3V	100.0

Table 13. Resolution error

Error source	Units	3 σ source error	Origin of 3 σ source error number	Error coefficient	Coefficient	3 σ error	Percent of total variance
Velocity increment (Calculation and execution)	m/sec	37.3 E-3 (1)	New estimate	1	1	37.3 E-3	50.5
Velocity tailoff error	m/sec	37. E-3	New estimate	1	1	37. E-3	49.5
Note: (1) This parenthetical number (in column three above) has been taken as a uniform distribution.					Total 3 σ Resolution Error (m/sec) =	52.5 E-3	100.0

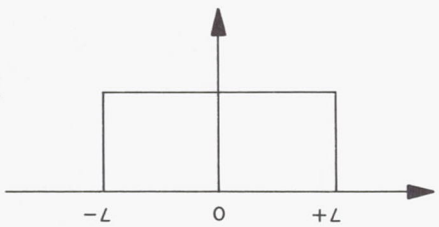

Fig. 40. Uniform density function

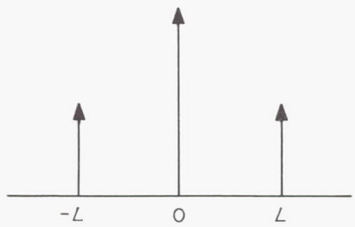

Fig. 41. Discrete density function

is the 3-σ value of the final error. The use of individually maximized coefficients tends to yield an upper bound on the 3-σ value if the individual errors are indeed statistically independent. By actually taking the square root of the sum of the errors squared, the pointing error is increased by approximately 4.8%.

The resulting 3-σ errors are assumed to have *Gaussian* distributions, except for sources 3, 7, 11, 18, 21, and 30 in Table 11, which are assumed to be uniformly distributed as shown in Fig. 40.

For a zero mean, uniformly distributed random variable, the 3-σ standard deviation is $3\sqrt{L}$.

It is possible that as a result of solar or other extraneous torques the limit-cycle errors, numbers 3, 7, and 11, would be forced to one or the other of their extreme values. Thus, they might approach a discrete distribution as shown in Fig. 41.

If this were the case, the 3-σ standard deviation for these errors would be $3L$ or $\sqrt{3}$ times their presently tabulated values.

D. Terminal Maneuver

The primary function of the terminal maneuver is to execute a pitch-yaw-pitch turn sequence so as to align the TV cameras' optical axes along the spacecraft's velocity vector just prior to impact; no motor burn is required. During this phase of the *Ranger* mission, the primary requirement imposed upon the attitude control system is the precise pointing of the directional antenna toward the Earth continuously. To do so, the first pitch turn is constrained to make the hinge angle 90 deg, so that the following yaw and pitch turns will not interfere with communications. The yaw and pitch turn points the camera and again requires the switching to a gyro-controlled turn and, therefore, the switching-in of the capacitors and the capacitor cycling. The terminal maneuver sequence is shown in Fig. 42.

1. Commanded Turns

The analysis for determining the gas consumed during the pitch-yaw-pitch turn sequence is identical to that presented in the midcourse discussion, Section III-C-1(a). Table 8 indicates the amount of gas used each time a pitch or yaw turn is made.

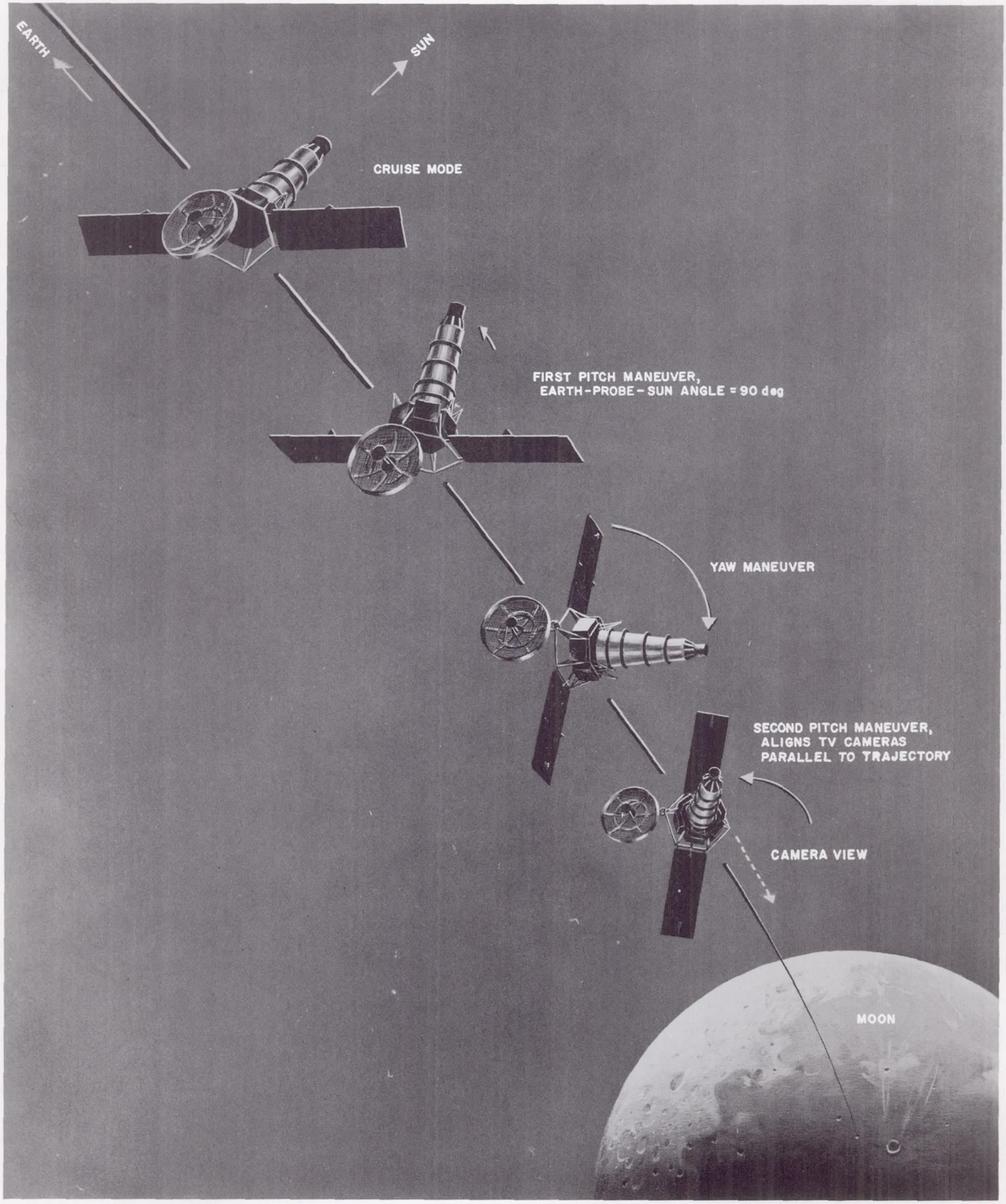

Fig. 42. Terminal maneuver

2. Terminal Maneuver Error Analysis

The error analysis of the terminal maneuver is reviewed in some detail in Appendix D. It should be noted that the technique for analyzing the terminal maneuver is quite different from that at midcourse due to the iterative scheme that must be employed in order to provide the desired results. Therefore, a detailed analysis must be made each time the trajectory information is varied, reflecting a complex computer program.

a. Effect of the Earth-probe-Sun angle. One of the factors influencing the accuracy of the *Ranger* terminal maneuver is the Earth-probe-Sun angle, β. The angle is nominally constrained to lie within the range $45 \text{ deg} < \beta < 135 \text{ deg}$. However, if this angle is increased in range to 140 deg, the accuracy is expected to vary slightly. To determine the effect of this increase in β, a study using the terminal maneuver accuracy program was conducted. For the pitch-yaw-pitch maneuver, the first pitch turn, θ_{P_1}, is a function of $\theta_{P_1} = 90 \text{ deg} - \beta$. The yaw turn and second pitch turn do not depend on β and were held constant. The results of this analysis are shown in Fig. 43; the graph shows how the spacecraft pointing errors are changed by varying the first pitch turn. The 3-σ rotation errors about the pitch, yaw, and roll axes are given in mrad and are denoted, respectively, as $3\sigma_x$, $3\sigma_y$, and $3\sigma_z$.

b. Camera pointing error. The error in pointing the camera axis is related to the spacecraft pointing errors as shown in Fig. 44. By assuming that the errors are small, the rotations may be represented by vectors. Hence, the rotation errors about the camera x and y axes are:

$$\sigma_{xc}^2 = \sigma_x^2 \tag{145}$$

$$\sigma_{yc}^2 = \cos^2\psi\sigma_y^2 + \sin^2\psi\sigma_z^2 - 2(\sin\psi\cos\psi)\sigma_{yz} \tag{146}$$

The quantities $3\sigma_{xc}$ and $3\sigma_{yc}$ are also plotted on the graph in Fig. 43. The value of $3\sigma_{yc}$ is determined by assuming $\sigma_{yz} = 0$. If the value of σ_{yz} were not equal to zero, then $3\sigma_{yc}$ would be smaller.

The above results indicate a general behavior of the pointing error. The larger the Earth-probe-Sun angle β, the more the y camera axis begins to increase as $1/\sin\beta$.

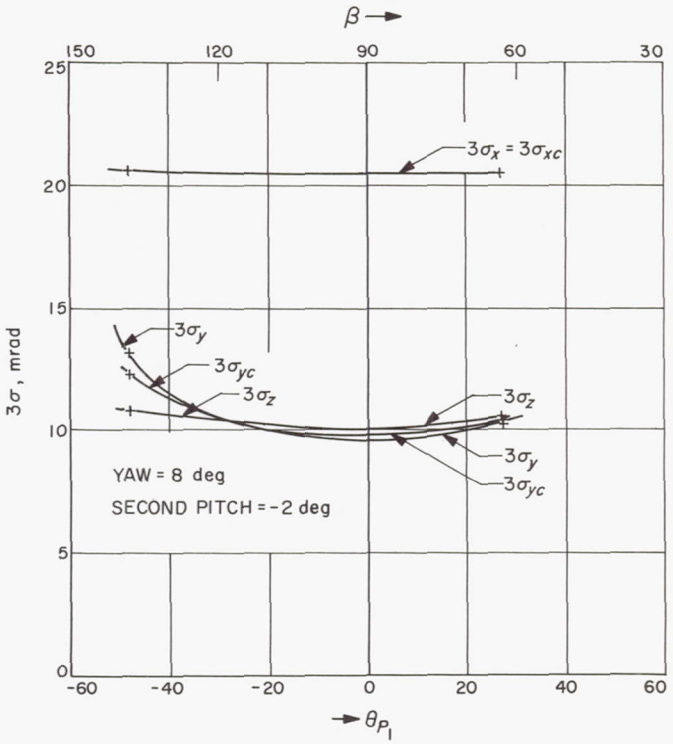

Fig. 43. Three-sigma terminal pointing errors as a function of the first pitch-turn magnitude

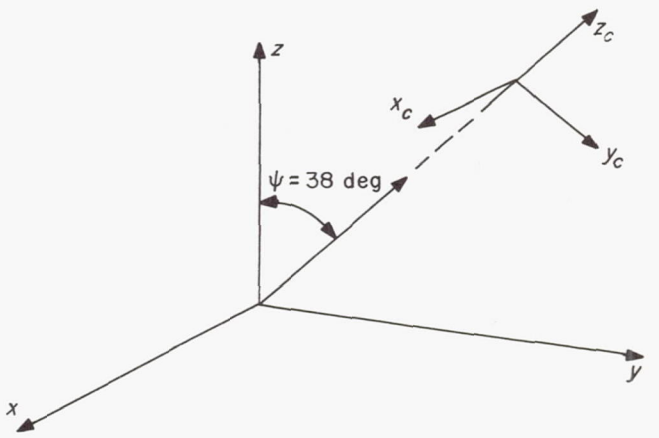

Fig. 44. Camera pointing error

Extrapolating from the graph, the camera pointing errors for $\beta = 140$ deg are approximately the following:

$$3\sigma_{xc} = 20.6 \text{ mrad}$$

$$3\sigma_{yc} = 13 \text{ mrad} \tag{147}$$

IV. SUMMARY AND CONCLUSIONS

This Report has covered the specific details of providing an attitude control system for the *Ranger* lunar spacecraft. As mentioned above in this Report, the function of the attitude control system is to maintain three-axis stabilization of the spacecraft during the lunar journey, and to provide correction capabilities for both (1) changing the trajectory in order to impact the Moon's surface and (2) photographing the Moon at some specific point.

The sequence which must be followed after the spacecraft separates from the *Agena* B second stage is first to command Sun acquisition. Simultaneously, the antenna rotates out to a pre-selected hinge angle and the initial injection rates are reduced since the gas jet system is activated and rate control is present. When the tumbling rates are sufficiently small, the vehicle's rate and position about the pitch and yaw axes are stabilized and controlled due to the gyro and Sun sensor position-error control.

Several hours later, the Earth acquisition command is transmitted to the spacecraft. The spacecraft is commanded to rotate about the Sun line (roll axis). The Earth sensor, mounted on the antenna arm, is activated and the antenna hinge, which is under servo control, changes position when the sensor first indicates the presence of Earth light. The sensor tracks the Earth and then locks onto it. The *Ranger* spacecraft is now under complete three-axis control in both rate and position.

Over 90% of the time in flight is considered to be in the cruise mode. This phase is characterized by low amplitude limit cycling. Control is obtained from both rate and position feedback. The cruise control system is designed to use a minimal amount of stored gas.

If the trajectory in which the spacecraft has been injected is not within the bounds of a successful lunar encounter, a midcourse maneuver is desirable. The maneuver requires an uncoupled commanded roll and pitch turn, and an increment of velocity added to the spacecraft's velocity vector by a midcourse rocket motor.

The maneuver requires that celestial position control be broken and that compensation networks integrated with the gyros provide both the rate and position signals during the maneuver. Following the maneuver, the Sun and Earth are re-acquired as the major bodies for position control in the same manner as discussed earlier. Finally, a terminal maneuver, consisting of an uncoupled pitch-yaw-pitch turn sequence, is initiated if the TV cameras' optical axis is not aligned within the specified tolerances for obtaining acceptable pictures of the lunar surface.

The *Ranger* mission requires a preciseness which can only be as good as the major subsystems of the attitude control system. For that reason, the inertial and celestial sensors, and the gas system must be highly accurate devices, designed to withstand external disturbances, temperature variations, etc., and to still maintain accurate operation.

In conclusion, the preciseness of the *Ranger* attitude control system as the controlling device for the stabilization, orientation, and course correction has been proven in the highly successful *Ranger* 6 and 7 missions, in January and July of 1964. The control of the spacecraft, as observed from the mission telemetry, indicates that the subsystems operated within the design specifications.

NOMENCLATURE

C	derived-rate capacitor
E_A	derived-rate amplifier electrical output
E_D	derived rate-decay voltage
E_{D_i}	initial conditions remaining from the charge-up of the derived-rate amplifier
E_N	noise in the switching amplifier
f	frequency of the cruise limit cycle
F	force due to the gas jets
G_{FB_P}	feedback gain in the pitch gyro-autopilot jet-vane loop

NOMENCLATURE (Cont'd)

G_{FB_Y} feedback gain in the yaw gyro-autopilot jet-vane loop

i_1 current output of the gyro amplifier

i_{cc} command current

i_T gyro torquer current

I_c, I_h, I_D specific impulse for a continuous discharge system, hysteresis type system, and derived-rate system

I, J moment of inertia of the spacecraft about each axis

I_{sp} specific impulse of the nitrogen gas

I_{xx}, I_{yy} moments of inertia about the pitch and yaw axes

I_{zz} moments of inertia about the roll axis

k_T gyro-torquer scale factor

K_A current scale factor, derived rate amplifier

K_D derived-rate gain

K_E Earth sensor scale factor

K_G rate sensor gain (gyro scale factor)

K_S position sensor gain (scale factor)

L lever arm of the gas jets

L_P, L_Y, L_R gas jet-valve moment arms for the pitch, yaw, and roll axes

n number of cycles in the limit cycle mode

R_T torque resistance

R_1, R_2 derived-rate amplifier feedback resistor

R_s derived-rate amplifier input resistor

R_T pure resistance

t_c duration of the control torque

t_m mission time

t_{off} gas jet *off* time

t_{on} gas jet *on* time

T_P pitch-turn period

T_R roll-turn period

t_s duration of the solar torque

V_1 torquer voltage

V_{out} gyro amplifier output voltage

W weight of the gas

$\dot{W}$ gas-weight flow rate

α spacecraft-acceleration constant due to the gas system

α_c acceleration due to the gas-jet torque

α_s acceleration due to solar energy

β Earth-probe-Sun angle (EPS)

Δt minimum on time

$\varepsilon(t)$ error signal actuating the switching amplifier

ε_{DB}, E_{DB} switching-amplifier electrical-deadband error signal

$\varepsilon_{S_s}, E_{S_s}$ Sun sensor saturated output (electrical)

θ_o initial position about the pitch, yaw, or roll axis

$\dot{\theta}_o$ initial rate about the pitch, yaw, or roll axis

$\dot{\theta}_a$ actual rate about the input axis of the gyro

$\dot{\theta}_c$ turn command rate

θ_{DB} equivalent switching-amplifier angular-position deadband

θ_{DB} rate deadband

θ_i vehicle angular position (general)

$\dot{\theta}_i$ vehicle angular rate (general)

$\dot{\theta}_{max}$ maximum acquisition rate

$\dot{\theta}_{max_{UL}}$ maximum upper limit of the acquisition rate

$\dot{\theta}_{min}$ minimum acquisition rate

$\dot{\theta}_{min_{LL}}$ minimum lower limit of the acquisition rate

$\dot{\theta}_{nom}$ nominal acquisition rate

θ_P pitch-turn angle

$\dot{\theta}_P$ pitch-turn rate

$\theta_P, \theta_Y, \theta_R$ pitch, yaw, and roll angular position

$\dot{\theta}_P, \dot{\theta}_Y, \dot{\theta}_R$ pitch, yaw, and roll rates

θ_{E_s} Earth sensor position saturation

NOMENCLATURE (Cont'd)

θ_h, θ_D limit cycle rate increment, hysteresis type system, and derived-rate system

θ_H antenna hinge angle

θ_R roll-turn angle

$\dot{\theta}_R$ roll-turn rate

θ_{S_s} equivalent Sun sensor saturation displacement

τ torque due to the gas jets

τ_1 spacecraft time constant in pitch or yaw (numerator zero)

τ_2 spacecraft time constant in pitch or yaw (denominator pole)

τ_c control torque due to the gas jets

$\dot{\tau}_c$ derived-rate charge-time constant

τ_D discharge time constant

τ_G ratio of the rate gain to the position gain

τ_s solar torque

τ_{s_m} marginal solar torque

BIBLIOGRAPHY

1. Acord, J. D., and J. Nicklas, "Theoretical and Practical Aspects of Solar Pressure Attitude Control for Interplanetary Spacecraft," *A.I.A.A., Guidance and Control Conference,* Massachusetts Institute of Technology, Cambridge, Mass., Paper No. 63-327, August 12–14, 1963.

2. *Attitude Control—Ranger Program Documentation Data,* Northrop Space Laboratories, Hawthorne, Calif., NASA/JPL Re-order No. 63-425, September 1963.

3. *Functional Specification, Ranger Block III Attitude Control and Autopilot Subsystems,* Jet Propulsion Laboratory, California Institute of Technology, Pasadena, Calif., Specification No. FR 3-4-420, Revised October 23, 1963.

4. *Functional Specification Spacecraft Ranger 6, 7, 8, 9 Flight Equipment Midcourse Autopilot System,* Jet Propulsion Laboratory, California Institute of Technology, Pasadena, Calif., Specification No. RL-4-460, January 22, 1962.

5. McLain, D., *Design Evaluation Recommendation, Attitude Control Sub-system,* Northrop Space Laboratories, Hawthorne, Calif., D.E.R. No. 0.0069, October 4, 1963.

6. Nicklas, J. C., and H. C. Vivian, *Derived-Rate Increment Stabilization, Its Application to the Attitude-Control Problem,* Jet Propulsion Laboratory, California Institute of Technology, Pasadena, Calif., Technical Report No. 32-69, July 31, 1961.

7. Scull, J., *Application of Optical Sensors for Lunar and Planetary Space Vehicles,* Jet Propulsion Laboratory, California Institute of Technology, Pasadena, Calif., Technical Report No. 32-274, May 31, 1963.

BIBLIOGRAPHY (Cont'd)

8. Sirri, N., *Space Vehicle Attitude Control,* Jet Propulsion Laboratory, California Institute of Technology, Pasadena, Calif., Technical Report No. 32-131, October 2, 1960.

9. Suggs, E., *Spacecraft Attitude Control Simulation,* Jet Propulsion Laboratory, California Institute of Technology, Pasadena, Calif., Section 343, RFP No. 1, March 4, 1961.

APPENDIX A

Spacecraft Dynamics

In the study of the midcourse maneuver, the dynamics of the vehicle play an important part in the determination of the response to the commanded turns and thrusting phase. The following discussion and analysis are provided to develop the approximate equations defining the structural dynamics and also to derive the transfer-function characteristics of the spacecraft.

1. Structural Dynamics

The flexibility in the hinge-type supports of the solar panels and the high-gain antenna necessitates a careful investigation of the spacecraft dynamics. First, the spacecraft structure in the midcourse configuration is of concern here and is approximated by a simplified model shown in Fig. A-1. In this model, all the structures are assumed rigid, and bendings take place only at the hinge or hinge lines. Thus, any compounded bending, cantilever bending, or torsional bending is neglected. The analysis is further simplified by neglecting structural crosscouplings. Therefore, the equations of motion about the yaw axis include only the solar panel bendings; the antenna bending is assumed only about the pitch axis. The equations are derived by using Lagrange's equations of motion, and are summarized in matrix forms. Detailed steps of the derivation for the yaw and pitch axes are shown in the following analyses.

It should be noted in Fig. A-1, that the directions of the major axes are chosen for sake of computational convenience, and may not agree with the practiced sign convention. The spacecraft attitude is measured with respect to an inertial reference whose coordinate axes

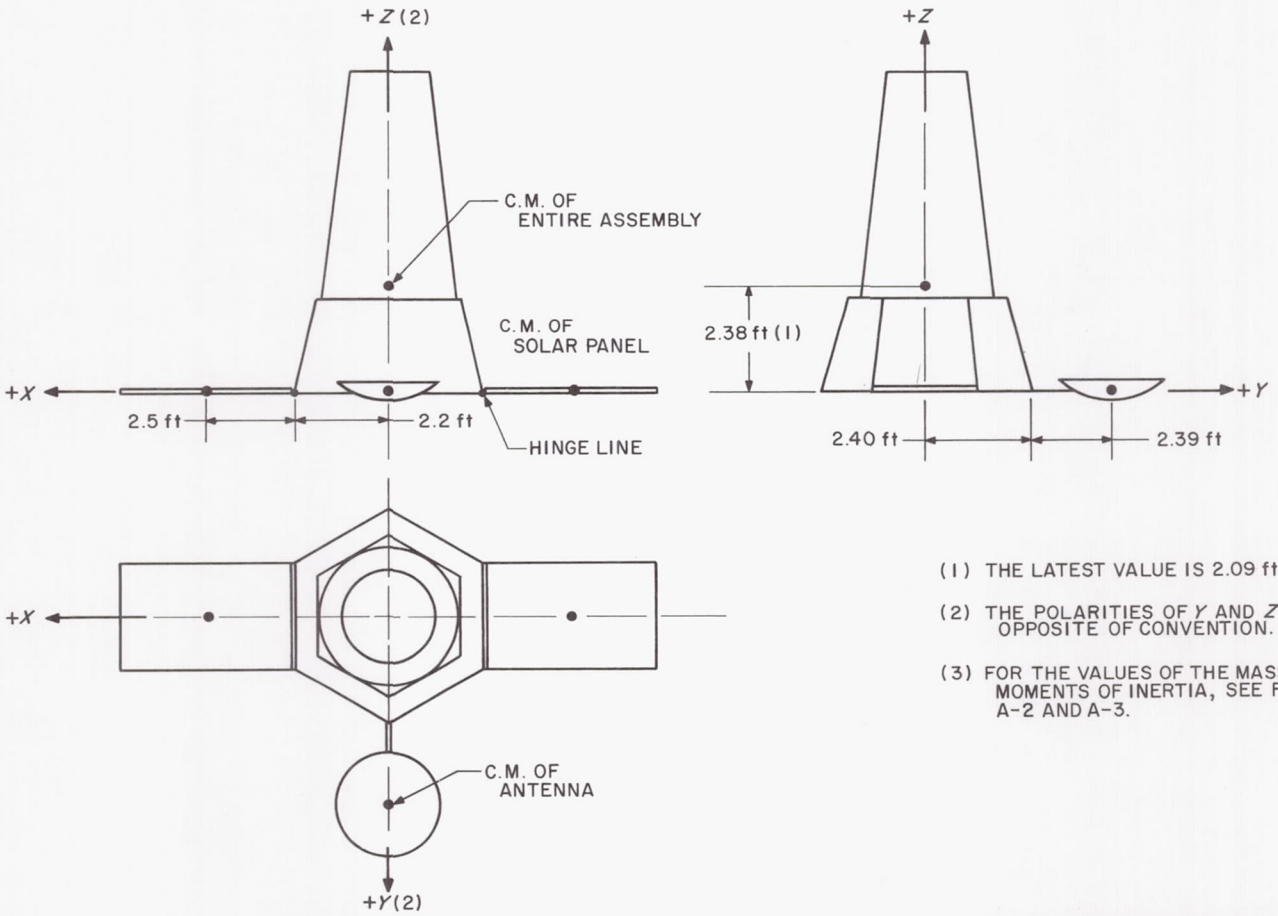

Fig. A-1. Spacecraft configuration

coincide with these major axes of the spacecraft, when all the gyro outputs are null.

Since the roll axis coincides very closely with the midcourse-motor thrust vector, the absolute value of the pointing error will not be affected appreciably by a small spacecraft roll. The roll-axis dynamics are approximated by a rigid body.

2. Derivation of Spacecraft Equations of Motion

The equations of motion which are characteristic of the *Ranger* spacecraft are derived based upon the Lagrangian equations. Thus,

$$\frac{d}{dt}\left(\frac{\partial T}{\partial \dot{q}_i}\right) - \frac{\partial T}{\partial q_i} + \frac{\partial V}{\partial q_i} = Q_i \qquad \text{(A-1)}$$

where

T = the total kinetic energy

V = the total potential energy

$\dot{q}_i$ = system variables: x, z, θ, ϕ_1 and ϕ_2

Q = the generalized input force

The equations for both the pitch and yaw axis are developed in the following sections.

a. Equations of motion, pitch axis. Based upon the simplified model of the spacecraft shown in Fig. A-2, the kinetic and potential energies are given, respectively, by

$$T = \frac{m_o v_o^2}{2} + \frac{m_3 v_3^2}{2} + \frac{m_4 v_4^2}{2} + \frac{I_o \theta^2}{2} + \frac{I_3}{2}(\theta + \phi_3)^2 \qquad \text{(A-2)}$$

$$V = \tfrac{1}{2} k_3 \phi_3^2 \qquad \text{(A-3)}$$

The parameters defining Fig. A-2 are given below:

A_o, A_3 = centers of mass of the spacecraft central structure and the communications antenna

0 = center of mass of the composite structure

line OB = line passing 0 and parallel to the spacecraft's z axis

C_3 = antenna hinge

k_3 = spring constant at C_3

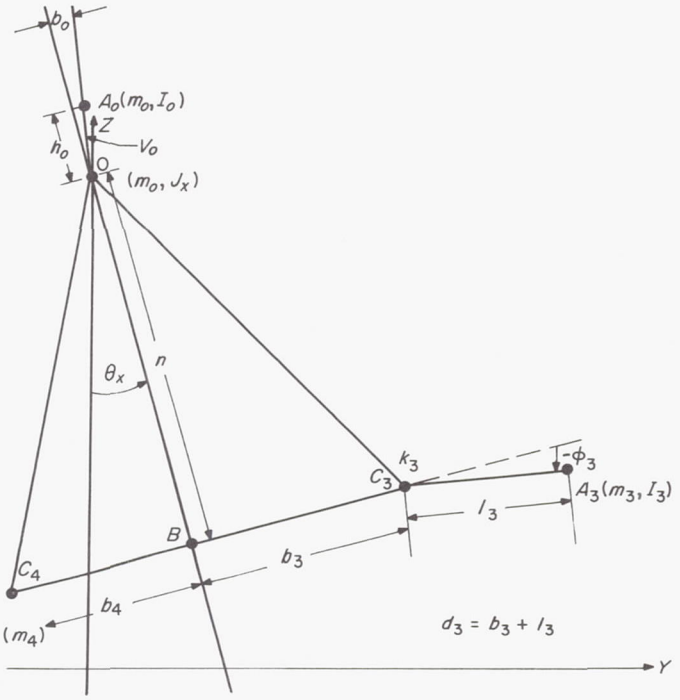

Fig. A-2. Simplified model of the spacecraft, pitch axis

C_4 = antenna counterbalance mass

$m_3 = 0.33$ slug

$M_o = m_o + m_3 + m_4 = 25$ slugs

I_3 = moment of inertia of the antenna about the line passing A_3 parallel to the X axis = 0.489 slug-ft^2/rad

Assuming infinitesimal rotations, the following approximations can be made.

$$v_o^2 = (\dot{y} - h_o\dot{\theta})^2 + (\dot{z} + b_o\dot{\theta})^2$$

$$v_3^2 = [\dot{z} + b_3\dot{\theta} + l_3(\dot{\theta} + \dot{\phi}_3)]^2 + [\dot{y} + h\dot{\theta}]^2$$

$$= [\dot{z} + d_3\dot{\theta} + l_3\dot{\phi}_3]^2 + [\dot{y} + h\dot{\theta}]^2$$

$$v_4^2 = (\dot{z} - b_4\dot{\theta})^2 + (\dot{y} + h\dot{\theta})^2$$

Now since

$$\frac{\partial T}{\partial z} = \frac{\partial T}{\partial y} = \frac{\partial T}{\partial \theta} = \frac{\partial T}{\partial \phi_3} = 0$$

and

$$\frac{\partial V}{\partial z} = \frac{\partial V}{\partial y} = \frac{\partial V}{\partial \theta} = 0$$

then, substitution into the first part of Eq. (A-1) yields the following forces and torques:

$$\frac{d}{dt}\left(\frac{\partial T}{\partial \dot{y}}\right) = (m_o + m_3 + m_4)\,\ddot{y} + (-m_o h_o + m_3 h + m_4 h)\,\ddot{\theta} = F_x$$

If we let

$$M_o = (m_o + m_3 + m_4)$$

then

$$F_x = M_o \ddot{y} \tag{A-4}$$

Also,

$$\frac{d}{dt}\left(\frac{\partial T}{\partial \dot{z}}\right) = (m_o + m_3 + m_4)\,\ddot{z} + (m_o b_o + m_3 d_3 - m_4 b_4)\,\ddot{\theta} + m_3 l_3 \ddot{\phi}_3 = F_z$$

and

$$F_z = M_o \ddot{z} + m_3 l_3 \ddot{\phi}_3 \tag{A-5}$$

Furthermore,

$$\frac{d}{dt}\left(\frac{\partial T}{\partial \dot{\theta}}\right) = (-m_o h_o + m_3 h + m_4 h)\,\ddot{y} + (m_o b_o + m_3 d_3 - m_4 b_4)\,\ddot{z} + [m_o (h_o^2 + b_o^2) + m_3 (h^2 + d_3^2) + m_4 (h^2 + b_4^2) + I_o + I_3]\,\ddot{\theta} + (m_3 l_3 \phi_3 + I_3)\,\ddot{\phi}_3 = \tau_x \tag{A-6}$$

Moreover,

$$\frac{d}{dt}\left(\frac{\partial T}{\partial \dot{\phi}_3}\right) = m_3 l_3 \ddot{z} + l_3 d_3 m_3 \ddot{\theta} + m_3 l_3^2 \ddot{\phi}_3 + I_3 (\ddot{\theta} + \ddot{\phi}_3) \tag{A-7}$$

also

$$\frac{\partial V}{\partial \phi_3} = k_3 \phi_3$$

and

$$0 = m_3 l_3 \ddot{z} + (I_3 + m_3 l_3 d_3)\,\ddot{\theta} + (I_3 + m_3 l_3^2)\ddot{\phi}_3 + k_3 \phi_3 \tag{A-8}$$

Now if we let

$$N_3 = m_3 l_3$$

$$J_3 = I_3 + m_3 l_3^2$$

$$J_{30} = I_3 + m_3 l_3 d_3$$

then Eq. (A-5), (A-6), and (A-8) can be written in the vector matrix notation as follows [Eq. (A-4) is not included since y is independent of the other variables]:

$$\begin{bmatrix} F_z \\ \tau_x \\ 0 \end{bmatrix} = \begin{bmatrix} M_o & 0 & N_3 \\ 0 & J_x & J_{30} \\ N_3 & J_{30} & \left(J_3 + \dfrac{k_3}{s^2}\right) \end{bmatrix} \begin{bmatrix} \ddot{z} \\ \ddot{\theta} \\ \ddot{\phi}_3 \end{bmatrix} \tag{A-9}$$

The matrix of coefficients is then given by

$$[X] = \begin{bmatrix} M_o & 0 & N_3 \\ 0 & J_x & J_{30} \\ N_3 & J_{30} & \left(J_3 + \dfrac{k_3}{s^2}\right) \end{bmatrix} \tag{A-10}$$

The transfer functions $\ddot{\theta}/\tau_x$ and $\ddot{\theta}/F_z$ can be determined by taking the inverse of Eq. (A-9) and substituting in the numerical values; therefore

$$\begin{bmatrix} \ddot{z} \\ \ddot{\theta} \\ \ddot{\phi}_3 \end{bmatrix} = \frac{1}{|X|} \begin{bmatrix} X_{11} & X_{21} \\ X_{12} & X_{22} \\ X_{13} & X_{23} \end{bmatrix} \begin{matrix} F_z \\ \\ \tau_x \end{matrix} \tag{A-11}$$

where X_{ij} is the cofactor of x_{ij}. The determinant is given as

$$|X| = \frac{M_o J_x k_3}{s^2}\left[\left(\frac{J_3}{k_3} - \frac{J_{30}^2}{J_x k_3} - \frac{N_3^2}{M_o k_3}\right) s^2 + 1\right] = \frac{M_o J_x k_3}{s^2}\left[\left(1 - \frac{J_{30}^2}{J_x J_3} - \frac{N_3^2}{M_o J_3}\right)\frac{s^2}{\omega_3^2} + 1\right] \tag{A-12}$$

where

$$\omega_3 = \sqrt{k_3/J_3}$$

The cofactors are

$$X_{12} = N_3 J_{30}$$

$$X_{22} = \frac{M_o k_3}{s^2}\left[\left(1 - \frac{N_3^2}{M_o J_3}\right)\frac{s^2}{\omega_3^2} + 1\right]$$

$$X_{13} = -N_3 J_x$$

$$X_{23} = -M_o J_{30}$$

The numerical values are given as

$$J_x = 109.0 \text{ slug-ft}^2$$

$$M_o = 25.0 \text{ slug}$$

$$N_3 = 0.788 \text{ ft-slug}$$

$$J_3 = 2.371 \text{ slug-ft}^2/\text{rad}$$

$$J_{30} = 4.27 \text{ slug-ft}^2/\text{rad}$$

Finally, upon substitution into the proper equations we obtain

$$\frac{\ddot{\theta}}{\tau_x} = \frac{\left(\frac{s^2}{(1.005)^2\,\omega_3^2} + 1\right)}{J_x\left(\frac{s^2}{(1.037)^2\,\omega_1^2} + 1\right)} \tag{A-13}$$

which can be approximated by

$$\frac{\ddot{\theta}}{\tau_x} \simeq \frac{\left(\frac{s^2}{\omega_1^2} + 1\right)}{J_x\left(\frac{s^2}{p_3\omega_1^2} + 1\right)} \tag{A-14}$$

where

$$\omega_1 = 18.1 \text{ rad/sec}$$

$$p_3 = 1.037$$

and

$$\frac{\ddot{\theta}}{F_z} = \frac{N_3 J_{30}}{J_x M_o J_3} \frac{\frac{s^2}{\omega_3^2}}{\left(\frac{s^2}{(1.037)^2\,\omega_3^2} + 1\right)} \tag{A-15}$$

b. Equations of motion, yaw axis. Similarly, the equations which are characteristic of the yaw axis are developed. With the aid of Fig. A-3, the kinetic and potential energy about the yaw axis is given as

$$T = \frac{m_o}{2} v_o^2 + \frac{m_1}{2} v_1^2 + \frac{m_2}{2} v_2^2 + \frac{I_o}{2}\dot{\theta}^2 + \frac{I_1}{2}(\dot{\theta} + \dot{\phi}_1) + \frac{I_2}{2}(\dot{\theta} + \dot{\phi}_2)^2 \tag{A-16}$$

$$V = \tfrac{1}{2}k_1\phi_1^2 + \tfrac{1}{2}k\phi_2^2 \tag{A-17}$$

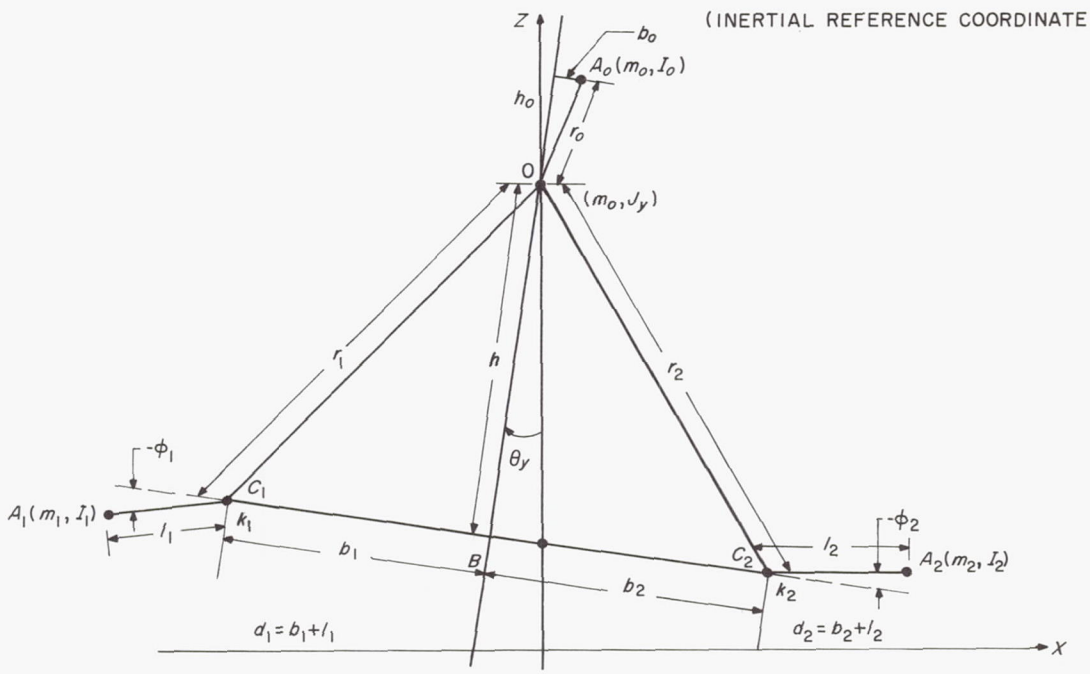

LEGEND:

A_o, A_1, A_2: CENTERS OF MASS OF THE SPACECRAFT CENTRAL STRUCTURE, SOLAR PANEL 1 AND SOLAR PANEL 2

O: CENTER OF MASS OF THE COMPOSITE STRUCTURE

LINE *OB*: THE LINE PASSING O AND PARALLEL TO THE SPACECRAFT *Z* AXIS

c: HINGELINE

k: SPRING CONSTANT ABOUT THE HINGE LINE

$m_1 \simeq m_2 = 0.73$ SLUG

$M_o = m_o + m_1 + m_2 = 25$ SLUGS

$I_1 \simeq I_2 = 1.9$ slug-ft^2/rad (MOMENT OF INERTIA OF THE SOLAR PANEL ABOUT LINE THROUGH *A*, PARALLEL TO THE *y* AXIS

$J_y = I_o + I_1 + I_2 + m_o r_o^2 + m_1(h^2 + d_1^2) + m_2(h^2 + d_2^2) = 109$ slug-ft^2/rad

Fig. A-3. Simplified model of the spacecraft, yaw axis

If all of the rotations are assumed to be infinitesimal, then the following approximations can be made:

$$v_o^2 = (\dot{x} + h_o\dot{\theta})^2 + (\dot{z} - b_o\dot{\theta})^2$$

$$v_1^2 = (\dot{x} - h\dot{\theta})^2 + [\dot{z} + b_1\dot{\theta} + l_1(\dot{\phi}_1 + \dot{\theta})]^2$$

$$v_2^2 = (\dot{x} - h\dot{\theta})^2 + [\dot{z} - b_2\dot{\theta} - l_2(\dot{\phi}_2 + \dot{\theta})]^2$$

Now since

$$\frac{\partial T}{\partial z} = \frac{\partial T}{\partial x} = \frac{\partial T}{\partial \theta} = \frac{\partial T}{\partial \phi_1} = \frac{\partial T}{\partial \phi_2} = 0$$

and

$$\frac{\partial V}{\partial \dot{z}} = \frac{\partial V}{\partial x} = \frac{\partial V}{\partial \theta} = 0$$

we obtain for the z axis:

$$\frac{d}{dt}\left(\frac{\partial T}{\partial \dot{z}}\right) = (m_o + m_1 + m_2)\ddot{z} + (-m_o b_o + m_1 d_1 - m_2 d_2)\ddot{\theta} + m_1 l_1 \ddot{\phi}_1 - m_2 l_2 \ddot{\phi}_2$$

$$F_z = (m_o + m_1 + m_2)\ddot{z} + m_1 l_1 \ddot{\phi}_1 - m_2 l_2 \ddot{\phi}_2 \qquad \text{(A-18)}$$

For the x axis:

$$\frac{d}{dt}\left(\frac{\partial T}{\partial \dot{x}}\right) = (m_o + m_1 + m_2)\ddot{x} + (m_o h_o - m_1 h_1 - m_2 h_2)\ddot{\theta}$$

$$F_x = (m_o + m_1 + m_2)\ddot{x} \qquad \text{(A-19)}$$

For θ:

$$\frac{d}{dt}\left(\frac{\partial T}{\partial \dot{\theta}}\right) = [m_o(h_o^2 + b_o^2) + m_1(h^2 + d_1^2) + m_2(h^2 + d_2^2) + I_o + I_1 + I_2]\ddot{\theta} + (I_1 + m_1 l_1 d_1)\ddot{\phi}_1 + (I_2 + m_2 l_2 d_2)\ddot{\theta}_2 = \tau_y \qquad \text{(A-20)}$$

For ϕ_1:

$$\frac{d}{dt}\left(\frac{\partial T}{\partial \dot{\phi}_1}\right) = (I_1 + m_1 l_1 d_1)\ddot{\theta} + (I_1 + m_1 l_1^2)\ddot{\phi}_1 + m_1 l_1 \ddot{z}$$

$$\frac{\partial V}{\partial \phi_1} = k_1 \phi_1$$

Therefore,

$$(I_1 + m_1 l_1 d_1)\ddot{\theta} + (I_1 + m_1 l_1^2)\ddot{\phi}_1 + k_1\phi_1 + m_1 l_1 \ddot{z} = 0 \qquad \text{(A-21)}$$

Similarly for ϕ_2:

$$(I_2 + m_2 l_2 d_2)\ddot{\theta} + (I_2 + m_2 l_2^2)\ddot{\phi}_2 + h_2\phi_2 - m_2 l_2 \ddot{z} = 0 \qquad \text{(A-22)}$$

Now, if we introduce the following substitutions:

$$M_o = (m_o + m_1 + m_2)$$

$$J_y = m_o(h_o^2 + b_o^2) + m_1(h^2 + d_1^2) + m_2(h^2 + d_2^2) + I_o + I_1 + I_2$$

$$J_1 = I_1 + m_1 l_1^2$$

$$J_{10} = I_1 + m_1 l_1 d_1$$

$$J_2 = I_2 + m_2 l_2^2$$

$$J_{20} = I_2 + m_2 l_2 d_2$$

$$N_1 = m_1 l_1$$

$$N_2 = m_2 l_2$$

then, the vector matrix equations can be written in the form below:

$$\begin{bmatrix} F_z \\ F_x \\ \tau_y \\ 0 \\ 0 \end{bmatrix} = \begin{bmatrix} M_o & 0 & 0 & N_1 & -N_2 \\ 0 & M_o & 0 & 0 & 0 \\ 0 & 0 & J_y & J_{10} & J_{20} \\ N_1 & 0 & J_{10} & \left(J_1 + \frac{k_1}{s^2}\right) & 0 \\ -N_2 & 0 & J_{20} & 0 & \left(J_2 + \frac{k_2}{s^2}\right) \end{bmatrix} \begin{bmatrix} \ddot{z} \\ \ddot{x} \\ \ddot{\theta} \\ \ddot{\phi}_1 \\ \ddot{\phi}_2 \end{bmatrix} \qquad \text{(A-23)}$$

From the above expression, it is clear that the term involving x may be removed from the equation so that we now have

$$\begin{bmatrix} F_z \\ \tau_y \\ 0 \\ 0 \end{bmatrix} = \begin{bmatrix} M_o & 0 & N_1 & -N_2 \\ 0 & J_y & J_{10} & J_{20} \\ N_1 & J_{10} & \left(J_1 + \frac{k_1}{s^2}\right) & 0 \\ -N_2 & J_{20} & 0 & \left(J_2 + \frac{k_2}{s^2}\right) \end{bmatrix} \begin{bmatrix} \ddot{z} \\ \ddot{\theta}_y \\ \ddot{\phi}_1 \\ \ddot{\phi}_2 \end{bmatrix} \tag{A-24}$$

The solutions to the above expression are obtained by solving for the inverse so that

$$\begin{bmatrix} F_z \\ \tau_y \\ 0 \\ 0 \end{bmatrix} = [Y] \begin{bmatrix} \ddot{z} \\ \ddot{\theta} \\ \ddot{\phi}_1 \\ \ddot{\phi}_2 \end{bmatrix}$$

and

$$\begin{bmatrix} \ddot{z} \\ \ddot{\theta} \\ \ddot{\phi}_1 \\ \ddot{\phi}_2 \end{bmatrix} = \frac{1}{|Y|} \begin{bmatrix} Y_{11} & Y_{21} \\ Y_{12} & Y_{22} \\ Y_{13} & Y_{23} \\ Y_{14} & Y_{24} \end{bmatrix} \begin{bmatrix} F_z \\ \tau_y \end{bmatrix} \tag{A-25}$$

where Y_{ij} is the cofactor of y_{ij}.

In order to simplify the problem somewhat, we can let solar panel 2 be slightly different from solar panel 1, and thus

$$m_2 = m_1 + \Delta m$$

$$l_2 = l_1 + \Delta l$$

$$k_2 = k_1 + \Delta k$$

Then $|Y|$ and Y_{ij} can be expressed in terms of solar panel 1 parameters and Δm, Δl, Δk. Furthermore, if we assume that

$$\lambda^2 = \frac{I_1}{m_1} = \frac{I_2}{m_2}$$

then,

$$J_1 = m_1(\lambda^2 + l_1^2)$$

$$J_2 = m_2(\lambda^2 + l_2^2)$$

$$J_{10} = m_1(\lambda^2 + l_1 d_1)$$

$$J_{20} = m_2(\lambda^2 + l_2 d_2)$$

Any variation in the error terms Δm and Δl affects moments of inertia J_{10}, J_2 and J_{20}, since d_1, d_2, l_2 and m_2 vary. Therefore, the above relationships are determined. The partial derivatives are taken at $m_1 = m_2$ and $l_2 = l_1$.

$$\left.\frac{\partial J_{10}}{\partial m_2}\right|_{l_2 = l_1} = \frac{2m_1 l_1 d_1}{M_o}$$

$$\left.\frac{\partial J_{10}}{\partial l_2}\right|_{m_2 = m_1} = \frac{m_1}{M_o} N_1$$

$$\left.\frac{\partial J_{20}}{\partial m_2}\right|_{\substack{l_1 = l_2 \\ m_1 = m_2}} = \frac{J_{10}}{m_1}$$

$$\left.\frac{\partial J_{20}}{\partial l_2}\right|_{\substack{l_1 = l_2 \\ m_1 = m_2}} = m_1\left(\frac{(m_o + m_1)}{M_o} l_1 + d_1\right)$$

$$\frac{\partial J_2}{\partial m_2} = \frac{J_1}{m_1}$$

$$\frac{\partial J_2}{\partial l_2} = 2N_1$$

Based upon the above expressions, the determinant and cofactors of Eq. (A-25) can be determined.

From the diagram in Fig. A-4, the distance from the tip of the solar panels to the central structure is determined as a function of an incremental offset.

Hence,

$$\begin{bmatrix} 0 \\ b + l_1 \\ b + l_2 \end{bmatrix} = \begin{bmatrix} m_o & m_1 & -m_2 \\ -1 & 1 & 0 \\ 1 & 0 & 1 \end{bmatrix} \begin{bmatrix} d_o \\ d_1 \\ d_2 \end{bmatrix} \tag{A-26}$$

Solving for d_1 and d_2 yields,

$$d_1 = \frac{m_o(b + l_1) + m_2(2b + l_1 + l_2)}{M_o} \tag{A-27}$$

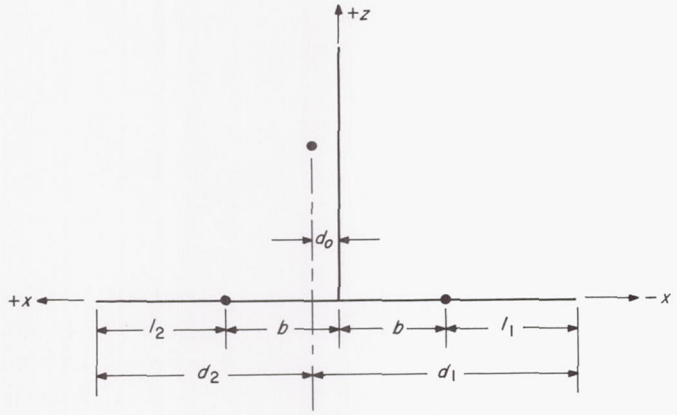

Fig. A-4. Distance from tip of solar panels to central structure, as function of incremental offset

and

$$d_2 = \frac{m_o(b + l_2) + m_1(2b + l_1 + l_2)}{M_o} \tag{A-28}$$

Therefore,

$$J_{10} = m_1\left\{\lambda^2 + l_1\left[\frac{m_o(b + l_1) + m_2(2b + l_1 + l_2)}{M_o}\right]\right\} \tag{A-29}$$

and

$$J_{20} = m_2\left\{\lambda^2 + l_2\left[\frac{m_o(b + l_2) + m_1(2b + l_1 + l_2)}{M_o}\right]\right\} \tag{A-30}$$

The determinant is now evaluated by analyzing the following expression:

$$|Y| = \begin{vmatrix} M_o & 0 & N_1 & -N_1 \\ 0 & J_y & J_{10} & J_{10} \\ N_1 & J_{10} & \left(J_1 + \frac{k_1}{s^2}\right) & 0 \\ -N_1 & J_{10} & 0 & \left(J_1 + \frac{k_1}{s^2}\right) \end{vmatrix}$$

$$+ \frac{\partial |Y|}{\partial m_2}\Delta m + \frac{\partial |Y|}{\partial l_2}\Delta l_2 + \frac{\partial |Y|}{\partial k_2}\Delta k$$

$$= \frac{k_1 J_y M_o}{s^4}\left(\frac{s^2}{\omega_1^2/(1-2\beta)} + 1\right)\left(\frac{s^2}{\omega_1^2/(1-2\alpha)} + 1\right)$$

$$+ \frac{\partial |Y|}{\partial m_2}\Delta m + \frac{\partial |Y|}{\partial l_2}\Delta l_2 + \frac{\partial |Y|}{\partial k_2}\Delta k \tag{A-31}$$

where

$$\omega_1^2 = \frac{k_1}{J_1}$$

$$\alpha = \frac{N_1^2}{J_1 M_o}$$

$$\beta = \frac{J_{10}^2}{J_1 J_y}$$

and

$$\frac{\partial |Y|}{\partial m_2} \simeq \frac{J_1 M_o J_y k_1}{m_1 s^2}(1 - 2\beta)\left(\frac{s^2}{\omega_1^2/(1-\beta)} + 1\right) \tag{A-32}$$

$$\frac{\partial |Y|}{\partial l_2} \simeq \frac{2N_1 M_o J_y k_1}{s^2}\left(1 - \frac{m_1}{M_o} - \frac{J_{10}}{J_y}\frac{(l_1 + d_1)}{l_1}\right) \times \left(\frac{s^2}{\omega_1^2/(1-\beta)} + 1\right) \tag{A-33}$$

$$\frac{\partial |Y|}{\partial k_2} = \frac{M_o J_y k_1}{s^4}\left(\frac{s^2}{\omega_1^2/(1-\alpha-\beta)} + 1\right) \tag{A-34}$$

Further approximations can be assumed since F_z is relatively large and θ, ϕ_1 and ϕ_2 are small. Therefore,

$$\frac{Y_{11}}{|Y|} \simeq \frac{1}{M_o}$$

$$Y_{12} \simeq 0 \tag{A-35}$$

Similarly, the remaining cofactors may be expressed as

$$Y_{22} = \frac{M_o k_1^2}{s^4}\left(\frac{s^2}{\omega_1^2/(1-2\alpha)} + 1\right)\left(\frac{s^2}{\omega_1^2} + 1\right) + \frac{\partial Y_{22}}{\partial m_2}\Delta m + \frac{\partial Y_{22}}{\partial l_2}\Delta l + \frac{\partial Y_{22}}{\partial k_2}\Delta k \tag{A-36}$$

where

$$\frac{\partial Y_{22}}{\partial m_2} \simeq \frac{M_o J_1 k_1}{m_1 s^2}(1 - 2\alpha)\left(\frac{s^2}{\omega_1^2/(1-\alpha)} + 1\right) \tag{A-37}$$

$$\frac{\partial Y_{22}}{\partial l_2} \simeq \frac{2N_1 M_o k_1}{s^2}\left(\frac{s^2}{\omega_1^2/(1-\alpha)} + 1\right) \tag{A-38}$$

$$\frac{\partial Y_{22}}{\partial h_2} = \frac{M_o k_1}{s^4}\left(\frac{s^2}{\omega_1^2/(1-\alpha)} + 1\right) \tag{A-39}$$

$$Y_{13} = -\frac{J_y N_1 k_1}{s^2}\left(\frac{s^2}{\omega_1^2/(1-2\beta)} + 1\right) + \Delta Y_{13} \tag{A-40}$$

$$\frac{\partial Y_{13}}{\partial m_2} = -\frac{J_y J_1 N_1}{m_1}\left(1 - 4\beta + 2\frac{m_1}{M_o}\frac{J_{10}}{J_y}\frac{l_1 d_1}{(\lambda^2 + l_1^2)}\right) \tag{A-41}$$

$$\frac{\partial Y_{13}}{\partial l_2} = -2N_1^2 J_y\left[1 - \left(\frac{J_{10}}{2J_y}\right) \times\left(\frac{\lambda^2 + \left(\frac{M_o + 2(m_o + m_1)}{M_o}\right)l_1^2 + 4l_1 d_1}{l_1^2}\right)\right] \tag{A-42}$$

$$\frac{\partial Y_{13}}{\partial k_2} = \frac{-J_y N_1}{s^2} \tag{A-43}$$

$$Y_{23} = -\frac{M_o J_{10} k_1}{s^2}\left(\frac{s^2}{\omega_1^2/(1-2\alpha)} + 1\right) + \Delta Y_{23} \tag{A-44}$$

$$\frac{\partial Y_{23}}{\partial m_2} = -\frac{2k_1 N_1 d_1}{s^2}\left[\left(1 - \alpha + \frac{(\lambda^2 + l_1 d_1) M_o}{2m_1 l_1 d_1}(1 - 4\alpha)\right)\frac{s^2}{\omega_1^2} + 1\right] \tag{A-45}$$

$$\frac{\partial Y_{23}}{\partial l_2} = -\frac{m_1 N_1 k_1}{s^2}\left(\frac{2M_o(\lambda^2 + l_1 d_1)}{m_1(\lambda^2 + l_1^2)} - \frac{2(\lambda^2 + 2l_1 d_1)}{(\lambda^2 + l_1^2)}\right)\frac{s^2}{\omega_1^2} + 1 \tag{A-46}$$

$$\frac{\partial Y_{23}}{\partial k_2} = -\frac{M_o J_{10}}{s^2} \tag{A-47}$$

$$Y_{14} = \frac{J_y N_1 k_1}{s^2}\left(\frac{s^2}{\omega_1^2/(1-2\beta)} + 1\right) + \Delta Y_{14} \tag{A-48}$$

$$\frac{\partial Y_{14}}{\partial m_2} = \frac{N_1 J_y k_1}{m_1 s^2}\left\{\left[1 - 2\beta\left(1 + 3\frac{m_1 l_1 d_1}{M_o(\lambda^2 + l_1 d_1)}\right)\right]\frac{s^2}{\omega_1^2} + 1\right\} \tag{A-49}$$

$$\frac{\partial Y_{14}}{\partial l_2} = \frac{N_1 J_y k_1}{l_1 s^2}\left\{\left[1 - \beta - \frac{J_3}{J_o} \times\left(\frac{l_1^2\left(1 + \frac{2m_1}{M_o}\right) + l_1 d_1}{\lambda^2 + l_1^2}\right)\right]\frac{s^2}{l_2} + 1\right\} \tag{A-50}$$

$$\frac{\partial Y_{14}}{\partial h_2} = 0 \tag{A-51}$$

$$Y_{24} = -\frac{M_o J_{10} k_1}{s^2}\left(\frac{s^2}{\omega_1^2/(1-2\alpha)} + 1\right) + \Delta Y_{24} \tag{A-52}$$

$$\frac{\partial Y_{24}}{\partial m_2} = -\frac{M_o J_{10} k_1}{m_1 s^2} \times\left[\frac{s^2}{\omega_1^2/[1 - 2\alpha_1(1 - m_1 l_1 d_1/M_o(\lambda^2 + l_1 d_1))]} + 1\right] \tag{A-53}$$

$$\frac{\partial Y_{24}}{\partial l_2} \simeq \frac{M_o N_1(l_1 + d_1)}{l_1 s^2} \times\left[\left(1 - \alpha_1 - \frac{m_1 l_1(\lambda^2 + l_1 d_1)}{M_o l_1 + d_1(\lambda^2 + l_1^2)}\right)\frac{s^2}{\omega_1^2} + 1\right] \tag{A-54}$$

$$\frac{\partial Y_{24}}{\partial h_2} = 0 \tag{A-55}$$

Now in order to obtain a set of numerical solutions, the values of the parameters must be substituted into the above equations; hence the parameters are given below as

$l_1 = 2.5$ ft

$d_1 = 4.7$ ft

$m_1 = 0.73$ slug

$M_o = 25.0$ slugs

$J_y = 109.0$ slug-ft^2/rad

$\lambda^2 = 2.6$ ft^2

$\alpha = 0.02062$

$\beta = 0.156$

$J_1 = 6.46$ slug-ft^2/rad

$J_{10} = 10.48$ slug-ft^2/rad

$N_1 = 1.825$ slug-ft^2/rad

$I_1 = 1.9$ slug-ft^2/rad

Substituting into the above equations, we get the following solutions in terms of several of the unknowns:

$$|Y| = \frac{k_1^2 J_y M_o}{s^4}\left[\left(\frac{s^2}{(1.206\omega_1)^2}+1\right)\left(\frac{s^2}{(1.021\omega_1)^2}+1\right) + 0.632\frac{\Delta m}{m}\frac{s^2}{\omega_1^2}\left(\frac{s^2}{(1.147\omega_1)^2}+1\right) + 0.978\frac{\Delta l}{l}\frac{s^2}{\omega_1^2}\left(\frac{s^2}{(1.136\omega_1)^2}+1\right) + \frac{\Delta k}{k}\left(\frac{s^2}{(1.102\omega_1)^2}+1\right)\right] \quad \text{(A-56)}$$

$$Y_{22} = \frac{M_o k_1^2}{s^4}\left[\left(\frac{s^2}{(1.021\omega_1)^2}+1\right)\left(\frac{s^2}{\omega_1^2}+1\right) + \left(\frac{s^2}{(1.01\omega_1)^2}+1\right)\left(0.959\frac{\Delta m}{m}\frac{s^2}{\omega_1^2} + 1.412\frac{\Delta l}{l}\frac{s^2}{\omega_1^2}+\frac{\Delta k}{k}\right)\right] \quad \text{(A-57)}$$

$$Y_{13} = -\frac{J_y N_1 k_1}{s^2}\left[\left(0.688 + 0.383\frac{\Delta m}{m} + \frac{0.674\Delta l}{l}\right)\frac{s^2}{\omega_1^2}+1+\frac{\Delta k}{k}\right] \quad \text{(A-58)}$$

$$Y_{23} = -\frac{M_o J_{10} k_1}{s^2}\left\{\frac{s^2}{(1.021\omega_1)^2}+1+0.048\frac{\Delta m}{m}\left[\left(\frac{19.25}{\omega_1}\right)^2+1\right]+0.0172\frac{\Delta l}{l}\left(\frac{102.7s^2}{\omega_1^2}+1\right)+\frac{\Delta k}{k}\right\} \quad \text{(A-59)}$$

$$Y_{14} \simeq \frac{J_y N_1 k_1}{s^2}\left(1+\frac{\Delta m}{m}+\frac{\Delta l}{l}\right)\left(\frac{s^2}{(1.206\omega_1)^2}+1\right) \quad \text{(A-60)}$$

$$Y_{24} \simeq -\frac{M_o J_{10} k_1}{s^2}\left(1+\frac{\Delta m}{m}+1.13\frac{\Delta l}{l}\right)\left(\frac{s^2}{(1.02\omega_1)^2}+1\right) \quad \text{(A-61)}$$

These parameters are now plotted as functions of $\Delta m/m$, $\Delta l/l$ and $\Delta k/k$ (up to $\pm 10\%$) for normalized frequency s/ω_1 in Fig. A-5 through A-7.

The figures are plotted by normalizing the frequency to that of the solar panel natural resonance ω_1 and assuming that the solar panels are identical. The equations then reduce to the following:

$$|Y| = \frac{k_1^2 J_y M_o}{s^4\,(1.206^2)\,(1.021^2)}\left(\frac{s^2}{\omega_1^2}+1.206^2\right)\left(\frac{s^2}{\omega_1^2}+1.021^2\right)$$

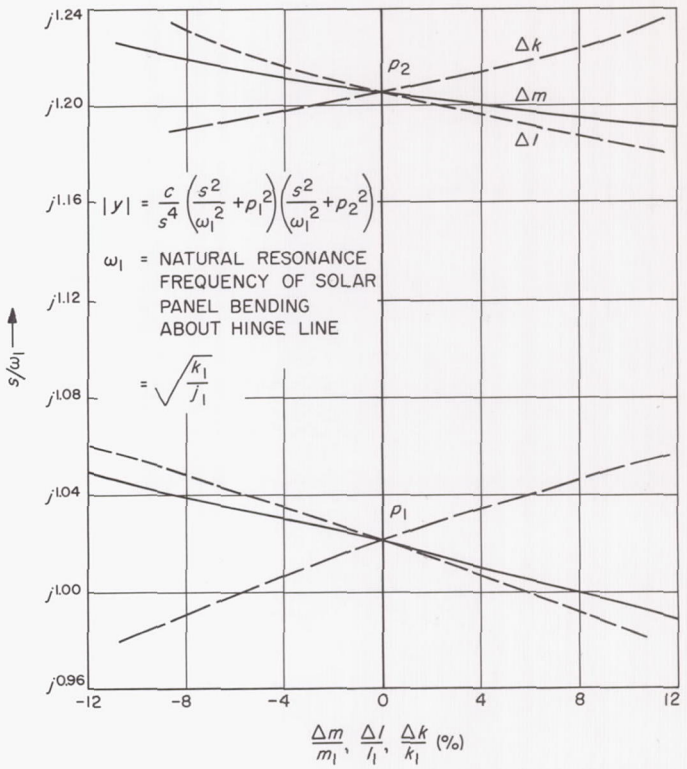

Fig. A-5. Variation of the roots of $|Y|$ due to the variation of Δm, Δl, or Δk

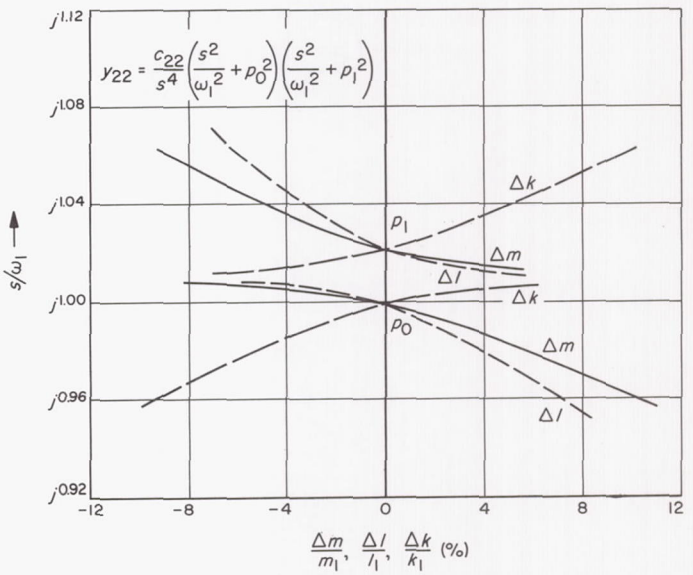

Fig. A-6. Variation of the roots of Y_{22} due to the variation of Δm, Δl, or Δk

If we let

$$C = \frac{k_1^2 J_y M_o}{(1.206^2)\,(1.021^2)}$$

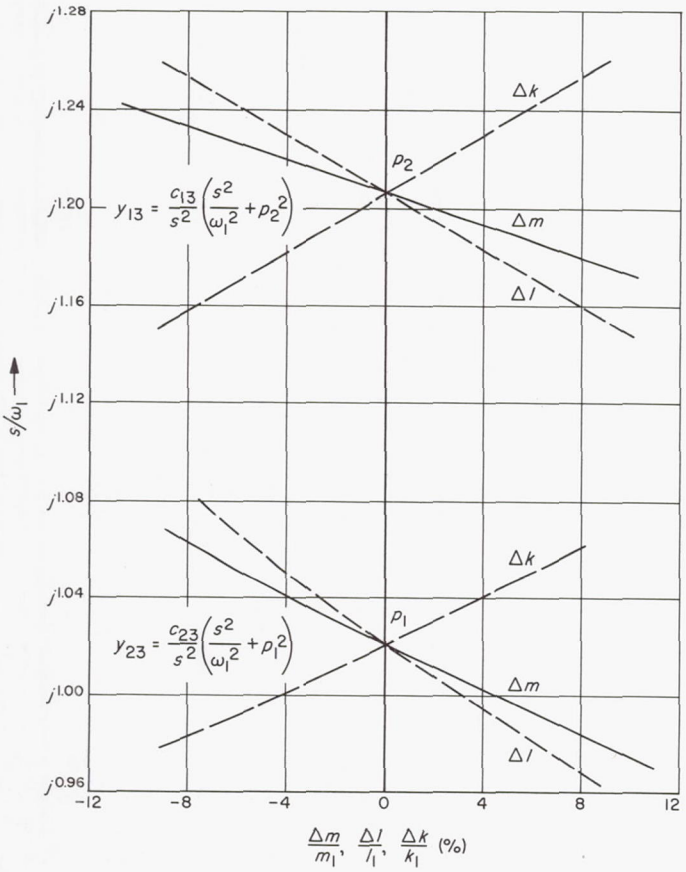

Fig. A-7. Variation of the roots of Y_{13} and Y_{23} due to the variation of Δm, Δl, or Δk

$$p_1 = 1.021$$

$$p_2 = 1.206$$

Then

$$|Y| = \frac{C}{s^4}\left(\frac{s^2}{\omega_1^2} + p_1^2\right)\left(\frac{s^2}{\omega_1^2} + p_2^2\right) \qquad \text{(A-62)}$$

The cofactors of Eq. (A-25) reduce to the following set of equations:

From Eq. (A-35)

$$Y_{11} \simeq \frac{|Y|}{M_o}$$

By substituting for $|Y|$ and M_o, the equation is given by

$$Y_{11} = \frac{C}{s^4 M_o}\left(\frac{s^2}{\omega_1^2} + p_1^2\right)\left(\frac{s^2}{\omega_1^2} + p_2^2\right)$$

for

$$C_{11} = \frac{C}{M_o}$$

The equation reduces to

$$Y_{11} = \frac{C_{11}}{s^4}\left(\frac{s^2}{\omega_1^2} + p_1^2\right)\left(\frac{s^2}{\omega_1^2} + p_2^2\right) \qquad \text{(A-63)}$$

Accordingly from Eq. (A-35)

$$Y_{12} \simeq 0$$

and

$$Y_{21} = Y_{12} \simeq 0$$

Now

$$Y_{22} = \frac{M_o k_1^2 (1 - 2\alpha)}{s^4}\left(\frac{s^2}{\omega_1^2} + \frac{1}{(1 - 2\alpha)}\right)\left(\frac{s^2}{\omega_1^2} + 1\right)$$

and letting

$$C_{22} = M_o k_1^2 (1 - 2\alpha)$$

we have

$$Y_{22} = \frac{C_{22}}{s^4}\left(\frac{s^2}{\omega_1^2} + p_1^2\right)\left(\frac{s^2}{\omega_1^2} + 1\right) \qquad \text{(A-64)}$$

Similarly

$$Y_{13} = -\frac{J_y N_1 k_1 (1 - 2\beta)}{s^2}\left(\frac{s^2}{\omega_1^2} + p_2^2\right)$$

and by letting

$$C_{13} = -J_y N_1 k_1 (1 - 2\beta)$$

and substituting back into Y_{13},

$$Y_{13} = \frac{C_{13}}{s^2}\left(\frac{s^2}{\omega_1^2} + p_2^2\right) \qquad \text{(A-65)}$$

The cofactor Y_{23} is given by

$$Y_{23} = -\frac{M_o J_{10} k_1 (1 - 2\alpha)}{s^2}\left(\frac{s^2}{\omega_1^2} + p_1^2\right)$$

and the coefficient is replaced by

$$C_{23} = -M_o J_{10} k_1 (1 - 2\alpha)$$

so that

$$Y_{23} = \frac{C_{23}}{s^2}\left(\frac{s^2}{\omega_1^2} + p_1^2\right) \qquad \text{(A-66)}$$

Finally,

$$Y_{14} = \frac{J_y N_1 k_1 (1 - 2\beta)}{s^2}\left(\frac{s^2}{\omega_1^2} + p_2^2\right)$$

and in terms of Eq. (A-64),

$$Y_{14} = -Y_{13} \qquad \text{(A-67)}$$

and

$$Y_{24} = -\frac{M_o J_{10} k_1 (1-2\alpha)}{s^2}\left(\frac{s^2}{\omega_1^2} + p_1^2\right)$$

and in terms of Eq. (A-65),

$$Y_{24} = Y_{23} \tag{A-68}$$

For the configuration of the spacecraft shown in Fig. A-1, the approximate natural frequency is $\omega_1 = 16.0$ rad/sec.

The plots (Fig. A-5 through A-7) describe graphically the effect of varying the mass of the solar panels, the relationship between the location of the center of mass of the panels' coordinates, and the changes due to perturbing the spring constants about the hinge line.

The roots of the determinant and cofactors vary as the solar panel parameters vary. The mode of variation was studied for the case when the parameters of one solar panel were varied with respect to those on the other panel. The results are indicated in the figures; however, the Y_{14} and Y_{24} terms are eliminated since they do not vary appreciably.

Finally, the result which we desire is the equations which affect the autopilot, since this transfer function will lead to the model to be used in the study of the autopilot mode. Therefore, we are interested in the transfer function $\ddot{\theta}_y/\tau_y$.

From Eq. (A-30),

$$\ddot{\theta} = \frac{1}{|Y|}(Y_{12}F_z + Y_{22}\tau_y)$$

For $F_z = 0$,

$$\ddot{\theta} = \frac{Y_{22}}{|Y|}\tau_y$$

But, from Eq. (A-62) and (A-64), we know Y_{22} and $|Y|$ so that

$$\frac{\ddot{\theta}}{\tau_y} = \frac{C_{22}}{C}\frac{\left(\frac{s^2}{\omega_1^2}+1\right)\left(\frac{s^2}{\omega_1^2}+p_b^2\right)}{\left(\frac{s^2}{\omega_1^2}+p_2^2\right)\left(\frac{s^2}{\omega_1^2}+p_a^2\right)} \tag{A-69}$$

From the above expression, as the differences between the solar panel characteristics become very small, then

$$\frac{C_{22}}{C} \rightarrow \frac{p_2^2}{J_y}$$

$$p_b \rightarrow p_1$$

$$p_a \rightarrow p_1$$

Thus for identical solar panels,

$$\frac{\ddot{\theta}_y}{\tau_y} = \frac{p_2^2}{J_y}\frac{\left(\frac{s^2}{\omega_1^2}+1\right)}{\left(\frac{s^2}{\omega_1^2}+p_2^2\right)}$$

$$= \frac{1}{J_y}\frac{\left(\frac{s^2}{\omega_1^2}+1\right)}{\left(\frac{s^2}{(\omega_1 p_2)^2}+1\right)}$$

and

$$\frac{\ddot{\theta}_y}{\tau_y} = \frac{1}{J_y}\frac{\left(\frac{s^2}{\omega_1^2}+1\right)}{\left(\frac{s^2}{\omega_2^2}+1\right)} \tag{A-70}$$

This is verified by the fact that $p_a \simeq p_b$ in Fig. A-5 and A-6. Hence, Eq. (A-70) is the approximate transfer function for the yaw axis when the solar panels are assumed to be approximately equal. The roll axis acceleration is given as

$$\ddot{\theta}_z = \frac{\tau_z}{J_z} \tag{A-71}$$

and the spacecraft is again assumed to be a rigid body.

The analysis of structural dynamics was supplemented by frequency response tests of a spacecraft, as described in Fig. A-7. The tests showed a good correlation between the actual response and the analysis for the solar panel bendings. On the other hand, the linearized model of the high-gain antenna was proven to be rather crude. As expected, the antenna exhibited various resonances, such as compounded bending and torsion. Some structural crosscoupling was also evident.

3. Spacecraft Frequency Response Test

The analytical study of the spacecraft dynamics was supplemented by a frequency response test. The spacecraft was suspended as shown in Fig. A-8, so that the effect of gravity was minimized. Torque was applied to the spacecraft about each principal axis by means of two linear force transducers. Measured were spacecraft angular velocities (by rate gyros) and solar panel movements (by linear transducers).

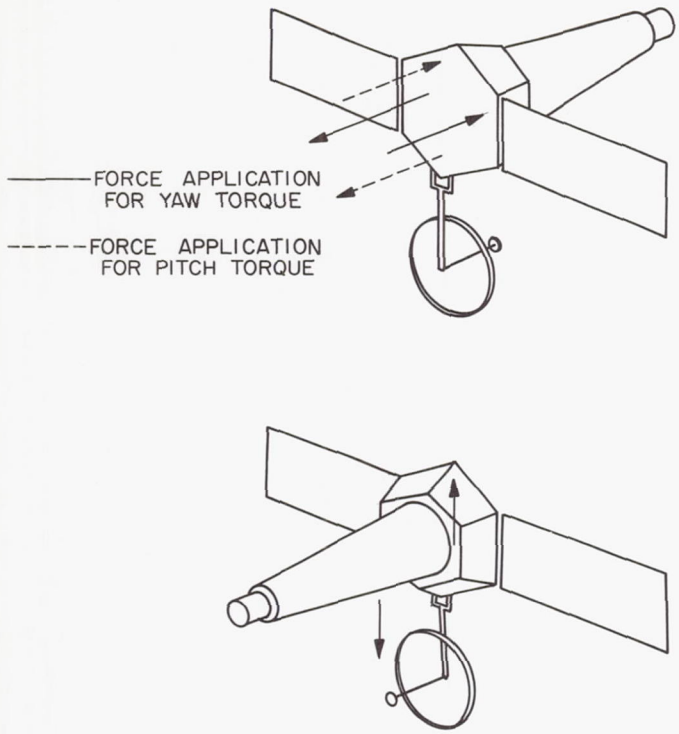

Fig. A-8. Test set up, spacecraft frequency response

Figures A-9 through A-14 show the gyro outputs for various torque inputs. Computed gyro outputs are also shown for comparison. The deviation of the experimental voltage from that computed in the low-frequency region is due to the suspension resonances (0.1 ~ 1 cps). The deviation in the high-frequency region is due to gyro poles (about 10 cps). Figures A-15 and A-16 show the solar panel movements. A sharp dip before the peak resonance exhibited by one of the panels indicates that the panels are not identical.

The test results can be summarized as follows:

1. The simplified model of the spacecraft assumed in the yaw axis analysis was found to be reasonably accurate and useful.

2. The pitch axis analysis was found to be oversimplified because of the complex bendings exhibited by the antenna. This simple model, however, was good enough to indicate the way the antenna bendings affect the pitch axis dynamics.

3. Nonlinearities in the structural bendings were indicated by shiftings of the resonance frequencies, when the magnitude of the input torque was varied. Solar panel bendings indicated existence of backlash in their supporting elements.

4. Considerable crosscouplings were observed. Their probable causes are the gyro crosscouplings, the structural resonances of the solar panels and the antenna, the products of inertia, and the suspension system. The extent of contribution by each factor cannot be determined, however. It should be noted here that not all the gyros showed outputs simultaneously for one input. This implies that the single-axis analyses are quite valid, since the crosscoupling terms in Euler's equations of motion can be neglected.

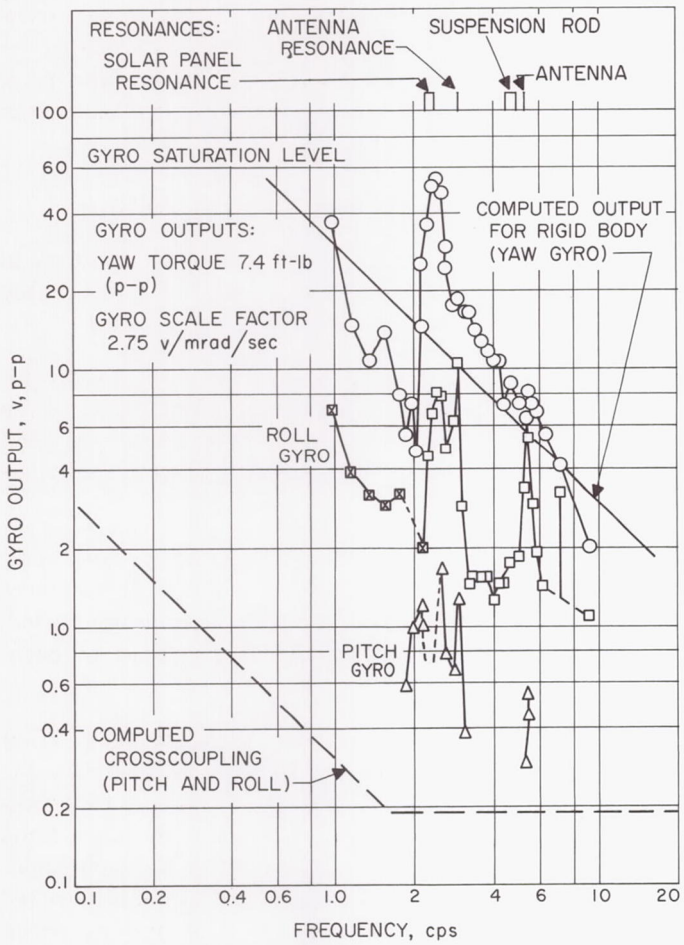

Fig. A-9. Gyro output, yaw torque 7.4 ft-lb (p-p)

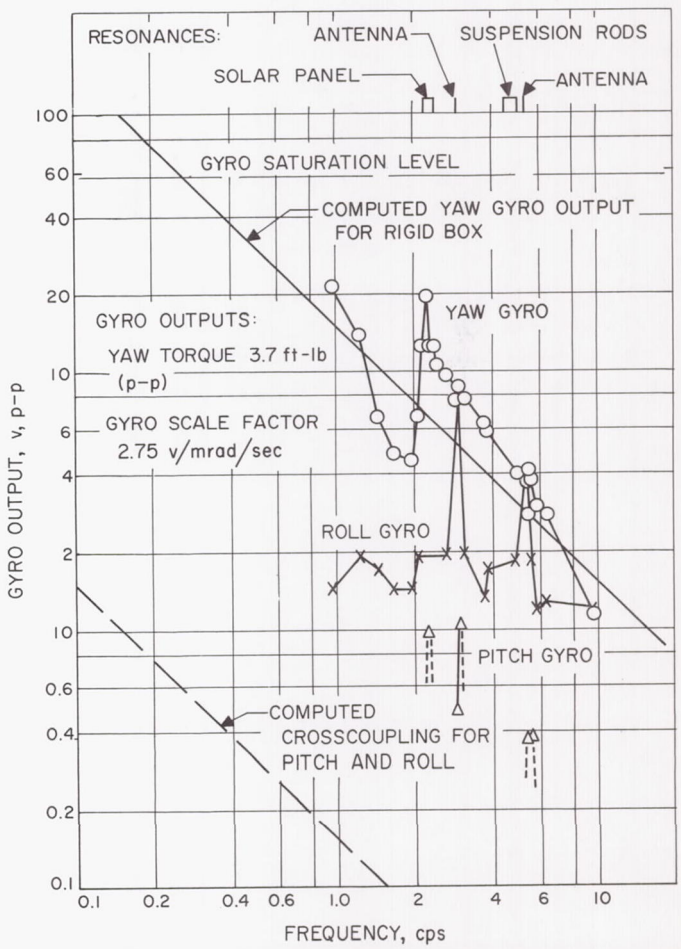

Fig. A-10. Gyro output, yaw torque 3.7 ft-lb (p-p)

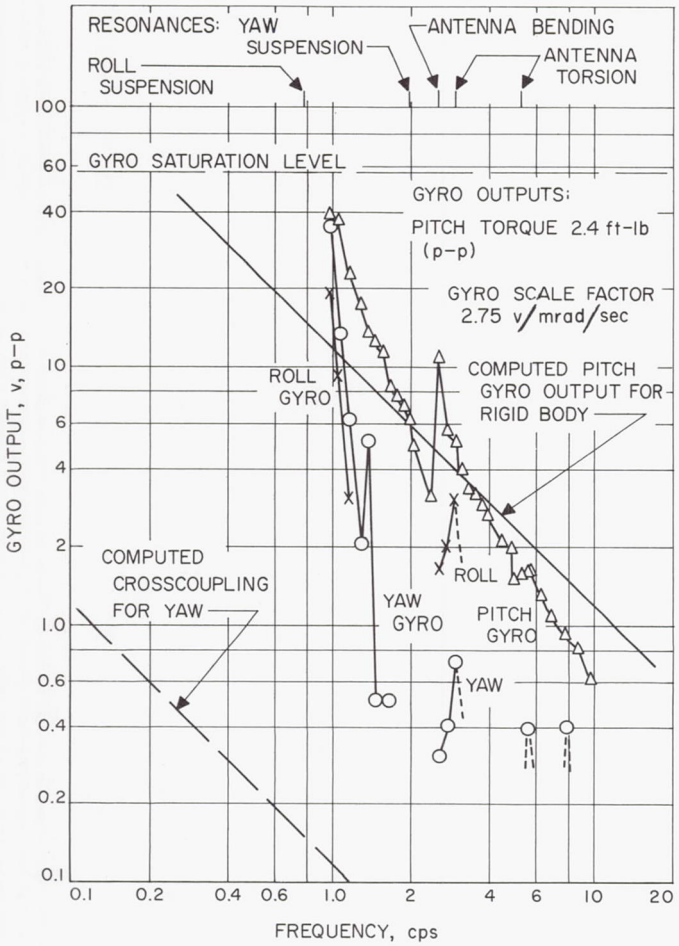

Fig. A-11. Gyro output, pitch torque 2.4 ft-lb (p-p)

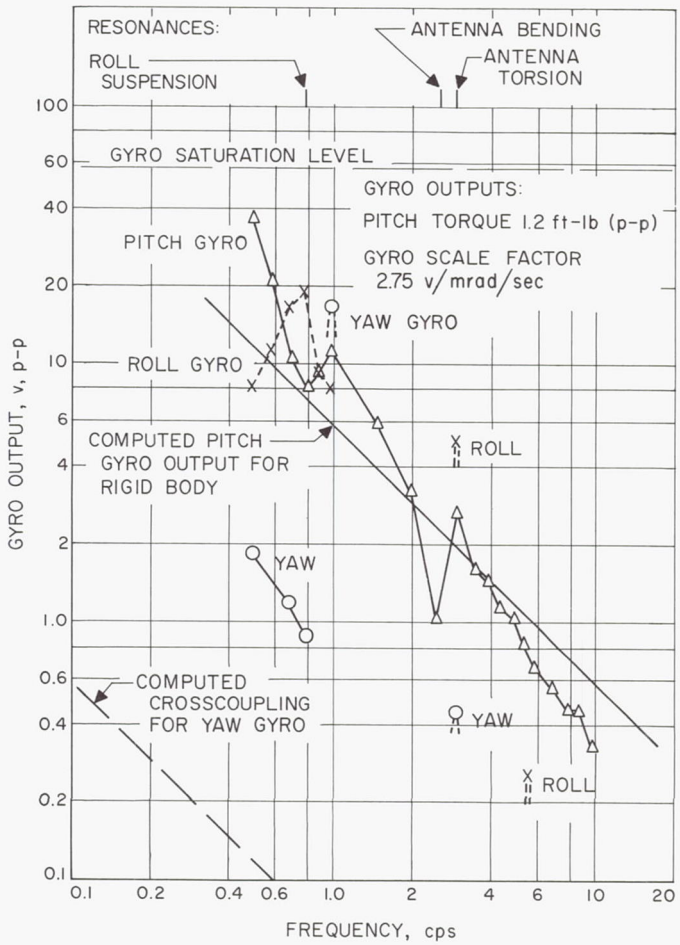

Fig. A-12. Gyro output, pitch torque 1.2 ft-lb (p-p)

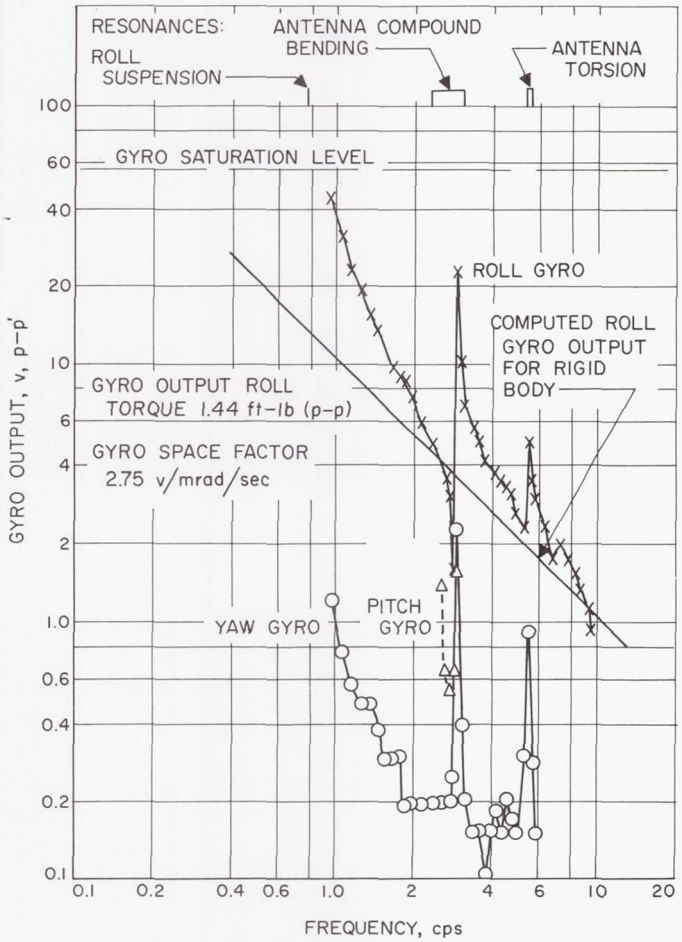

Fig. A-13. Gyro output, roll torque 1.44 ft-lb (p-p)

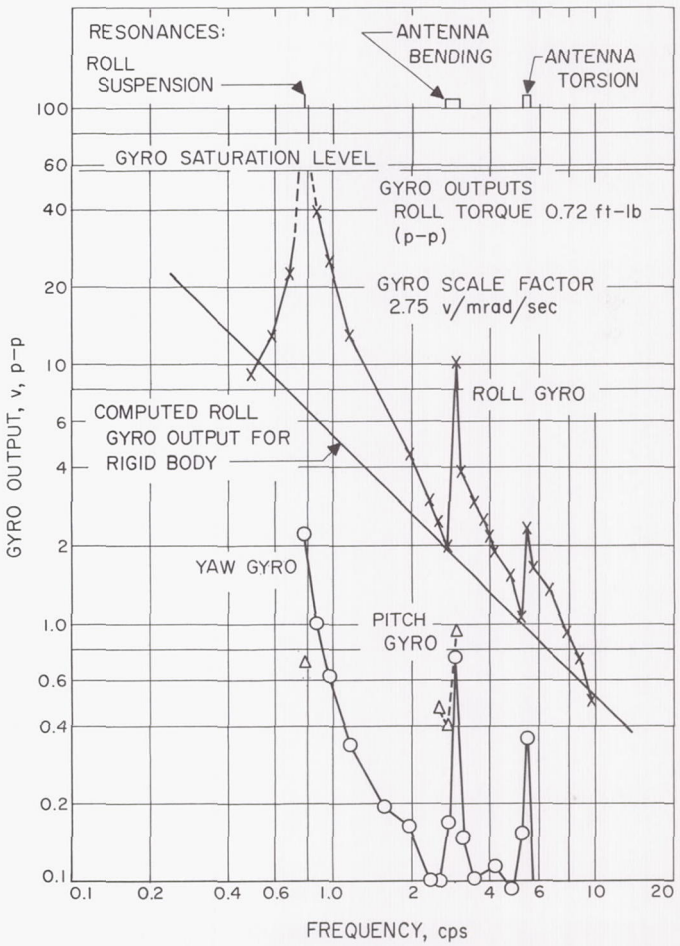

Fig. A-14. Gyro output, roll torque 0.72 ft-lb (p-p)

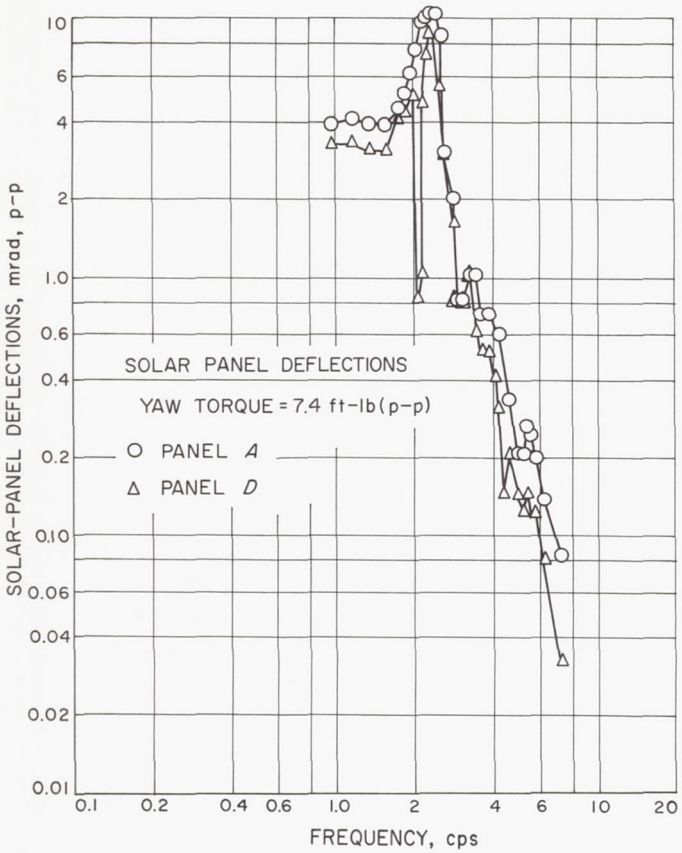

Fig. A-15. Solar panel deflection, yaw torque 7.4 ft-lb (p-p)

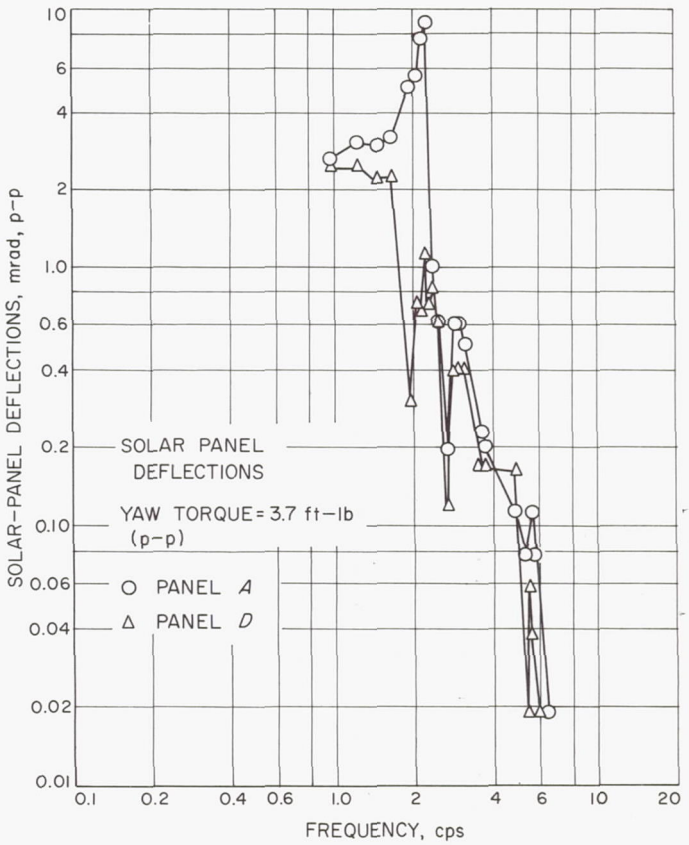

Fig. A-16. Solar panel deflection, yaw torque 3.7 ft-lb (p-p)

APPENDIX B

Jet-Vane Actuator Analysis

The study of the characteristics of the jet-vane actuator must preclude the analysis of the autopilot loop since the jet-vane actuator is the autopilot controller. A discussion of the physical actuator leads to the formulation of a block diagram defining the closed-loop characteristics of the controller and allows for a detailed study of the stability of the actuator loop.

1. Jet-Vane Actuator Loop Analysis

There are four jet vanes on the spacecraft, arranged as shown in Fig. B-1. Each jet-vane actuator loop deflects a jet vane by an angle proportional to the gyro-loop output signal it receives. Figure B-2 shows the mixing of the various signals which control the motion of the actuators, and Fig. B-3 is a typical block diagram.

A pitch command is produced by a signal at the inputs to the No. 1 and 3 actuator amplifiers. An input to the No. 2 and 4 actuator amplifiers produces a yaw command to the actuator surfaces. Roll commands to the actuators are introduced by the differential inputs between the No. 1 and 3 and between the No. 2 and 4 amplifier inputs.

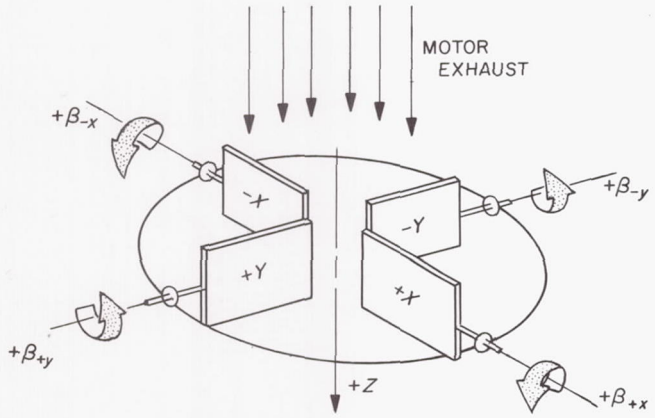

(a) JET VANES - DEFINITION OF POSITIVE ROTATIONS

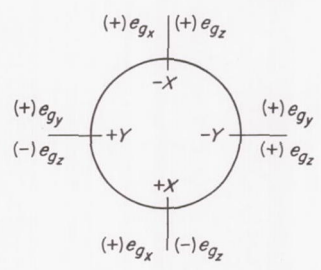

NOTES: (1) POLARITIES DEFINED PER SPEC. FR 3-4-420, OCT. 21, 1963, PARA. 4.4.

(2) POLARITIES OF THE COORDINATE AXES ARE DIFFERENT FROM THOSE IN FIG. A-1.

(3) $\beta_{\pm x,y}$ = JET VANE ANGLE
$e_{g_{x,y,z}}$ = GYRO SIGNAL

(b) GYRO-SIGNAL POLARITIES FOR POSITIVE JET-VANE DEFLECTIONS

Fig. B-1. Jet vanes

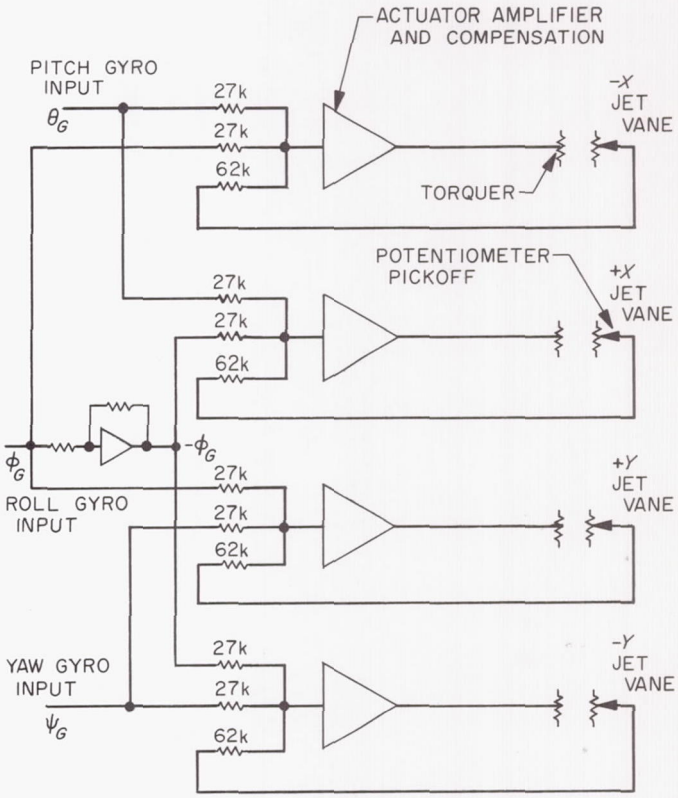

Fig. B-2. Jet-vane actuator loops

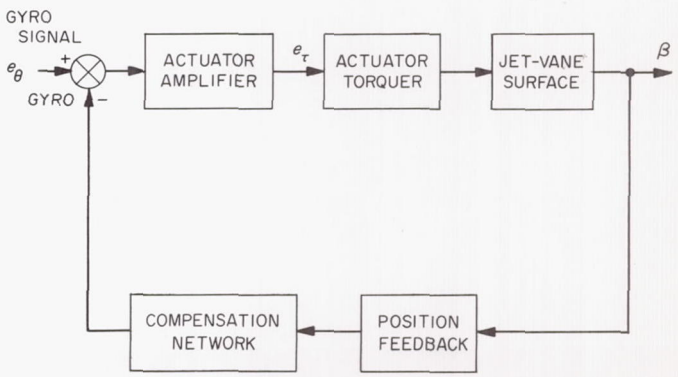

Fig. B-3. Block diagram, jet-vane actuator loop

The differential roll signal is obtained by the use of a roll-inverting amplifier. Each actuator amplifier has three input signals, as shown in Fig. B-2; these are described below:

1. Pitch and yaw rate plus position (from the gyros).
2. Roll-signal input.
3. Jet-vane-angle feedback signal.

The thrust-vector deflection in pitch is measured by summing the No. 1 and 3 jet-vane potentiometer outputs.

A schematic diagram of the actuator amplifier including the compensation network is shown in Fig. B-4. The amplifier is used as an operational amplifier to obtain the proper loop gain. The circuit is direct coupled and has a Class B output stage. The gain and phase compensation are produced by a lag-lead network in the feedback path. The maximum phase lead is 56 deg at 12 cps. The maximum output of the amplifier is ±20 v across a 160 Ω load. The roll-inverting amplifier employs essentially the same circuit as the actuator amplifier with the exception of the feedback network which is designed for unity gain.

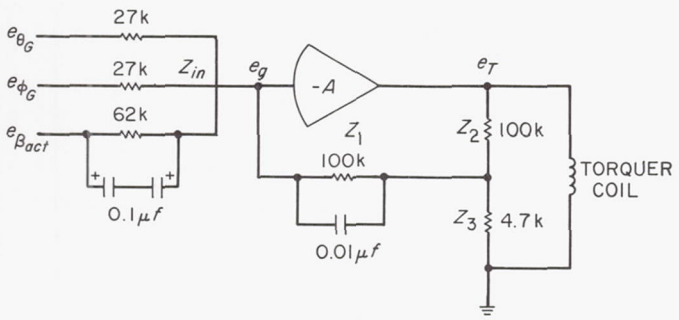

Fig. B-4. Jet-vane actuator amplifier

2. Actuator Model and Transfer Function

The following analysis is a complete derivation of the jet-vane actuator-loop transfer function. The actuator is described mathematically by analyzing the characteristics of the actuator amplifier, the actuator, the feedback elements, and then studying the models through root-locus and frequency-response analysis.

a. Actuator amplifier. The block diagram of the amplifier is found by studying the amplifier circuit in Fig. B-4. The actuator amplifier is a dc operational amplifier; therefore, we may assume high gain in studying that loop. By taking Kirchoff's node equations, the ratio

$$\frac{e_T}{e_\theta} = -\frac{(Z_1Z_2 + Z_1Z_3 + Z_2Z_3)}{Z_{in}Z_3} \tag{B-1}$$

where Z_{in}, Z_2 and Z_3 are resistances. Similarly, the ratio

$$\frac{e_T}{e_\beta} = -\frac{(Z_1Z_2 + Z_1Z_3 + Z_2Z_3)}{Z_{in}Z_3} \tag{B-2}$$

but in this case, Z_{in} is an impedance. By the substitution of the values of the parameters into Eq. (B-1) and (B-2), where

$$Z_1 = \frac{100\text{k}}{10^{-3}s + 1}$$

$$Z_2 = 100\text{k}$$

$$Z_3 = 4.7\text{k}$$

$$Z_{in_G} = 27\text{k}$$

$$Z_{in_\beta} = \frac{62\text{k}}{3.1 \times 10^{-3}s + 1}$$

we obtain

$$\frac{e_T}{e_{\theta_{gyro}}} = -3.71\,\frac{(s + 23{,}300)}{(s + 1000)} \tag{B-3}$$

and

$$\frac{e_T}{e_{\beta_{act}}} = -5.0 \times 10^{-3}\,\frac{(s + 323)\,(s + 23{,}300)}{(s + 1000)} \tag{B-4}$$

The above equations can be rewritten in a reduced form since the zero located at 23,300 is far enough away from the other poles and zeros so as to be considered only a gain term. The equations then reduce to

$$\frac{e_T}{e_{\theta_{gyro}}} = -86.2 \times 10^3\left(\frac{1}{s + 100}\right) \tag{B-5}$$

and

$$\frac{e_T}{e_{\beta_{act}}} = -116.5\,\frac{(s + 323)}{(s + 1000)} \tag{B-6}$$

Finally, from Eq. (B-5) and (B-6), the relationship between the two expressions is given as

$$\frac{e_T}{e_{\beta_{act}}} = \frac{1.35 \times 10^{-3}}{(s + 1000)}\,\frac{e_T}{e_{\theta_{gyro}}} \tag{B-7}$$

The equivalent block diagram is shown below in Fig. B-5. (The frequency response of the amplifier to both a gyro

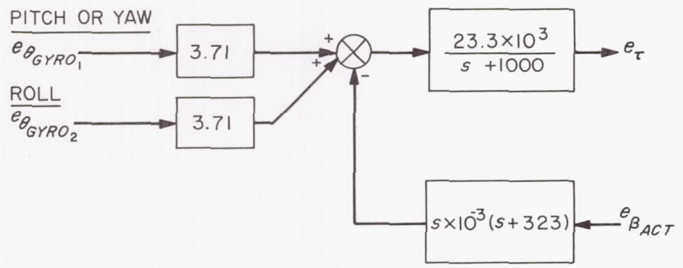

Fig. B-5. Equivalent block diagram of actuator amplifier

signal and actuator position signal is shown in a later figure—Fig. B-13; the range of the unit-to-unit variation due to component tolerances is also indicated; the output impedance of the amplifier is unsymmetrical about its null; the resulting gain discrepancy between the positive and negative sides is about 10 to 15%.)

b. Actuator description. The actuator block diagram is shown in Fig. B-6. The nonlinear portion of the actuator contains coulomb friction in the rotor and vane inertia. The nonlinearity is evaluated in the ensuing analysis. By linearizing the actuator model, the inductance of the torquer coil is neglected since the ratio of the torquer resistance to inductance, $(R/L)\,\tau$, is greater than 4000.

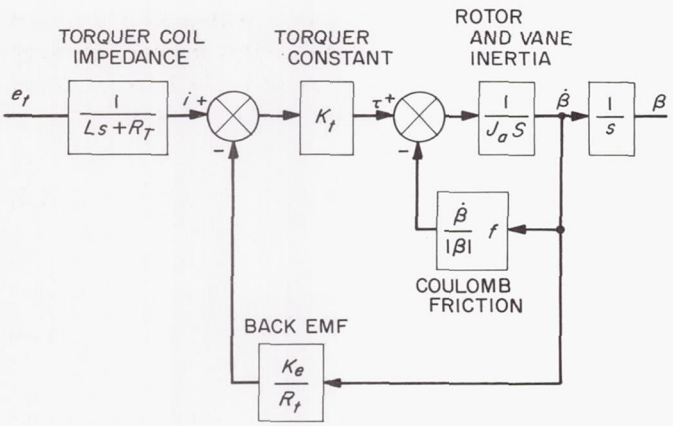

Fig. B-6. Jet-vane actuator equivalent block diagram

Nonlinear analysis of actuator friction. The loop representing the coulomb friction is analyzed through the use of the describing function technique. The block diagram of the nonlinearity is drawn below, in Fig. B-7.

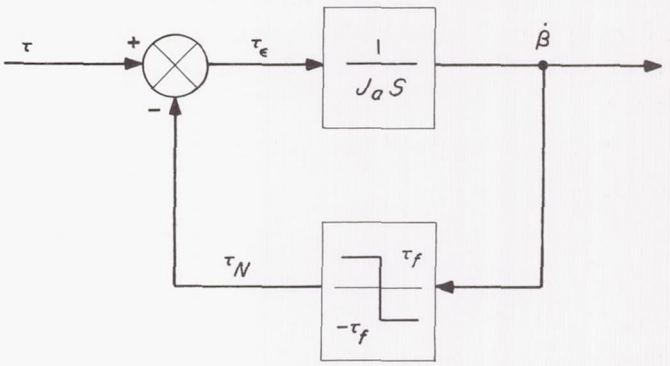

Fig. B-7. Nonlinear loop containing coulomb friction

At this time, we are interested in developing the transfer function for the nonlinear loop $\dot\beta/\tau$. To do so, the following assumptions are made:

1. The input to the summing junction is assumed to be sinusoidal and of the form

$$\tau = \tau_0 \sin \omega t \tag{B-8}$$

2. The output is assumed to be a characteristic of a sinusoid except for a change in amplitude and variation in phase, so that

$$\dot\beta = C \sin(\omega t + \theta) \tag{B-9}$$

where

C = the amplitude of the output

θ = the phase change of the output

3. Finally, the output of the nonlinear element is assumed to be a characteristic of the first fundamental of a square wave and is given by

$$\tau_N = \frac{4\tau_f}{\pi} \sin(\omega t + \theta) \tag{B-10}$$

Now from the block diagram, the following set of equations may be generated:

$$\dot\beta = \frac{\tau_\epsilon}{J_a s} \tag{B-11}$$

and

$$\tau_\epsilon = \tau - \tau_N \tag{B-12}$$

By re-writing Eq. (B-11) and substituting (B-9) into it, we have

$$\tau_\varepsilon = Js\dot{\beta}$$

$$= J\frac{d}{dt}(\dot{\beta})$$

$$= J\frac{d}{dt}[C\sin(\omega t + \theta)]$$

and finally

$$\tau_\varepsilon = JC\frac{d}{dt}[\sin(\omega t + \theta)] \tag{B-13}$$

Since the $\sin(\omega t + \theta)$ can be expanded trigonometrically, we have after differentiating

$$\tau_\varepsilon = JC\omega(\cos\omega t\cos\theta - \sin\theta\sin\omega t) \tag{B-14}$$

Now the nonlinearity, Eq. (B-10), can also be written as

$$\tau_N = \frac{4\tau_f}{\pi}(\sin\omega t\cos\theta + \sin\theta\cos\omega t) \tag{B-15}$$

Substitution of Eq. (B-14) and (B-15) into the torque-error expression (B-12) yields

$$JC\omega(\cos\omega t\cos\theta - \sin\theta\sin\omega t)$$

$$= \tau_o\sin\omega t - \frac{4\tau_f}{\pi}(\sin\omega t\cos\theta + \sin\theta\cos\omega t) \tag{B-16}$$

From the above expression, we desire to obtain relationships for the amplitude C and the angle θ. To do so, the sine and cosine terms on each side of the above equation are equated, therefore

$$JC\omega\cos\theta = -\frac{4\tau_f}{\pi}\sin\theta \tag{B-17}$$

and

$$-JC\omega\sin\theta = \tau_o - \frac{4\tau_f}{\pi}\cos\theta \tag{B-18}$$

Multiplying Eq. (B-17) by $\sin\theta$ and (B-18) by $\cos\theta$ and adding, we get

$$\tau_o\cos\theta - \frac{4\tau_f}{\pi}\cos^2\theta - \frac{4\tau_f}{\pi}\sin^2\theta = 0$$

Letting

$$\tau_o = \frac{\tau_f}{\lambda} \tag{B-19}$$

$$\frac{\tau_f}{\lambda}\cos\theta - \frac{4\tau_f}{\pi}(\cos^2\theta + \sin^2\theta) = 0$$

and

$$\frac{\tau_f}{\lambda}\cos\theta - \frac{4\tau_f}{\pi} = 0$$

finally, we get

$$\theta = \cos^{-1}\frac{4\lambda}{\pi} \tag{B-20}$$

Substituting the above solution into Eq. (B-17) and solving for C, we get

$$JC\omega\left(\frac{4\lambda}{\pi}\right) = -\frac{4\tau_f}{\pi}\sin\theta$$

and

$$C = \frac{\tau_f}{\lambda J\omega}\sin\theta$$

or

$$C = \frac{\tau_f}{\lambda J\omega}(1 - \cos^2\theta)^{1/2}$$

$$= \frac{\tau_f}{\lambda J\omega}\left[1 - \left(\frac{4\lambda}{\pi}\right)^2\right]^{1/2}$$

And since

$$\lambda = \frac{\tau_f}{\tau_o}$$

then

$$C = \frac{\tau_o}{J\omega}\left[1 - \left(\frac{4\lambda}{\pi}\right)^2\right]^{1/2} \tag{B-21}$$

Obviously, λ must be small for this type of approximation to hold. Therefore, the transfer function of the output amplitude is given by substituting the expression above for C into Eq. (B-9), which yields

$$\frac{|\dot{\beta}|}{\tau} = \frac{1}{J_a s}\left[1 - \left(\frac{4\tau_f}{\pi\tau_o}\right)^2\right]^{1/2} \tag{B-22}$$

To simplify the above transfer function, we let

$$a = \left[1 - \left(\frac{4\tau_f}{\pi\tau_o}\right)^2\right]^{1/2} \tag{B-23}$$

and finally we have

$$\frac{|\beta|}{\tau} = \frac{a}{Js} \tag{B-24}$$

In the above expression, the term a acts as a gain term that deteriorates the signal; if the nonlinearity did not affect the loop, then the transfer function would simply be $1/Js$. The diagram describing this nonlinearity is shown in Fig. B-8. Now the jet-vane actuator loop may be simplified by the addition of this nonlinear approximation as shown in Fig. B-9. The block diagram is further reduced in Fig. B-10, and the actuator transfer function is then given by

$$\frac{\beta}{e_\tau} = \frac{1}{K_e}\left(\frac{\alpha}{s(s+\alpha)}\right) \tag{B-25}$$

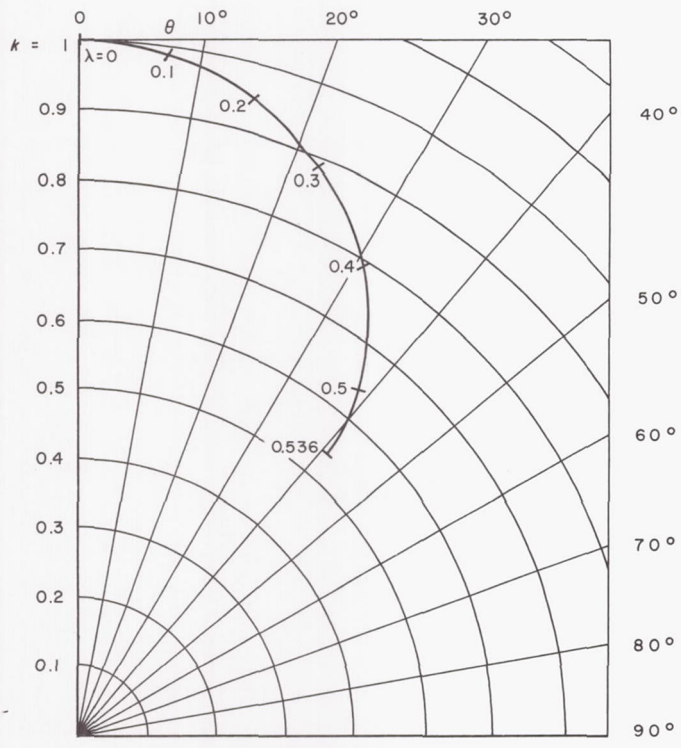

Fig. B-8. Torquer-describing function when coulomb friction is assumed

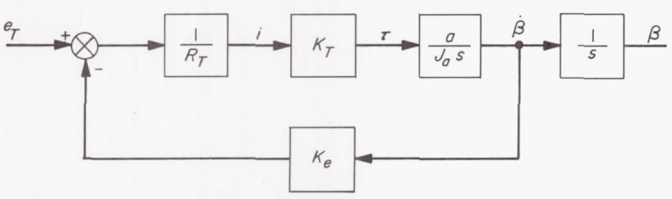

Fig. B-9. Simplified actuator block diagram

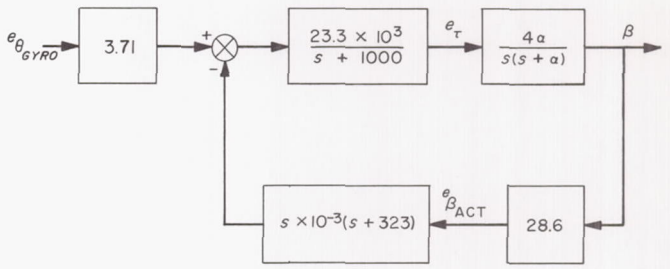

Fig. B-10. Block diagram, jet-vane actuator model

where

$$\alpha = \frac{K_e K_T a}{R_T J_a} \tag{B-26}$$

The back emf constant, K_e, is approximately 0.25 v/rad/sec in the linear region. The saturation characteristics of the back emf were not investigated due to measurement difficulties. The inertia of the actuator motor is given by

$$J_a = 5.6 \times 10^{-6}\left(\frac{\text{ft-lb-sec}^2}{\text{rad}}\right)$$

The position feedback is sensed by a potentiometer; the scale factor is given as 28.6 v/rad. Therefore, the final block diagram of the actuator is given in Fig. B-11. Empirical tests studying the response to a square-wave input indicate that the value of α ranges between 20 and 30 rad/sec. The extreme range of variation is estimated to be from 10 to 50 rad/sec.

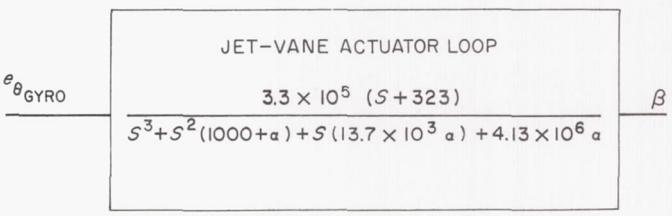

Fig. B-11. Block diagram, jet-vane actuator closed-loop transfer function as a function of the nonlinear elements α

c. Root-locus analysis. The final transfer function of the actuator loop is given as

$$\frac{\beta}{e_{\theta_{gyro}}} = \frac{3.3 \times 10^5 (s + 323)}{(s^3 + s^2(1000 + \alpha) + s(13.7 \times 10^3\alpha) + 4.13 \times 10^6\alpha)} \tag{B-27}$$

The root locus is found by examining the characteristic equation of the transfer function; hence,

$$1 + KGH(s) = 1 + 1.27 \times 10^4 \frac{(s + 323)}{s(s + \alpha)(s + 1000)} = 0 \tag{B-28}$$

and

$$1.27 \times 10^4 \alpha \frac{(s + 323)}{s(s + \alpha)(s + 1000)} = -1 \tag{B-29}$$

A value of $\alpha = 10$ rad/sec is used to represent the *worst case* condition and is shown in Fig. B-12. The effect of compensation variation on the loci is also indicated in this plot. The root-locus also shows the locus for $\alpha = 50$ rad/sec in order to point out the range of variation. The results of the analysis indicate that the actuator loop is unconditionally stable. Typically, the transfer function of the actuator is given for $\alpha = 25$, by

$$\frac{\beta}{e_{\theta_{gyro}}} = \frac{3.3 \times 10^5 (25)}{(s + 753)(s^2 + 272s + 1.37 \times 10^5)} \tag{B-30}$$

For the above transfer function, the frequency is approximately $f_n = 60$ cps, and the damping ratio is $\zeta \simeq 0.366$. Finally, an approximate transfer function can be given by

$$\frac{\beta}{e_{\theta_{gyro}}} = \frac{0.08 \text{ rad/v}}{\frac{s^2}{\omega_n^2} + \frac{2\zeta s}{\omega_n} + 1} \tag{B-31}$$

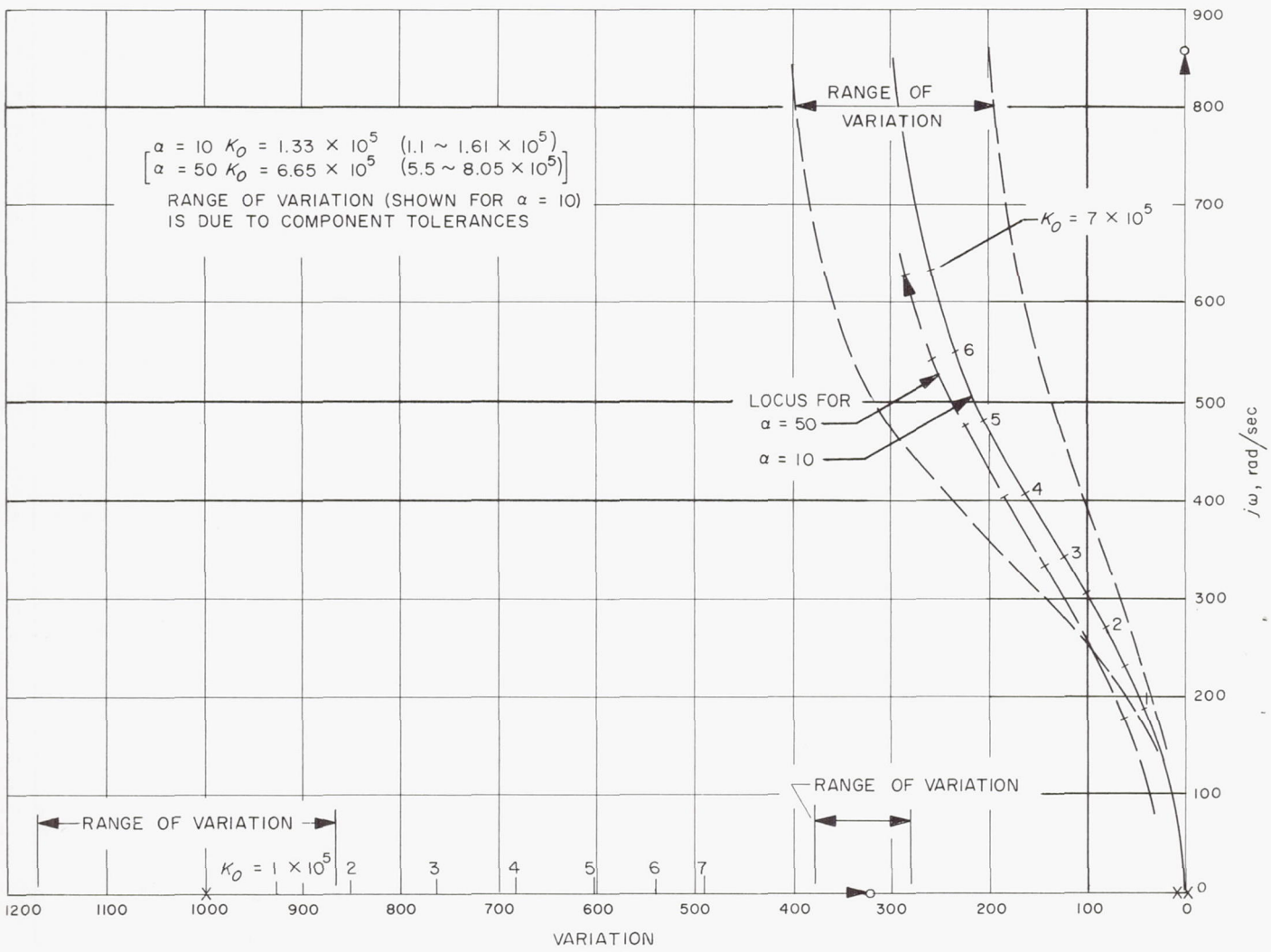

Fig. B-12. Root loci, jet-vane actuator loop

3. Jet-Vane Actuator Characteristics

The frequency response of the amplifier to both gyro signal and actuator position signal is shown in Fig. B-13. The description in Section 2a (Appendix B) discussed the essential information.

Due to the coulomb friction in the actuator, the actuator loop exhibits hysteresis characteristics. The magnitude of the hysteresis corresponds to ± 0.055 v of input voltage, or ± 0.11 mrad of spacecraft attitude. The dc characteristics of the actuator are shown in Fig. B-14.

The closed-loop actuator was studied in several ways. First, according to root-loci, the bandwidth of the actuator loop should be above 50 cps under normal conditions ($K_o \simeq 2.5 \times 10^5$, $\alpha = 20$). However, such response is realizable only for very small input signals. As shown in Fig. B-15, the frequency band is limited for large input signals. This is due to amplifier saturation, which effectively reduces the loop gain. The amplifier saturation also causes jump resonance in the shaded region of the Fig. B-15.

The effect of the amplifier saturation is also evident in the step-input response, as shown in Fig. B-16. For a small input signal, the rise time is less than 7 msec. However, it increases to about 15 msec, as the magnitude of the input increases. The mechanical limit will be reached for a step-input above 5 v.

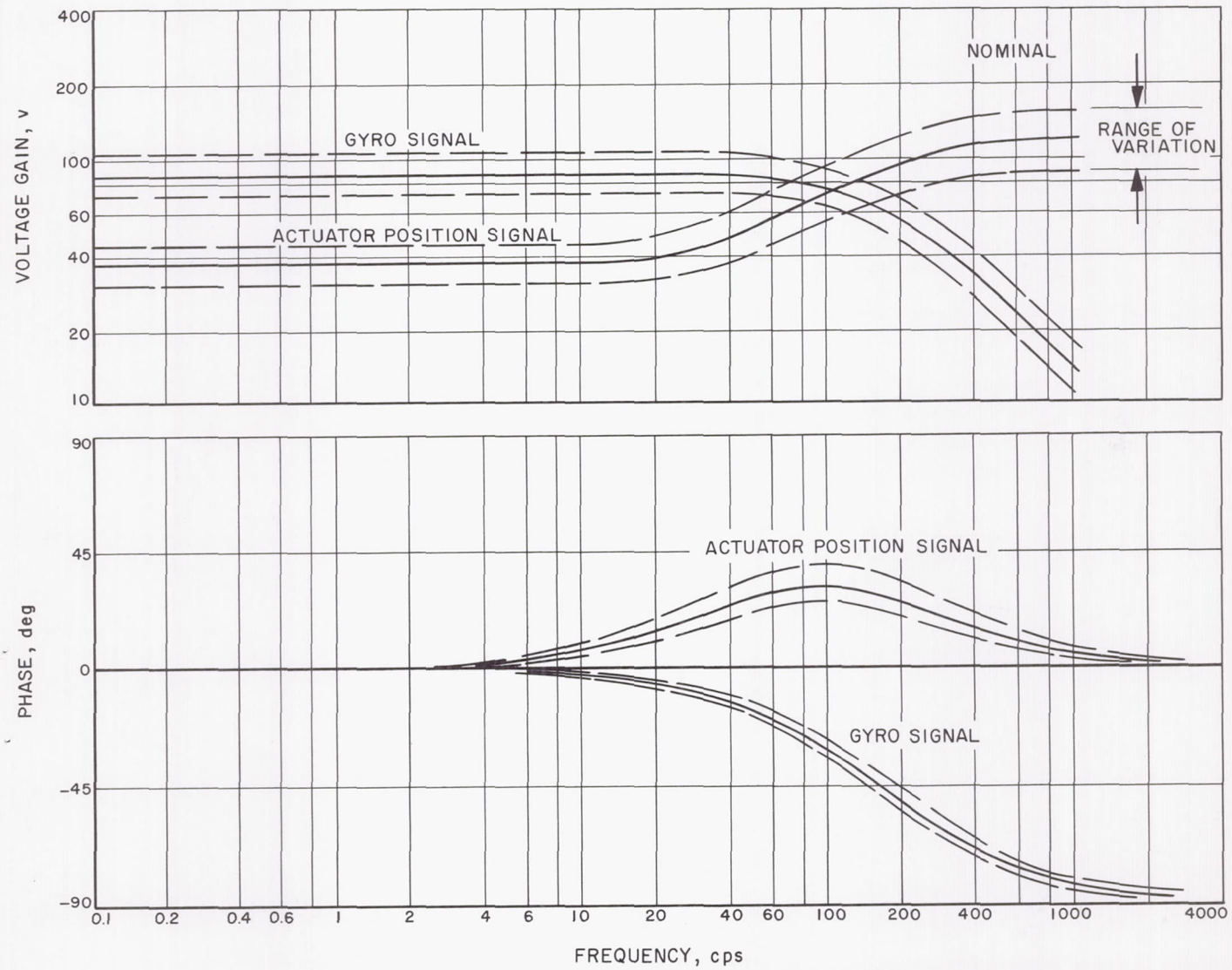

Fig. B-13. Jet-vane actuator amplifier, frequency response

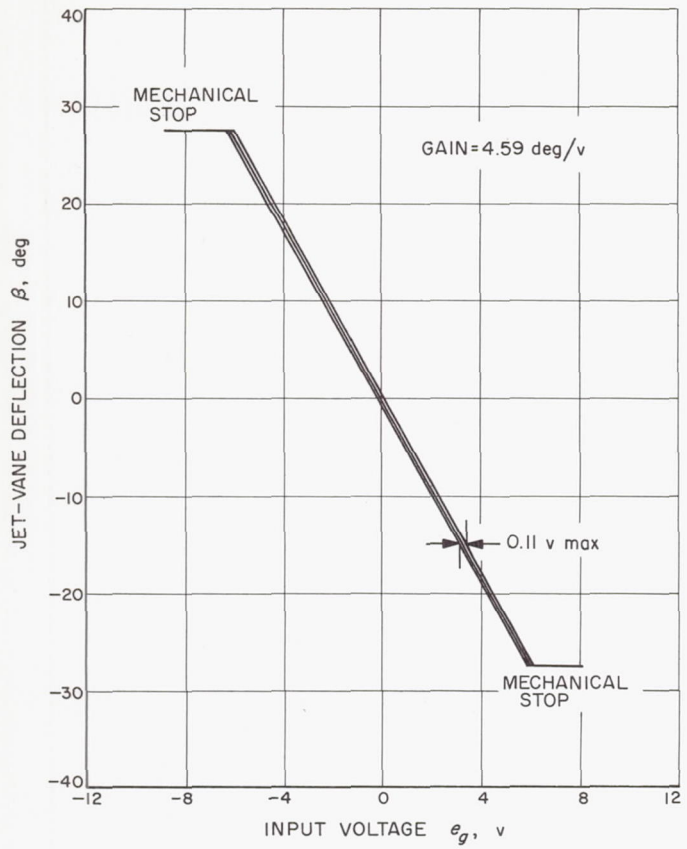

Fig. B-14. Jet-vane actuator loop, dc characteristics

Despite the nonlinearities in the loop, such as saturation and friction, various tests indicate a reasonably good correlation with linear analysis. The jet-vane actuator loop dynamic characteristics can be summarized as follows:

1. The loop is stable under any normal conditions.

2. The loop is sensitive to ±0.11 mrad of spacecraft attitude.

3. The frequency response is flat to at least 10 cps.

4. The loop will exhibit jump resonance, but the effect on the actuator is not considered detrimental.

5. For a step input signal, the rise time ranges from 7 to 15 msec, and the overshoot is less than 21%.

4. Effects of Torque and Thrust

Assuming that the deflections of the jet vanes are relatively small, the torque characteristics of the vanes are approximated by constants. Therefore,

$$K_{\tau_x} = \frac{\tau_x}{\beta_x} = 16.1 \text{ ft-lb/rad (for 2 vanes)}$$

$$K_{\tau_y} = K_{\tau_x} = 16.1 \text{ ft-lb/rad (for 2 vanes)}$$

$$K_{\tau_z} = 1.67 \text{ ft-lb/rad (for 4 vanes)}$$

The value for K_{τ_x}, or K_{τ_y}, is dependent on the torque arm length or the distance between the center of lift and the center of mass of the spacecraft. The value of 16.1 ft-lb/rad corresponds to an arm length of 2.16 ft. In more recent studies, this arm length has been determined to be smaller, or 1.87 ft. The corresponding value of K_{τ_x} for this new moment arm is 13.9 ft-lb/rad. However, the analog-computer simulation is conducted based upon the earlier measured value; for simpler analyses, both values are used.

The orientation of the motor thrust with respect to spacecraft structure is shown in Fig. B-17. From this diagram, approximate expressions for F_x, F_y, F_z, and τ_x and τ_y can be derived as functions of the motor thrust, F_o, and the jet vane deflections β_x and β_y.

For the yaw axis,

$$\begin{bmatrix} F_z \\ F_x \\ \tau_y \end{bmatrix} \simeq \begin{bmatrix} F_o \\ (x \text{ component of } F_o) + \text{lift} \\ \tau_{D_y} + \tau_{S_y} \end{bmatrix}$$

$$= \begin{bmatrix} 1 & 0 \\ +(\theta + \Delta_A)_y & K_L \\ C_1(\rho - \Delta_A)_y & -K_{\tau_y} \end{bmatrix} \begin{bmatrix} F_o \\ \beta_y \end{bmatrix} \quad \text{(B-32)}$$

For the pitch axis,

$$\begin{bmatrix} F_z \\ F_y \\ \tau_x \end{bmatrix} \simeq \begin{bmatrix} 1 & 0 \\ -(\theta + \Delta_A)_x & -K_L \\ C_1(\rho - \Delta_A)_x & -K_{\tau_x} \end{bmatrix} \begin{bmatrix} F_o \\ \beta_x \end{bmatrix} \quad \text{(B-33)}$$

where

τ_D = disturbance torque

τ_S = corrective torque applied by the jet vanes

$K_L = K_\tau/\beta$ = lift constant of two jet vanes

C_o = C.G. offset from motor centerline

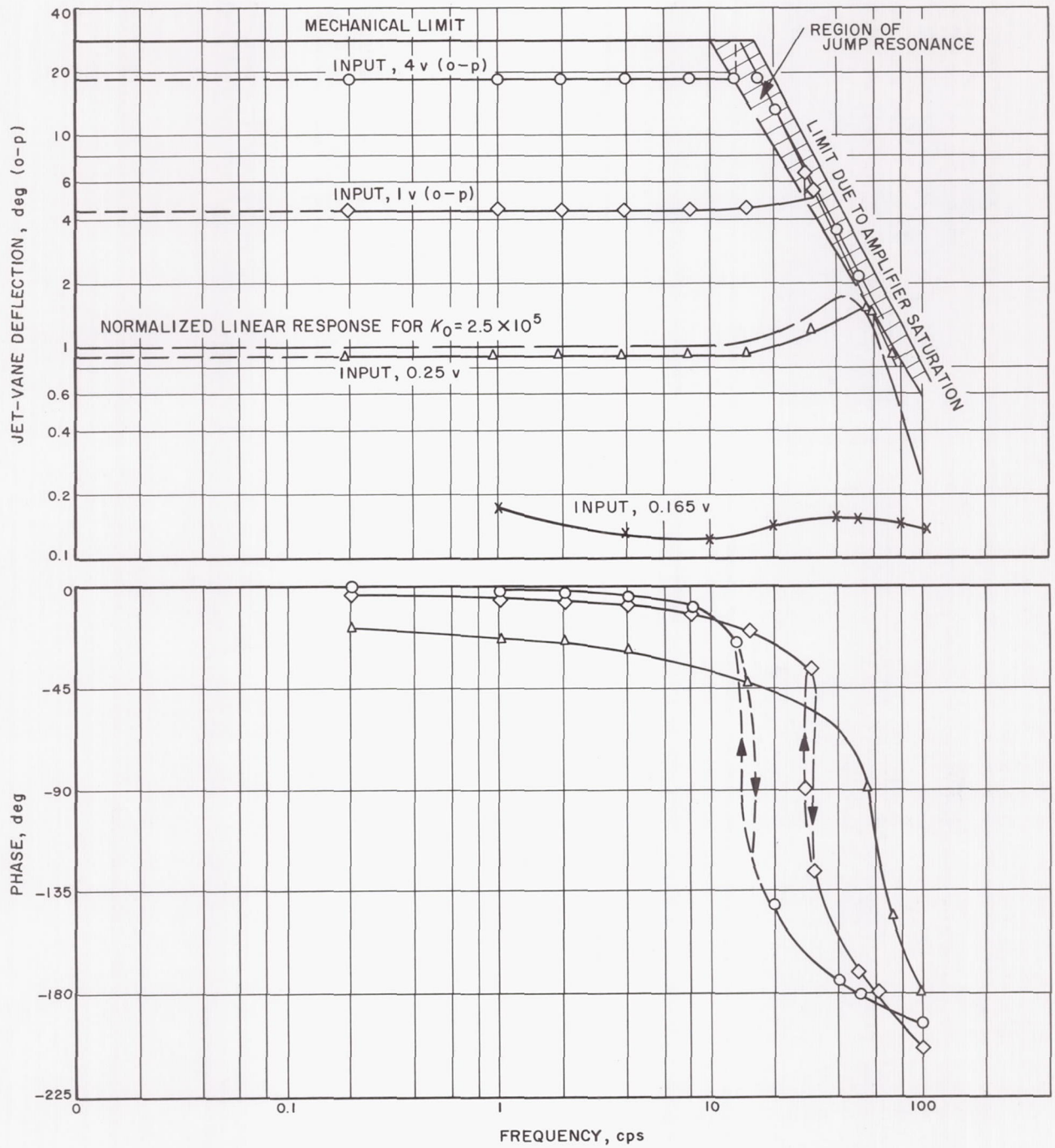

Fig. B-15. Jet-vane actuator loop, frequency response

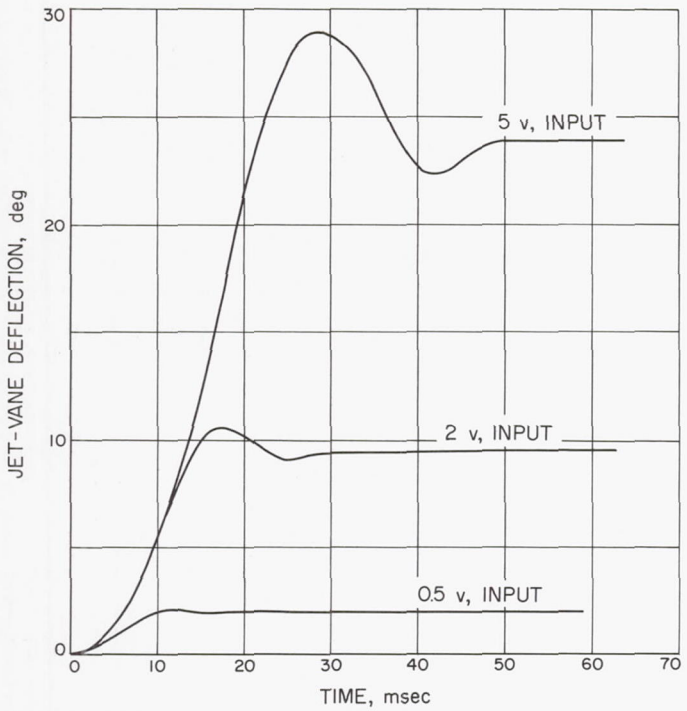

Fig. B-16. Jet-vane actuator loop, step input response

C_1 = distance between planes of C.G. and pressure center

C_2 = distance between planes of C.G. and lift center

Δ_A = angle between motor centerline and thrust vector

$\rho = C_o/C_1$

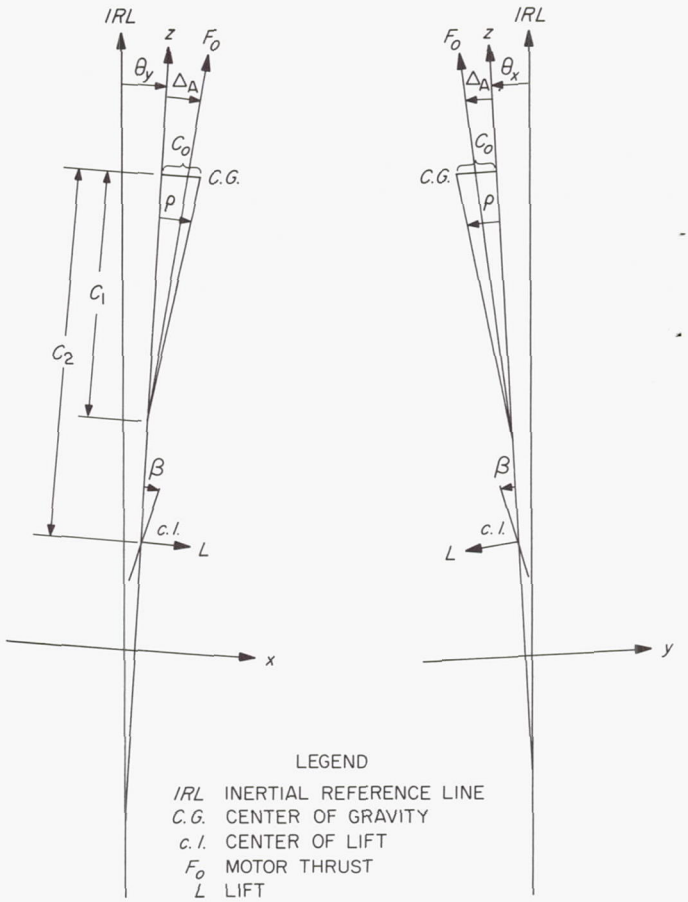

Fig. B-17. Midcourse motor-thrust orientation with respect to the spacecraft

APPENDIX C

Spacecraft Autopilot Mode

The spacecraft control loop is altered during the midcourse thrust phase by the addition of the jet-vane actuator loop. The jet-vane loop is included as part of the attitude control system in order to maintain the thrust vector of the midcourse motor pointed through the center of gravity of the vehicle, and thus to provide for the stability of the spacecraft. The block diagram of this phase of the attitude control of the *Ranger* spacecraft is composed of the block diagrams developed in Appendices A and B. The autopilot loop is shown in Fig. C-1.

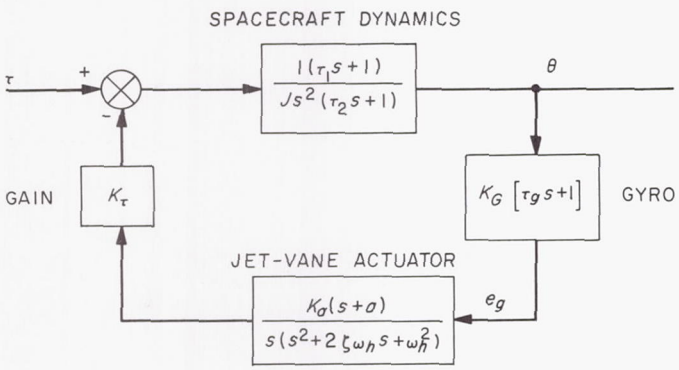

Fig. C-1. Autopilot loop, midcourse thrust phase

The following sections discuss an analog-computer simulation and analysis of the closed-loop autopilot mode.

1. Closed-Loop Autopilot Characteristics

When the autopilot loops are integrated into the attitude control system, Eq. (A-9), (A-24), and (A-66) are modified since the torque is now also a function of the jet-vane correction torques; therefore

$$\tau_i = \tau_{D_i} - \tau_{S_i} = \tau_{D_i} - \ddot{\theta}_i H_i(s) \qquad i = x, y, z \tag{C-1}$$

where

$H(s)$ = transfer function $\frac{\tau_{S_i}}{\ddot{\theta}_i} = K_G G_G(s)\, K_a G_a(s)\, K_\tau$

τ_D = disturbance torque

τ_S = corrective torque applied by the jet vanes

These equations are introduced into the expressions defining each of the axes and solved through the use of both analytical and analog computer simulation techniques. A detailed description of the pitch and yaw channels is analyzed, and the roll channel is also discussed.

a. Pitch axis autopilot. The closed-loop equation for the pitch axis is obtained by substituting the expression

$$\tau_x = \tau_{D_x} - \ddot{\theta}_x H_x(s) \tag{C-2}$$

into Eq. (A-9); therefore,

$$\begin{bmatrix} F_z \\ \tau_{D_x} - \ddot{\theta}_x H_x(s) \\ 0 \end{bmatrix} = \begin{bmatrix} M_o & 0 & N_3 \\ 0 & J_x & J_{30} \\ N_3 & J_{30} & \left(J_3 + \frac{k_3}{s^2}\right) \end{bmatrix} \begin{bmatrix} \ddot{z} \\ \ddot{\theta} \\ \ddot{\phi}_3 \end{bmatrix} \tag{C-3}$$

The above matrix expression can now be rewritten and generalized so that

$$\begin{bmatrix} F_z \\ \tau_{D_x} \\ 0 \end{bmatrix} = \begin{bmatrix} x_{11} & x_{12} & x_{13} \\ x_{21} & x_{22} + H_x(s) & x_{23} \\ x_{31} & x_{32} & x_{33} \end{bmatrix} \begin{bmatrix} \ddot{z} \\ \ddot{\theta}_x \\ \ddot{\phi}_3 \end{bmatrix} = [X'] \begin{bmatrix} \ddot{z} \\ \ddot{\theta}_x \\ \ddot{\phi}_3 \end{bmatrix} \tag{C-4}$$

To solve the above matrix, we take the inverse

$$\begin{bmatrix} \ddot{z} \\ \ddot{\theta}_x \\ \ddot{\phi}_3 \end{bmatrix} = \frac{1}{|X'|} \begin{bmatrix} X'_{11} & X'_{21} \\ X'_{12} & X'_{22} \\ X'_{13} & X'_{23} \end{bmatrix} \begin{bmatrix} F_z \\ \tau_{D_x} \end{bmatrix} \tag{C-5}$$

where

$$|X'| = |X| + H_x(s)\, X'_{22}$$

$$X'_{11} = X_{11} + H_x(s)\, x_{33}$$

$$X'_{12} = X_{12}$$

$$X'_{13} = X_{13} - H_x(s)\, x_{31}$$

$$X'_{21} = X_{21}$$

$$X'_{22} = X_{22}$$

$$X'_{23} = X_{23}$$

Now the simplified pitch autopilot loop in Fig. C-2 is used to obtain the equation to construct the root locus

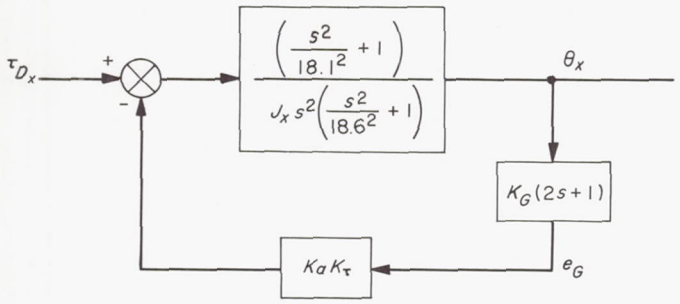

Fig. C-2. Closed-loop pitch autopilot

in Fig. C-3. Therefore, from Eq. (A-14) and Fig. C-2, we obtain the transfer function

$$\frac{\theta_x}{\tau_{D_x}} = \frac{\left(\frac{s^2}{\omega_1^2}+1\right)\Big/ J_x s^2\left(\frac{s^2}{\omega_2^2}+1\right)}{1+\frac{K_\tau K_a K_G}{J_x}\frac{(\tau_G s+1)\left(\frac{s^2}{\omega_2^2}+1\right)}{s^2\left(\frac{s^2}{\omega_2^2}+1\right)}}$$

which reduces to

$$\frac{\theta_x}{\tau_{D_x}} = \frac{X'_{22}}{s^2\,|X'|} = \frac{1.54\,\text{mrad/ft-lb}\left(\frac{s^2}{18.1^2}+1\right)}{\left(\frac{s}{0.5}+1\right)\left(\frac{s}{14}+1\right)\left(\frac{s^2}{18.4^2}+\frac{0.02s}{18.4}+1\right)} \tag{C-6}$$

when the following substitutions are made:

$$\omega_1 = 18.1\,\text{rad/sec}$$
$$\omega_2 = 18.6\,\text{rad/sec}$$
$$J_x = 90.0\,\text{slug-ft}^2\text{/rad}$$
$$K_G = 505\,\text{v/rad}$$
$$K_a = 0.08\,\text{rad/v}$$
$$K_\tau = 16.1\,\text{ft-lb/rad}$$

The root locus is constructed from the characteristic equation

$$K_o\,\frac{(2s+1)\left(\frac{s^2}{18.1^2}+1\right)}{s^2\left(\frac{s^2}{18.6^2}+1\right)} = -1 \tag{C-7}$$

where

$$K_o = \frac{K_G K_a K_\tau}{J_x} \tag{C-8}$$

The value of K_o is chosen as 7.2 rad/sec^2 for the transfer functions in Eq. (C-7). The value of K_o is smaller in the analog computer simulations since the moment of inertia was larger, i.e., when

$$K_o = 7.2\,\text{rad/sec}^2, \quad J_x = 90\,\text{slug-ft}^2\text{/rad}$$

and

$$K_o = 5.96\,\text{rad/sec}^2, \quad J_x = 109\,\text{slug-ft}^2\text{/rad}$$

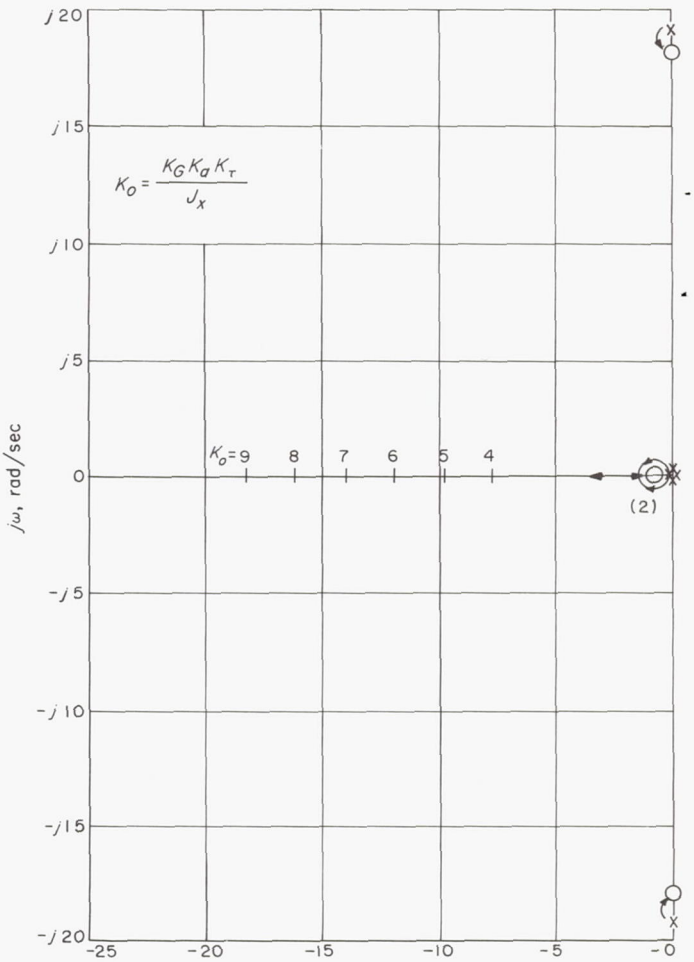

Fig. C-3. Root loci, simplified autopilot pitch axis

From the analog computer simulation, the step input responses to step inputs of F_z and τ_{D_x} are shown in Fig. C-4 and C-5, respectively. The lightly damped oscillations produced by the antenna are quite evident here. The antenna eventually ceases to oscillate under constant linear acceleration.

b. Yaw axis autopilot. The analysis of the yaw axis is difficult due to the effects of the solar panels. However, under the proper assumptions and approximations, the analysis can be undertaken.

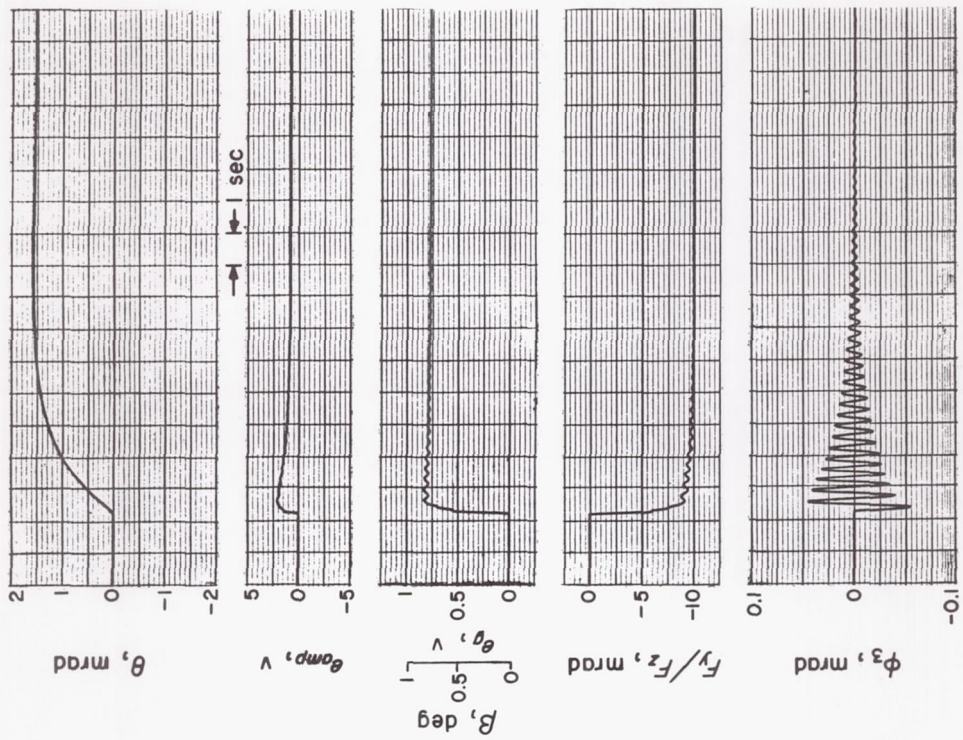

Fig. C-5. Pitch-axis response to a step input in the pitch axis of $\tau_{D_x} = 1$ ft-lb

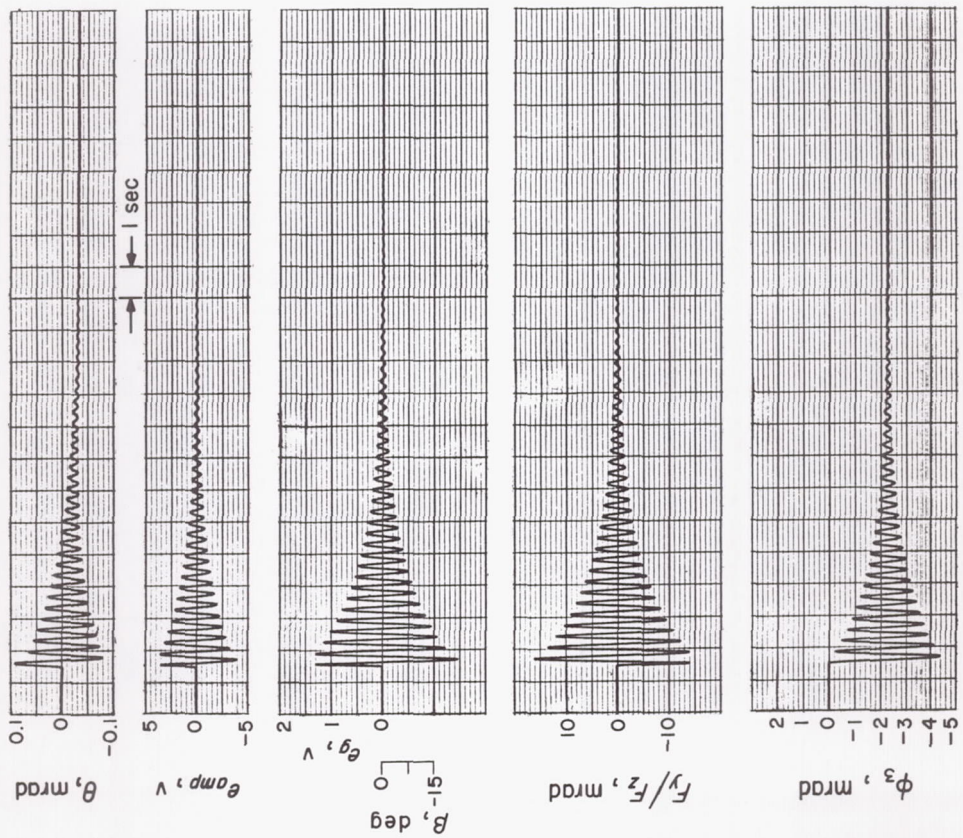

Fig. C-4. Pitch-axis response to a step input in the pitch axis of $F_z = 55$ lb

The inclusion of the autopilot loop in the yaw channel necessitates the changing of the closed-loop transfer function; therefore, by substituting into Eq. (A-23) with

$$\tau_y = \tau_{D_y} - \tau_{S_y} = \tau_{D_y} - \ddot{\theta}_y H_y(s) \tag{C-9}$$

we have

$$\begin{bmatrix} F_z \\ \tau_y \\ 0 \\ 0 \end{bmatrix} = \begin{bmatrix} F_z \\ \tau_{D_y} - \ddot{\theta}_y H_y(s) \\ 0 \\ 0 \end{bmatrix} = \begin{bmatrix} y_{11} & y_{12} & y_{13} & y_{14} \\ y_{21} & y_{22} & y_{23} & y_{24} \\ y_{31} & y_{32} & y_{33} & y_{34} \\ y_{41} & y_{42} & y_{43} & y_{44} \end{bmatrix} \begin{bmatrix} \ddot{z} \\ \ddot{\theta}_y \\ \ddot{\phi}_1 \\ \ddot{\phi}_2 \end{bmatrix} \tag{C-10}$$

and therefore

$$\begin{bmatrix} F_z \\ \tau_{D_y} \\ 0 \\ 0 \end{bmatrix} = \begin{bmatrix} y_{11} & y_{12} & y_{13} & y_{14} \\ y_{21} & y_{22} + H_y(s) & \cdots & \cdots \\ y_{31} & \cdots & \cdots & \cdots \\ y_{41} & \cdots & \cdots & \cdots \end{bmatrix} \begin{bmatrix} \ddot{z} \\ \ddot{\theta}_y \\ \ddot{\phi}_1 \\ \ddot{\phi}_2 \end{bmatrix} \equiv [Y'] \begin{bmatrix} \ddot{z} \\ \ddot{\theta}_y \\ \ddot{\phi}_1 \\ \ddot{\phi}_2 \end{bmatrix} \tag{C-11}$$

The primes denote the matrices and elements for the closed-loop autopilot. The inverse of Eq. (C-11) becomes

$$\begin{bmatrix} \ddot{z} \\ \ddot{\theta}_y \\ \ddot{\phi}_1 \\ \ddot{\phi}_2 \end{bmatrix} = \frac{1}{|Y'|} \begin{bmatrix} Y'_{11} & Y'_{21} \\ Y'_{12} & Y'_{22} \\ Y'_{13} & Y'_{23} \\ Y'_{14} & Y'_{24} \end{bmatrix} \begin{bmatrix} F_z \\ \tau_{D_y} \end{bmatrix} \tag{C-12}$$

where Y_{ij} is the cofactor of y_{ij}.

Since $[Y']$ differs from $[Y]$ in only one element Y'_{22}, Eq. (C-12) can be rewritten in terms of the open-loop parameters without additional complexity, as follows:

$$|Y'| = |Y| + H_y(s)\, y_{22}$$

$$Y'_{11} = Y_{11} + H_y(s)\, y_{33} y_{44}$$

$$Y'_{12} = Y_{12}$$

$$Y'_{13} = Y_{13} - H_y(s)\, y_{31} y_{44}$$

$$Y'_{14} = Y_{14} - H_y(s)\, y_{41} y_{33}$$

$$Y'_{21} = Y_{21}$$

$$Y'_{22} = Y_{22}$$

$$Y'_{23} = Y_{23}$$

$$Y'_{24} = Y_{24}$$

The roots of $|Y'|$ are shown in a root-locus plot in Fig. C-6 and for a simplified yaw axis loop in Fig. C-7. The second-order poles of the gyro loop and the actuator loop are ignored. In plotting these loci, the solar panels are assumed to be identical or nearly identical. The loop gains indicated along the loci are expressed in terms of

$$K_o = \frac{K_G K_a K_\tau}{J_y} \tag{C-13}$$

where, again, K_G, K_a, and K_τ are the dc gains of the gyro loop, actuator loop, and torquing constant, respectively. For

$$K_\tau = 16.1 \text{ ft-lb/rad}, \quad K_o = 5.96 \text{ rad/sec}^2$$

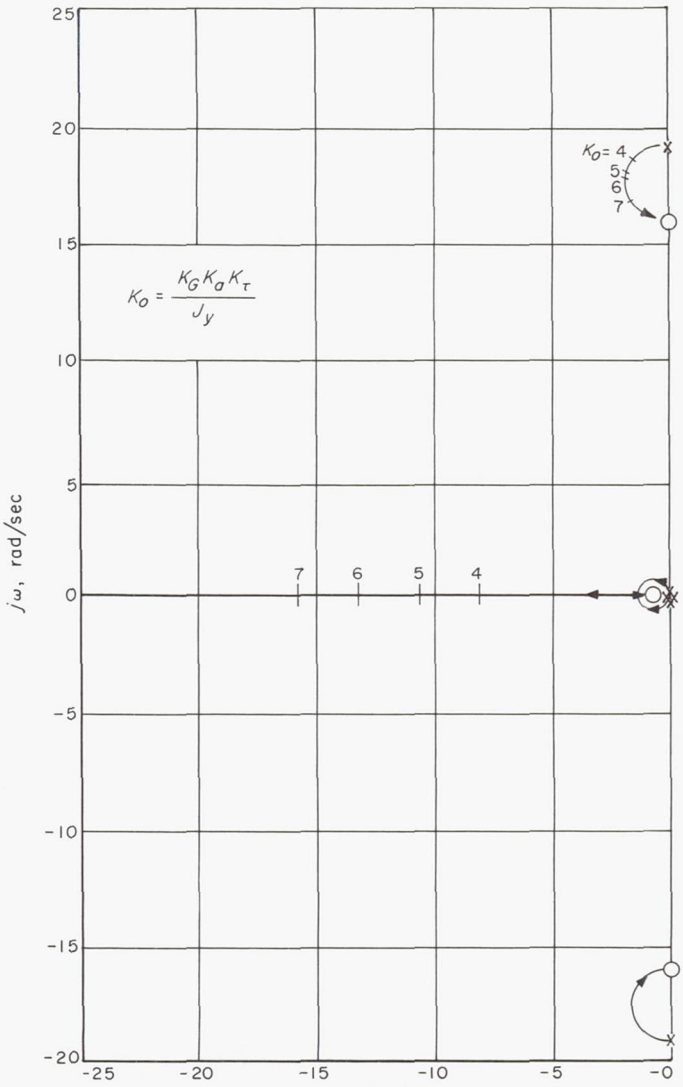

Fig. C-6. Root loci, simplified autopilot yaw axis

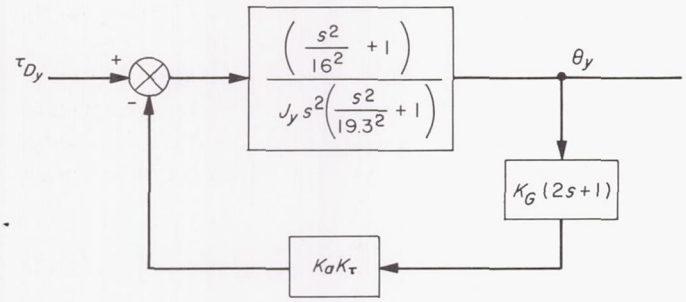

Fig. C-7. Simplified block diagram, yaw axis autopilot

and for

$$K_\tau = 13.9\,\text{ft-lb/rad}, \quad K_o = 5.15\,\text{rad/sec}^2$$

The effectiveness of the autopilot loop can be expressed in the form of θ/τ_D characteristics, as shown in Fig. C-8. The approximate transfer function for $K_o = 5.96$ rad/sec^2 and $\omega_1 = 16$ rad/sec is

$$\frac{\theta_y}{\tau_{D_y}} = \frac{Y'_{22}}{s^2\,|Y'|} \simeq \frac{1.54\,\text{mrad/ft-lb}\left(\frac{s^2}{16^2}+1\right)}{\left(\frac{s}{0.5}+1\right)\left(\frac{s}{13.0}+1\right)\left(\frac{s^2}{18^2}+\frac{0.2s}{18}+1\right)} \tag{C-14}$$

An interesting result to be noted here is the behavior of the solar panels. When τ_{D_y} is the only input to the autopilot,

$$\frac{\phi_1}{\tau_{D_y}} = \frac{Y'_{23}}{s^2\,|Y'|} = \frac{Y_{23}}{s^2\,(|Y| + H_y(s)\,Y_{22})}$$

$$= -\frac{2.5\,\text{mrad/ft-lb}\left(\frac{s^2}{16.33^2}\right)}{\left(\frac{s}{0.5}+1\right)\left(\frac{s}{13}+1\right)\left(\frac{s^2}{18^2}+\frac{0.2s}{18}+1\right)} \tag{C-15}$$

When F_z is the only input,

$$\frac{\phi_1}{F_z} = \frac{Y'_{13}}{s^2\,|Y'|} = \frac{0.0442\,\text{mrad/lb}\,(s^2)}{\left(\frac{s}{0.5}+1\right)\left(\frac{s}{13}+1\right)\left(\frac{s^2}{16.33^2}+1\right)} \tag{C-16}$$

Thus, F_z and τ_{D_y} excite the solar panels at different frequencies. Moreover, the solar panel oscillation due to τ_D decays, while that due to F_z does not. This phenomenon is evident in the analog computer simulation to be discussed.

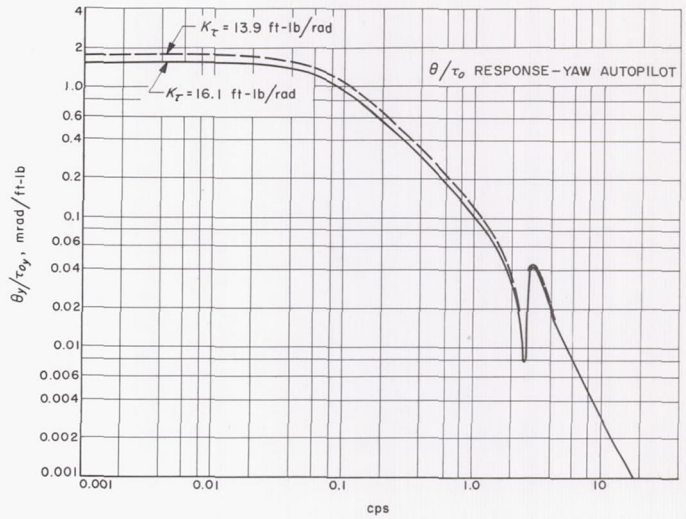

Fig. C-8. Frequency response, yaw autopilot

The effects of the higher-order poles of the gyro loop and the actuator loop are studied next. The spacecraft is assumed to be a rigid body. The root-locus of Fig. C-9 shows the autopilot behavior when the *worst-case* transfer function is used for the gyro loop, and the actuator loop is approximated by a transfer function for a large signal. For example,

$$\frac{e_g}{\theta} = K_G G_G(s) = \frac{K_G\left(\frac{s}{0.5}+1\right)}{\left(\frac{s^2}{60^2}+\frac{0.6s}{60}+1\right)} \tag{C-17}$$

$$\frac{\beta}{e_g} = K_a G_a(s) = \frac{K_a}{\left(\frac{s^2}{\omega_a^2}+\frac{2\zeta_a s}{\omega_a}+1\right)}$$

$$= \frac{K_a}{\left(\frac{s^2}{70^2}+\frac{1.2s}{70}+1\right)} \tag{C-18}$$

Figure C-10 shows the root loci for smaller signals, i.e., $\omega_a = 300$ rad/sec and $\zeta_a = 0.3$. As is depicted in Fig. C-6, C-9, and C-10, the linear analysis indicates that the stability of the autopilot is in no way threatened, although some of the complex poles are lightly damped.

When the higher-order poles of the gyro loop and the actuator loop were incorporated into Eq. (C-10), the complexity of its solution increased considerably. Therefore, the autopilot model was simulated on the analog computer. (The mechanization of the computer model is drawn in Fig. C-39.) A summary of the results from the

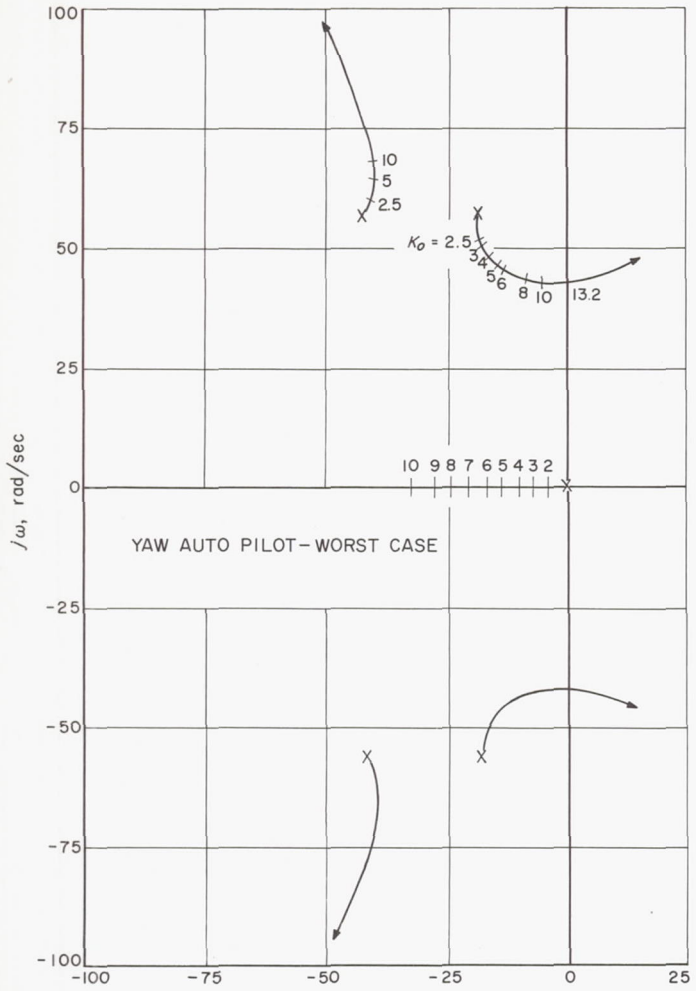

Fig. C-9. Root loci of gyro and actuator poles, yaw autopilot, worst case

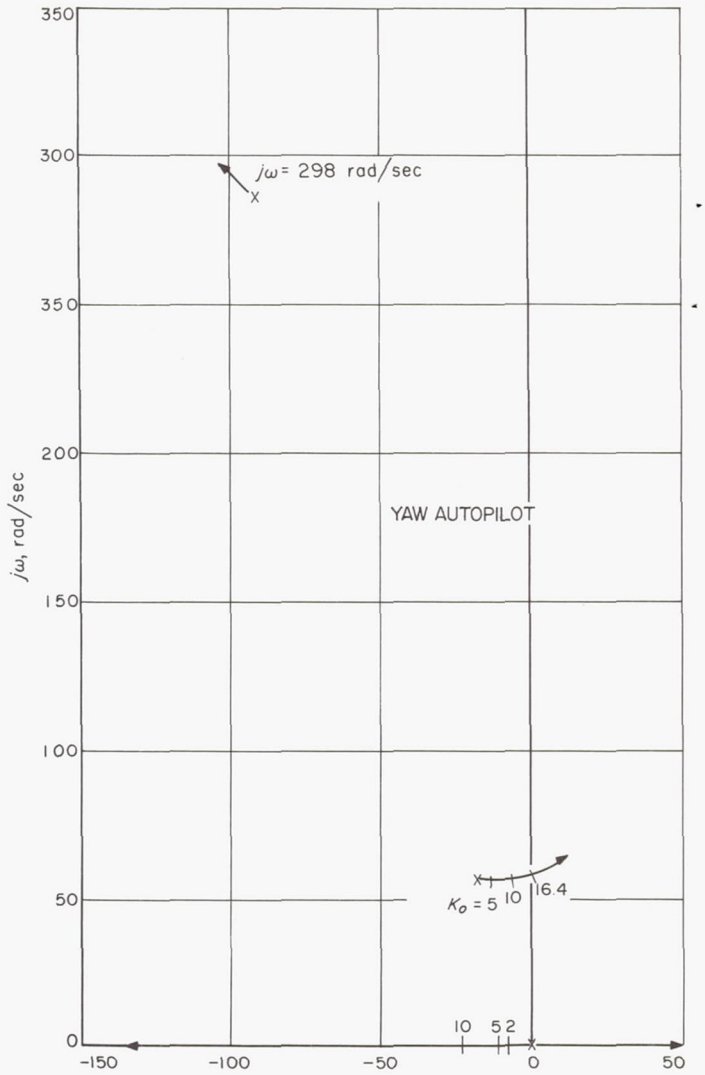

Fig. C-10. Root loci of gyro and actuator poles, yaw autopilot

simulation are presented in a series of traces from the computer outputs. For step inputs of $F_z = 55$ lb thrust and $\tau_{D_y} = 1$ ft-lb of torque, Fig. C-11 and C-12 show the spacecraft response, respectively (the solar panels are assumed to be identical). Recorded on the traces are the spacecraft attitude, θ; the gyro amplifier output, e_{amp}; the instantaneous pointing error, F_x/F_z; and the solar panel deflections, ϕ_1 and ϕ_2. The behavior of the solar panels mentioned before can be observed in these figures (C-11, C-12). The effects of the two solar panels not being identical were studied next by changing the parameters of one solar panel, while those of the other panel remained fixed. The parameters varied were the mass, the distance between the solar panel center of gravity and the hinge line, and the spring constant about the hinge line. The results are shown in Fig. C-13 through C-18 for a 5% variation of these parameters. It should be noted here that the parametric variations do not affect the spacecraft attitude very much.

c. Roll axis autopilot. Since the spacecraft is assumed to be rigid about the roll axis, the root loci are identical to those shown in Fig. C-9 and C-10. The loop gain, K_o, however, will be 1.15 rad/sec^2. For the reasons stated previously, the roll axis autopilot is not studied in any greater detail.

2. Autopilot Pointing Error

The autopilot characteristics discussed above are useful in the analysis of the study of the error in the corrective

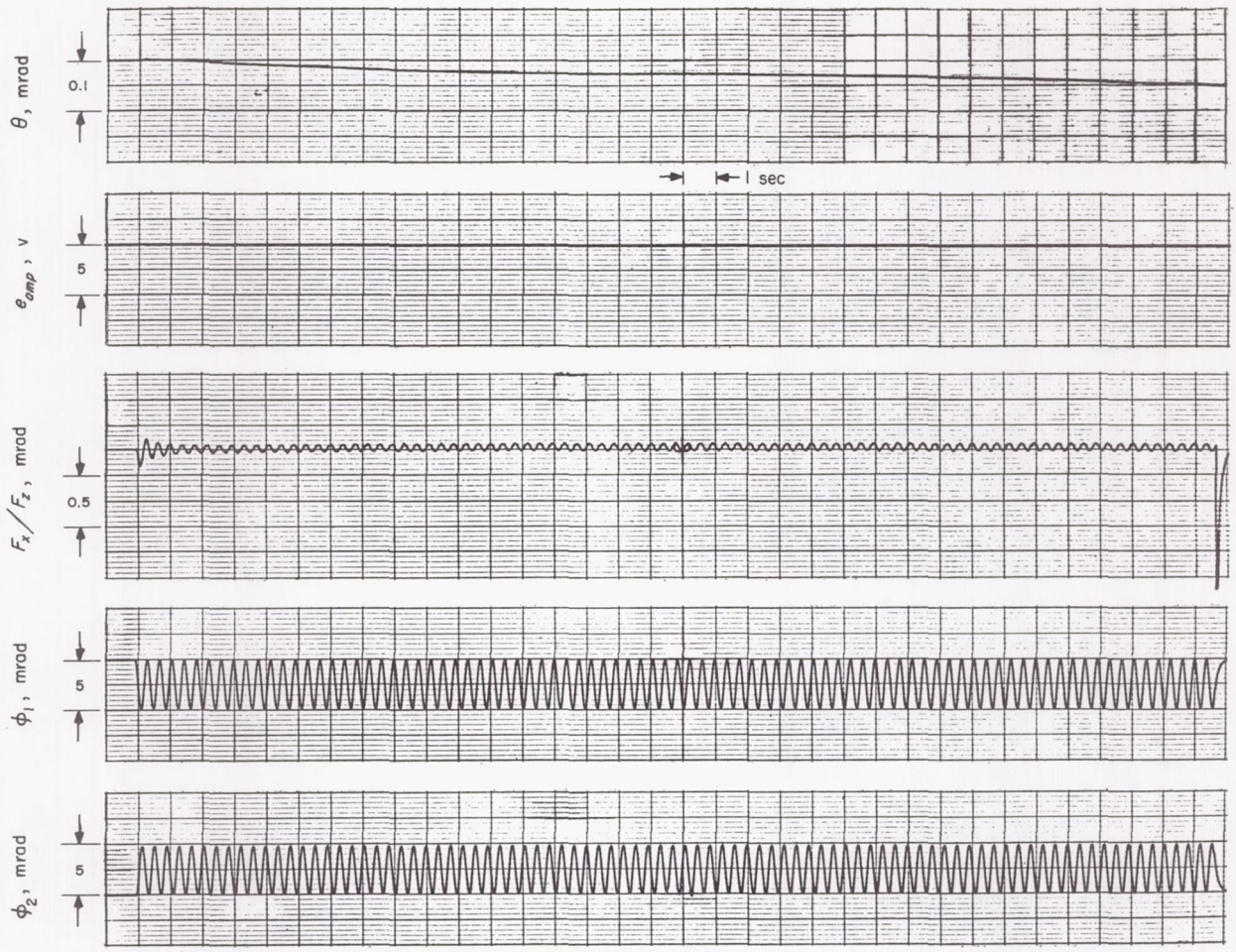

Fig. C-11. Yaw axis response to a force, $F_z = 55$ lb, assuming identical solar panels

velocity increment produced during the midcourse maneuver. Since the function of the autopilot is to maintain the thrust vector in the direction of the desired corrective velocity (inertial reference line), the error discussed here is limited to the directional error. This error is caused by a transverse force due to the deviation of the motor-thrust vector from the inertial reference line. The directional error is henceforth called a *pointing error* and expressed by the ratio of the transverse velocity to the total velocity achieved at the completion of the midcourse maneuver. Therefore, we have

$$\left.\frac{v_T}{v_z}\right|_{t_f} = \left.\frac{(v_x^2 + v_y^2)^{1/2}}{v_z}\right|_{t_f}$$

$$= \frac{\left[\left(\int_0^{t_f} F_x\,dt\right)^2 + \left(\int_0^{t_f} F_y\,dt\right)^2\right]^{1/2}}{\int_0^{t_f} F_z\,dt} \quad \text{(C-19)}$$

where

t_f = the duration of the thrust on time

v_T = transverse velocity

v_i = components of the velocity produced by the midcourse motor thrust, $i = x, y, z$

F_i = components of the motor thrust, $i = x, y, z$ and $F_o \simeq F_z$

The pointing error is analyzed under the following assumptions:

1. When all the gyro-loop signals are null, the angle between the z-axis and the inertial reference line is zero.
2. The centerline of the midcourse motor coincides with the z-axis.

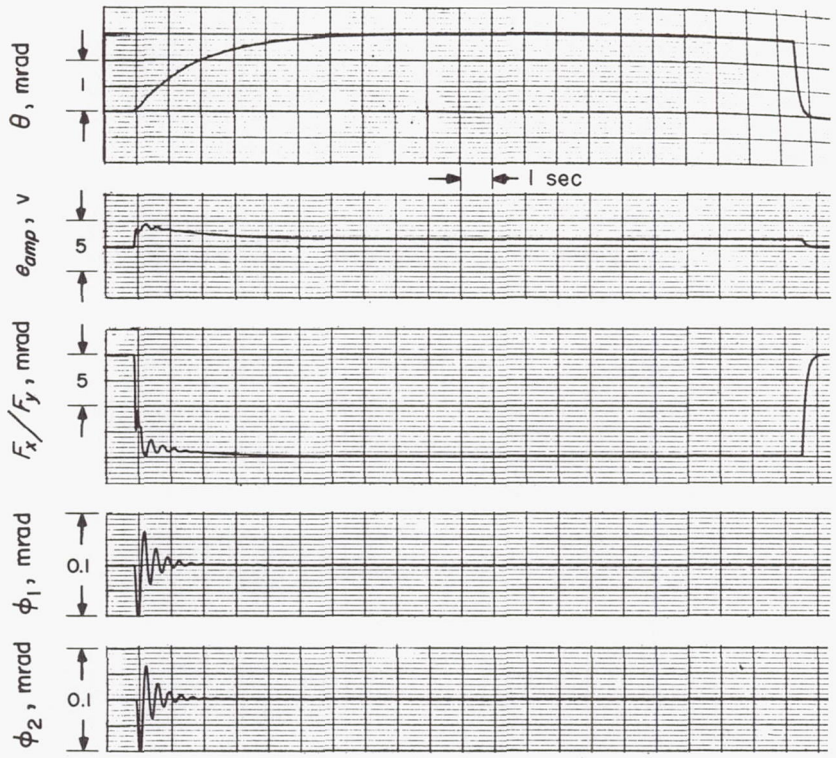

Fig. C-12. Yaw axis response to a torque, τ_{D_y} = 1 ft-lb, assuming identical solar panels

3. Uncertainties in the location of the center of the spacecraft mass and in the thrust direction are distributed circularly about the z-axis; no crosscoupling exists between the x and y axes. What these imply is that the computation of the maximum pointing error is resolved to single-axis computation. Hence, Eq. (C-19) becomes:

$$\left.\frac{v_T}{v_z}\right|_{t_f} = \frac{\int_0^{t_f} F_x\,dt}{\int_0^{t_f} F_z\,dt} = \frac{\int_0^{t_f} F_y\,dt}{\int_0^{t_f} F_z\,dt} \qquad \text{(C-20)}$$

4. The motor thrust is a step function.
5. Misalignment in the jet vanes is negligible.
6. All the rotations involved are small enough that small angle approximations hold.

The following analyses are made for both the rigid and non-rigid body cases.

a. Rigid body case. A simple computation is first made to estimate the magnitude of the pointing error by assuming a rigid body for the spacecraft dynamics. Under this assumption,

$$|F_x| = |F_y|$$

Equation (C-20) can be further simplified by neglecting the transient portion of the spacecraft response, as follows:

$$\left.\frac{v_T}{v_z}\right|_{t_f} \simeq \frac{F_{x_f}}{F_z} = \frac{F_{x_f}}{F_o} = \frac{F_{y_f}}{F_o} \qquad \text{(C-21)}$$

where the subscript f denotes the final time.

From Eq. (B-32):

$$F_x = F_o(\theta_f + \Delta_A)_y + K_L\beta_y \qquad \text{(C-22a)}$$

$$F_{x_f} = F_o(\theta_f + \Delta_A)_y + K_L\beta_{y_f} \qquad \text{(C-22b)}$$

Since

$$K_L\beta_{y_f} = -\frac{\tau_{S_f}}{C_2} = \frac{\tau_D}{C_2} = \frac{C_1F_o}{C_2}(\rho - \Delta_A)\,y$$

and

$$\theta_f = \frac{\tau_{D_y}}{J_yK_o} = \frac{C_1F_o}{J_yK_o}(\rho - \Delta_A)\,y$$

Eq. (C-22b) becomes:

$$F_{x_f} = F_o\left[\frac{C_1F_o}{J_yK_o}(\rho - \Delta_A)_y + \Delta_{A_y} + \frac{C_1}{C_2}(\rho - \Delta_A)_y\right] \qquad \text{(C-23a)}$$

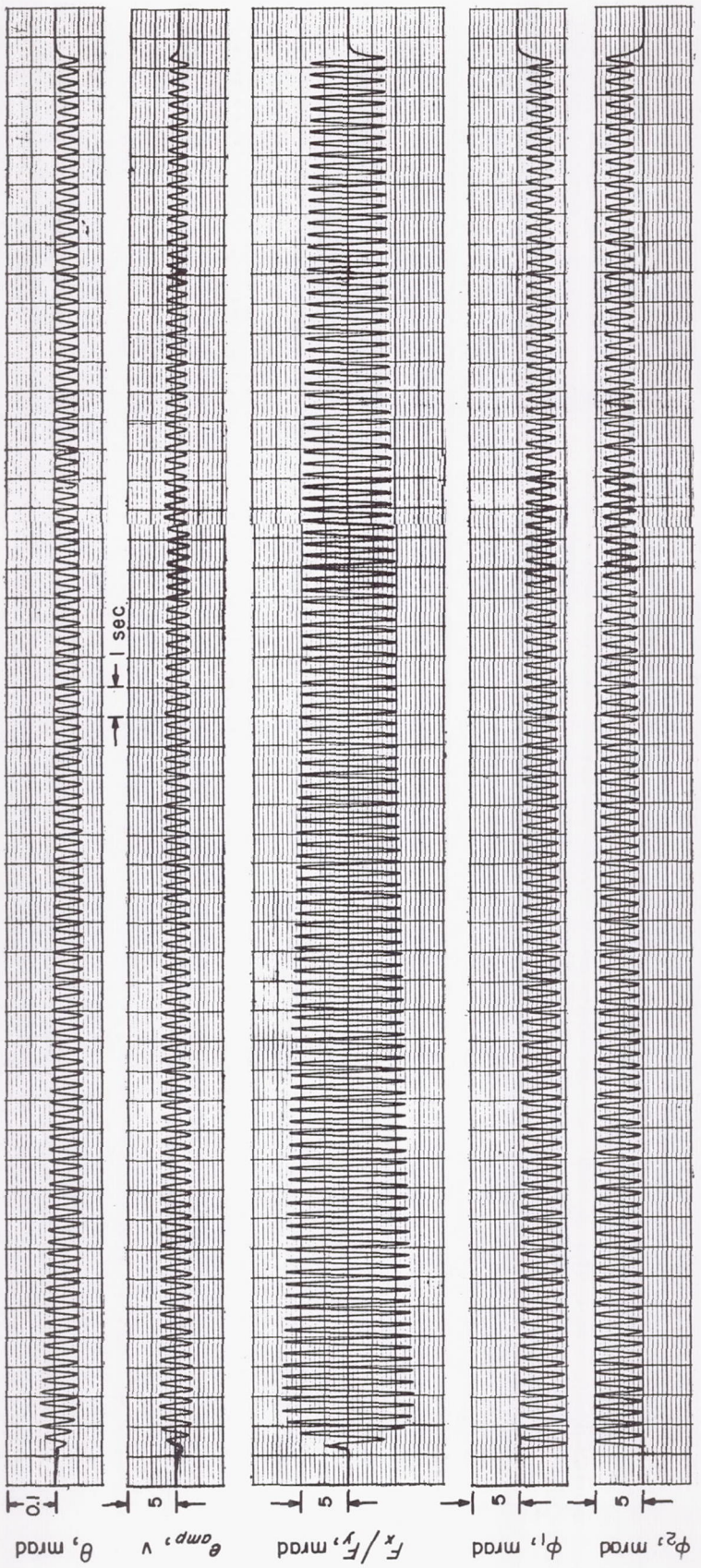

Fig. C-13. Yaw axis response for $F_z = 55$ lb, $\Delta m/m = \pm 5\%$

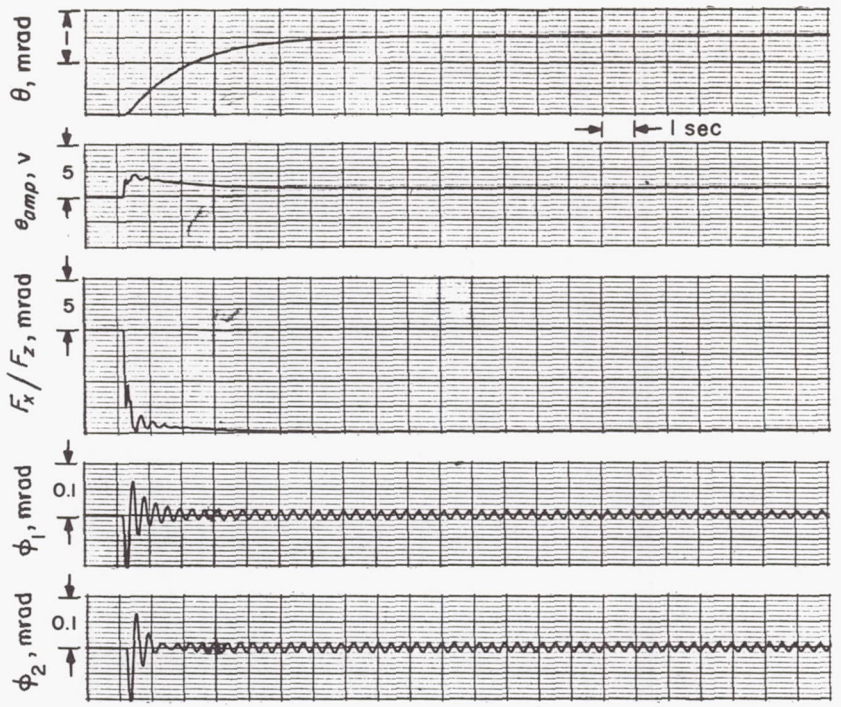

Fig. C-14. Yaw axis response, τ_{D_y} = 1 ft-lb, $\Delta m/m = +5\%$

and

$$\frac{F_{x_f}}{F_o} = \left(\frac{C_1 F_o}{J_y K_o} + \frac{C_1}{C_2}\right)\rho_y + \left(1 - \frac{C_1 F_o}{J_y K_o} - \frac{C_1}{C_2}\right)\Delta_{A_y} \tag{C-23b}$$

Solutions to the above equations were determined for the following cases (referring back to Fig. B-17): For $C_1 = 1.79$ ft, $C_2 = 2.16$ ft, and $K_o = 5.96$ rad/sec^2,

$$\frac{F_{x_f}}{F_o} \simeq 0.98\rho_y + 0.02\Delta_{A_y} \tag{C-24}$$

and for $C_1 = 1.5$ ft, $C_2 = 1.87$ ft, and $K_o = 5.15$ rad/sec^2,

$$\frac{F_{x_f}}{F_o} \simeq 0.95\rho_y + 0.05\Delta_{A_y} \tag{C-25}$$

From the *Ranger* spacecraft specifications, the following values were obtained:

$$\rho = \frac{C_o}{C_1} = 4.66\,\text{mrad} \qquad (C_1 = 1.79\,\text{ft}) \tag{C-26}$$

and

$$\rho = \frac{C_o}{C_1} = 5.56\,\text{mrad} \qquad (C_1 = 1.5\,\text{ft}) \tag{C-27}$$

$$\Delta_A = 3.49\,\text{mrad} \tag{C-28}$$

With these values, Eq. (C-24) and (C-25) give

$$\frac{F_{x_f}}{F_o} = 4.63\,\text{mrad} \tag{C-29}$$

and

$$\frac{F_{x_f}}{F_o} = 5.46\,\text{mrad} \tag{C-30}$$

respectively, for the maximum pointing error. An interesting fact to note here is that the pointing error is highly dependent upon the parameter ρ and is effected little by Δ_A.

b. Non-rigid body case. In this section, the effects of the structural resonances on the pointing error are investigated by simulating the midcourse-maneuver propulsion phase on the analog computer (details of the simulation are described in this Appendix C, 4). The pointing error is expressed as the ratio of F_x/F_z and F_y/F_z to simplify the computer mechanization. This is somewhat justified (but not too rigorously) below.

Since the autopilot is stable, F_x is bounded and can be written as

$$F_x = f_o + f_1 + f_2 \tag{C-31}$$

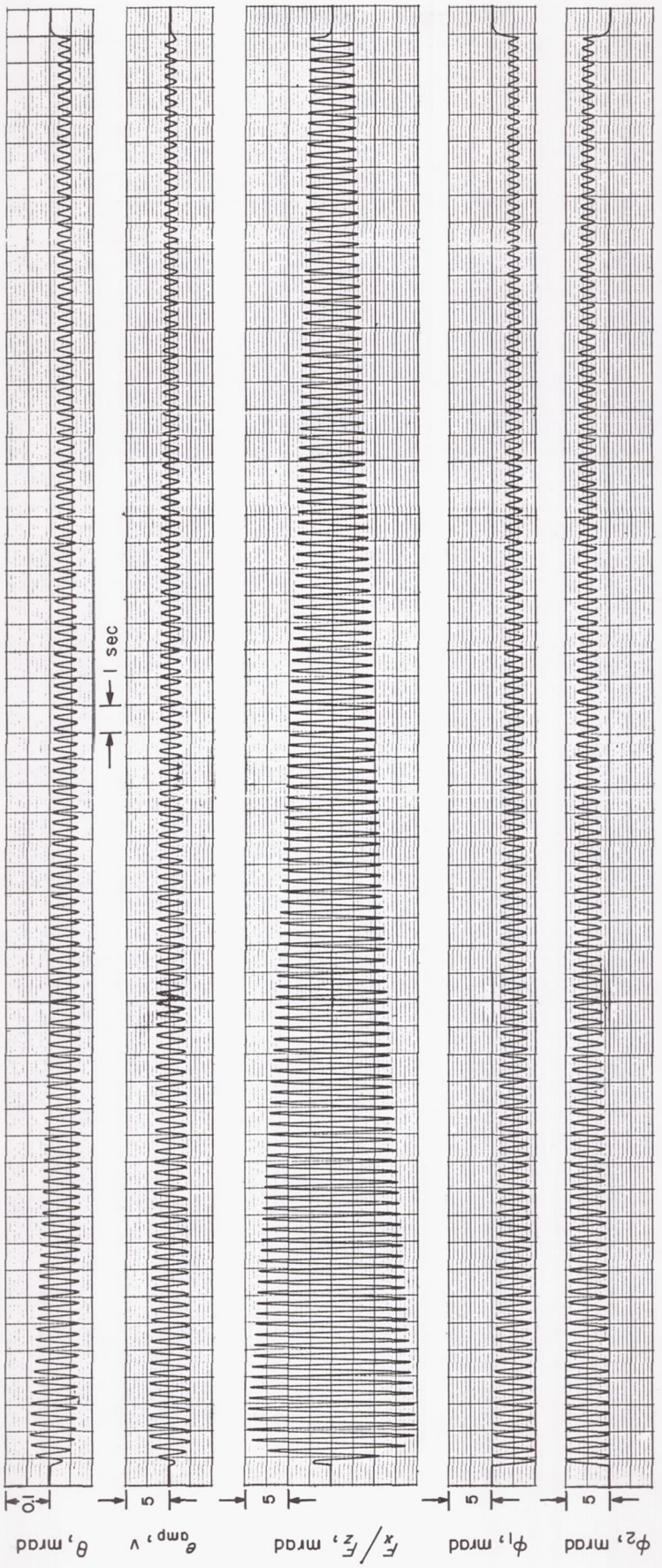

Fig. C-15. Yaw axis response, $F_z = 55$ lb, $\Delta I/I = +5\%$

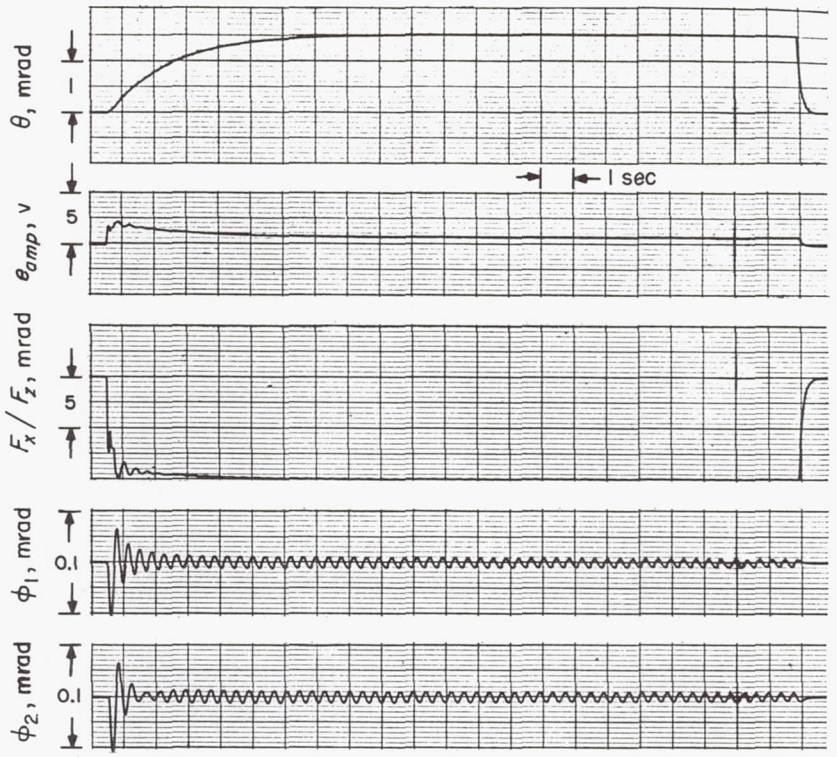

Fig. C-16. Yaw axis response, $\tau_{D_y} = 1$ ft-lb, $\Delta I/I = +5\%$

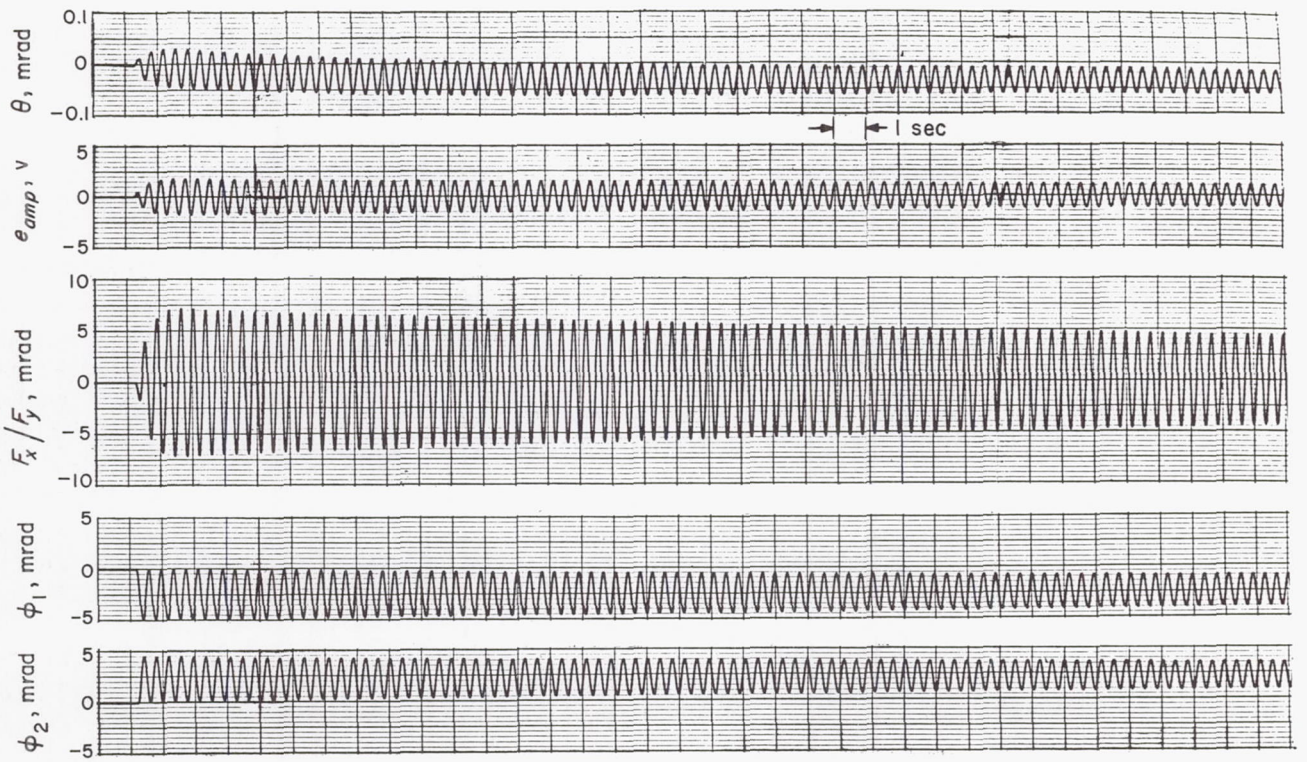

Fig. C-17. Yaw axis response, $F_z = 55$ lb, $\Delta k/k = +5\%$

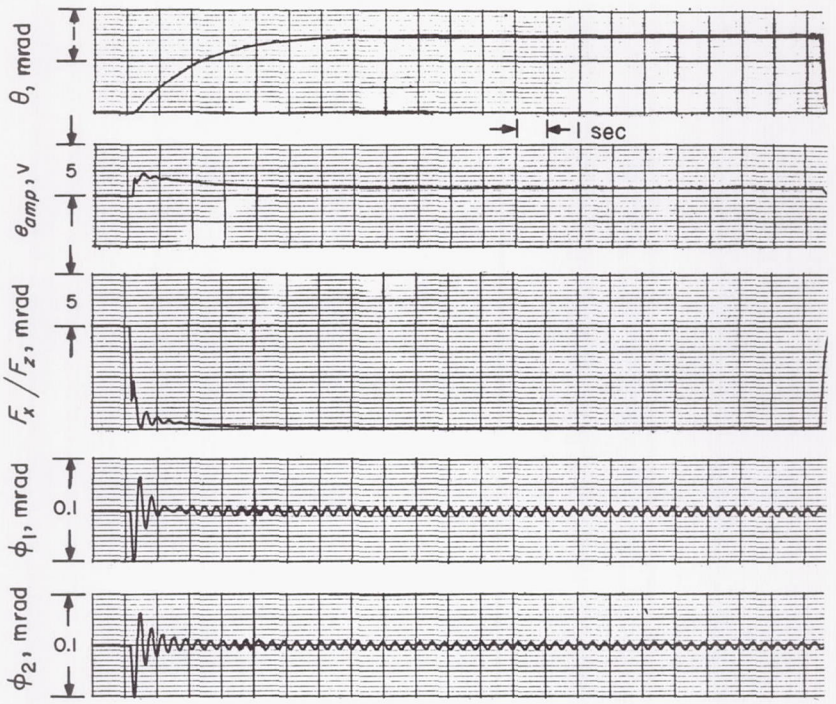

Fig. C-18. Yaw axis response, τ_{D_y} = 1 ft-lb, $\Delta k/k = +5\%$

where

f_o = constant force

f_1 = decaying force

$f_2 = F_2 \sin \omega t$ = a sustained oscillation

Then Eq. (C-31) can be rewritten as

$$\frac{v_T}{v_z} = \frac{\int_0^t F_x\, d\tau}{\int_0^t F_z\, d\tau} = \frac{f_o t}{F_o t} + \frac{\int_0^t f_1\, d\tau}{F_o t} + \frac{\int_0^t f_2\, d\tau}{F_o t}$$

$$= \frac{f_o}{F_o} + \frac{\int_0^t \frac{f_1}{F_o}\, d\tau}{t} - \frac{F_z}{\omega t F_o} \cos \omega t \qquad \text{(C-32)}$$

As the time increases, the value of the second and third terms of the above equation decreases; hence,

$$\frac{v_T}{v_z} \rightarrow \frac{f_o}{F_o}$$

Rewriting Eq. (C-31) in another form,

$$\frac{F_x}{F_o} = \frac{f_o}{F_o} + \frac{f_1}{F_o} + \frac{F_2}{F_o} \sin \omega t \qquad \text{(C-33)}$$

it can be seen that the dc portion of F_x/F_o approaches the pointing error as time increases.

The midcourse analysis was conducted by simulating the following parameters:

$$\rho = \pm 5.0 \text{ mrad}$$

$$\Delta_A = \pm 4.0 \text{ mrad}$$

A compilation of the results obtained from the analog computer simulation is presented in the following discussion. Figures C-19 and C-20 show the response for the yaw axis when the solar panels are assumed to be identical. It should be noted here that the value $(F_x/F_z + 2\Delta_A)$ is recorded instead of the ratio F_x/F_z. This is due to a sign reversal in Δ_A in mechanizing Eq. (B-32). Since Δ_A is constant, we simply subtract $2\Delta_A$ from the trace. The effect of the spacecraft being misorientated by ± 5.0 mrad during the thrust phase is shown in Fig. C-21 through C-24. The perturbation of the solar panel characteristic parameters is presented in a series of traces, Fig. C-25 through C-32. The results in the traces for F_x/F_o are related to Eq. (C-32), i.e., oscillations in v_T/v_z reflected in F_x/F_o should decrease considerably in magnitude after a sufficient interval of time (estimated to be approximately 10 sec). Figures C-33 through C-38

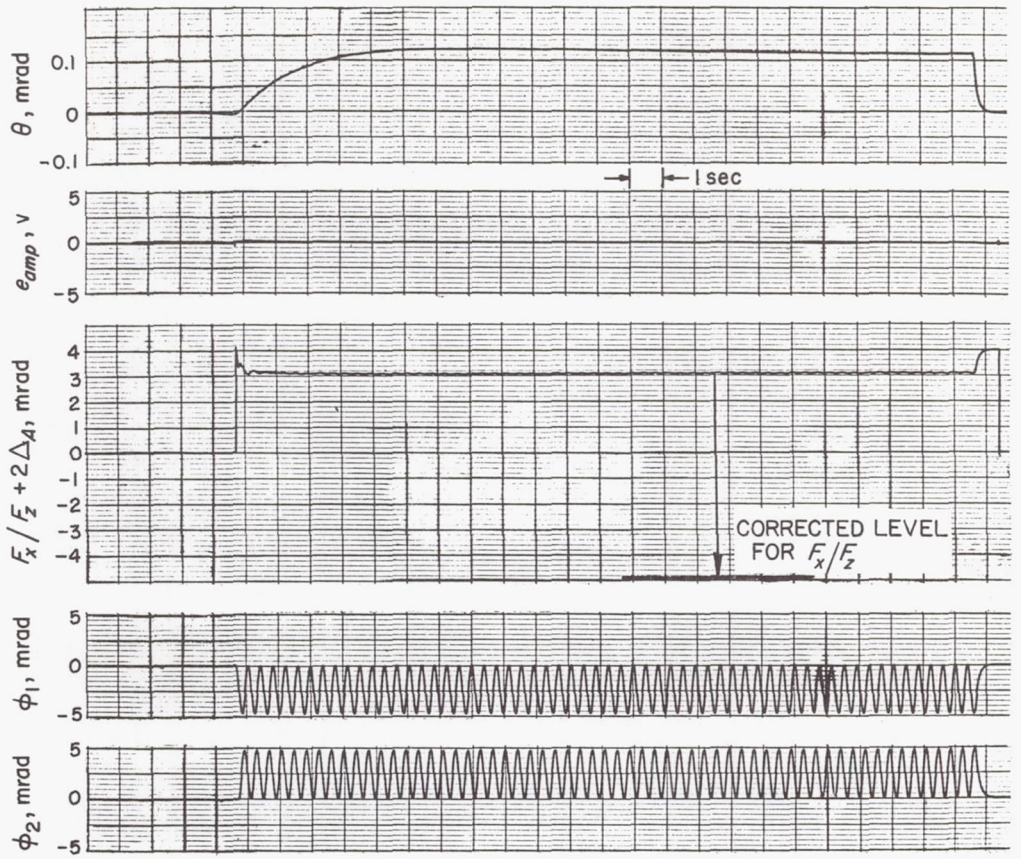

Fig. C-19. Simulated midcourse, yaw axis, $\rho = +5$ mrad, $\Delta_A = +4$ mrad, $\theta_o = 0$, identical solar panels

show the simulated results of a similar study for the pitch axis.

The following characteristics are summarized based upon the simulation results:

1. The maximum pointing error is about 5 mrad.

2. The gyro amplifier voltage seldom exceeds ± 5 v and never exceeds ± 10 v.

3. Unmatched solar panels affect the transient response of the spacecraft considerably, but the final pointing error is not affected appreciably.

4. The effects of the gyro-loop poles are negligible.

5. The duration of transients in F_x/F_z is short (less than 3 sec) when compared with that of the midcourse propulsion duration. This means that the pointing error can be computed by Eq. (C-23b) with sufficient accuracy.

6. The maximum jet-vane deflection is approximately 15 deg.

3. Summary of the Autopilot Analysis

The results of the autopilot analysis are summarized below:

1. The autopilot is stable at the present loop-gain settings of

$$K_o = \frac{K_G K_a K_T}{J} = 5 \sim 7 \text{ rad/sec}^2$$

for pitch and yaw, and

$$K_o = 1.15 \text{ rad/sec}^2$$

for the roll axis. The gain margin in the yaw or pitch axis is such that the gain can be approximately doubled, before the loop exhibits unstable characteristics.

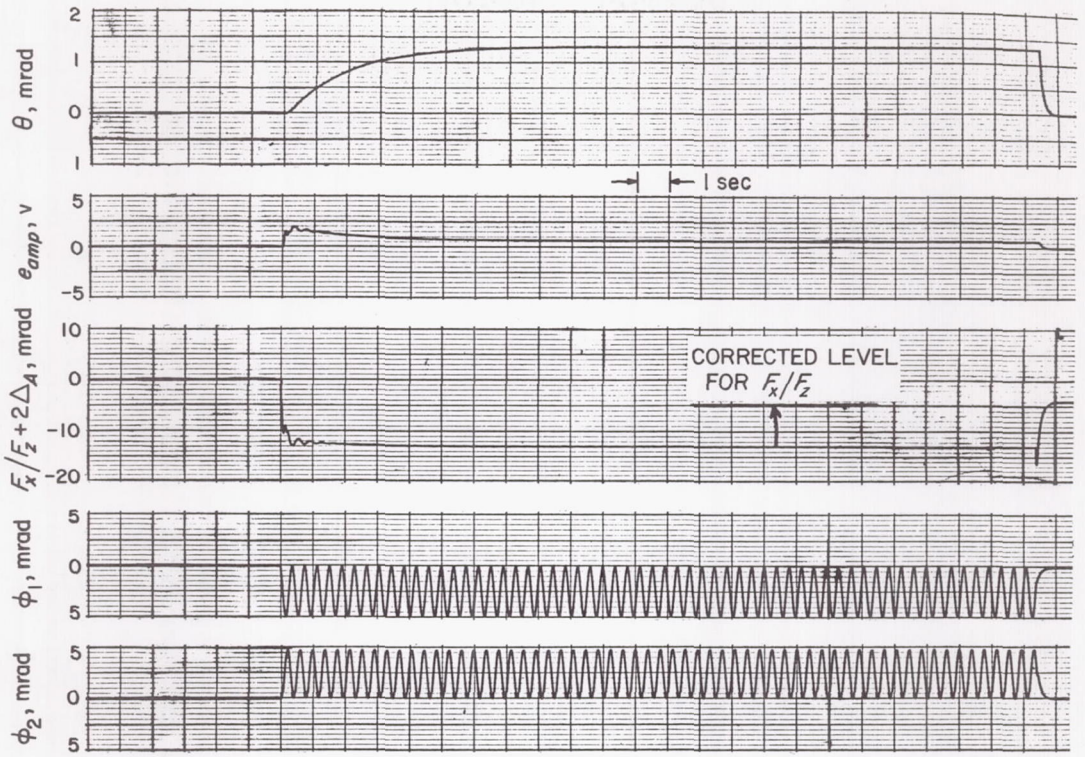

Fig. C-20. Simulated midcourse firing, yaw axis, identical solar panels, $\rho = +5$ mrad, $\Delta_A = -4$ mrad, $\theta_o = 0$

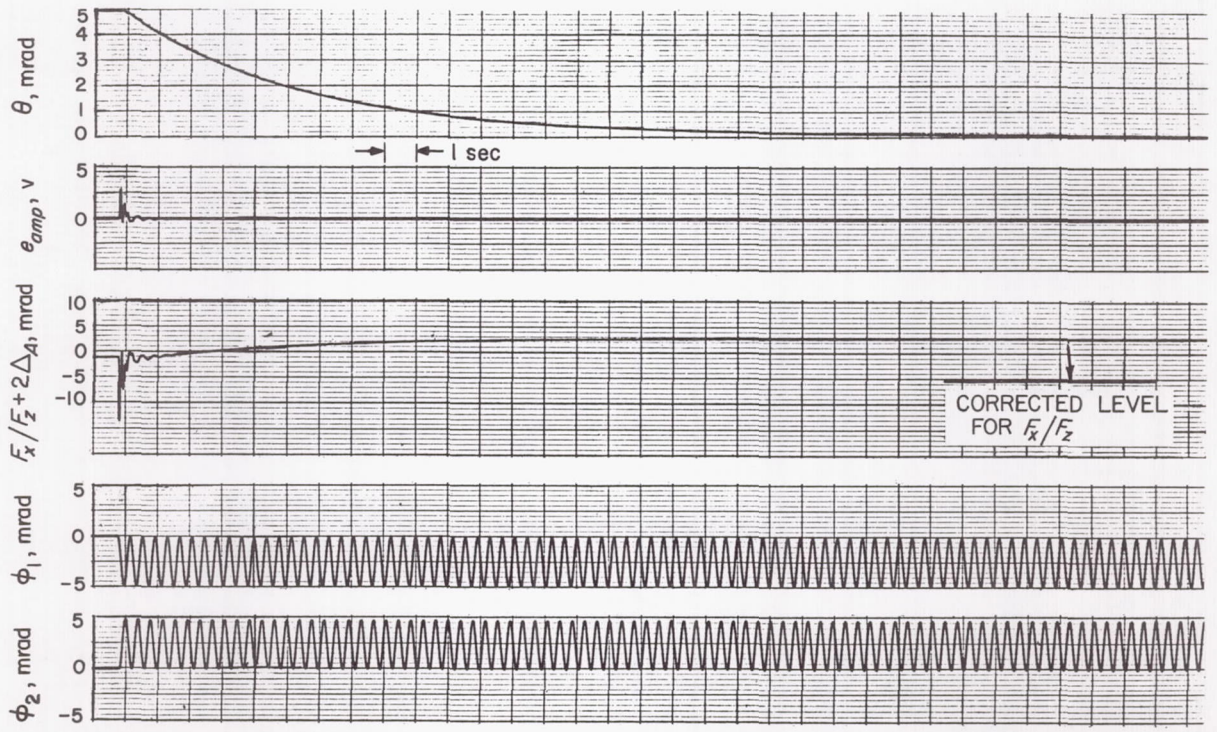

Fig. C-21. Simulated midcourse, yaw axis, $\rho = +5$ mrad, $\Delta_A = +4$ mrad, $\theta_o = +5$ mrad, identical solar panels

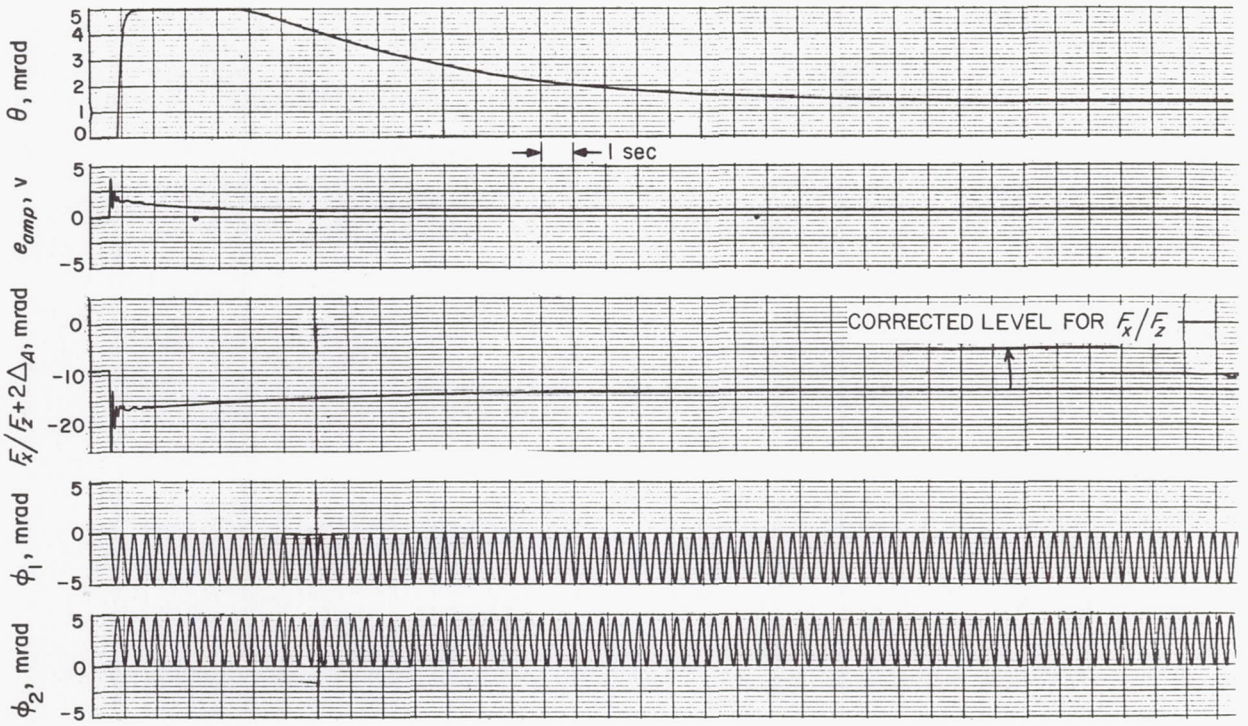

Fig. C-22. Simulated midcourse, yaw axis, $\rho = +5$ mrad, $\Delta_A = -4$ mrad, $\theta_o = +5$ mrad, identical solar panels

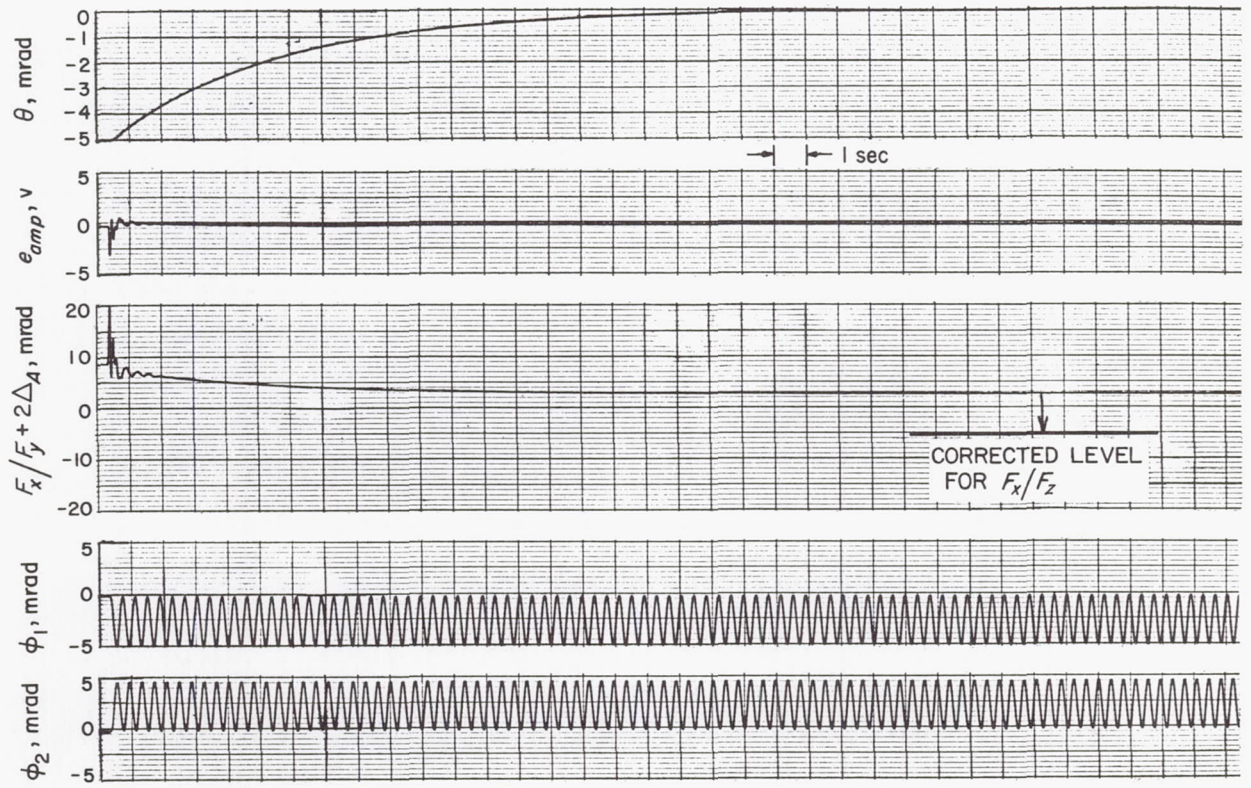

Fig. C-23. Simulated midcourse, yaw axis, $\rho = +5$ mrad, $\Delta_A = +4$ mrad, $\theta_o = -5$ mrad, identical solar panels

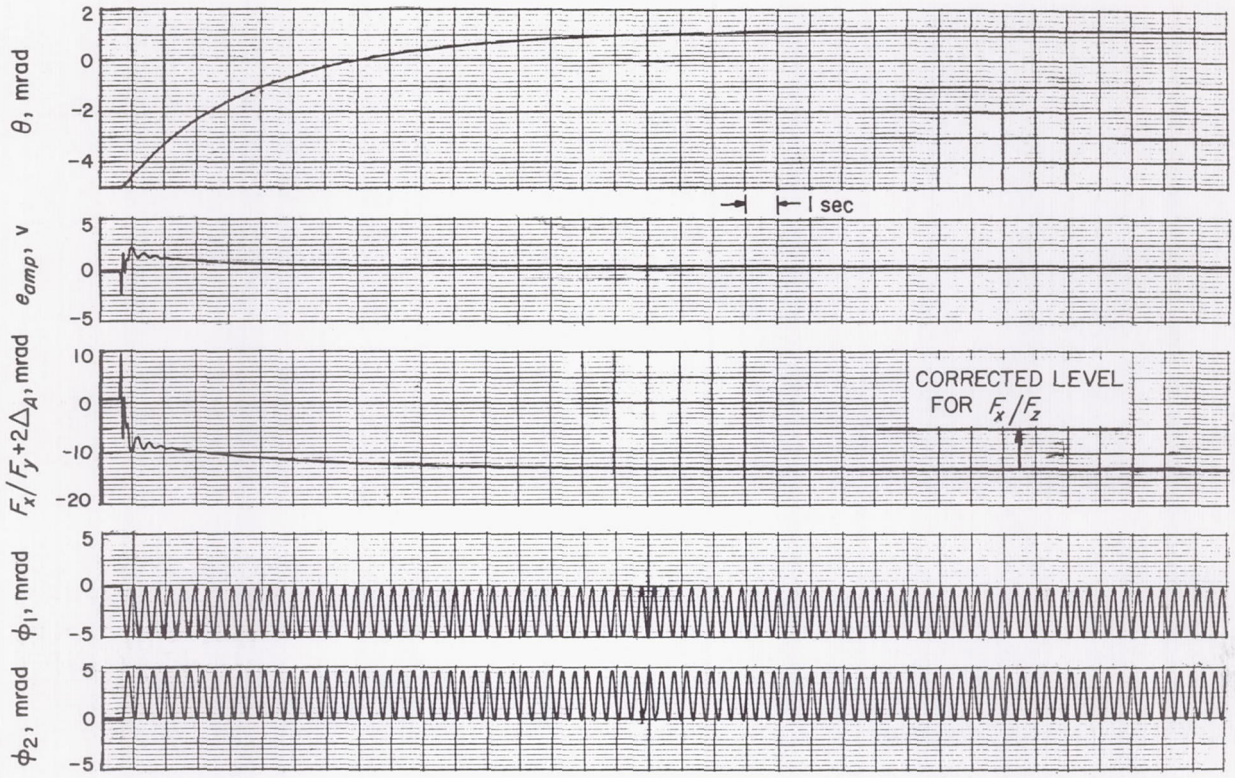

Fig. C-24. Simulated midcourse, yaw axis, $\rho = +5$ mrad, $\Delta_A = -4$ mrad, $\theta_o = -5$ mrad, identical solar panels

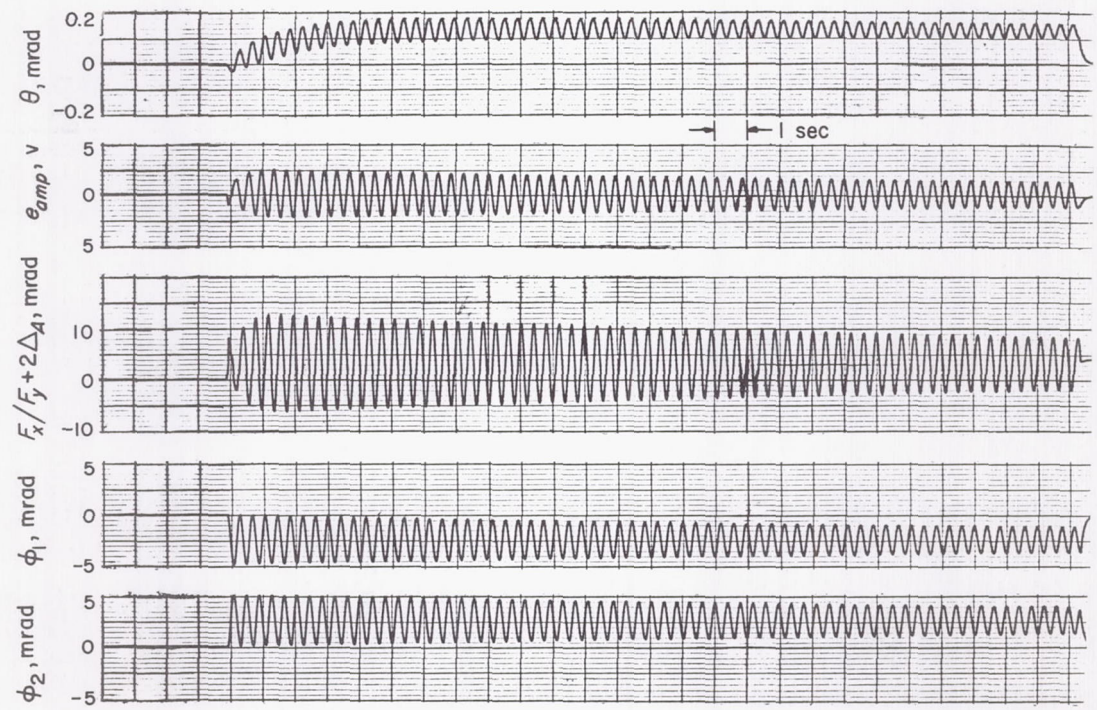

Fig. C-25. Simulated midcourse, yaw axis, $\rho = +5$ mrad, $\Delta_A = +4$ mrad, $\theta_o = 0$, $\Delta m/m = \Delta l/l = \Delta k/k = +5\%$

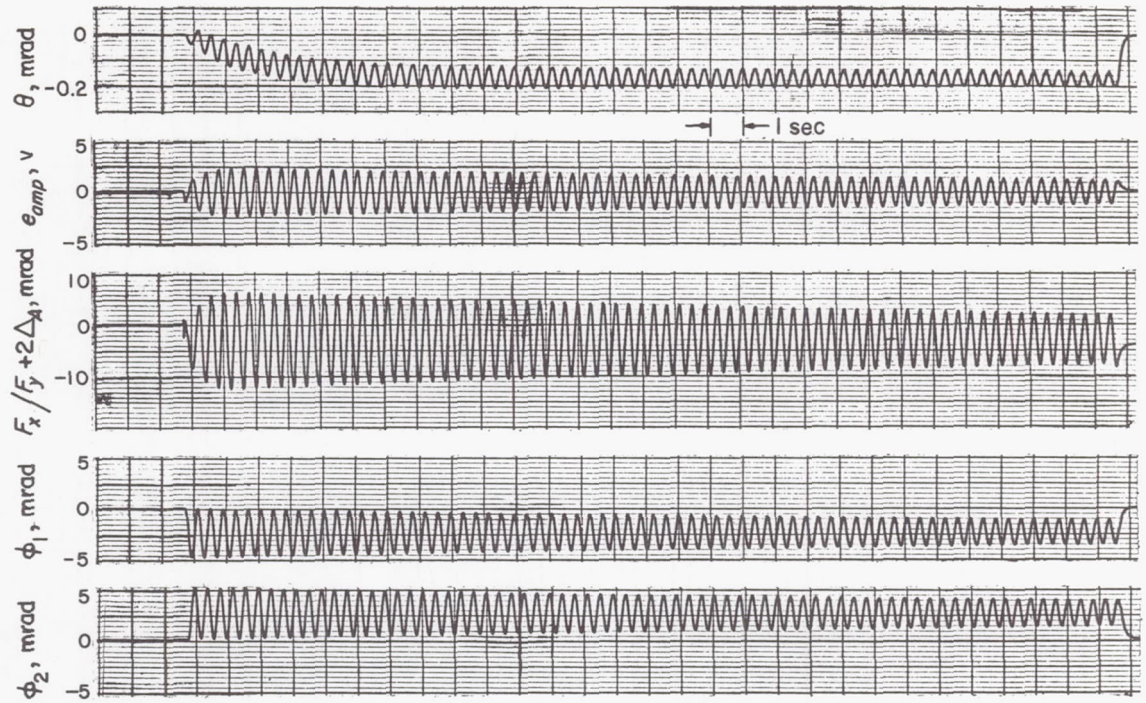

Fig. C-26. Simulated midcourse, yaw axis, $\rho = -5$ mrad, $\Delta_A = -4$ mrad, $\theta_o = 0$, $\Delta m/m = \Delta I/I = \Delta k/k = +5\%$

2. During the *worst-case* analysis (5% mismatch in the solar panel parameters), the gyro amplifier voltage remains below 10 v. Therefore, the amplifier should be well within the saturation level, even when cross-coupling and noise are taken into account.

3. During the *worst-case* analysis, the jet vanes do not reach their mechanical limits and therefore do not saturate. The maximum deflection observed is about 15 deg.

4. Gyro and structural crosscouplings do not appear to be detrimental to the autopilot stability. Additional pointing error due to crosscouplings is estimated to be 2 or 3 mrad at most.

5. The maximum expected pointing error of the midcourse propulsion phase due to the autopilot alone (single axis) is 6 mrad.

6. If the midcourse propulsion were to last for a short period of time (say less than 4 sec), then the pointing error v_T/v_z, might be higher than expected due to transients, although v_T itself would be small.

7. The directional accuracy of the thrust vector depends mostly upon the spacecraft C.G. offset, and very little on the uncertainty in the direction of the motor's thrust.

8. Flexible structures, such as the solar panels and high-gain antenna affect the transient response considerably. The final pointing error, however, is not affected appreciably, when the solar panel parameters are matched within 5%.

There are several areas in which additional studies are recommended. These are:

1. The effect of the unmatched solar panels on the pointing error during the first few seconds of midcourse motor thrust is of interest (in terms of v_T/v_z and v_T rather than F_x/F_z).

2. Analysis of gyro voltages during the three-axis operation of the autopilot is also of interest.

4. Analog Computer Mechanization

The recordings presented in the preceding section are based on the analog computer model discussed in this section. The parameters, equations of motion, and forcing functions are each presented.

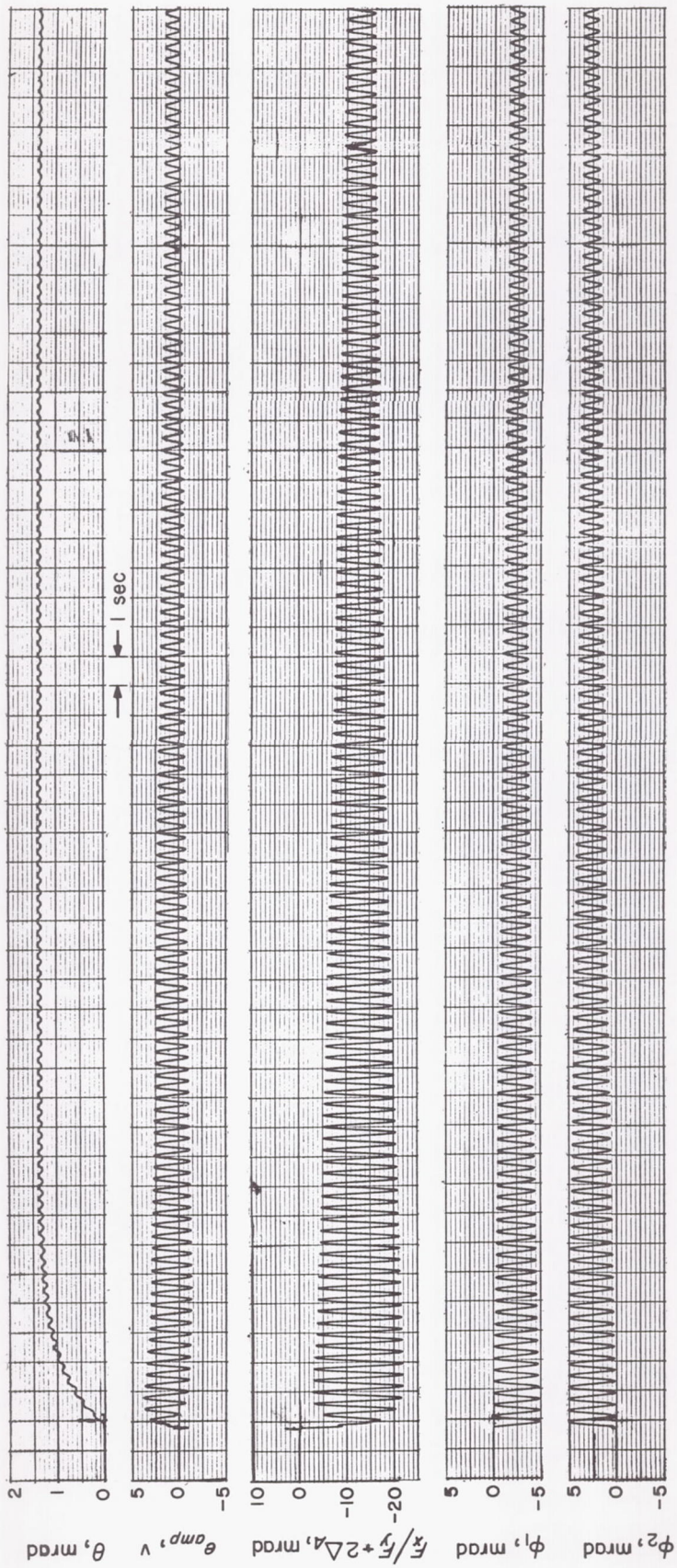

Fig. C-27. Simulated midcourse, yaw axis, $\rho = +5$ mrad, $\Delta_A = -4$ mrad, $\theta_o = 0$, $\Delta m/m = \Delta I/I = \Delta k/k = +5\%$

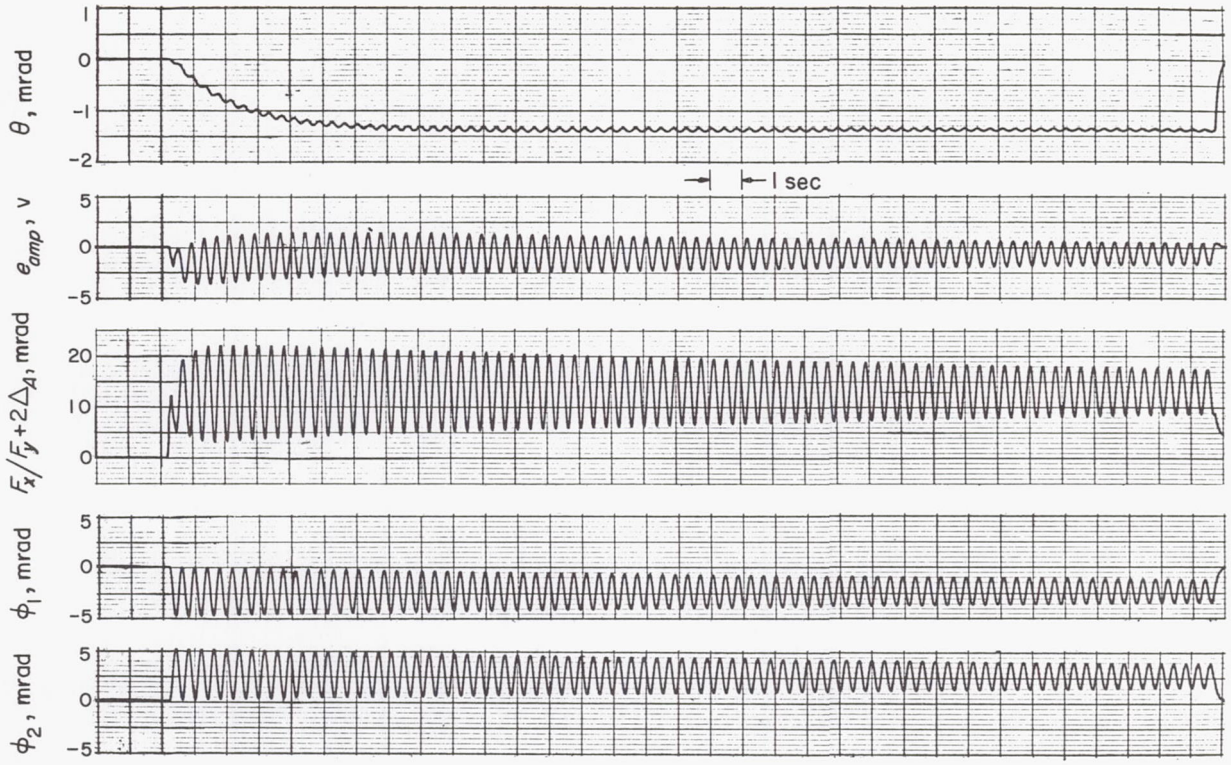

Fig. C-28. Simulated midcourse, yaw axis, $\rho = -5$ mrad, $\Delta_A = +4$ mrad, $\theta_o = 0$, $\Delta m/m = \Delta l/l = \Delta k/k = +5\%$

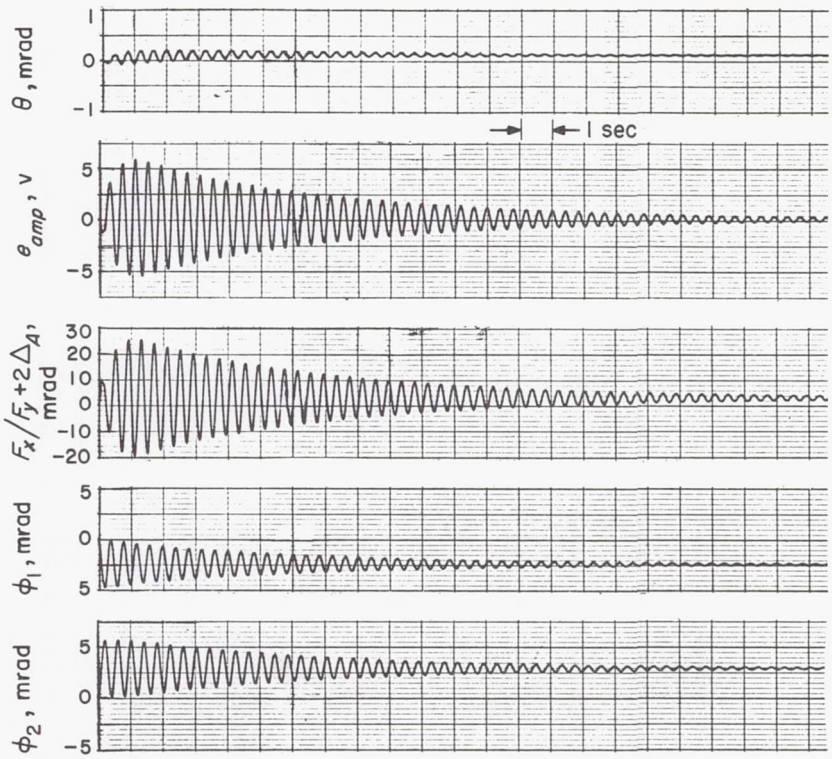

Fig. C-29. Simulated midcourse, yaw axis, $\rho = +5$ mrad, $\Delta_A = +4$ mrad, $\theta_o = 0$, $\Delta m/m = \Delta l/l = +5\%$, $\Delta k/k = -5\%$

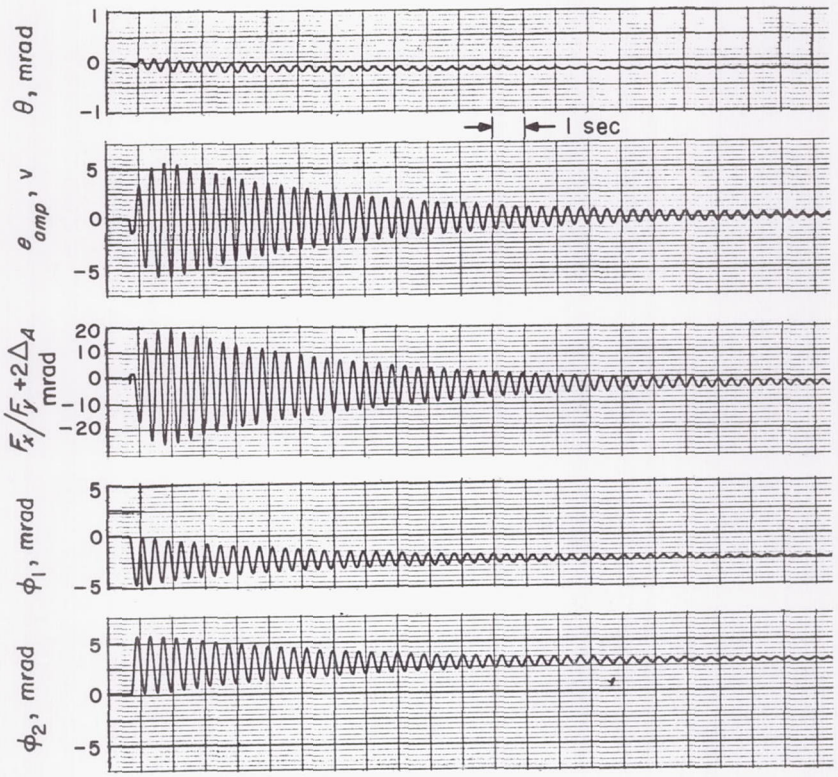

Fig. C-30. Simulated midcourse, yaw axis, $\rho = -5$ mrad, $\Delta_A = -4$ mrad, $\theta_0 = 0$, $\Delta m/m = \Delta I/I = +5\%$, $\Delta k/k = -5\%$

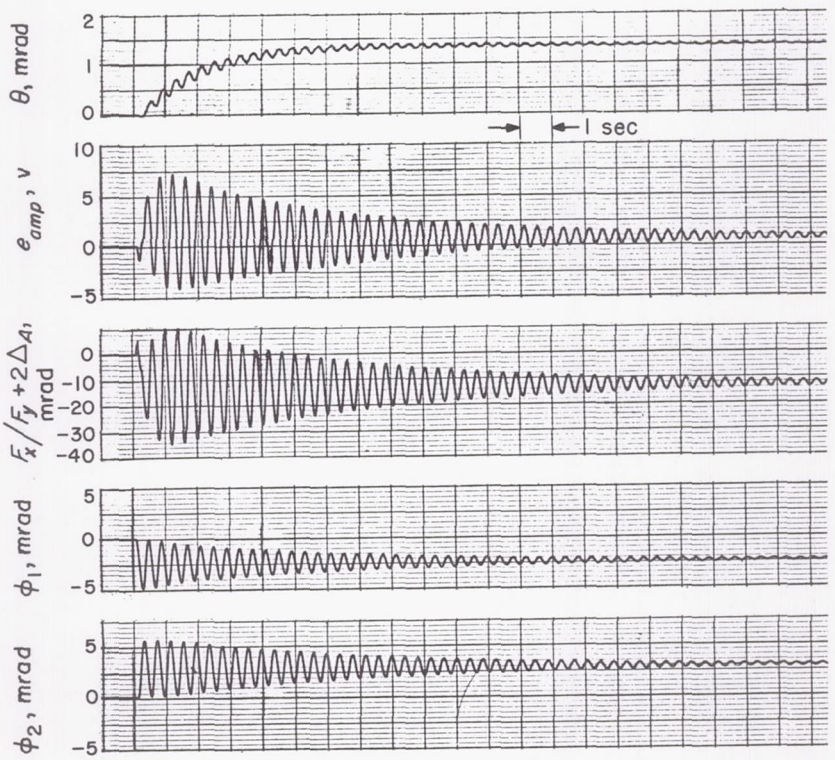

Fig. C-31. Simulated midcourse, yaw axis, $\rho = +5$ mrad, $\Delta_A = -4$ mrad, $\theta_0 = 0$, $\Delta m/m = \Delta I/I = +5\%$, $\Delta k/k = -5\%$

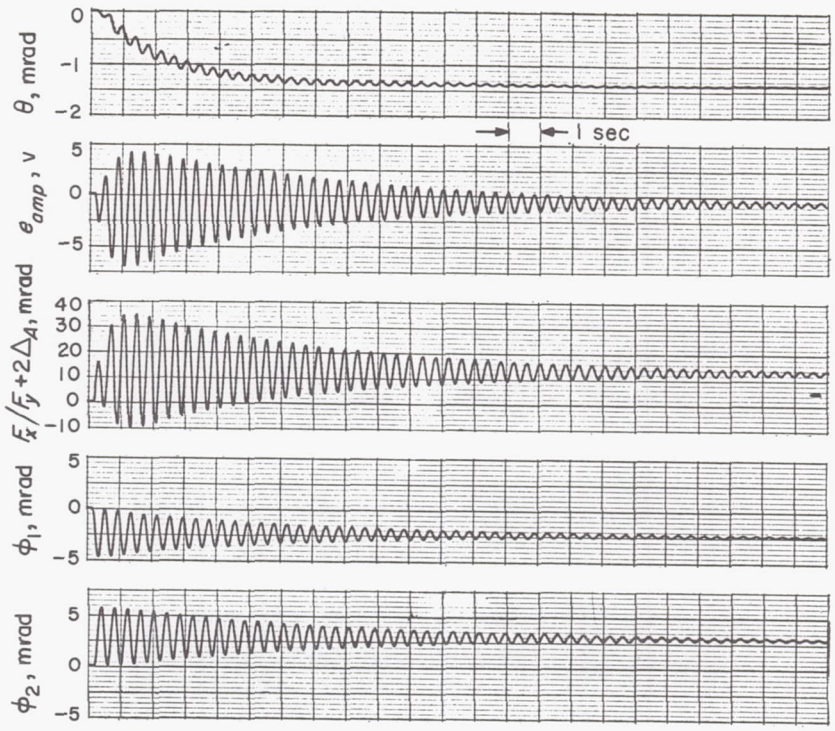

Fig. C-32. Simulated midcourse, yaw axis, $\rho = -5$ mrad, $\Delta_A = +4$ mrad, $\theta_o = 0$, $\Delta m/m = \Delta I/I = +5\%$, $\Delta k/k = -5\%$

a. Parameters. The characteristic parameters of the spacecraft model and the associated gyro and actuator models are written below.

$$M_o = 25 \text{ slugs}$$
$$J_x = J_y = 109 \text{ slug-ft}^2/\text{rad}$$
$$J_1 = J_2 = 6.46 \text{ slug-ft}^2/\text{rad}$$
$$J_3 = 2.37 \text{ slug-ft}^2/\text{rad}$$
$$J_{10} = J_{20} = 10.48 \text{ slug-ft}^2/\text{rad}$$
$$J_{30} = 4.27 \text{ slug-ft}^2/\text{rad}$$

$$N_1 = N_2 = 1.825 \text{ slug-ft}$$
$$N_3 = 0.788 \text{ slug-ft}$$
$$\omega_1^2 = \frac{k_1}{J_1} = \frac{16^2}{\text{sec}^2} = 256 \text{ rad/sec}^2$$
$$\omega_2^2 = \frac{k_3}{J_3} = \frac{18^2}{\text{sec}^2} = 324 \text{ rad/sec}^2$$

Additionally,

$$F_o = 55 \text{ lb}$$
$$K = 16.1 \text{ ft-lb/rad}$$
$$K_L = 7.45 \text{ lb/rad}$$
$$\rho = \pm 5 \text{ mrad}$$
$$\Delta_A = \pm 4 \text{ mrad}$$
$$C_1 = 1.79 \text{ ft}$$

The choice of scale factors for the simulation was:

$$1 \text{ mrad} = 1 \text{ v}$$
$$1 \text{ ft} = 1 \text{ v}$$
$$1 \text{ lb} = 1 \text{ v}$$

b. Model equations. The equations used in this simulation are written below and programmed on the computer based upon the parameters given above.

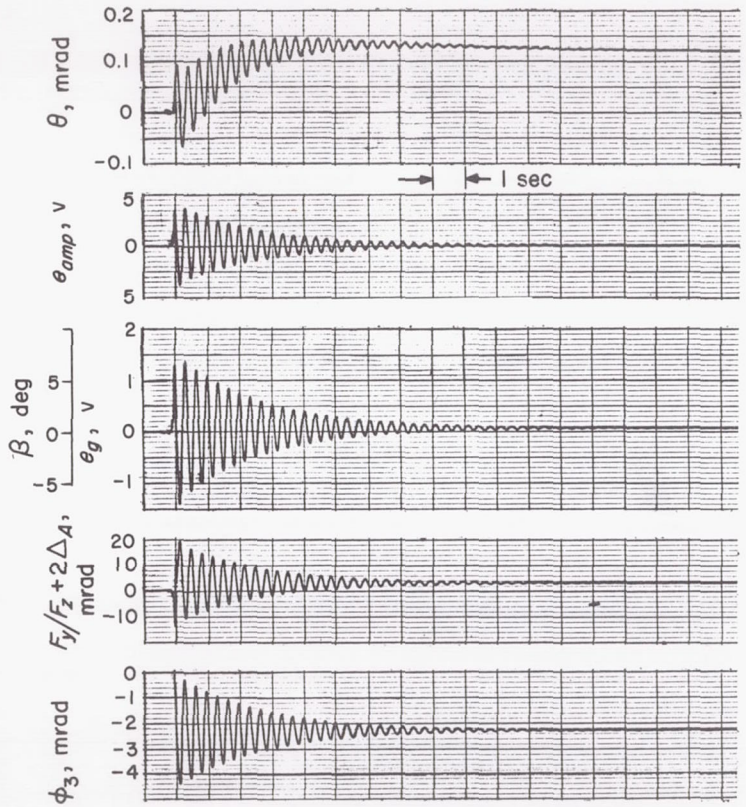

Fig. C-33. Simulated midcourse, pitch axis, $\rho = +5$ mrad, $\Delta_A = +4$ mrad, $\theta_o = 0$

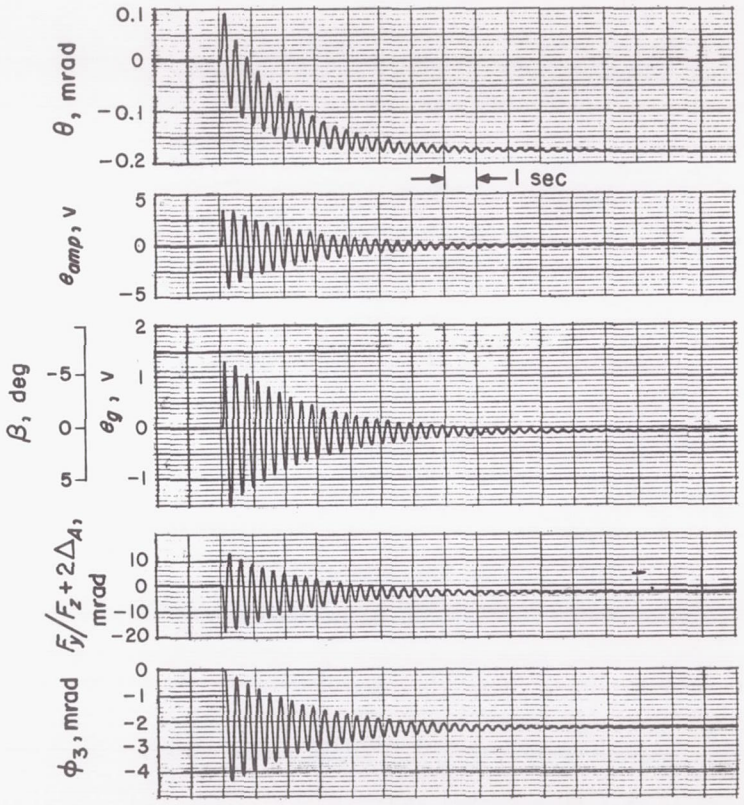

Fig. C-34. Simulated midcourse, pitch axis, $\rho = -5$ mrad, $\Delta_A = -4$ mrad, $\theta_o = 0$

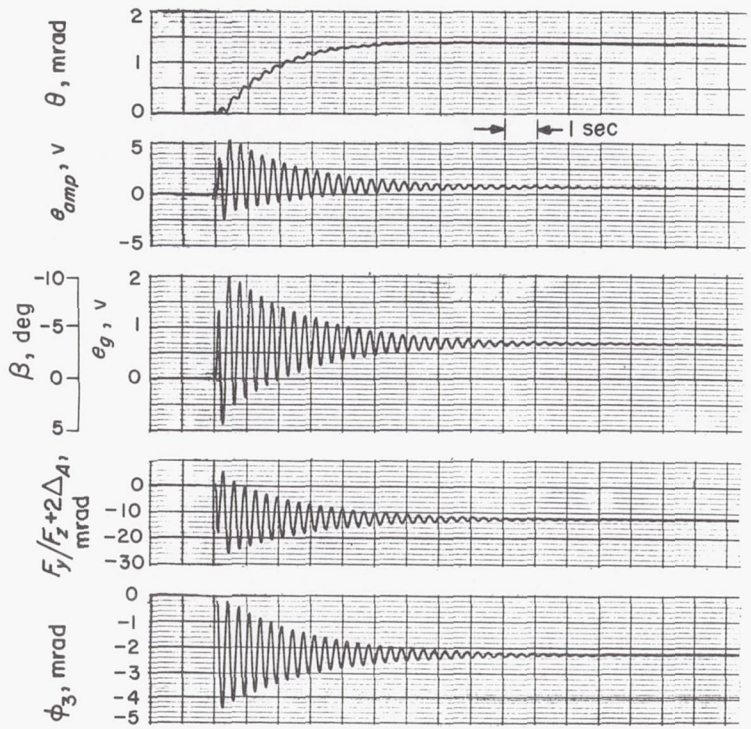

Fig. C-35. Simulated midcourse, pitch axis, $\rho = +5$ mrad, $\Delta_A = -4$ mrad, $\theta_o = 0$

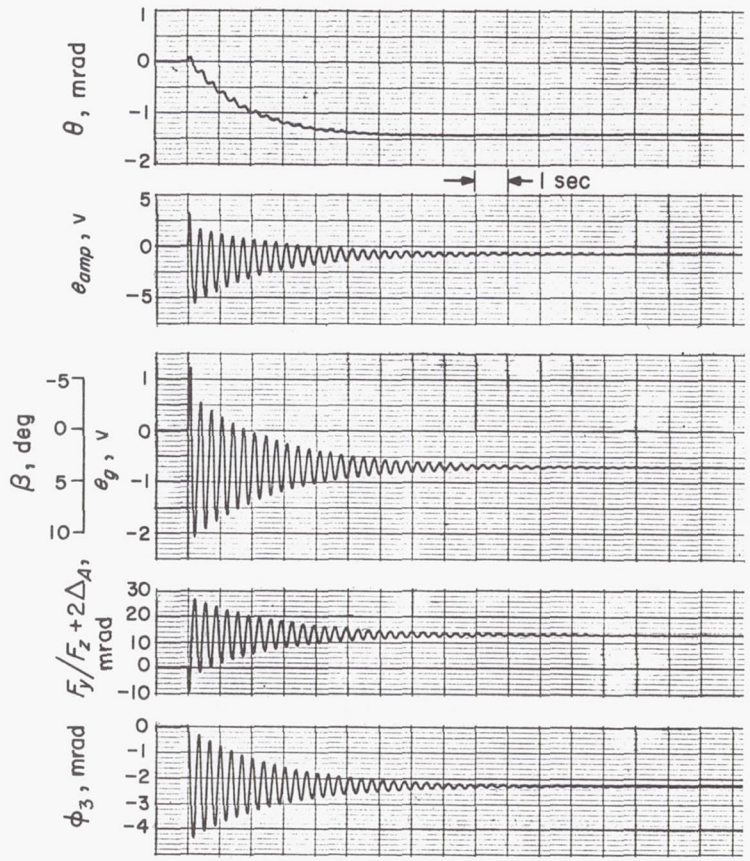

Fig. C-36. Simulated midcourse, pitch axis, $\rho = -5$ mrad, $\Delta_A = +4$ mrad, $\theta_o = 0$

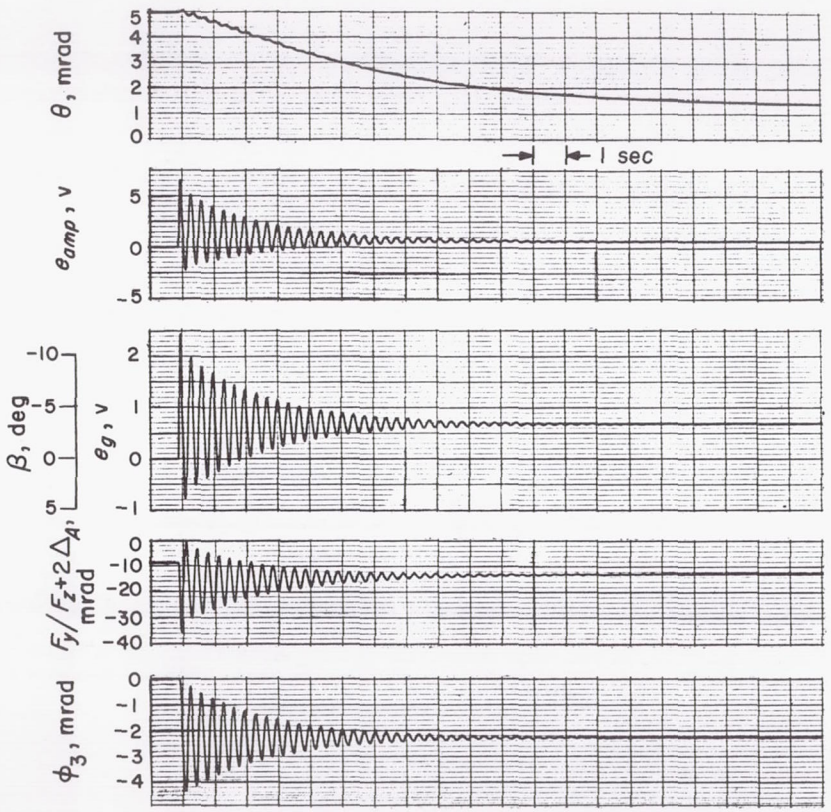

Fig. C-37. Simulated midcourse, pitch axis, $\rho = +5$ mrad, $\Delta_A = -4$ mrad, $\theta_o = 5$ mrad

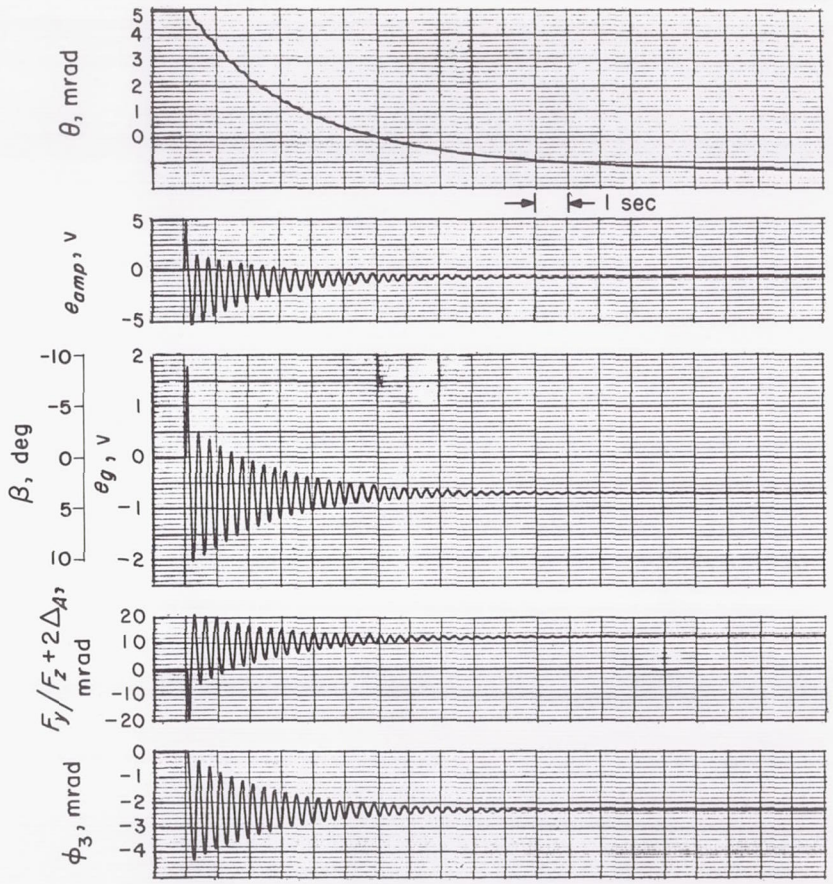

Fig. C-38. Simulated midcourse, pitch axis, $\rho = -5$ mrad, $\Delta_A = +4$ mrad, $\theta_o = 5$ mrad

Spacecraft dynamics. This study was based upon a single axis simulation of the pitch and yaw axes. The equations were developed from the matrices below:

Yaw Axis

$$\begin{bmatrix} F_z \\ \tau_y \\ 0 \\ 0 \\ 0 \\ 0 \end{bmatrix} = \begin{bmatrix} M_o & 0 & N_1 & -N_2 & 0 & 0 \\ 0 & J_y & J_{10} & J_{20} & 0 & 0 \\ N_1 & J_{10} & J_1 & 0 & k_1 & 0 \\ -N_2 & J_{20} & 0 & J_2 & 0 & k_2 \\ 0 & 0 & -1/s^2 & 0 & 1 & 0 \\ 0 & 0 & 0 & -1/s^2 & 0 & 1 \end{bmatrix} \begin{bmatrix} \ddot{z} \\ \ddot{\theta}_y \\ \ddot{\phi}_1 \\ \ddot{\phi}_2 \\ \phi_1 \\ \phi_2 \end{bmatrix} \tag{C-34}$$

Making a change in variable in the angular components of the vector, i.e., $\ddot{\theta}^*$ (rad/sec^2) = 1000 $\ddot{\theta}$ (mrad/sec^2), we have

$$\begin{bmatrix} 0.400F_z \\ 9.174\tau_y \\ 0 \\ 0 \\ 0 \\ 0 \end{bmatrix} = \begin{bmatrix} 10 & 0 & 0.00073 & -0.00073 & 0 & 0 \\ 0 & 1 & 0.0961 & 0.0961 & 0 & 0 \\ 28.25 & 0.1622 & 0.1 & 0 & 25.6 & 0 \\ -28.25 & 0.1622 & 0 & 0.1 & 0 & 25.6 \\ 0 & 0 & -1/s^2 & 0 & 1 & 0 \\ 0 & 0 & 0 & -1/s^2 & 0 & 1 \end{bmatrix} \begin{bmatrix} \ddot{z} \\ \ddot{\theta}_Y^* \\ \ddot{\phi}_1^* \\ \ddot{\phi}_2^* \\ \phi_1^* \\ \phi_2^* \end{bmatrix} \tag{C-35}$$

Pitch Axis

$$\begin{bmatrix} F_z \\ \tau_x \\ 0 \\ 0 \end{bmatrix} = \begin{bmatrix} M_o & 0 & N_3 & 0 \\ 0 & J_x & J_{30} & 0 \\ N_3 & J_{30} & J_3 & k_3 \\ 0 & 0 & -1/s^2 & 1 \end{bmatrix} \begin{bmatrix} \ddot{z} \\ \ddot{\theta}_x \\ \ddot{\phi}_3 \\ \phi_3 \end{bmatrix} \tag{C-36}$$

which reduces to

$$\begin{bmatrix} 0.4000F_z \\ 9.174\tau_x \\ 0 \\ 0 \end{bmatrix} = \begin{bmatrix} 10 & 0 & 0.00031 & 0 \\ 0 & 1 & 0.0391 & 0 \\ 33.3 & 0.18 & 0.1 & 32.4 \\ 0 & 0 & -1/s^2 & 1 \end{bmatrix} \begin{bmatrix} \ddot{z} \\ \ddot{\theta}_x^* \\ \ddot{\phi}_3^* \\ \phi_3^* \end{bmatrix} \tag{C-37}$$

When the solar panel parameters m, l, and k are varied, N_2, J_2, J_{10}, J_{20}, and ω_2^2 are affected. Their approximate relationships are expressed in a matrix form, as follows:

$$\begin{bmatrix} \frac{\Delta N_2}{N_2} \\ \frac{\Delta J_2}{J_2} \\ \frac{\Delta J_{10}}{J_{10}} \\ \frac{\Delta J_{20}}{J_{20}} \\ \frac{\Delta \omega_2^2}{\omega_2^2} \end{bmatrix} = \begin{bmatrix} 1 & 1 & 0 \\ 1 & \frac{2l_1^2}{(\lambda^2 + l_1^2)} & 0 \\ \frac{2m_1 l_1 d_1}{M_o(\lambda^2 + l_1 d_1)} & \frac{m_1}{M_o}\frac{l_1^2}{(\lambda^2 + l_1 d_1)} & 0 \\ 1 & \frac{\frac{(M_o + m_1)}{M_o} l_1^2 + l_1 d_1}{(\lambda^2 + l_1 d_1)} & 0 \\ -1 & \frac{-2l_1^2}{\lambda^2 + l_1^2} & 1 \end{bmatrix} \begin{bmatrix} \frac{\Delta m}{m} \\ \frac{\Delta l}{l} \\ \frac{\Delta k}{k} \end{bmatrix} \tag{C-38}$$

where $N_1 = N_2$, $J_1 = J_2$, $J_{10} = J_{20}$, and $\omega_1 = \omega_2$.

The above matrix is given numerically as the following:

$$[B] = \begin{bmatrix} 1 & 1 & 0 \\ 1 & 1.412 & 0 \\ 0.056 & 0.0127 & 0 \\ 1 & 1.24 & 0 \\ -1 & -1.412 & 1 \end{bmatrix} \tag{C-39}$$

Gyro model. The equation of the gyro loop is given by

$$K_G G_G(s) = \frac{e_g}{\theta} = \frac{505\ \text{v/rad}\left(\frac{s}{0.495} + 1\right)}{\left(\frac{s^2}{62.8^2} + \frac{0.6s}{62.8} + 1\right)} \tag{C-40}$$

Now we can write

$$\frac{e_g}{\theta} = \left(\frac{e_{amp}}{\theta}\right)\left(\frac{e_g}{e_{amp}}\right) \tag{C-41}$$

where

$$\frac{e_{amp}}{\theta} = 0.505\frac{\left(\frac{s}{0.183} + 1\right)}{\left(\frac{s^2}{62.8^2} + \frac{0.6s}{62.8} + 1\right)} \tag{C-42}$$

Therefore,

$$\frac{e_g}{e_{amp}} = \frac{\left(\frac{s}{0.495} + 1\right)}{\left(\frac{s}{0.183} + 1\right)} \tag{C-43}$$

Jet-vane actuator model. The jet-vane actuator is approximated in this analysis by

$$K_a G_a(s) = \frac{\beta}{e_g} = 0.080 \text{ rad/v} \qquad \text{(C-44)}$$

Since this is a constant, the value e_g was directly fed into the spacecraft model.

Forcing functions. The torque and force inputs used to drive the system are developed for both the yaw and pitch axes.

Yaw Axis

$$\begin{bmatrix} F_z \\ \tau_y \end{bmatrix} = \begin{bmatrix} 1 & 0 \\ C_1(\rho - \Delta_A) & -K_L \end{bmatrix} \begin{bmatrix} F_o \\ \beta_y \end{bmatrix} \qquad \text{(C-45)}$$

$$F_x = (\theta + \Delta_A) F_o + K_\tau \beta_y \qquad \text{(C-46)}$$

Pitch Axis

$$\begin{bmatrix} F_z \\ \tau_x \end{bmatrix} = \begin{bmatrix} 1 & 0 \\ C_1(\rho - \Delta_A) & -K_L \end{bmatrix} \begin{bmatrix} F_o \\ \beta_x \end{bmatrix} \qquad \text{(C-47)}$$

$$F_y = -(\theta + \Delta_A) F_o - K_\tau \beta_x \qquad \text{(C-48)}$$

The inputs to the spacecraft model are generated by substituting the parameters given in this Appendix C, 4. The equations are:

$$\begin{bmatrix} F_z \\ \tau_{y,x} \end{bmatrix} = \begin{bmatrix} 1 & 0 \\ \dfrac{1.79(\rho - \Delta_A)}{1000} & -1.288 \end{bmatrix} \begin{bmatrix} F_o \\ e_g \end{bmatrix} \qquad \text{(C-49)}$$

$$F_x = \left(\frac{\theta + \Delta_A}{1000}\right) F_o + 0.596 e_{g_y} \qquad \text{(C-50)}$$

$$F_y = -\left(\frac{\theta + \Delta_A}{1000}\right) F_o - 0.596 e_{g_x} \qquad \text{(C-51)}$$

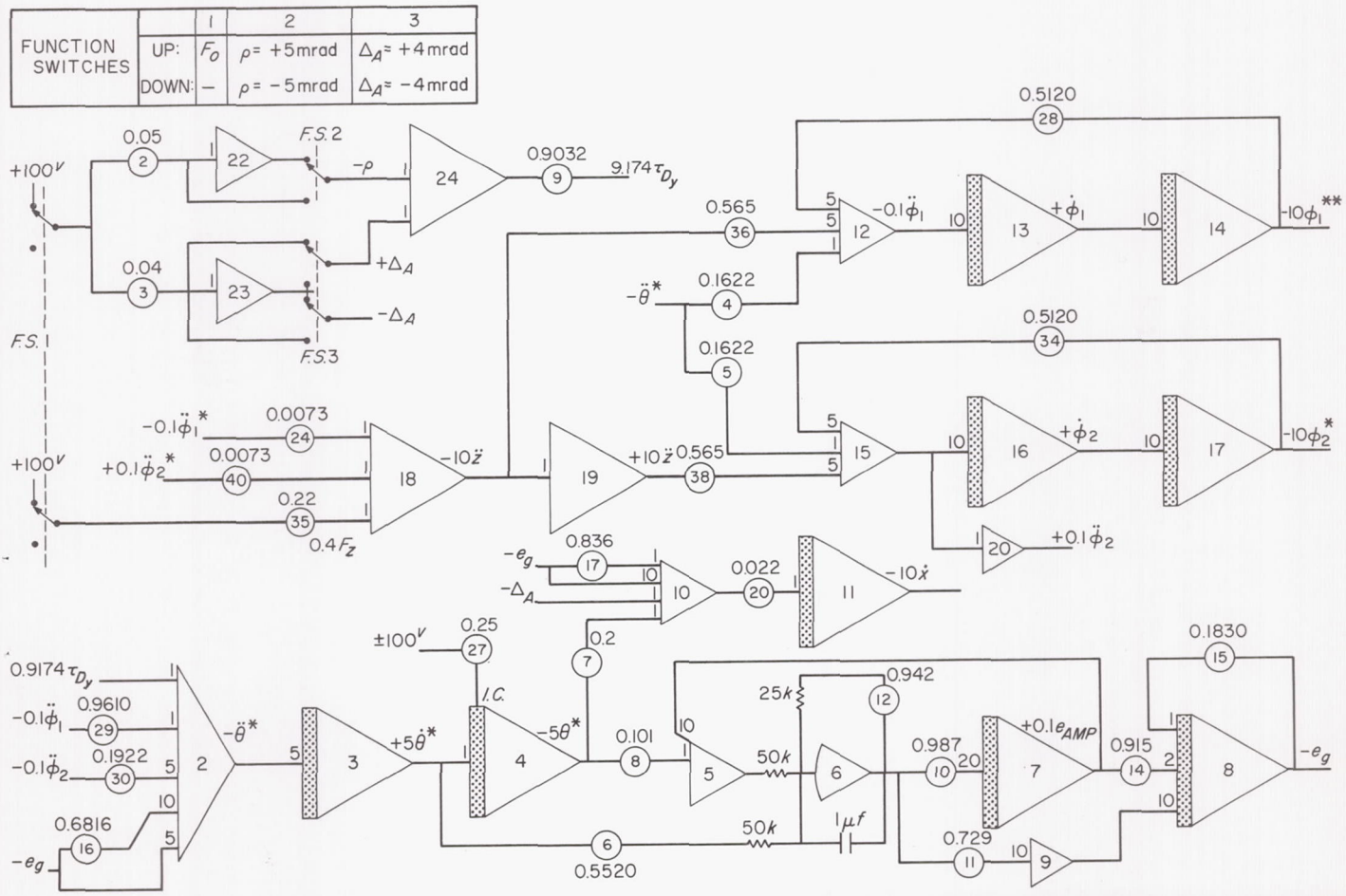

Fig. C-39. Autopilot simulation, yaw axis

c. Computer model and potentiometer settings. The mechanization of the equations given above is shown in Fig. C-39 and C-40. The potentiometer settings are given in Tables C-1 and C-2.

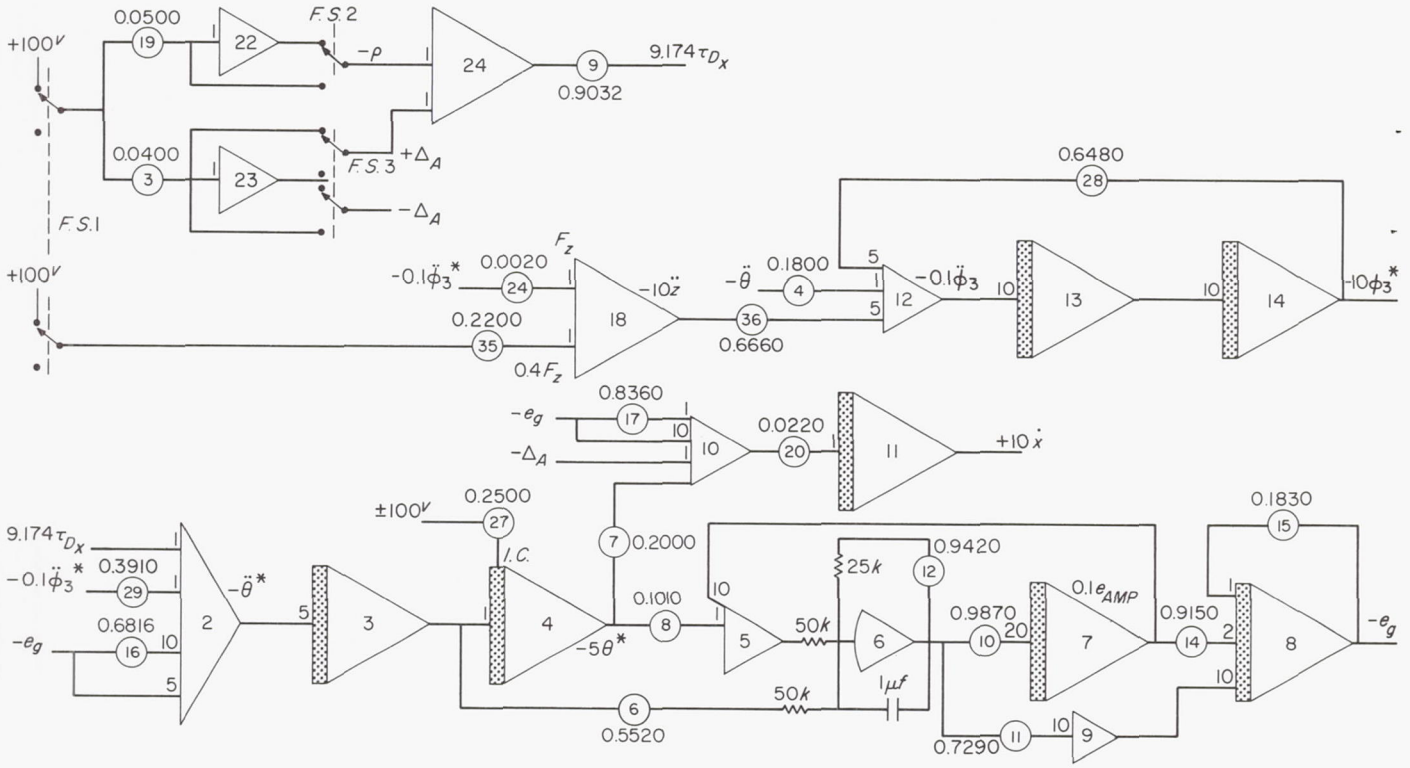

Fig. C-40. Autopilot simulation, pitch axis

Table C-1. Potentiometer settings, pitch axis

Potentiometer	Setting	Potentiometer	Setting
3	0.0400	16	0.6816
4	0.1800	17	0.8360
6	0.5520	19	0.0500
7	0.2000	20	0.0220
8	0.1010	24	0.0020
9	0.9032	27	0.2500
10	0.9870	28	0.6480
11	0.7290	29	0.3910
12	0.9420	35	0.2200
14	0.9150	36	0.6660
15	0.1830		

Table C-2. Potentiometer settings, yaw axis

Potentiometer number	Identical solar panels	$\frac{\Delta M}{M} = +5\%$	$\frac{\Delta I}{I} = +5\%$	$\frac{\Delta k}{k} = +5\%$	$\frac{\Delta M}{M} = +5\%$ $\frac{\Delta I}{I} = +5\%$ $\frac{\Delta k}{k} = +5\%$	$\frac{\Delta M}{M} = +5\%$ $\frac{\Delta I}{I} = +5\%$ $\frac{\Delta k}{k} = -5\%$
2	0500					
3	0400					
4	1622	1627	1623	(1622)	1628	1628
5	1622	(1622)	1609	(1622)	1609	1609
6	5520					
7	2000					
8	1010					
9	9032					
10	9870					
11	7290					
12	9420					
14	9150					
15	1830					
16	6816					
17	8360					
20	0220					
24	0073					
27	2500					
28	5120					
29	9610	9637	9616	(9610)	9643	9643
30	1922	2018	2041	(1922)	2143	2143
34	5120	4877	4782	5376	4782	4327
35	2200					
36	5650					
38	5650	(5650)	5542	(5650)	5542	5542
40	0073					

APPENDIX D

Error Analyses

A measure of the accuracy of changing from one trajectory to another is derived by combining all possible errors into an equation defining the re-orientation of the vehicle and substituting the known system errors into the equation. Thus, the statistical error in the sense of the 3-σ variations may be obtained and applied toward such things as the pointing vector, resolution, and velocity increment. The error analysis for both the midcourse and terminal maneuver are developed in this appendix and the results are interpreted in terms of the physical quantities, such as the displacement error introduced by the maneuver.

This appendix is divided into two sections: the first discusses the analysis of the midcourse maneuver; the terminal maneuver is described in the second part.

1. Midcourse Maneuver Analysis

As was indicated in Section III (Trajectory Corrections) of this Report, the midcourse rocket is not ignited until the commanded turns have been completed. Prior to the maneuver, the roll axis is kept pointed toward the Sun by a two-axis (pitch and yaw) Sun sensor, and the roll axis is controlled by an Earth sensor error signal.

The midcourse maneuver is initiated by first breaking the Earth lock (with the Sun sensor still controlling pitch and yaw), and rolling to the pre-computed angle. The spacecraft then goes under inertial control (Sun sensor control broken), and the pitch turn is performed.

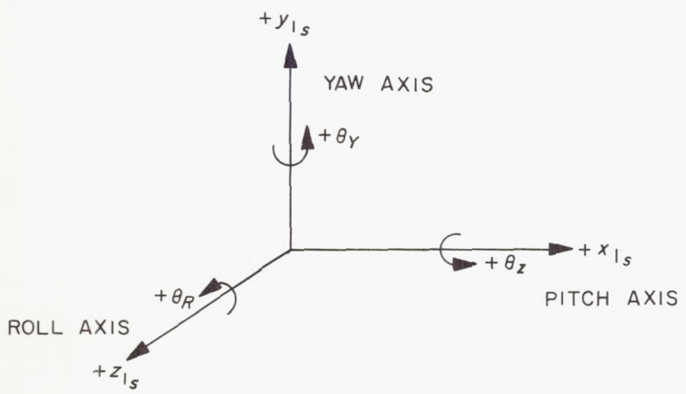

Fig. D-1. Midcourse maneuver coordinates

a. Coordinate notation. The following parameters define the coordinate system and describe the relationships between the various rotations of the spacecraft (see Fig. D-1 and Table D-1).

b. Roll turn analysis. The direction of the spacecraft body axes is known with respect to inertial space, and forms an orthogonal right-handed coordinate system. The spacecraft is assumed to be in a limit-cycle oscillation during the roll maneuver. The standard roll turn, including only the commanded-turn error, is described below.

If $\mathbf{W}_{1_s}$ is a vector which represents the initial orthogonal set of coordinates

$$\begin{bmatrix} x_1 \\ y_1 \\ z_1 \end{bmatrix}_s$$

then a new set of spacecraft body coordinates is defined by

$$\mathbf{W}_{2_s} = [\Theta_R]\,\mathbf{W}_{1_s} \qquad \text{(D-1)}$$

Table D-1. Midcourse maneuver parameter description

Parameter	Description
x_j, y_j, z_j	Spacecraft body-axis coordinates (pitch, yaw, and roll axes) where the index j indicates the following: $j = 1$: axes before any turn $j = 2$: axes after the roll turn $j = 3$: axes after the pitch turn j_s: standard or initial coordinates
$\mathbf{W} = \begin{bmatrix} x \\ y \\ z \end{bmatrix}$	A vector in x, y, z coordinates
θ_i	Standard angle, where the index i indicates a rotation about the following: P = pitch Y = yaw R = roll
$\Delta\theta_i$	Initial angle errors due to the spacecraft limit cycle
$\delta\theta_i$	Commanded-turn errors
Θ_i	Standard-turn matrix
Φ_i	Turn matrix with errors
Λ	Matrix of initial angle errors due to the spacecraft limit cycle

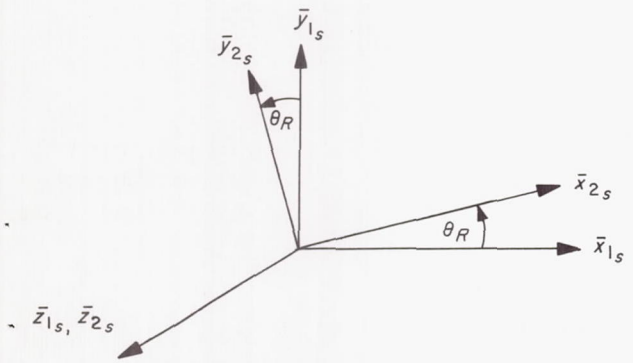

Fig. D-2. Coordinate transformation due to a roll maneuver

where, from Fig. D-2,

$$[\Theta_R] = \begin{bmatrix} \cos\theta_R & \sin\theta_R & 0 \\ -\sin\theta_R & \cos\theta_R & 0 \\ 0 & 0 & 1 \end{bmatrix} \tag{D-2}$$

and

$$\mathbf{W}_{2_s} = \begin{matrix} x_2 \\ y_2 \\ z_2 \end{matrix}\Bigg]_s$$

define the spacecraft orientation after an error-free roll maneuver.

Assuming that the commanded roll turn contributes incremental angular errors, then the error-laden turn matrix is defined as

$$[\Phi_R] = \begin{bmatrix} \cos(\theta_R + \delta\theta_R) & \sin(\theta_R + \delta\theta_R) & 0 \\ -\sin(\theta_R + \delta\theta_R) & \cos(\theta_R + \delta\theta_R) & 0 \\ 0 & 0 & 1 \end{bmatrix} \tag{D-3}$$

Therefore, the position of the vehicle after the turn is given by

$$\mathbf{W}_{2_{Turn}} = [\Phi_R]\,\mathbf{W}_{1_s} \tag{D-4}$$

so that

$$\mathbf{W}_{2_{Turn}} = \begin{matrix} x_2 \\ y_2 \\ z_2 \end{matrix}\Bigg]_{Turn} = \begin{bmatrix} \cos(\theta_R + \delta\theta_R) & \sin(\theta_R + \delta\theta_R) & 0 \\ -\sin(\theta_R + \delta\theta_R) & \cos(\theta_R + \delta\theta_R) & 0 \\ 0 & 0 & 1 \end{bmatrix} \begin{matrix} x_1 \\ y_1 \\ z_1 \end{matrix}\Bigg]_s \tag{D-5}$$

However, the above expression does not completely express the new coordinates. Displacement errors, introduced by the limit-cycle oscillation about each of the major axes, must be included. Figure D-3 shows the additional error which must be added due to roll, pitch, and yaw errors. The error matrix $[\Lambda]$ is defined in Eq. (D-7).

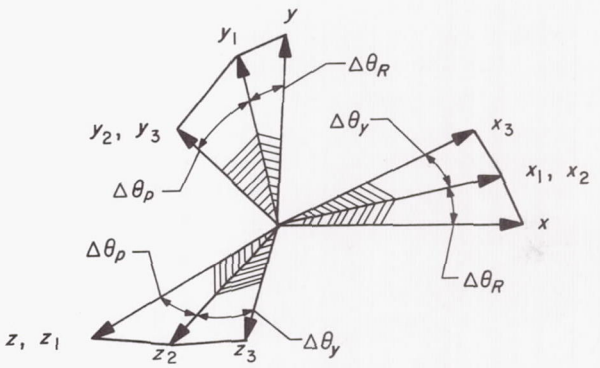

Fig. D-3. Errors due to a roll, pitch, and yaw limit cycle

Finally, the new set of coordinates is given by the equation

$$\mathbf{W}_2 = [\Lambda]\,\mathbf{W}_{2_{Turn}} \tag{D-6}$$

where

$$[\Lambda] = \begin{bmatrix} +\cos\Delta\theta_Y(\cos\Delta\theta_R) - \sin\Delta\theta_Y\sin\Delta\theta_P\sin\Delta\theta_R & +\cos\Delta\theta_Y\sin\Delta\theta_R + \sin\Delta\theta_Y\sin\Delta\theta_P\cos\Delta\theta_R & -\sin\Delta\theta_Y\cos\Delta\theta_P \\ -\cos\Delta\theta_P\sin\Delta\theta_R & \cos\Delta\theta_P\cos\Delta\theta_R & \sin\Delta\theta_P \\ +\cos\Delta\theta_Y\sin\Delta\theta_P\sin\Delta\theta_R + \sin\Delta\theta_Y\cos\Delta\theta_R & -\cos\Delta\theta_Y\sin\Delta\theta_P\cos\Delta\theta_R + \sin\Delta\theta_Y\sin\Delta\theta_R & +\cos\Delta\theta_Y\cos\Delta\theta_P \end{bmatrix} \tag{D-7}$$

By assuming small perturbations, $\sin\theta \simeq \theta$, $\cos\theta \simeq 1$, and the product $\sin\theta_1 \sin\theta_2 \simeq 0$. Therefore, the coordinates are given by

$$\mathbf{W}_2 = [\Lambda]\,[\Phi_R]\,\mathbf{W}_{1_s} \tag{D-8}$$

and, by substitution,

$$\mathbf{W}_2 = \begin{bmatrix} X_2 \\ Y_2 \\ Z_2 \end{bmatrix} = \begin{bmatrix} 1 & \Delta\theta_R & \Delta\theta_Y \\ -\Delta\theta_R & 1 & \Delta\theta_P \\ \Delta\theta_Y & -\Delta\theta_P & 1 \end{bmatrix} \begin{bmatrix} \cos(\theta_R + \delta\theta_R) & \sin(\theta_R + \delta\theta_R) & 0 \\ -\sin(\theta_R + \delta\theta_R) & \cos(\theta_R + \delta\theta_R) & 0 \\ 0 & 0 & 1 \end{bmatrix} \begin{bmatrix} X_1 \\ Y_1 \\ Z_1 \end{bmatrix}_s \tag{D-9}$$

If the commanded turn errors $\delta\theta_R$ are very small, they may be included with the roll limit-cycle errors so that Eq. (D-9) is written as

$$\mathbf{W}_2 = [\Lambda + \delta\Theta_R]\,[\Theta_R]\,\mathbf{W}_{1_s} \tag{D-10}$$

$$\mathbf{W}_2 = \begin{bmatrix} X_2 \\ Y_2 \\ Z_2 \end{bmatrix} = \begin{bmatrix} 1 & (\Delta\theta_R + \delta\theta_R) & -\Delta\theta_Y \\ -(\Delta\theta_R + \delta\theta_R) & 1 & \Delta\theta_P \\ \Delta\theta_Y & -\Delta\theta_P & 1 \end{bmatrix} \begin{bmatrix} \cos\theta_R & \sin\theta_R & 0 \\ -\sin\theta_R & \cos\theta_R & 0 \\ 0 & 0 & 1 \end{bmatrix} \begin{bmatrix} X_1 \\ Y_1 \\ Z_1 \end{bmatrix}_s \tag{D-11}$$

Equation (D-11) is the position of the spacecraft coordinates, after the commanded-roll turn referred back to the initial set of axes.

c. Pitch-turn analysis. Upon completion of the roll maneuver, the gyros take over control of the pitch and yaw attitude, and the Sun sensor error signal no longer controls the spacecraft. The pitch maneuver is executed by commanding a specific gyro turn rate. The turn is made about the coordinates defined in Eq. (D-10) and shown in Fig. D-4.

The pitch gyro input axis is assumed to be offset from the pitch axis by the angles ε_R and $-\varepsilon_Y$ about the roll and yaw axes, respectively.

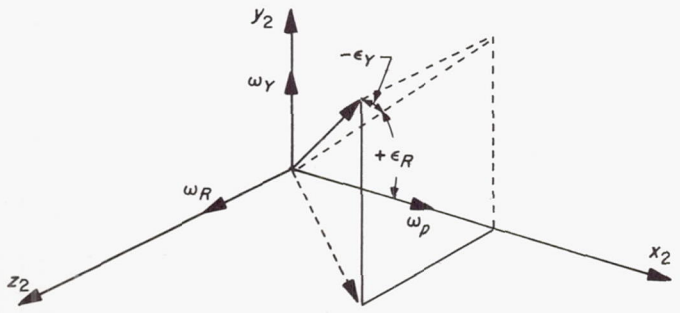

Fig. D-4. Pitch maneuver orientation

Additional errors are introduced by gyro drift rates ω_R, ω_P, and ω_Y. The commanded pitch rate for the gyro controlled turn is $\dot{\theta}_P$.

The total angular rate is therefore given by the vector

$$\begin{aligned} \dot{\boldsymbol{\theta}}_P = {} & (\dot{\theta}_P \cos(+\varepsilon_Y)\cos(-\varepsilon_R) + \omega_P)\,\mathbf{x} \\ & + (\dot{\theta}_P \cos(+\varepsilon_Y)\sin(-\varepsilon_R) + \omega_Y)\,\mathbf{y} \\ & + (\dot{\theta}_P \sin(+\varepsilon_Y) + \omega_R)\mathbf{z} \end{aligned} \tag{D-12}$$

Small perturbation analysis. An infinitesimal rotation is an orthogonal transformation of coordinate axes in which the components of a vector are almost the same in both sets of axes; the change is infinitesimal, as shown in Eq. (D-13) for Fig. D-5:

$$\mathbf{x}_1' = \mathbf{x}_1 + [\varepsilon_{11}\mathbf{x}_1 + \varepsilon_{12}\mathbf{x}_2 + \varepsilon_{13}\mathbf{x}_3] \tag{D-13}$$

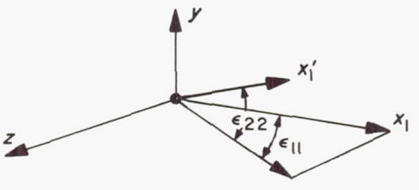

Fig. D-5. Infinitesimal rotations

The matrix elements ε_{11}, ε_{12}, ε_{13} are considered to be infinitesimals; hence, in subsequent calculation, only the first nonvanishing order in ε_{ij} needs to be retained. For any general component x'_1, the equations of the perturbed transformation can be written as

$$\mathbf{X}'_i = \mathbf{X}_i + \sum_j [\varepsilon_{ij}]\,\mathbf{X}_j$$

or

$$\mathbf{X}'_i = \sum_j [\delta_{ij} + \varepsilon_{ij}]\,\mathbf{X}_j \qquad \text{(D-14)}$$

where δ_{ij} is the element of the unit matrix and appears in matrix notation as

$$\mathbf{X}' = [1 + \varepsilon]\,\mathbf{X} \qquad \text{(D-15)}$$

Now Eq. (D-14) states that the typical form for the matrix of an infinitesimal transformation is $[1 + \varepsilon]$, i.e., it is almost the identical transformation differing at most by an infinitesimal operator.

It can be seen that the sequence of rotations is unimportant for infinitesimal transformations; in other words, they commute. An example of this is shown below. If

$$[A_1]\,[A_2] = [1 + \varepsilon_1]\,[1 + \varepsilon_2] = 1^2 + \varepsilon_1 + \varepsilon_2 + \varepsilon_1\varepsilon_2$$

then, by neglecting higher-order terms,

$$[A_1]\,[A_2] = 1 + \varepsilon_1 + \varepsilon_2 = [I] + [\varepsilon] \qquad \text{(D-16)}$$

where

$$[I] = \begin{bmatrix} 1 & 0 & 0 \\ 0 & 1 & 0 \\ 0 & 0 & 1 \end{bmatrix} \qquad \text{(D-17)}$$

and

$$[\varepsilon] = \begin{bmatrix} 0 & \varepsilon_1 & \varepsilon_2 \\ -\varepsilon_1 & 0 & 0 \\ -\varepsilon_2 & 0 & 0 \end{bmatrix} \qquad \text{(D-18)}$$

The diagonal elements of ε are zero, and the nonvanishing off-diagonal elements are the negative of the elements situated symmetrically across the diagonal. A matrix with these characteristics is said to be antisymmetric or skew-symmetric. This property is not peculiar to the particular matrix considered; for the ε matrix of every infinitesimal rotation is antisymmetric. The quantities ε_1 and ε_2 are clearly to be identified with the two independent parameters specifying the rotation. These two quantities also form the components of a vector. Applying the above analysis to the Pitch-Turn Analysis section of this Appendix, simplifies the expression for the pitch-turn vector.

Pitch turn—small perturbations. Now Eq. (D-12) can be rewritten as

$$\dot{\boldsymbol{\theta}}'_p = (\dot{\theta}_p + \omega_p)\,\mathbf{x} + (-\dot{\theta}_p\varepsilon_R + \omega_Y)\,\mathbf{y} + (\dot{\theta}_p\varepsilon_Y + \omega_R)\,\mathbf{z} \qquad \text{(D-19)}$$

Factoring Eq. (D-19) and assuming that $\dot{\theta} > \omega_p$,

$$\dot{\theta}'_p = (\dot{\theta}_p + \omega_p)\left\{\mathbf{x} + \left(-\varepsilon_R + \frac{\omega_Y}{\dot{\theta}_p}\right)\mathbf{y} + \left(+\varepsilon_Y + \frac{\omega_R}{\dot{\theta}_p}\right)\mathbf{z}\right\} \qquad \text{(D-20)}$$

The vector within the brackets in Eq. (D-20) can be identified as the pitch-turn axis. Now if we let

$$\varepsilon_1 = \left(-\varepsilon_R + \frac{\omega_Y}{\dot{\theta}_p}\right)$$

and (D-21)

$$\varepsilon_2 = \left(\varepsilon_Y + \frac{\omega_R}{\dot{\theta}_p}\right)$$

then a skew-symmetric matrix of the turn axis can be formulated in the same format as Eq. (D-16); hence, we can let

$$[T_p] = [I] + [\varepsilon] \qquad \text{(D-22)}$$

Now the pitch-turn matrix is defined as

$$[\Phi_P] = [T_P]^{-1}\,[\Theta_P + \delta\theta_P]\,[T_P] \qquad \text{(D-23)}$$

where

Θ_P = pitch-turn angle matrix

$\delta\theta_P$ = pitch angular-error matrix due to pitch command

This equation may be reduced by assuming small perturbations and neglecting higher-order terms; therefore,

$$
\begin{aligned}
[\Phi_P] &= [1-\varepsilon]\,[\Theta_P + \delta\Theta_P]\,[1+\varepsilon] \\
&= \{[1-\varepsilon]\,[\Theta_P] + [\delta\Theta_P] - [\varepsilon]\,[\delta\Theta_P]\}\,[1+\varepsilon] \\
&= [1-\varepsilon]\,[\Theta_P]\,[1+\varepsilon] + [\delta\Theta_P] - [\varepsilon]\,[\delta\overset{o}{\Theta}_P] \\
&\quad + [\delta\overset{o}{\Theta}_P]\,[\varepsilon] - [\varepsilon]\,[\delta\overset{o}{\Theta}_P]\,[\varepsilon] \\
&= [\Theta_P] + [\Theta_P]\,[\varepsilon] - [\varepsilon]\,[\Theta_P] \\
&\quad - [\varepsilon]\,[\overset{o}{\Theta}_P]\,[\varepsilon] + [\delta\Theta_P] \qquad \text{(D-24)}
\end{aligned}
$$

and

$$
[\Phi_P] = [\Theta_P] + [\Theta_P\varepsilon - \varepsilon\Theta_P + \delta\Theta_P] \qquad \text{(D-25)}
$$

The last three terms of the above expression represent the errors added to the pitch turn and are given by

$$
[\Delta\Theta_P] = [\Theta_P\varepsilon - \varepsilon\Theta_P + \delta\Theta_P] \qquad \text{(D-26)}
$$

The first term expresses the error-free pitch-turn matrix which is shown in Fig. D-6 and is given by

$$
\mathbf{W}_{3_s} = [\Theta_P]\,\mathbf{W}_2 \qquad \text{(D-27)}
$$

where

$$
[\Theta_P] = \begin{bmatrix} 1 & 0 & 0 \\ 0 & \cos\theta_P & \sin\theta_P \\ 0 & -\sin\theta_P & \cos\theta_P \end{bmatrix} \qquad \text{(D-28)}
$$

Therefore, the turn matrix is given by the expression

$$
[\Phi_P] = [\Theta_P] + [\Delta\Theta_P] \qquad \text{(D-29)}
$$

Now if the assumption were made that the turn contained errors due to the command, then

$$
\begin{bmatrix} x_3 \\ y_3 \\ z_3 \end{bmatrix} = \begin{bmatrix} 1 & 0 & 0 \\ 0 & \cos(\theta_P + \delta\theta_P) & \sin(\theta_P + \delta\theta_P) \\ 0 & -\sin(\theta_P + \delta\theta_P) & \cos(\theta_P + \delta\theta_P) \end{bmatrix} \begin{bmatrix} x_2 \\ y_2 \\ z_2 \end{bmatrix} \qquad \text{(D-30)}
$$

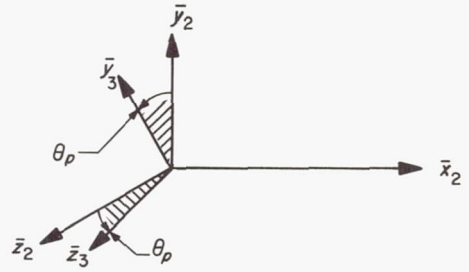

Fig. D-6. Coordinate transformation due to a pitch turn

The above matrix is expanded into the sum of two matrices (small angle approximations are again assumed). Therefore,

$$
\begin{bmatrix} x_3 \\ y_3 \\ z_3 \end{bmatrix} = \left\{ \begin{bmatrix} 1 & 0 & 0 \\ 0 & \cos\theta_P & \sin\theta_P \\ 0 & -\sin\theta_P & \cos\theta_P \end{bmatrix} + \begin{bmatrix} 0 & 0 & 0 \\ 0 & -\sin\theta_P\,\delta\theta_P & \cos\theta_P\,\delta\theta_P \\ 0 & -\cos\theta_P\,\delta\theta_P & -\sin\theta_P\,\delta\theta_P \end{bmatrix} \right\} \begin{bmatrix} x_2 \\ y_2 \\ z_2 \end{bmatrix} \qquad \text{(D-31)}
$$

where $[\Theta_P]$ = Eq. (D-28)

$$
[\delta\Theta_P] = \begin{bmatrix} 0 & 0 & 0 \\ 0 & -\sin\theta_P\,\delta\theta_P & \cos\theta_P\,\delta\theta_P \\ 0 & -\cos\theta_P\,\delta\theta_P & -\sin\theta_P\,\delta\theta_P \end{bmatrix} \qquad \text{(D-32)}
$$

and

$$
\mathbf{W}_3 = ([\Theta_P] + [\Delta\Theta_P])\,\mathbf{W}_2 \qquad \text{(D-33)}
$$

In order to completely define the pitch turn, the matrix $\Delta\Theta_P$ must be determined. Substitution of Eq. (D-18), (D-21), (D-28) and (D-32) into Eq. (D-26) yields the following solution:

$$
[\Delta\Theta_P] = \begin{bmatrix} 0 & \varepsilon_1(1-\cos\theta_P) + \varepsilon_2\sin\theta_P & -\varepsilon_1\sin\theta_P + \varepsilon_2(1-\cos\theta_P) \\ \varepsilon_1(1-\cos\theta_P) - \varepsilon_2\sin\theta_P & -\sin\theta_P\,\delta\theta_P & \cos\theta_P\,\delta\theta_P \\ \varepsilon_1\sin\theta_P + \varepsilon_2(1-\cos\theta_P) & -\cos\theta_P\,\delta\theta_P & -\sin\theta_P\,\delta\theta_P \end{bmatrix} \qquad \text{(D-34)}
$$

Equation (D-34) specifies the position of the spacecraft after the pitch maneuver with respect to the coordinates defining the location of the vehicle in inertial space, following the roll maneuver. The final position of the vehicle with respect to the initial set of coordinates is of actual interest and is given by substituting Eq. (D-10) into (D-33). Hence,

$$\mathbf{W}_3 = [\Theta_P + \Delta\Theta_P]\,\{[\Lambda + \delta\Theta_R]\,[\Theta_R]\,\mathbf{W}_{1_s}\} \tag{D-35}$$

Ideally, if both the roll and pitch turns could be executed without producing errors of any type, then the coordinates following the turn would be given by

$$W_{3_s} = [\Theta_P]\,[\Theta_R]\,W_{1_s} \tag{D-36}$$

Rewriting Eq. (D-36) with respect to the standard pre-maneuver coordinates

$$\mathbf{W}_{1_s} = [\Theta_R]^{-1}\,[\Theta_P]^{-1}\,\mathbf{W}_{3_s} \tag{D-37}$$

and substituting into Eq. (D-35), the actual post maneuver is given in terms of error matrices, the actual commanded turns, and the desired post maneuver coordinates, as shown below:

$$\mathbf{W}_3 = [\Theta_P + \Delta\Theta_P]\,[\Lambda + \delta\Theta_R]\,[\Theta_R]\,[\Theta_R]^{-1}\,[\Theta_P]^{-1}\,\mathbf{W}_{3_s} \tag{D-38}$$

It follows that

$$\mathbf{W}_3 = \{[\Theta_P]\,[\Lambda + \delta\Theta_R]\,[\Theta_P]^{-1} + [\Delta\Theta_P]\,[\Lambda + \delta\Theta_R]\,[\Theta_P]^{-1}\}\,\mathbf{W}_{3_s} \tag{D-39}$$

and from Eq. (D-10) and (D-11),

$$[\Lambda + \delta\theta_R] = \begin{bmatrix} 1 & (\Delta\theta_R + \delta\theta_R) & -\Delta\theta_Y \\ -(\Delta\theta_R + \delta\theta_R) & 1 & \Delta\theta_P \\ \Delta\theta_Y & -\Delta\theta_P & 1 \end{bmatrix}$$

$$= \begin{bmatrix} 1 & 0 & 0 \\ 0 & 1 & 0 \\ 0 & 0 & 1 \end{bmatrix} + \begin{bmatrix} 0 & (\Delta\theta_R + \delta\theta_R) & -\Delta\theta_Y \\ -(\Delta\theta_R + \delta\theta_R) & 0 & \Delta\theta_P \\ \Delta\theta_Y & -\Delta\theta_P & 0 \end{bmatrix} \tag{D-40}$$

The above expression has the form

$$[\Lambda + \delta\Theta_R] = \begin{bmatrix} 1 & 0 & 0 \\ 0 & 1 & 0 \\ 0 & 0 & 1 \end{bmatrix} + \begin{bmatrix} 0 & \xi_R & -\xi_Y \\ -\xi_R & 0 & \xi_P \\ \xi_Y & -\xi_P & 0 \end{bmatrix} \tag{D-41}$$

$$[\Lambda + \delta\Theta_R] = [I] + [\varepsilon_T] \tag{D-42}$$

where

$[I]$ = the identity matrix

$[\varepsilon_T]$ = matrix of errors due to the maneuvers

Equation (D-42) is now substituted into only the second part of Eq. (D-39) in order to reduce the expression by eliminating higher-order terms; therefore,

$$\mathbf{W}_3 = \{[\Theta_P]\,[\Lambda + \delta\Theta_R]\,[\Theta_P]^{-1} + [\Delta\Theta_P]\,[I + \varepsilon_T]\,[\Theta_P]^{-1}\}\,\mathbf{W}_{3_s} \tag{D-43}$$

Equation (D-43) reduces to

$$\mathbf{W}_3 = \{[\Theta_P]\,[\Lambda + \delta\Theta_R]\,[\Theta_P]^{-1} + [\Delta\Theta_P]\,[\Theta_P]^{-1}\}\,\mathbf{W}_{3_s} \tag{D-44}$$

where

Θ_P = commanded pitch-turn angle

Λ = angular errors due to the limit cycle

$\delta\Theta_R$ = errors due to the roll command

$\Delta\Theta_P$ = offset errors due to the pitch command

$\mathbf{W}_{3_s}$ = position of the spacecraft for error-free turns

The above expression may be simply written in matrix notation as

$$\mathbf{W}_3 = [A]\,\mathbf{W}_{3_s} \tag{D-45}$$

where, upon the proper substitution,

$$[A] = \begin{bmatrix} 1 & \begin{matrix}\varepsilon_1(\cos\theta_P - 1) + \varepsilon_2 \sin\theta_P \\ + (\Delta\theta_R + \delta\theta_R)\cos\theta_P \\ - \Delta\theta_Y \sin\theta_P\end{matrix} & \begin{matrix}-\varepsilon_1 \sin\theta_P + \varepsilon_2(\cos\theta_P - 1) \\ - (\Delta\theta_R + \delta\theta_R)\sin\theta_P \\ - \Delta\theta_Y \cos\theta_P\end{matrix} \\ \begin{matrix}\varepsilon_1(1 - \cos\theta_P) - \varepsilon_2(\sin\theta_P) \\ - (\Delta\theta_R + \delta\theta_R)\cos\theta_P \\ + \Delta\theta_Y \sin\theta_P\end{matrix} & 1 & (\Delta\theta_P + \delta\theta_P) \\ \begin{matrix}\varepsilon_1(\sin\theta_P) + \varepsilon_2(1 - \cos\theta_P) \\ + (\Delta\theta_R + \delta\theta_R)\sin\theta_P \\ + \Delta\theta_Y \cos\theta_P\end{matrix} & -(\Delta\theta_P + \delta\theta_P) & 1 \end{bmatrix} \tag{D-46}$$

The matrix A defined above assumes infinitesimal perturbations and neglects higher-order terms. Upon the substitution of $[A]$ into Eq. (D-45), an orthogonal set of equations specifying the position of the spacecraft after the commanded maneuvers, as a function of the errors contributed to the turns and the desired position, is obtained.

d. Spacecraft position after the commanded turns. The vector representing the final position of the roll axis with respect to the ideal or standard roll, pitch turn is obtained by performing the indicated matrix multiplication in Eq. (D-46). Three simultaneous vector equations are obtained. The desired equation is given as

$$\begin{aligned}\mathbf{z}_3 = {} & \{\varepsilon_1(\sin\theta_P) + \varepsilon_2(1 - \cos\theta_P) \\ & + (\Delta\theta_R + \delta\theta_R)\sin\theta_P + \Delta\theta_Y \cos\theta_P\}\,\mathbf{x}_{3_s} \\ & - (\Delta\theta_P + \delta\theta_P)\,\mathbf{y}_{3_s} + \mathbf{z}_{3_s}\end{aligned} \tag{D-47}$$

This equation is represented pictorially by the vector in Fig. D-7.

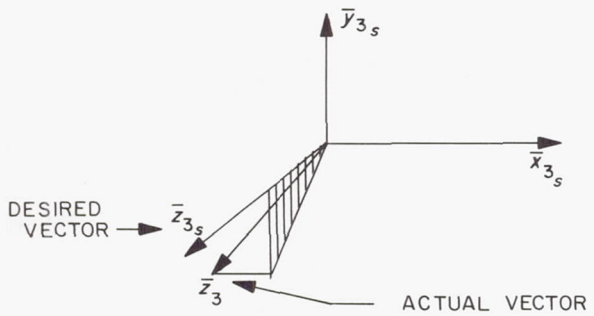

Fig. D-7. Roll-position vector following the roll, pitch turn

The vector components of Eq. (D-47) represent the total pitch and yaw errors introduced by the turns. The pitch error is given as the $\mathbf{y}_{3_s}$ component of $\mathbf{z}_3$; therefore,

$$\theta_{\varepsilon_P} = -(\Delta\theta_P + \delta\theta_P) \tag{D-48}$$

The yaw error is the $\mathbf{x}_{3_s}$ component; therefore,

$$\begin{aligned}\theta_{\varepsilon_Y} = {} & -\{\varepsilon_1(\sin\theta_P) + \varepsilon_2(1 - \cos\theta_P) \\ & + (\Delta\theta_R + \delta\theta_R)\sin\theta_P + \Delta\theta_Y \cos\theta_P\}\end{aligned} \tag{D-49}$$

Equations (D-48) and (D-49) represent the errors contributed to the roll axis of the spacecraft for a non-perfect turn. Again, it is mentioned that the errors were assumed as infinitesimal so that an approximate solution could be developed.

e. Velocity increment error. The thrust phase of the midcourse maneuver follows the commanded turns. A correction velocity increment V_R is added along the spacecraft z axis by the midcourse propulsion unit. At this time, thrust attitude is maintained in the required direction by control from the autopilot. As mentioned in Appendix B, jet-vane actuators are located downstream of the rocket exhaust and provide the necessary feedback information from the vane deflections.

This portion of the analysis assumes that the velocity increment is in error by a value δV, and that the autopilot introduces additional errors in pitch and yaw attitude of δ_p and δ_y, respectively (Fig. D-8).

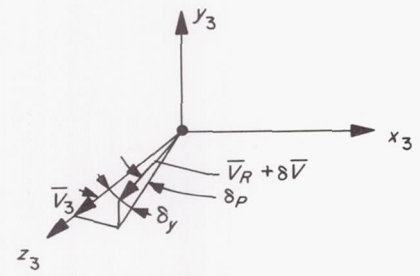

Fig. D-8. Velocity increment errors

From the Pitch Turn—Small Perturbations section in this Appendix D, Eq. (D-45) defined the final position of the vehicle after the turns. The addition of the autopilot errors leads to the extension of the expression, so that

$$\mathbf{W}_4 = [\delta_{A/P}]\,\mathbf{W}_3 \tag{D-50}$$

Replacing $\mathbf{W}_3$ by Eq. (D-45) yields

$$\mathbf{W}_4 = [\delta_{A/P}]\,[A]\,\mathbf{W}_{3_s} \tag{D-51}$$

where

$$[\delta_{A/P}] = \begin{bmatrix} 1 & 0 & -\delta_y \\ 0 & 1 & \delta_p \\ \delta_y & -\delta_p & 1 \end{bmatrix} \tag{D-52}$$

Equation (D-36) is now substituted into Eq. (D-51), and the extended matrix vector equation is given in terms of the initial standard coordinates as

$$\mathbf{W}_{1_s} = [\theta_R]^{-1}\,[\theta_P]^{-1}\,[A]^{-1}\,[\delta_{A/P}]^{-1}\,\mathbf{W}_4 \tag{D-53}$$

The above expression defines the complete transformation matrix. The velocity vector increment can therefore be defined as

$$\mathbf{V}_{W_{1_s}} = [\theta_R]^{-1}\,[\theta_P]^{-1}\,[A]^{-1}\,[\delta_{A/P}]^{-1}\,\mathbf{V}_{W_4} \tag{D-54}$$

where

$$\mathbf{V}_{W_{1_s}} = \left.\begin{matrix} V_x \\ V_y \\ V_z \end{matrix}\right]_s \tag{D-55}$$

$$\mathbf{V}_{W_4} = \left.\begin{matrix} 0 \\ 0 \\ (V_R + \delta V) \end{matrix}\right] \tag{D-56}$$

and

$$\mathbf{V}_4 = \left.\begin{matrix} 0 \\ 0 \\ V_R \end{matrix}\right] \tag{D-57}$$

$$\delta\mathbf{V}_4 = \left.\begin{matrix} 0 \\ 0 \\ \delta V \end{matrix}\right] \tag{D-58}$$

The incremental error transformed back to the premaneuver coordinates is obtained by first expanding Eq. (D-54).

$$\mathbf{V}_{W_{1_s}} = \{[\theta_R]^{-1}\,[\theta_P]^{-1}\,[A]^{-1}\,[\delta_{A/P}]^{-1}\}\,\mathbf{V}_4 + \{[\theta_R]^{-1}\,[\theta_P]^{-1}\,[A]^{-1}\,[\delta_{A/P}]^{-1}\}\,\delta\mathbf{V}_4 \tag{D-59}$$

Rewriting in terms of $\delta\mathbf{V}_4$

$$\delta\mathbf{V}_4 = [\delta_{A/P}]\,[A]\,[\theta_P]\,[\theta_R]\,\mathbf{V}_{W_{1_s}} - \mathbf{V}_4 \tag{D-60}$$

Now if

$$\delta\mathbf{V}_4 = [\delta_{A/P}]\,[A]\,[\theta_P]\,[\theta_R]\,\delta\mathbf{V}_{W_{1_s}} \tag{D-61}$$

and from Eq. (D-51)

$$\mathbf{V}_4 = [\delta_{A/P}]\,[A]\,\mathbf{V}_{W_{3_s}}$$

where

$$\mathbf{V}_{W_{3_s}} = \left.\begin{matrix} 0 \\ 0 \\ V_R \end{matrix}\right] \tag{D-62}$$

then upon substitution back into Eq. (D-60)

$$\delta\mathbf{V}_{W_{1_s}} = \mathbf{V}_{W_{1_s}} - [\theta_R]^{-1}\,[\theta_P]^{-1}\,\mathbf{V}_{W_{3_s}} \tag{D-63}$$

The solution of the above velocity-increment vector matrix is obtained by first solving for the term $\mathbf{V}_{W_{1_s}}$, where from Eq. (D-54)

$$\mathbf{V}_{W_{1_s}} = [\theta_R]^{-1}\,[\theta_P]^{-1}\,[A]^{-1}\,[\delta_{A/P}]^{-1}\,\mathbf{V}_{W_4} \tag{D-64}$$

and

$$[\theta_R]^{-1}[\theta_P]^{-1} = \begin{bmatrix} \cos\theta_R & -\sin\theta_R\cos\theta_P & \sin\theta_R\sin\theta_P \\ \sin\theta_R & \cos\theta_R\cos\theta_P & -\cos\theta_R\sin\theta_P \\ 0 & \sin\theta_P & \cos\theta_P \end{bmatrix} \tag{D-65}$$

$$[A]^{-1} = \begin{bmatrix} 1 & \begin{matrix}\varepsilon_1(1-\cos\theta_P) - \varepsilon_2\sin\theta_P \\ -(\Delta\theta_R + \delta\theta_R)\cos\theta_P \\ +\Delta\theta_Y\sin\theta_P\end{matrix} & \begin{matrix}\varepsilon_1\sin\theta_P + \varepsilon_2(1-\cos\theta_P) \\ +(\Delta\theta_R + \delta\theta_R)\sin\theta_P \\ +\Delta\theta_Y\cos\theta_P + \delta_y\end{matrix} \\ \begin{matrix}\varepsilon_1(\cos\theta_P - 1) + \varepsilon_2\sin\theta_P \\ +(\Delta\theta_R + \delta\theta_R)\cos\theta_P \\ -\Delta\theta_Y\sin\theta_P\end{matrix} & 1 & -(\Delta\theta_P + \delta\theta_P + \delta_p) \\ \begin{matrix}-\varepsilon_1\sin\theta_P + \varepsilon_2(\cos\theta_P - 1) \\ -(\Delta\theta_R + \delta\theta_R)\sin\theta_P \\ -\Delta\theta_Y\cos\theta_P + \delta_y\end{matrix} & -(\Delta\theta_P + \delta\theta_P + \delta_p) & 1 \end{bmatrix} \tag{D-66}$$

$$[\delta_{A/P}]^{-1} = \begin{bmatrix} 1 & 0 & \delta_y \\ 0 & 1 & -\delta_p \\ -\delta_y & \delta_p & 1 \end{bmatrix} \tag{D-67}$$

(again assuming small perturbations and neglecting higher-order terms).

Since the $\mathbf{V}_x$ and $\mathbf{V}_y$ components of the $\mathbf{V}_{W_4}$ vector in Eq. (D-56) are zero, Eq. (D-64) can be written as

$$\mathbf{V}_{W_{1_s}} = \begin{bmatrix} \cos\theta_R & -\sin\theta_R\cos\theta_P & \sin\theta_R\sin\theta_P \\ \sin\theta_R & \cos\theta_R\cos\theta_P & -\cos\theta_R\sin\theta_P \\ 0 & \sin\theta_P & \cos\theta_P \end{bmatrix} \begin{bmatrix} \varepsilon_1\sin\theta_P + \varepsilon_2(1-\cos\theta_P) \\ +(\Delta\theta_R + \delta\theta_R)\sin\theta_P + \Delta\theta_Y\cos\theta_P + \delta_y \\ (\Delta\theta_P + \delta\theta_P + \delta_p) \\ 1 \end{bmatrix} (V_R + \delta V) \tag{D-68}$$

The second part of Eq. (D-63) leads to the expression

$$[\theta_R]^{-1}[\theta_P]^{-1}\mathbf{V}_{W_{3_s}} = \begin{bmatrix} \cos\theta_R & -\sin\theta_R\cos\theta_P & \sin\theta_R\sin\theta_P \\ \sin\theta_R & \cos\theta_R\cos\theta_P & -\cos\theta_R\sin\theta_P \\ 0 & \sin\theta_P & \cos\theta_P \end{bmatrix} \begin{bmatrix} 0 \\ 0 \\ 1 \end{bmatrix} (V_R) \tag{D-69}$$

Subtracting Eq. (D-69) from Eq. (D-63) and normalizing with respect to the velocity V_R, we obtain

$$\frac{\delta \mathbf{V}_{W_{1_s}}}{V_R} = \begin{bmatrix} \cos\theta_R & -\sin\theta_R\cos\theta_P & \sin\theta_R\sin\theta_P \\ \sin\theta_R & \cos\theta_R\cos\theta_P & -\cos\theta_R\sin\theta_P \\ 0 & \sin\theta_P & \cos\theta_P \end{bmatrix} \begin{bmatrix} \varepsilon_1\sin\theta_P + \varepsilon_2(1-\cos\theta_P) \\ +(\Delta\theta_R + \delta\theta_R)\sin\theta_P + \Delta\theta_Y\cos\theta_P + \delta_y \\ -(\Delta\theta_P + \delta\theta_P + \delta_p) \\ \left(\frac{\delta V}{V_R}\right) \end{bmatrix} \tag{D-70}$$

Factoring the above equation gives

$$\frac{\delta \mathbf{V}_{W_{1_s}}}{V_R} = \begin{bmatrix} \cos\theta_R(1-\cos\theta_P) & \cos\theta_R\sin\theta_P & \cos\theta_R\cos\theta_P & \cos\theta_R & \sin\theta_R\cos\theta_P & \sin\theta_R\sin\theta_P \\ \sin\theta_R(1-\cos\theta_P) & \sin\theta_R\sin\theta_P & \sin\theta_R\cos\theta_P & \sin\theta_R & -\cos\theta_R\cos\theta_P & -\cos\theta_R\sin\theta_P \\ 0 & 0 & 0 & 0 & -\sin\theta_P & \cos\theta_P \end{bmatrix} \begin{bmatrix} \varepsilon_2 \\ \varepsilon_1 + \Delta\theta_R + \delta\theta_R \\ \Delta\theta_Y \\ \delta_y \\ \Delta\theta_P + \delta\theta_P + \delta_p \\ \left(\frac{\delta V}{V_R}\right) \end{bmatrix} \tag{D-71}$$

The above expression is of the form

$$\frac{\delta \mathbf{V}_{W_{1_s}}}{V_R} = [B]\,\boldsymbol{\varepsilon} \tag{D-72}$$

The matrix B is the ideal-turn matrix; $\boldsymbol{\varepsilon}$ is the error vector.

Velocity increment error vector. The velocity-increment matrix equation in Eq. (D-72) can now be expanded by relating the error components to $\boldsymbol{\varepsilon}$.

$$V = V_R + \delta V \tag{D-73}$$

where V_R = velocity increment, and

$$\delta V = (V_R C_V + \eta_{\dot{V}} T + V_T) \tag{D-74}$$

where

C_V = accelerometer scale-factor error (absolute + stability)

$\eta_{\dot{V}}$ = accelerometer null offset

$\bar{\dot{V}}$ = average acceleration

V_T = velocity command error and tailoff variations

Equation (D-74) is rewritten as

$$\frac{\delta V}{V_R} = C_V + \frac{\eta_{\dot{V}}}{\bar{\dot{V}}} + \frac{V_T}{V_R} \tag{D-75}$$

Now from Eq. (D-71), if we study just the velocity increment error, then

$$\frac{\delta V_{W_{1_s}}}{V_R}\Bigg] = \begin{bmatrix} \sin\theta_R\sin\theta_P \\ -\cos\theta_R\sin\theta_P \\ \cos\theta_P \end{bmatrix} \left(\frac{\delta V}{V_R}\right) \tag{D-76}$$

From Eq. (D-76), it is seen that the shut-off and resolution errors are derived from the z coefficient and are given by

$$\begin{bmatrix} \frac{\delta V_x}{V_R} \\ \frac{\delta V_y}{V_R} \\ \frac{\delta V_z}{V_R} \end{bmatrix} = \begin{bmatrix} \sin\theta_R \sin\theta_P \\ -\cos\theta_R \sin\theta_P \\ \cos\theta_P \end{bmatrix} \left(C_V + \frac{\eta\dot{v}}{\dot{V}} + \frac{V_T}{V_R} \right)$$

so

$$\frac{\delta V_z}{V_R} = \cos\theta_P \left(C_V + \frac{\eta\dot{v}}{\dot{V}} + \frac{V_T}{V_R} \right) \qquad \text{(D-77)}$$

or rewriting

$$\delta V_z = (V_R \cos\theta_P)\, C_V + \left(\frac{V_R}{V_T} \cos\theta_P \right) \eta\dot{v} + (\cos\theta_P)\, V_T \qquad \text{(D-78)}$$

f. Description of pointing error vector components. Several of the components of the error vector ε can be shown to be a function of the attitude control subsystem. For example, the error $\Delta\theta_i$ is a function of the limit cycle. Figure D-9 shows the Earth sensor hinge axis which corresponds to the clock (roll reference) and cone (Sun-probe-Earth) angles α and β. Roll control is maintained by a tight sensor tracking loop by simply feeding back the roll-error signal. The error $\Delta\theta_i$ is the summation of errors due to the sensor characteristics and the location of the roll position in the limit cycle and is given by

$$\theta_i = \eta_i + \lambda_i \qquad \text{(D-79)}$$

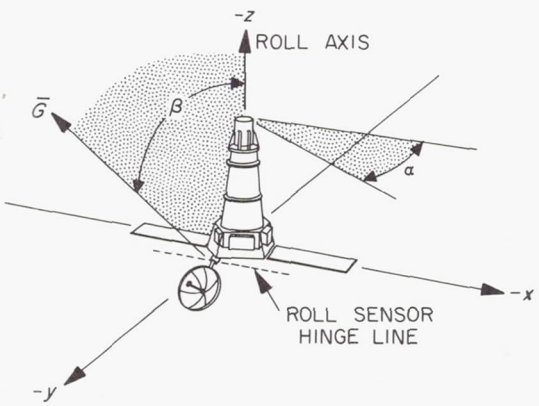

Fig. D-9. Roll-attitude control coordinates

where

η_i = pitch or yaw Sun sensor null offset

λ_i = position in the limit cycle

The error contributed to the turn by the command is based on a commanded rate $\dot{\theta}_i$ which is *on* for a specified time duration, t_i.

$$\begin{aligned} \delta\theta_i &= -\delta\dot{\theta}_i T_i - \dot{\theta}_i \delta T_i + \omega_i T_i \\ &= -\theta_i \left(\frac{\delta\dot{\theta}_i}{\dot{\theta}_i} \right) - \dot{\theta}_i \delta T_i + \omega_i T_i \end{aligned} \qquad \text{(D-80)}$$

where

$\delta\dot{\theta}_i$ = commanded rate calibration error about the i^{th} axis

δT_i = resolution error in timing the turn

ω_i = gyro drift rate

$$T_i = \frac{\theta_i}{\dot{\theta}_i}$$

$$C_i = \frac{\delta\dot{\theta}_i}{\dot{\theta}_i}$$

Equations (D-79) and (D-80) are substituted into Eq. (D-48) and (D-49), and the total pitch and yaw errors are given by

Pitch error:

$$\begin{aligned} \theta_{\varepsilon_P} &= -(\Delta\theta_i + \delta\theta_i) \\ &= -\eta_P - \lambda_P + \theta_P \left(\frac{\delta\dot{\theta}_P}{\dot{\theta}_P} \right) + \theta_P \delta T_P - \omega_i T_i \end{aligned} \qquad \text{(D-81)}$$

Yaw error:

$$\begin{aligned} \theta_{\varepsilon_Y} = &-\sin\theta_P \left(-\varepsilon_R + \frac{\omega_Y}{\dot{\theta}_P} \right) - (1 - \cos\theta_P) \left(+\varepsilon_Y + \frac{\omega_R}{\dot{\theta}_P} \right) \\ &- \sin\theta_P \left\{ (\eta_R + \lambda_R) - \theta_R \left(\frac{\delta\dot{\theta}_R}{\dot{\theta}_R} \right) + \omega_R T_R - \dot{\theta}_R \delta T_R \right\} \\ &- \cos\theta_P (\eta_Y + \lambda_Y) \end{aligned} \qquad \text{(D-82)}$$

Equations (D-81) and (D-82) are combined and reformulated as the following error matrix:

$$\begin{bmatrix} \theta_{\varepsilon_P} \\ \theta_{\varepsilon_Y} \end{bmatrix} = \begin{bmatrix} -1 & 0 & 0 & -T_P & 0 & 0 & \theta_P & 0 & \dot{\theta}_P & 0 & 0 & 0 \\ 0 & -\sin\theta_P & -\cos\theta_P & 0 & \left\{\frac{(\cos\theta_P - 1)}{\dot{\theta}_P} - T_R \sin\theta_P\right\} & -\frac{\sin\theta_P}{\dot{\theta}_P} & 0 & \theta_R \sin\theta_P & 0 & \dot{\theta}_R \sin\theta_P & (\cos\theta_P - 1) & \sin\theta_P \end{bmatrix} \begin{bmatrix} (\eta_P + \lambda_P) \\ (\eta_R + \lambda_R) \\ (\eta_Y + \lambda_Y) \\ \omega_P \\ \omega_R \\ \omega_Y \\ C_x \\ C_z \\ \delta T_P \\ \delta T_R \\ \varepsilon_Y \\ \varepsilon_Z \end{bmatrix} \tag{D-83}$$

The errors may be further reduced by breaking the null offsets into their components.

Therefore, the pitch sensor electrical offset is given by ηx_e and the mechanical offset is ηx_m. The offset is shown in Fig. D-10.

After the roll turn, the spacecraft switches to inertial control and therefore introduces the pitch sensor null position as its zero reference. The pitch switching amplifier also introduces a null offset. A positive offset ηx_{SA} creates a positive angular displacement. This error is multiplied by the factor 2 since the amplifier is offset from the optical reference which is, in turn, used as the inertial reference. Therefore, the total offset is $+2\eta x_{SA}$ and

$$\eta_P = +\eta x_e + \eta x_m + 2\eta x_{SA} \tag{D-84}$$

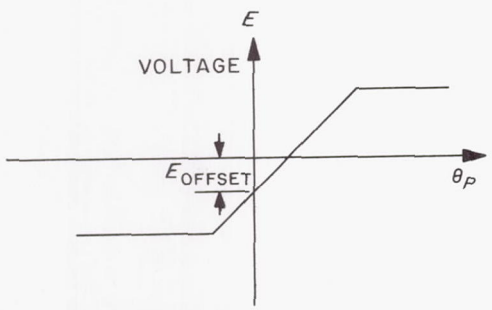

Fig. D-10. Pitch-sensor null offset

The error introduced by the limit cycle provides an error in the reference for the inertial instruments since the position in the limit cycle is taken as the inertial null position. The error λ acts in the opposite sense to the offsets mentioned above. Therefore,

$$\eta_P + \lambda_P = +\eta x_e + \eta x_m + 2\eta x_{SA} - \lambda_X \tag{D-85}$$

and the matrix is given by

$$\eta_P + \lambda_P = [+1 \quad +1 \quad +2 \quad -1]^T \begin{bmatrix} \eta x_e \\ \eta x_m \\ \eta x_{SA} \\ \lambda_X \end{bmatrix} \tag{D-86}$$

where the pitch coefficients are

$$\begin{bmatrix} 1 \\ 1 \\ 2 \\ -1 \end{bmatrix} \tag{D-87}$$

Similarly, the roll offsets are given by

$$\eta_R + \lambda_R = +\eta z_e + \eta z_m + 2\eta z_{SA} - \lambda_Z \tag{D-88}$$

However, in this instance the errors are present at the initiation of the roll turn. The limit-cycle error again acts in the opposite direction.

In addition, the error created by the roll albedo asymmetry ηz_a is introduced. This error is introduced through the assumption that the Earth is a point source of light. Therefore, the sensor may not be looking at the center of the Earth, and the additional error is created.

The total error is therefore,

$$\eta_R + \lambda_R = +\eta z_e + \eta z_m + 2\eta z_{SA} + \eta z_a - \lambda_Z \tag{D-89}$$

The yaw axes offset errors are introduced during optical control and create a roll displacement, such that the spacecraft must realign the roll reference; they are also present during inertial control.

The offset errors are given by

$$\eta_Y = +\eta_{Y_e} + \eta_{Y_m} + 2\eta_{Y_{SA}} \tag{D-90}$$

However, the yaw limit cycling while the roll axis is optically controlled introduces error, as discussed above in this section of Appendix D. When the yaw axis is switched to inertial control, this position in the limit cycle acts as an error; however, due to the randomness of the limit cycle, these errors are not necessarily in the same direction, and therefore the coefficient is obtained by taking the root sum square (RSS) of the coefficient error sources. The yaw initial deadzone error is given as

$$\theta_{\varepsilon_Y} = (\sqrt{\cos^2\theta_P + \sin^2\theta_P \cot^2\beta})\,\delta_{Y_P} \tag{D-91}$$

The gyro drift-rate errors are introduced at the time the spacecraft is put under inertial control. Therefore, the instant the changeover is complete, the addition of the drift errors must be accounted for.

The pitch drift-rate error is a function of the pitch turn period and is given by

$$\theta_{\varepsilon_P} = T_P \omega_P \tag{D-92}$$

where T_P = drift rate-error coefficient as given by Eq. (D-80).

The yaw-gyro drift-rate errors are introduced following the roll turn and enter in the pitch axis, both during the commanded pitch turn (for a yaw coefficient of error) and after the turn (but before midcourse burn). Therefore, this condition is expressed by

$$\theta_{\varepsilon_Y} = -\left[\left(\frac{\sin\theta_P}{\dot\theta_P}\right) + \left(T_P - \frac{\theta_P}{\dot\theta_P}\right)\right]\omega_Y \tag{D-93}$$

The roll-gyro drift creates a rotation about the z axis during the roll turn and changes the axis of rotation during the pitch turn. Therefore,

$$\theta_{\varepsilon_R} = -\left[T_R \sin\theta_P + \left(1 - \frac{\cos\theta_P}{\theta_P}\right)\right]\omega_R \tag{D-94}$$

Additional error sources.

1. *Capacitor leakage.* The commanded turns are directly related to the charge on the gyro capacitors. Leakage in the capacitor creates a yaw error which is given by

$$\theta_{\varepsilon_Y} = (\sin\theta_P)\,\alpha_R \tag{D-95}$$

where α_R = roll capacitor leakage; and a pitch error

$$\theta_{\varepsilon_P} = (-1)\,\alpha_P \tag{D-96}$$

where α_P = pitch capacitor leakage.

2. *Roll sensor hinge misalignment.* The antenna hinge, which also acts in the roll sensor control loop, provides an incremental error in that the hinge line of the sensor is not truly parallel to the x-axis due to a slight yaw misalignment b_y. Therefore,

$$\theta_{\varepsilon_Y} = (-\cot\beta \sin\theta_P)\,b_y \tag{D-97}$$

Similarly, since the hinge line is not parallel to the x-axis, an incremental roll misalignment is introduced, so that

$$\theta_{\varepsilon_Y} = \sin\theta_P b_z \tag{D-98}$$

3. *Center of gravity (c.g.) offset.* The center of gravity (c.g.) of the spacecraft is not necessarily located in the position that is specified. Figure D-11 shows the effect of the c.g. offset. The c.g. offset angle in pitch is given by

$$\rho = \frac{\delta}{1-h} \tag{D-99}$$

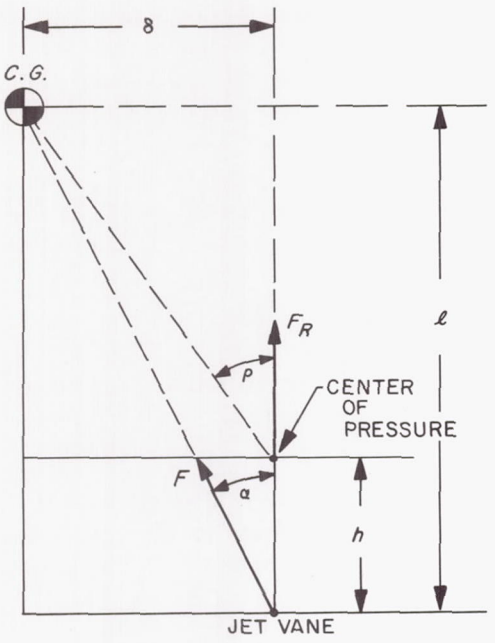

Fig. D-11. Center-of-gravity offset

The necessary thrust-vector deflection desired to compensate for the c.g. offset error is

$$\alpha = \frac{1}{G_{FB}}\rho \tag{D-100}$$

where

G_{FB} = feedback gain

ρ = c.g. offset angle

α = spacecraft deflection necessary for autopilot error signal.

However,

$$\theta = \alpha + \rho \tag{D-101}$$

so

$$\theta_{\varepsilon_P} = \left(1 + \frac{1}{G_{FB}}\right)\rho_X \tag{D-102}$$

Similarly, the angular error in yaw due to the c.g. offset is given by

$$\theta_{\varepsilon_Y} = \left(1 + \frac{1}{G_{FBY}}\right)\rho_y \tag{D-103}$$

4. *Thrust vector angular error.* Finally an error, due to the fact that the thrust vector does not pass through the centerline of the rocket motor and that the jet-vane null position is such that the thrust vector does not pass through the c.g., is introduced. Therefore in pitch, the angular error is

$$\theta_{\varepsilon_P} = \left(-\frac{1}{G_{FBP}}\right)\beta_p \tag{D-104}$$

and in yaw

$$\theta_{\varepsilon_Y} = \left(-\frac{1}{G_{FBY}}\right)\beta_y \tag{D-105}$$

Roll error caused by yaw limit cycle. The optical coupling of the yaw-limit cycle motion into the roll-error channel, when the high-gain antenna hinge angle is different from 90 deg, is of concern.

The axis system used for attitude control is not completely orthogonal since the Earth-probe-Sun angle is not, in general, equal to 90 deg. Since the antenna hinge is parallel to the pitch axis, the roll-error signal seen by the Earth sensor is proportional to the actual roll error multiplied by sin β, where β is the Earth-probe-Sun angle. In addition, motion in yaw produces a component in the roll channel proportional to the actual yaw motion multiplied by the cos β. Pitch motion will not produce a component in the roll channel. A complete description of the above phenomena follows.

Analysis of roll error. By using the unit sphere, a graphical description of the effect of the antenna hinge angle on Earth sensor roll-error signals, as a function of spacecraft roll and yaw error, is shown in Fig. D-12. The following nomenclature is used:

θ_R = roll error

θ_{ε_R} = error signal in Earth sensor caused by θ_R

β = hinge angle (Earth-probe-Sun angle)

θ_Y = yaw error

θ_{ε_Y} = error signal in Earth sensor caused by θ_Y

λ_{z_o} = roll deadzone

λ_{y_p} = yaw deadzone

η_z = null offset—roll sensor, electrical and mechanical $(\eta_{z_e} + \eta_{z_m})$

η_Y = null offset—yaw sensor, electrical and mechanical $(\eta_{Y_e} + \eta_{Y_m})$

$\eta_{z_{SA}}$ = null offset—roll switching amplifier

$\eta_{Y_{SA}}$ = null offset—yaw switching amplifier

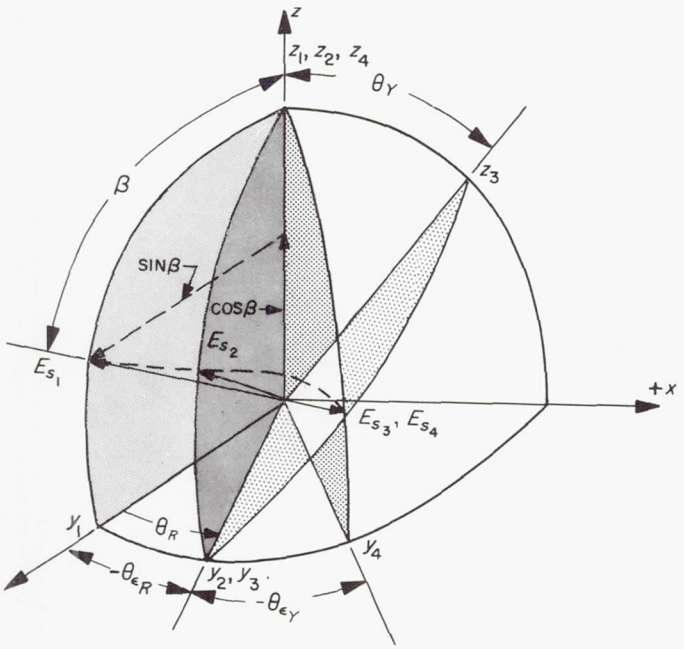

Fig. D-12. Effect-of-roll error caused by yaw limit cycle

From the above figure, the combined roll and yaw errors are shown in respective order. The errors are assumed small enough, such that small-angle approximations may be used. For the purpose of this analysis, the arc length

$$E_{S_1}E_{S_2} = -\theta_{\epsilon_R} = -\theta_R \sin\beta$$

and

$$E_{S_2}E_{S_4} = -\theta_{\epsilon_Y} = -\theta_R \cos\beta \qquad \text{(D-106)}$$

The block diagrams of the roll and yaw channels are shown in Fig. D-13 and D-14.

The effect of a null offset on the sensors and on the switching amplifier is shown in Fig. D-15 and D-16.

The output of the sensor is given as

$$E = K_S\theta \pm E_o \qquad \text{(D-107)}$$

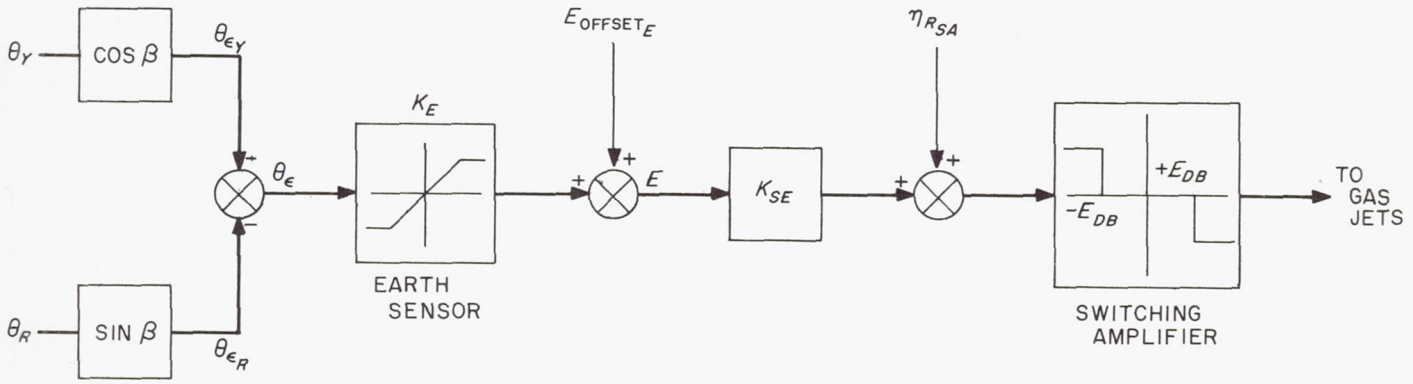

Fig. D-13. Roll channel

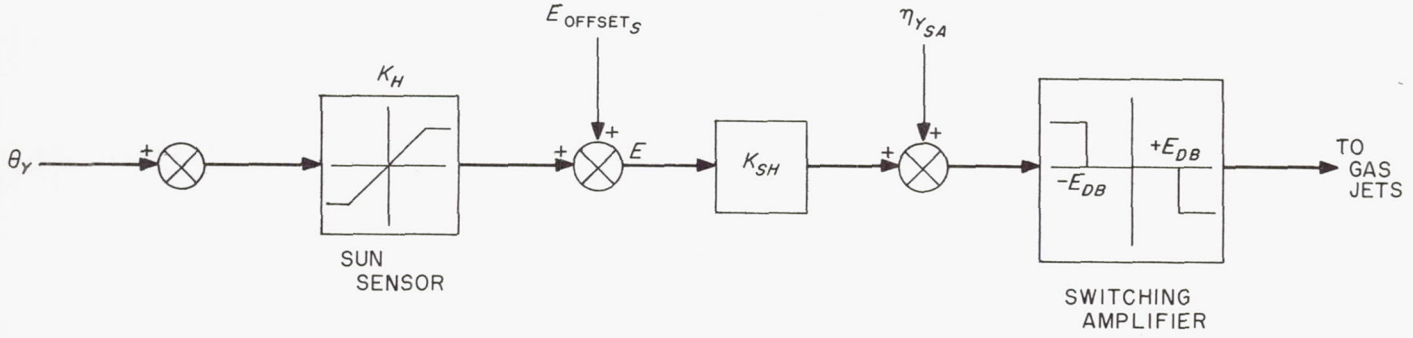

Fig. D-14. Yaw channel

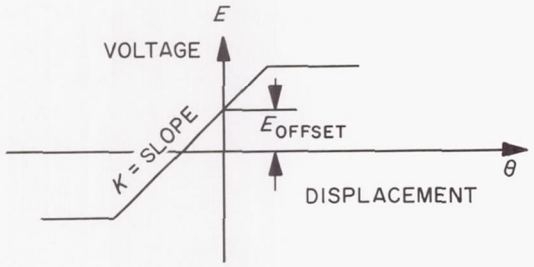

Fig. D-15. Sensor null-offset effect

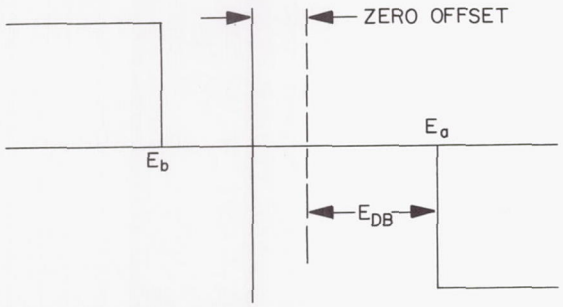

Fig. D-16. Switching amplifier null-offset effect

where

K_S = sensor gain (Sun or Earth sensor)

E_o = voltage null offset

$\theta_{\cdot} = (\theta_{DB})$ actual mechanical angle of the spacecraft when switching occurs.

The voltage output of the switching amplifier is described by the following equation:

$$\pm E_{DB} = K_{SA}E \pm \eta_{SA} \qquad \text{(D-108)}$$

where

E_{DB} = switching amplifier deadband voltage

E = sensor output

K_{SA} = switching amplifier gain

η_{SA} = switching amplifier null offset

Now, substituting Eq. (D-107) into (D-108) yields

$$\pm E_{DB} = K_{SA}(K_S\theta \pm E) \pm \eta_{SA}$$

and in terms of the displacement,

$$\theta = \pm \frac{E_{DB}}{K_{SA}K_S} \mp \frac{\eta_{SA}}{K_{SA}K_S} \mp \frac{E_o}{K_S} \qquad \text{(D-109)}$$

For the yaw channel, Eq. (D-109) is re-written as

$$\theta_Y = \pm \frac{E_{DB_Y}}{K_{SH}K_S} \mp \frac{\eta_{Y_{SA}}}{K_{SH}K_S} \mp \frac{E_{Y_o}}{K_S} \qquad \text{(D-110)}$$

where

K_{SH} = yaw switching amplifier gain

K_H = yaw Sun sensor gain

Similarly, the expression for the roll channel may be obtained by noting that from Fig. D-13,

$$\begin{aligned}\theta_\varepsilon &= -(\theta_{\varepsilon_R} + \theta_{\varepsilon_Y}) \\ &= -(\theta_R \sin\beta + \theta_Y \cos\beta) \qquad \text{(D-111)}\end{aligned}$$

and equating (D-111) to (D-109) and rewriting in terms of θ_R,

$$\theta_R = \left[\mp \frac{E_{DB_R}}{K_{SE}K_E} \pm \frac{\eta_{R_{SA}}}{K_{SE}K_E} \pm \frac{E_{R_o}}{K_E}\right] \frac{1}{\sin\beta} - \theta_Y \cot\beta \qquad \text{(D-112)}$$

where

K_{SE} = roll switching amplifier gain

K_E = roll Earth sensor gain

The actual size of the roll limit cycle is determined by substituting Eq. (D-110) into (D-112), and therefore,

$$\begin{aligned}\theta_R = &\left[\mp \frac{E_{DB_R}}{K_{SE}K_E} \pm \frac{\eta_{R_{SA}}}{K_{SE}K_E} \pm \frac{E_{R_o}}{K_E}\right] \frac{1}{\sin\beta} \\ &+ \left[\mp \frac{E_{DB_Y}}{K_{SH}K_H} \pm \frac{\eta_{Y_{SA}}}{K_{SH}K_H} \pm \frac{E_{Y_o}}{K_H}\right] \cot\beta\end{aligned} \qquad \text{(D-113)}$$

Now, if the following substitutions are made,

$\lambda_{z_o} = \dfrac{E_{DB_R}}{K_{SE}K_E}$ = effective roll deadband

$\lambda_{y_p} = \dfrac{E_{DB_Y}}{K_{SH}K_H}$ = effective yaw deadband

$\eta_z = \dfrac{E_{R_o}}{K_E}$ = roll sensor null offset (electrical and mechanical)

$\eta_y = \dfrac{E_{Y_o}}{K_H}$ = yaw sensor null offset (electrical and mechanical)

$$\eta_{z_s} = \frac{R_{SA}}{K_{SE}K_E} = \text{roll switching amplifier null offset}$$

$$\eta_{y_s} = \frac{Y_{SA}}{K_{SH}K_H} = \text{yaw switching amplifier null offset}$$

then Eq. (D-113) can be rewritten as

$$\theta_R = \frac{(\eta_z + \eta_{z_s} - \lambda_{z_o})}{\sin\beta} + (\eta_y + \eta_{y_s} - \lambda_{y_p})\cot\beta \tag{D-114}$$

Due to the switching-amplifier null offset, η, there is a roll error equal to η. When the sensors are switched out and the gyros are switched in, the gyro output is zero, but the offset is still there as an input and will cause the spacecraft to roll by an amount of the offset (since the sensor is no longer bucking it). This means that a total offset error of 2_{η_z} is present. The yaw offset isn't added twice because it goes through the Earth sensor and is switched out when the gyro is switched in. Hence, the roll limit cycle is given as

$$\theta_R = \frac{(\eta_{z_e} + \eta_{z_m} - \lambda_{z_o} + 2\eta_{z_s})}{\sin\beta} + (\eta_{y_e} + \eta_{y_m} - \lambda_{y_p} + \eta_{y_s})\cot\beta \tag{D-115}$$

Therefore, from the roll-pitch maneuver, the error in yaw due to an error in roll is given by

$$\theta_Y = -\theta_R \sin\theta_P \tag{D-116}$$

and by substituting Eq. (D-109) into the above expression, we obtain

$$\theta_Y = -(\eta_{z_e} + \eta_{z_m} - \lambda_{z_o})\frac{\sin\theta_P}{\sin\beta} - (\eta_{z_s})\frac{2\sin\theta_P}{\sin\beta} - (\eta_{y_e} + \eta_{y_m} - \lambda_{y_p})\sin\theta_P\cot\beta - (\eta_{y_s})\sin\theta_P\cot\beta \tag{D-117}$$

Now the yaw coefficients of the errors must include those due to the limit cycle. The error analysis is now altered by the following coefficients:

Yaw Coefficient	*Error Symbol*
$-\cos\theta_P - \sin\theta_P\cot\beta$	$\eta_{y_e} + \eta_{y_m} - \lambda_{y_p}$
$-2\cos\theta_P - \sin\theta_P\cot\beta$	η_{y_s}
$-\frac{\sin\theta_P}{\sin\beta}$	$\eta_{z_e} + \eta_{z_m} - \lambda_{z_o}$
$-\frac{2\sin\theta_P}{\sin\beta}$	η_{z_s}

(D-118)

Error matrix formulation, pointing vector. Now the pointing-error matrix Eq. (D-83) is expanded to include the error sources given in the preceding sections. To ease the writing of this equation which is a 30×2 matrix, a tabulated form is adopted. The form is given in Table D-2 as

$$\begin{bmatrix} \theta_{\varepsilon_P} \\ \theta_{\varepsilon_Y} \end{bmatrix} = [E]^T \Sigma\varepsilon]$$

where

E = error matrix

$\Sigma\varepsilon$ = source-error vector

Table D-2. Pointing error thrust vector, midcourse maneuver

E matrix		$\Sigma\varepsilon$ vector
Pitch coefficient	Yaw coefficient	Error symbol
-1	0	$\eta_{X_e} + \eta_{X_m} - \lambda_X$
-2	0	$\eta_{X_{SA}}$
0	$-\cos\theta_P - \cot\beta\sin\theta_P$	$\eta_{Y_e} + \eta_{Y_m}$
0	$-\sqrt{\cos^2\theta_P + \cot^2\beta\sin^2\theta_P}$	$-\lambda_Y$
0	$-2\cos\theta_P - \cot\beta\sin\theta_P$	$\eta_{Y_{SA}}$
0	$-\sin\theta_P/\sin\beta$	$\eta_{Z_e} + \eta_{Z_m} + \eta_Z - \lambda_Z$
0	$-2\sin\theta_P/\sin\beta$	$\eta_{Z_{SA}}$
$-T_P$	0	ω_P
0	$-\frac{\sin\theta_P}{\dot\theta_P} - \left(T_P - \frac{\theta_P}{\dot\theta_P}\right)$	ω_Y
0	$-T_R\sin\theta_P - \frac{\text{ver}\,\theta_P}{\dot\theta_P}$	ω_R
0	$\theta_R\sin\theta_P$	C_Z
0	$-\sin\theta_P$	α_R
0	$\dot\theta_R\sin\theta_P$	δT_R
θ_P	0	C_X
-1	0	α_P
$\dot\theta_P$	0	δT_P
0	$\sin\theta_P$	ε_Z
0	$-\text{ver}\,\theta_P$	ε_Y
0	$\cot\beta\sin\theta_P$	b_y
0	$-\sin\theta_P$	b_z
$1 + \frac{1}{G_{FB_P}}$	0	ρ_z
$-\frac{1}{G_{FB_P}}$	0	β_p
0	$\left(1 + \frac{1}{G_{FB_Y}}\right)$	ρ_y
0	$-\frac{1}{G_{FB_Y}}$	β_y

g. Numerical error analysis. The preceding sections have expressed the errors following the midcourse maneuver, as a function of an error-turn matrix and the error-source vector. In order to obtain a numerical value for the pointing, shutoff, and resolution errors, an approximation is devised by computing the root-sum square of the individual error sources multiplied by the maximum value of the particular coefficient. In other words, the angles θ_P, θ_R and β are chosen so as to maximize each individual coefficient of the error matrix. The 3-σ error is given by the square root of the sum of the individual products squared. The results of this technique are given in Table 11, Section III (Trajectory Correction), in the main body of this Report.

To emphasize that this approximation is valid, the root-sum square of the complete equation is derived and compared to the results of Section III of this Report.

Comparison of techniques. The 3-σ error is normally given by the general form of the root-sum square expression

$$\varepsilon = \left[\sum_{n=1}^{N} \{(P_{c_n} + Y_{c_n})\,\varepsilon_{s_n}\}^2\right]^{1/2}$$

$$= \left[\sum_{n=1}^{N} \{\varepsilon'\}\right]^{1/2} = (\varepsilon'')^{1/2} \qquad \text{(D-119)}$$

where

ε_{s_n} = source error; $n = 1 \rightarrow N$

P_{c_n} = pitch coefficient component of pointing vector

Y_{c_n} = yaw coefficient component of the pointing vector

The 3-σ source errors and coefficients are given in Table D-3. Substituting these parameters into Eq. (D-119), squaring, and multiplying, etc., the value of ε'' can be regrouped as a function of $\sin\theta_P$, $\cos\theta_P$, and so on. The constants associated with this analysis are given as:

$\dot{\theta}_R$ = roll turn rate = 3.5 mrad/sec

$\dot{\theta}_P$ = pitch turn rate = 3.5 mrad/sec

T_R = roll turn period = 570 sec

T_P = pitch turn period = 1020 sec

G_{FB_P} = pitch feedback, gyro-autopilot jet-vane loop = 4.0

G_{FB_Y} = yaw feedback, gyro-autopilot jet-vane loop = 4.0

Substituting these values into the expression for ε'' yields

$$\varepsilon'' = (229.75) + (\sin^2\theta_P)\left(\frac{388}{\sin^2\beta} + 37.84\cot\beta + 9\theta_R^2 + 5.3\right) + (\sin\theta_P\cos\theta_P)(14.18\cot\beta - 7.66) + (\sin\theta_P)(21.5 - 3.85\,\theta_P) + (\cos\theta_P)(-8.52) + (\theta_P^2)(10.92) + (\theta_P)(-13.71) \qquad \text{(D-120)}$$

In order to further reduce this expression, the variables θ_R and θ_P, which lie over the respective ranges, (-90 deg $\leq \theta_R \leq 90$ deg) and (45 deg $\leq \beta \leq 135$ deg), must be chosen to maximize ε''. By choosing $\theta_R = 90$ deg and $\beta_{max} = 45$ deg, the value of θ_P that makes ε'' a maximum can be found. Therefore, assuming θ_R and β are constant, the maximum is determined from

$$\frac{d\varepsilon''}{d\theta_P} = 0 \qquad \text{(D-121)}$$

Therefore,

$$\frac{d\varepsilon''}{d\theta_P} = (\sin\theta_P\cos\theta_P)(1682.50) - \sin^2\theta_P(13.08) + \cos\theta_P(21.65) - 3.85\theta_P\cos\theta_P + \sin\theta_P(4.67) + \theta_P(21.84) - 7.27 \qquad \text{(D-122)}$$

The value of θ_P that makes the derivative go to zero is 90.5 deg. By substituting this value into Eq. (D-122), then

$$\varepsilon'' = 1089.89 \qquad \text{(D-123)}$$

is obtained. The actual 3-σ error is given by Eq. (D-119) as

$$\varepsilon' = (1089.89)^{1/2} \qquad \text{(D-124)}$$

Therefore, the 3-σ error is

$$\varepsilon_{3\sigma} = 33.02 \qquad \text{(D-125)}$$

Now, by referring again to the 3-σ value obtained from Table 11 (Sect. III of this Report), the difference in the error is found. For example,

$$\frac{\text{true error} - \text{approximate error}}{\text{true error}} \times 100 = 4.8\% \qquad \text{(D-126)}$$

Table D-3. Error analysis and coefficients for the pointing error

Error source parameter		Units	3σ source error	Pitch coefficient	Yaw coefficient
η_{X_e}	Pitch sensor null offset—*E*	mrad	0.5	-1	0
η_{X_m}	Pitch sensor null offset—*M*	mrad	2.2	-1	0
λ_X	Pitch initial dead zone position	mrad	5.0	$+1$	0
$\eta_{X_{SA}}$	Pitch switch amp. null offset	mrad	1.0	-2	0
η_{Y_e}	Yaw sensor null offset—*E*	mrad	0.5	0	$-(\cos\theta_P + \cot\beta \sin\theta_P)$
η_{Y_m}	Yaw sensor null offset—*M*	mrad	2.2	0	$-(\cos\theta_P + \cot\beta \sin\theta_P)$
λ_Y	Yaw initial dead zone position	mrad	5.0	0	$+\sqrt{\cos^2\theta_P + \cot^2\beta \sin^2\theta_P}$
$\eta_{Y_{SA}}$	Yaw switch amp. null offset	mrad	1.0	0	$-(2\cos\theta_P + \cot\beta \sin\theta_P)$
η_{Z_e}	Roll sensor null offset—*E*	mrad	8.0	0	$-(\sin\theta_P/\sin\beta)$
η_{Z_m}	Roll sensor null offset—*M*	mrad	1.73	0	$-(\sin\theta_P/\sin\beta)$
λ_Z	Roll initial dead zone position	mrad	15.0	0	$+(\sin\theta_P/\sin\beta)$
$\eta_{Z_{SA}}$	Roll switch amp. null offset	mrad	1.0	0	$-(2\sin\theta_P/\sin\beta)$
ω_P	Pitch gyro drift	mrad/sec	4.85×10^{-3}	$-T_P$	0
ω_Y	Yaw gyro drift	mrad/sec	4.85×10^{-3}	0	$-\left(\frac{\sin\theta_P}{\dot\theta_P} + T_P - \frac{\theta_P}{\dot\theta_P}\right)$
ω_R	Roll gyro drift	mrad/sec	4.85×10^{-3}	0	$-\left(T_R \sin\theta_P + \frac{1}{\dot\theta_P} - \frac{\cos\theta_P}{\dot\theta_P}\right)$
C_Z	Roll turn calibration	mrad/rad	3.0	0	$\theta_R \sin\theta_P$
α_R	Roll capacitor leakage	mrad	5.0	0	$-(\sin\theta_P)$
δ_{T_R}	Roll turn time resolution	sec	0.867	0	$\theta_R \sin\theta_P$
C_X	Pitch turn calibration	mrad/rad	3.0	θ_P	0
α_P	Pitch capacitor leakage	mrad	5.0	-1	0
δ_{T_P}	Pitch turn time resolution	sec	0.867	θ_P	0
ε_z	Yaw gyro roll misalignment	mrad	1.53	0	$\sin\theta_P$
ε_y	Roll gyro yaw misalignment	mrad	1.53	0	$-(1 - \cos\theta_P)$
b_y	Roll sensor hinge misalignment (yaw)	mrad	2.6	0	$\cot\beta \sin\theta_P$
b_z	Roll sensor hinge misalignment (roll)	mrad	2.6	0	$-(\sin\theta_P)$
ρ_X	C.G. location, angular error (pitch)	mrad	5.0	$1 + 1/G_{FB_P}$	0
β_P	Thrust vector, angular error (pitch)	mrad	2.8	$-1/G_{FB_P}$	0
ρ_Y	C.G. location, angular error (yaw)	mrad	5.0	0	$1 + 1/G_{FB_Y}$
β_Y	Thrust vector, angular error (yaw)	mrad	2.8	0	$-1/G_{FB_Y}$
η_{Z_a}	Roll sensor albedo asymmetry	mrad	9.6	0	$-(\sin\theta_P \sin\beta)$

The results of Eq. (D-126) show that a difference of 4.8% in the derivation of the 3-σ error is obtained by maximizing the individual components of the error, then root-sum squaring instead of maximizing the entire expression and then taking the square root to obtain the 3-σ error. This brief analysis shows that the technique for obtaining the 3-σ pointing error described in the body of the Report is adequate.

2. Terminal Maneuver

The terminal maneuver is critical in that the spacecraft orientation must provide precise positioning of the television cameras so as to fulfill the mission objective of obtaining close-up pictures of the lunar surface.

To do so, the attitude control system maneuvers the spacecraft through a pitch-yaw-pitch turn sequence.

The maneuver requires that celestial control be broken about the pitch and yaw (Sun) axes and inertial control be reinstated. Hence, the gyros are commanded to turn the spacecraft in some pre-computed manner and thus point the cameras parallel to the trajectory of the spacecraft and the Moon. The roll axis remains under Earth sensor error signal control, and the directional antenna is constantly pointed toward the Earth, providing the communications capability for sending the TV pictures back to the Earth.

The maneuver, as presented above, is critical and the errors introduced by the turn must be considered; therefore, an error analysis is considered.

a. Constraints on the turns. The Earth-probe-Sun angle constraints imposed on the maneuver are enumerated below.

1. Prior to the maneuver, the antenna angle (during the Earth lock) shall be less than $\theta_H = 136.5$ deg–½ (apparent Earth diameter).
2. The EPS angle must be greater than 47 deg when Sun lock is broken at the initiation of the terminal maneuver.
3. During the terminal maneuver, the Earth-probe (near-lit-limb of the Moon) angle shall be greater than 15 deg.
4. During the terminal maneuver, the antenna angle must be less than 137 deg.

Discussion of the constraints. At the time of pre-terminal maneuver, it is not enough to have the main optical axis unobstructed. Accuracy considerations require that the entire Earth sensor field of view be unobstructed; hence, the following antenna angle constraint formulation is presented:

$$\theta_H = 150 \text{ deg} - 10 \text{ deg} - \tfrac{1}{2}(\text{apparent Earth diameter}) - 3.5 \text{ deg}$$
$$= 136.5 \text{ deg} - \tfrac{1}{2}(\text{apparent Earth diameter})$$

where the 10-deg angle is ½ of the field of view of the Earth sensor.

When Sun lock is broken at the initiation of the terminal maneuver, the EPS angle must be greater than 47 deg, again a result of reflected light testing. During the terminal maneuver, after the turns have been completed, the antenna angle is constrained to be less than 137 deg, again a reflected light consideration.

One last constraint, not on the EPS angle, is that during terminal maneuver, to prevent acquisition of the Moon, the Earth-probe (near-lit-limb of the Moon) angle must be greater than 15 deg.

b. Axis of rotation. The axis of rotation during any given turn is defined by the intersection of the two null control planes operating during the turn. For example, the sequence of turns is:

1. A pitch turn which places the spacecraft x-y plane parallel to the probe-Earth line of sight.
2. A yaw turn which places the spacecraft z-axis in some desired plane.
3. A pitch turn which places the spacecraft z-axis parallel to some desired line.

Therefore, during the pitch turn the null planes will be roll and yaw null planes, where the roll is determined by the antenna hinge axis and the line to the Earth and the yaw null plane is formed by the spin and output axes of the yaw gyro. If the roll plane were given by the vector cross product

$$\mathbf{R} = \mathbf{X}_H \times \mathbf{G}$$

where

$\mathbf{X}_H$ = hinge axis

$\mathbf{G}$ = line of sight to the Earth

and the yaw plane is denoted by

$$\mathbf{Y} = \mathbf{Y}_{GS} \times \mathbf{Y}_{GO}$$

where

$\mathbf{Y}$ = yaw gyro input axis = unit vector j

$\mathbf{Y}_{GS}$ = yaw gyro spin axis = unit vector k

$\mathbf{Y}_{GO}$ = yaw gyro output axis = unit vector i

then the intersection of the roll and yaw null planes is given by $\mathbf{Y} \times \mathbf{R}$, and this is the instantaneous axis of rotation of the spacecraft for a pitch turn. That the axis moves during a given turn is evidenced by noting that $\mathbf{X}_H$, $\mathbf{Y}_{GS}$, and $\mathbf{Y}_{GO}$ are fixed to and move with the spacecraft, and $\mathbf{G}$ is fixed in inertial space. This procedure for determining the axis of rotation will, for an error-free condition, produce the x and y axis spacecraft axes as nominal pitch and yaw axes, respectively.

c. Method of analysis of the terminal errors. The determination of the error in orientation of the vehicle at

the conclusion of the terminal maneuver is achieved by comparing (1) a vector taken through an error-free transformation to (2) the same vector taken through an error-laden transformation. This is similar to the midcourse maneuver error analysis. Therefore, we can write

$\mathbf{V}_s$ = an error-free vector

$\mathbf{V}_e$ = an arbitrary error-laden vector

and $\mathbf{V}_e$ can be colinearized with $\mathbf{V}_s$ by an infinitesimal error rotation matrix E, so

$$\mathbf{V}_s = [E]\,\mathbf{V}_e \tag{D-127}$$

where

$$[E] = \begin{bmatrix} 1 & +e_{roll} & -e_{yaw} \\ -e_{roll} & 1 & +e_{pitch} \\ +e_{yaw} & -e_{pitch} & 1 \end{bmatrix} \tag{D-128}$$

The development and generation of the error matrix E is achieved as follows.

Let $\mathbf{V}_o$ be a pre-maneuver vector in body axes coordinates; then under an error-free transformation,

$$\mathbf{V}_s = [A_s]\,\mathbf{V}_o \tag{D-129}$$

The desired relationship between $\mathbf{V}_s$ and $\mathbf{V}_e$ is found from Eq. (D-127) and (D-129) as

$$\mathbf{V}_s = [A_s]\,[A]^{-1} \quad \mathbf{V} = [E]\,\mathbf{V} \tag{D-130}$$

The elements of $[E]$ describe the set of infinitesimal rotations required to align the error-laden vector with the error-free vector. To verify that $[A_s]\,[A]^{-1} = [E]$, it is necessary to discuss the nature of the rotation matrix A.

Discussion of the integrating matrix. The rotation matrix A is made up of three turns of the vehicle; i.e., pitch, yaw, and pitch, as well as some error rotation e. The conventional development of a rotation matrix of three or four finite rotations is not strictly applicable for this study since the error, e, may give rise to a moving axis of rotation during the turns. A satisfactory solution to this difficulty lies in the development of a numerically integrated turn matrix.

Consider the arbitrary vector $\mathbf{V}$ which is taken through the transformation $[A]$, that is

$$\mathbf{V} = [A]\,\mathbf{V}_o \tag{D-131}$$

The matrix A is to be made up of a number of increments $d\theta$. If $\mathbf{V}$ is defined to be the axis of rotation, then a change in the axis of rotation $\mathbf{dV}$ is given by

$$\mathbf{dV} = \mathbf{d\theta} \times \mathbf{V} \tag{D-132}$$

where, from Fig. D-17 below,

$$\mathbf{V} = V\cos\alpha_1\,\mathbf{i} + V\cos\alpha_2\,\mathbf{j} + V\cos\alpha_3\,\mathbf{k}$$

$$\mathbf{d\theta} = d\theta\cos\alpha_1\,\mathbf{i} + d\theta\cos\alpha_2\,\mathbf{j} + d\theta\cos\alpha_3\,\mathbf{k} \tag{D-133}$$

Therefore, the crossproduct gives

$$\mathbf{dV} = \begin{vmatrix} i & j & k \\ V\cos\alpha_1 & V\cos\alpha_2 & V\cos\alpha_3 \\ d\theta\cos\alpha_1 & d\theta\cos\alpha_2 & d\theta\cos\alpha_3 \end{vmatrix}$$

$$= \begin{bmatrix} V\cos\alpha_2 & d\theta\cos\alpha_3 & -V\cos\alpha_3 & d\theta\cos\alpha_2 \\ V\cos\alpha_3 & d\theta\cos\alpha_1 & -V\cos\alpha_1 & d\theta\cos\alpha_3 \\ V\cos\alpha_1 & d\theta\cos\alpha_2 & -V\cos\alpha_2 & d\theta\cos\alpha_1 \end{bmatrix}$$

$$= \begin{bmatrix} 0 & d\theta\cos\alpha_3 & -d\theta\cos\alpha_2 \\ -d\theta\cos\alpha_3 & 0 & d\theta\cos\alpha_1 \\ d\theta\cos\alpha_2 & -d\theta\cos\alpha_1 & 0 \end{bmatrix} \begin{bmatrix} V\cos\alpha_1 \\ V\cos\alpha_2 \\ V\cos\alpha_3 \end{bmatrix} \tag{D-134}$$

Now

$$\mathbf{V} + \mathbf{dV} = \begin{bmatrix} 1 & d\theta\cos\alpha_3 & -d\theta\cos\alpha_2 \\ -d\theta\cos\alpha_3 & 1 & d\theta\cos\alpha_1 \\ d\theta\cos\alpha_2 & -d\theta\cos\alpha_1 & 1 \end{bmatrix} \mathbf{V} \tag{D-135}$$

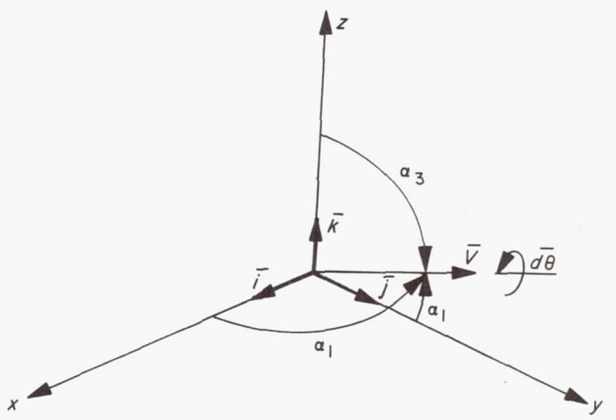

Fig. D-17. Coordinate description, terminal maneuver

At this time, we can introduce a shorter set of notations and relate $\mathbf{V} + \mathbf{dV}$ to the pre-maneuver vector $\mathbf{V}_o$.

Let

$$\mathbf{V} = [A]\,\mathbf{V}_o$$

$$\mathbf{dV} = [dA]\,\mathbf{V}$$

where

$$[dA] = \begin{bmatrix} 0 & +d\theta\cos\alpha_3 & -d\theta\cos\alpha_2 \\ -d\theta\cos\alpha_3 & 0 & +d\theta\cos\alpha_1 \\ d\theta\cos\alpha_2 & -d\theta\cos\alpha_1 & 0 \end{bmatrix} \quad \text{(D-136)}$$

and the form of the above expression is the same as that derived in the Small Perturbation Analysis section of this Appendix D. Now adding $\mathbf{V}$ and $\mathbf{dV}$ leads to the expression

$$\begin{aligned} \mathbf{V} + \mathbf{dV} &= [A]\,\mathbf{V}_o + \mathbf{dAV} \\ &= [A]\mathbf{V}_o + [dA]\,[A]\,\mathbf{V}_o \\ &= [I + dA]\,[A]\,\mathbf{V}_o \\ &= [I + dA]\,\mathbf{V} \end{aligned} \quad \text{(D-137)}$$

Now, this set of equations suggests the following iterative formula for updating the turn matrix for successive increments of $d\theta$, as follows:

$$\mathbf{V}^{n+1} = [A^{n+1}]\,\mathbf{V}_o = [I + dA]\,[A^n]\,\mathbf{V}_o \quad \text{(D-138)}$$

since

$$[A^{n+1}] = [I + dA]\,[A^n] \quad \text{(D-139)}$$

Integrating matrix iteration procedure. The process of solving the integrating matrix is similar to an open-loop iteration; the formula is given by

$$[A^{n+1}] = \begin{bmatrix} 1 & \cos\alpha_3\,d\theta & -\cos\alpha_2\,d\theta \\ -\cos\alpha_3\,d\theta & 1 & \cos\alpha_1\,d\theta \\ \cos\alpha_2\,d\theta & -\cos\alpha_1\,d\theta & 1 \end{bmatrix} [A^n] \quad \text{(D-140)}$$

As an example, if a pitch turn is performed, Eq. (D-140) reduces to

$$[A^{n+1}] = \begin{bmatrix} 1 & 0 & 0 \\ 0 & 1 & d\theta \\ 0 & -d\theta & 1 \end{bmatrix} [A^n]$$

$$[A^o] = \begin{bmatrix} 1 & 0 & 0 \\ 0 & 1 & 0 \\ 0 & 0 & 1 \end{bmatrix} \quad \text{(D-141)}$$

Now by looking at the components of $[A^{n+1}]$ in Eq. (D-141), the following formulas are obtained:

$$\begin{aligned} a_{22}^{n+1} &= (1)\,(a_{22}^n) + (d\theta)\,(a_{32}^n) \\ a_{23}^{n+1} &= (1)\,(a_{23}^n) + (d\theta)\,(a_{33}^n) \\ a_{33}^{n+1} &= a_{22}^{n+1} \\ a_{32}^{n+1} &= -a_{23}^{n+1} \end{aligned} \quad \text{(D-142)}$$

For n successive increments of $d\theta$, the following elements are generated and are shown in Table D-4, below.

Table D-4. Integrating matrix coefficients

n	a_{22}	
0	1	$= 1$
1	$1 + 0$	$= 1$
2	$1 + (d\theta)\,(-d\theta)$	$= 1 - d^2\theta$
3	$1 - d^2\theta + (d\theta)\,(-2d\theta)$	$= 1 - 3d^2\theta$
4	$1 - 3d^2\theta + d\theta\,(-3d\theta + d^3\theta)$	$= 1 - 6d^2\theta + d^4\theta$
5	$1 - 6d^2\theta + d^4\theta + d\theta\,(4d\theta - 4d^3\theta)$	$= 1 - 10d^2\theta + 5d^4\theta$
6	$1 - 10d^2\theta + 5d^4\theta + d\theta\,(5d\theta - 10d^3\theta + d^5\theta)$	$= 1 - 15d^2\theta + 15d^4\theta - d^6\theta$
7	. . . . .	
. . .	. . . . .	
n	$1 - \frac{n(n-1)\,d^2\theta}{2} + \frac{n(n-1)(n-2)(n-3)\,d^4\theta}{24} + \cdots$	

n	a_{23}	
0	0	$= 0$
1	$0 + d\theta$	$= 1d\theta$
2	$d\theta + d\theta$	$= 2d\theta$
3	$2d\theta + d\theta\,(1 - d^2\theta)$	$= 3d\theta - d^3\theta$
4	$3d\theta - d^3\theta + d\theta\,(1 - 3d^2\theta)$	$= 4d\theta - 4d^3\theta$
5	$4d\theta - 4d^3\theta + d\theta\,(1 - 6d^2\theta + d^4\theta)$	$= 5d\theta - 10d^3\theta + d^5\theta$
6	$5d\theta - 10d^3\theta + d^5\theta + d\theta\,(1 - 10d^2\theta + 5d^4\theta)$	$= 6d\theta - 20d^3\theta + 6d^5\theta$
7	. . . . .	
. . .	. . . . .	
n	$n\,d\theta - \frac{n(n-1)(n-2)\,d^3\theta}{6} + \frac{n(n-1)(n-2)(n-3)(n-4)\,d^5\theta}{120} + \cdots$	

As the turns for the maneuver develop, the coefficients of the rotation matrix approximate those for a finite turn rotation, as

$$a_{22} = 1 - \frac{n(n-1)\theta^2}{2n^2} + \frac{n(n-1)(n-2)(n-3)\theta^4}{24n^4} - \cdots \quad \text{(D-143)}$$

$$a_{23} = \theta - \frac{n(n-1)(n-2)\theta^3}{2n^3} + \frac{n(n-1)(n-2)(n-3)(n-4)\theta^5}{120n^5}$$

where n = the index of $d\theta$ and $\theta = n\,d\theta$.

From the above expressions, it can be seen that as n becomes progressively larger, a_{22} and a_{23} approach the cosine and sine series expansions, as follows:

$$\sin\theta = \theta - \frac{\theta^3}{6} + \frac{\theta^5}{120} - \cdots$$

$$\cos\theta = 1 - \frac{\theta^2}{2} + \frac{\theta^4}{24} - \cdots$$

Using this iterative rotation matrix method, the pre-maneuver vector is given by

$$\mathbf{V}_s = [A_s]\,\mathbf{V}_o \quad \text{(D-144)}$$

and

$$\mathbf{V}_e = [I + dA]\,[A_s]\,\mathbf{V}_o \quad \text{(D-145)}$$

when transformed through an error-free and an error-laden maneuver, respectively. Now $[I + dA]$ can be identified with a set of infinitesimal rotations required to align $\mathbf{V}_s$ with $\mathbf{V}_e$, that is to say that,

$$\begin{aligned} e_{pitch} &= \cos\alpha_1\,d\theta \\ e_{yaw} &= \cos\alpha_2\,d\theta \\ e_{roll} &= \cos\alpha_3\,d\theta \end{aligned} \quad \text{(D-146)}$$

Effect of null offset in roll. As an example of the above method, the effect of the static null offset in the roll channel is studied. Let the roll offset, η, be defined, for which the small angle assumption holds. The vector **G**, which defines the probe-Earth line, nominally lies in the y-z plane of the spacecraft. However, a null offset will cause the probe-Earth line to lie out of the spacecraft y-z plane, and, hence, the vector **G** can be represented with a small angle assumption of η, as

$$\mathbf{G}_o = \eta\mathbf{i} - \sin\beta\mathbf{j} - \cos\beta\mathbf{k} \quad \text{(D-147)}$$

$$\beta = EPS \text{ angle} < 90 \text{ deg} \quad \text{(D-148)}$$

Now if the first pitch turn θ_{p_1} is executed, the vector **G** can be written as

$$\mathbf{G}(\theta_{p_1}) = \begin{bmatrix} 1 & 0 & 0 \\ 0 & \cos\theta_{p_1} & \sin\theta_{p_1} \\ 0 & -\sin\theta_{p_1} & \cos\theta_{p_1} \end{bmatrix} \begin{matrix} \eta \\ -\sin\beta \\ -\cos\beta \end{matrix}$$

$$= \begin{matrix} \eta \\ -\cos\theta_{p_1}\sin\beta - \sin\theta_{p_1}\cos\beta \\ \sin\theta_{p_1}\sin\beta - \cos\theta_{p_1}\cos\beta \end{matrix} \quad \text{(D-149)}$$

using the trigonometric substitution

$$\mathbf{G}(\theta_{p_1}) = \begin{matrix} \eta \\ -\sin(\theta_{p_1} + \beta) \\ -\cos(\theta_{p_1} + \beta) \end{matrix} \quad \text{(D-150)}$$

The roll null plane during the first pitch turn is given by

$$\mathbf{R} = \mathbf{X}_H \times \mathbf{G}(\theta_{p_1}) = \begin{vmatrix} i & j & k \\ 1 & 0 & 0 \\ \eta & -\sin(\theta_{p_1} + \beta) & -\cos(\theta_{p_1} + \beta) \end{vmatrix}$$

$$= \begin{matrix} 0 \\ \cos(\theta_{p_1} + \beta) \\ -\sin(\theta_{p_1} + \beta) \end{matrix} \quad \text{(D-151)}$$

The yaw null plane is given by

$$\mathbf{Y} = \mathbf{Y}_{GS} \times \mathbf{Y}_{GO} = \mathbf{j} \quad \text{(D-152)}$$

The axis of rotation of the spacecraft during the first pitch turn is then given by the intersection of the roll null plane and the yaw null plane, as

$$\mathbf{V} = \mathbf{Y} \times \mathbf{R}_{o_{p_1}} \quad \text{(D-153)}$$

$$\mathbf{V} = \begin{vmatrix} i & j & k \\ 0 & 1 & 0 \\ 0 & \cos(\theta_{p_1} + \beta) & -\sin(\theta_{p_1} + \beta) \end{vmatrix} = \begin{bmatrix} \sin(\theta_{p_1} + \beta) \\ 0 \\ 0 \end{bmatrix} \tag{D-154}$$

Note that the range of the first pitch turn is

$$0° \leq \theta_{p_1} \leq (90° - \beta°)$$

so that the axis of rotation is about the nominal spacecraft x-axis throughout the entire first pitch turn. At the completion of the turn,

$$\mathbf{G}(\theta_{p_1}) = \mathbf{G}_1 = \begin{bmatrix} \eta \\ -1 \\ 0 \end{bmatrix} \tag{D-155}$$

Following the pitch turn, the yaw turn commences about the nominal spacecraft y-axis; the motion of the instantaneous axis of rotation is determined below, as

$$\mathbf{G}_1(\theta_y^n) = \begin{bmatrix} \cos\theta_y^n & 0 & \sin\theta_y^n \\ 0 & 1 & 0 \\ -\sin\theta_y^n & 0 & \cos\theta_y^n \end{bmatrix} \begin{bmatrix} \eta \\ -1 \\ 0 \end{bmatrix} = \begin{bmatrix} \eta\cos\theta_y^n \\ -1 \\ -\eta\sin\theta_y^n \end{bmatrix} \tag{D-156}$$

Note: The G vector will describe a cone about the nominal spacecraft $-y$-axis as seen in body fixed coordinates i, j, and k. The roll null plane is determined by

$$\mathbf{R}(\theta_y^n) = \mathbf{X}_H \times \mathbf{G}_1(\theta_y^n) = \begin{vmatrix} i & j & k \\ 1 & 0 & 0 \\ \eta\cos\theta_y^n & -1 & -\eta\sin\theta_y^n \end{vmatrix} = \begin{bmatrix} 0 \\ +\eta\sin\theta_y^n \\ -1 \end{bmatrix} \tag{D-157}$$

During the yaw turn the pitch gyro is operative, and the pitch null plane can be denoted by the cross product of the spin axis and the output axis of the pitch gyro, as

$$\mathbf{P} = 1\dot{\mathbf{r}}$$

so that the instantaneous axis of rotation of the spacecraft during the yaw turn is given by

$$\mathbf{V}(\theta_y^n) = \mathbf{P} \times \mathbf{R}(\theta_y^n) = \begin{vmatrix} i & j & k \\ 1 & 0 & 0 \\ 0 & \eta\sin\theta_y^n & -1 \end{vmatrix} = \begin{bmatrix} 0 \\ +1 \\ \eta\sin\theta_y^n \end{bmatrix} \tag{D-158}$$

Note: The axis of rotation at the commencement of the yaw turn is

$$\mathbf{V}(\theta_y) = \mathbf{j}$$

and, at the conclusion of the yaw turn, is

$$\mathbf{V}(\theta_y) = \mathbf{j} + \sin\theta_y\mathbf{k}$$

If the axis of rotation is specified by the direction cosines of α_1, α_2, α_3 and if these are to be updated during the yaw turn, then

$$\alpha_1 = \frac{\pi}{2}$$

$$\alpha_2 = |\eta \sin\theta_y|$$

$$\alpha_3 = \frac{\pi}{2} - \eta\sin\theta_y$$

The range of θ_y is $0 \rightarrow \theta_y$ final. If the rotation matrix is denoted by $A(\theta_y)$, identification with the integration matrix previously developed is obtained. It is possible to describe the angles α_i with the **G** vector by observing that

$$-\eta\sin\theta_y = g_3(\theta_y)$$

and g_3 is the k component of **G**. Now,

$$\alpha_1 = \frac{\pi}{2}$$

$$\alpha_2 = |g_3|$$

$$\alpha_3 = \frac{\pi}{2} - g_3$$

Remembering that the integration rotation matrix A is the composite of all previous turns, the instantaneous value of **G** is given at all times by the relationship

$$\mathbf{G}_i = [A^n]\,\mathbf{G}_o$$

The coordinates of the probe-Earth vector during the second pitch turn are now given by

$$\mathbf{G}(\theta_y, \theta_{p_2}) = \begin{bmatrix} 1 & 0 & 0 \\ 0 & \cos\theta_{p_2} & \sin\theta_{p_2} \\ 0 & -\sin\theta_{p_2} & \cos\theta_{p_2} \end{bmatrix} \begin{bmatrix} \eta\cos\theta_y \\ -1 \\ -\eta\sin\theta_y \end{bmatrix} \tag{D-159}$$

$$= \begin{bmatrix} \eta\cos\theta_y \\ -\cos\theta_{p_2} - \eta\sin\theta_{p_2}\sin\theta_y \\ \sin\theta_{p_2} - \eta\cos\theta_{p_2}\sin\theta_y \end{bmatrix}$$

$$= \begin{bmatrix} g_1(\theta_y) \\ g_2(\theta_y, \theta_{p_2}) \\ g_3(\theta_y, \theta_{p_2}) \end{bmatrix}$$

The roll null plane is expressed by

$$\mathbf{R}(\theta_y, \theta_{p_2}) = \mathbf{X}_H \times \mathbf{G}(\theta_y, \theta_{p_2})$$

$$= \begin{vmatrix} i & j & k \\ 1 & 0 & 0 \\ g_1(\theta_y) & g_2(\theta_{y_1}, \theta_{p_2}) & g_3(\theta_y, \theta_{p_2}) \end{vmatrix} \tag{D-160}$$

$$= g_2(\theta_y, \theta_{p_2})\,\mathbf{i}$$

This shows that during the second pitch turn the instantaneous axis of rotation is the nominal spacecraft x-axis.

Effect of the roll limit cycle. In the previous section, the axis of rotation was shown to be invariant during the first pitch turn. The probe-Earth vector is given as

$$\mathbf{G}(\theta_{p_1}) = \begin{bmatrix} \eta \\ -\sin(\theta_{p_1} + \beta) \\ -\cos(\theta_{p_1} + \beta) \end{bmatrix} \tag{D-161}$$

At this time, we are interested in showing that the effect of the roll limit cycle should be taken into account in the digital computer program for the error analysis. If we let η be a dynamic offset due to the limit cycling rather than the static null offset, then the amplitude of the roll limit cycle is a function of the *EPS* angle β, and is shown in Fig. D-18, where the parameters are the following:

θ_r = roll angle about the z axis

η = arc length amplitude of the limit cycle measured at the Earth sensor

G = reference or true Earth-probe vector

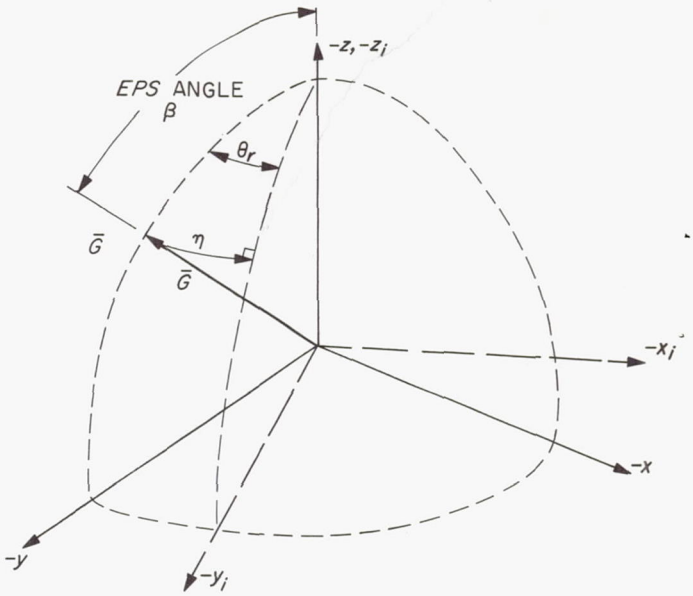

Fig. D-18. Roll-limit cycle geometry

x, y, z = spacecraft coordinates such that G_{ref} lies in the x-y plane

x_i, y_i, z_i = instantaneous, actual spacecraft coordinates

β = Earth-probe-Sun angle (EPS)

By solving the θ_r, η, β spherical triangle, the relationship

$$\frac{\sin\beta}{\sin 90^\circ} = \frac{\sin\eta}{\sin\theta_r}$$

is obtained. Since η and θ_r are assumed to be small angles,

$$\theta_r \simeq \frac{\eta}{\sin\beta}$$

The amplitude of the roll limit cycle is referenced to a hinge angle of 90 deg (equivalent to $\beta = 90$ deg). Therefore,

$$\theta_r \simeq \eta \simeq \theta_r(90^\circ)$$

The roll amplitude for an arbitrary β is

$$\theta_r \simeq \frac{\theta_r(90^\circ)}{\sin\beta}$$

Some numerical values for the roll limit cycle, assuming $\beta = 90$ deg, are

limit cycle amplitude = ± 5.0 mrad

limit cycle rate = ± 14.7 mrad/sec

These data imply that the period of oscillation is

$$T = \frac{10.0 \text{ mrad}}{14.7 \text{ mrad/sec}} \times 2 = 1360 \text{ sec}$$

Since the turning rate is given as $\dot{\theta} = 3.5$ mrad/sec $= 0.2$ deg/sec, we have approximately 0.37 cycles/deg θ_{p_1}. If a typical turn of $\theta_{p_1} = 16.7$ deg is considered, the period for the turn is determined to be 84 sec. The maximum time allotted for the turn is 450 sec. This is therefore about one-third of the time required to complete a cycle of the roll oscillation, and the amplitude of the roll limit cycle will not reach the minimum value obtained when $\beta = 90$ deg, before the yaw turn is commenced.

APPENDIX E

Celestial Sensors

The Sun is the primary reference toward which the axis of symmetry (roll axis) of the spacecraft is directed in response to signals from an array of photoconductive cells. The Earth reference is acquired using a two-axis optical sensor mechanized around three photo-multiplier tubes. This sensor is mounted to and moves with the high-gain antenna hinge motion (about pitch axis) and is directed toward the Earth by the hinge motion and by rolling the spacecraft. The Earth sensor thus controls the roll attitude of the spacecraft and the hinge angle of the antenna to keep the antenna pointed toward the Earth.

1. Sun Sensor

The *Ranger* Sun sensors are optical devices which use a shadow technique on a photoconductive detector. The primary Sun sensor detector was originally cadmium selenide and was changed to cadmium sulphide since the cadmium-sulphide doping used a low-temperature coefficient of resistance at high light levels and a low hysteresis value. The sensors are divided into primary and secondary units. The primary units (Fig. E-1) are mounted on the frame of the spacecraft and nominally point at the Sun during the flight limit-cycle operation. The secondary units (Fig. E-1) are used to complete a spherical field of view requirement and are mounted on the underside of the solar panel tips; they function only during acquisition of the Sun.

a. Sensor description. The detectors are connected in a bridge circuit (Fig. E-2). The output signal is a voltage developed across the 110 K resistance load. In the spacecraft, this load will be the input resistance of a switching amplifier and telemetry impedance. The sensor positive and negative supplies will be *zener* regulated to 16.8 v from the spacecraft's 26-v supplies.

b. Analytical description. An analysis of the circuit (Fig. E-2) leads to the following equation for the primary Sun sensor voltage output:

$$E_o = \frac{E(R_2 - R_1)}{R_1 + R_2 + \dfrac{R_1 R_2}{R_L}} \qquad \text{(E-1)}$$

where R_1 and R_2 are the resistance values of primary detectors A and F.

Due to the shadowing method on the semiconductor, the resistances of the cell as a function of angle from null are very closely approximated by

$$R_{1,2} = Ae^{-b\Delta\theta} \qquad \text{(E-2)}$$

where $\Delta\theta$ is the angular deviation of sensor from null in degrees.

The sign on the exponent is opposite for two opposed detectors. Although the constants A and b vary with the particular cell chosen, paired detectors with these constants approximately equal have been obtained through a matching process. The nominal values are $A = 6$ K ohms and $b = 0.962$ deg^{-1}. Using these forms for R_1 and

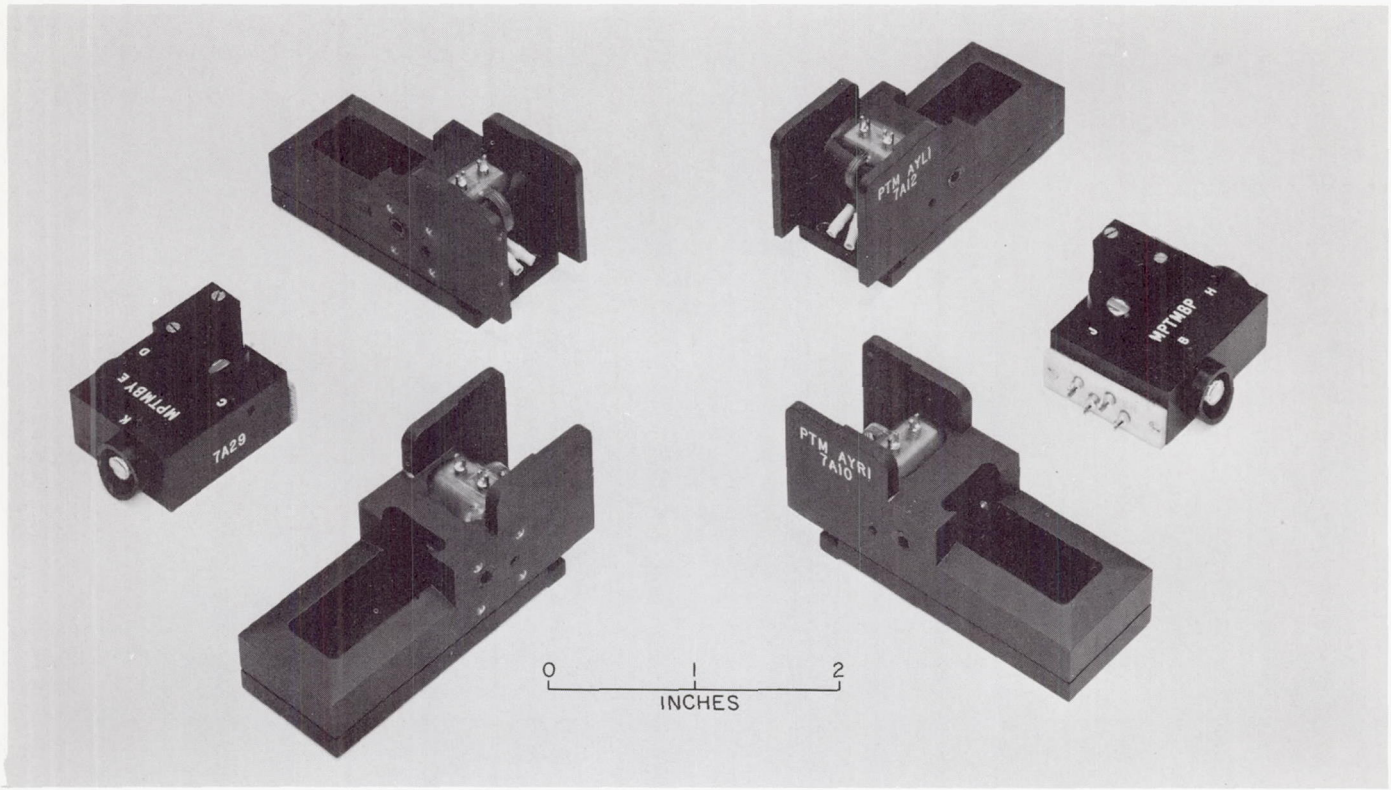

Fig. E-1. Sun sensors

R_2, the voltage output as a function of angle from null becomes

$$E_o = \frac{2E \sinh (b\Delta\theta)}{2 \cosh (b\Delta\theta) + \dfrac{A}{R_L}} \qquad \text{(E-3)}$$

To better understand the effect of each environmental condition on Sun sensor performance, accurate before-and-after data were taken. The information is tabulated in Table E-1.

c. Mounting sensors. The secondary Sun sensors are mounted on the solar panels and may undergo a significant thermal shock between injection and Sun acquisition due to removal of the hot shroud. Unpotted detectors in their housings were subjected to a thermal shock of 18°F/min from 250 to −100°F with no damage or change in characteristics. However, in potted units which underwent the same test, the enclosed glass detector cracked.

Table E-1. Sun sensor statistical test results (group of 24 primary pairs)

Null offset	Average value (sec of arc)	1σ distribution about the mean (sec of arc)
At 70°F	+0.72	12
At 40°F	−5.0	22
At 140°F	+0.72	28 (only 16 pairs sampled)
At 160°F	+15.5	31 (only 8 pairs sampled)
At 0.7 solar constant	+0.72	12
At 0.5 solar constant	+2.1	— } only 6 pairs
At 0.35 solar constant	−3.3	15 } sampled
After flight acceptance testing	−2.5	20
Scale factor	**Average change (%)**	**1σ distribution (%)**
At 70°F	0	—
At 40°F	−1.15	2.9
At 140°F	+3.14	1.6 (only 16 pairs sampled)
At 160°F	+10.26	4.8 (only 8 pairs sampled)
At 0.7 solar constant	0	—
At 0.5 solar constant	−0.74	0.316 } only 6 pairs
At 0.35 solar constant	−0.76	0.7 } sampled
After flight acceptance testing	+0.17	2.16

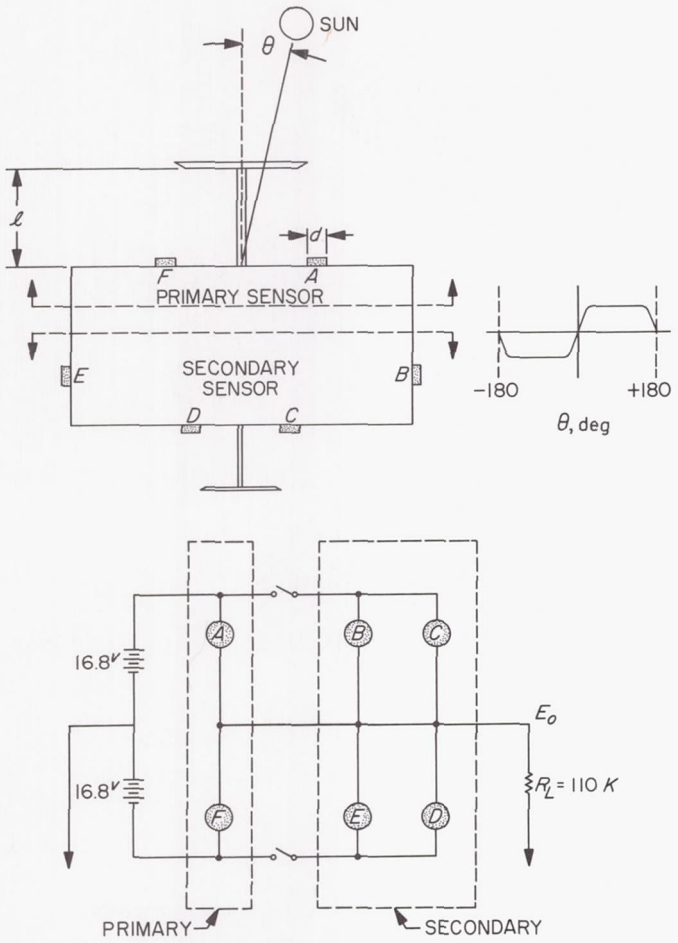

Fig. E-2. Sun-sensor schematic

The problem of mounting the Sun sensor detector has been solved by employment of quad-rings. The quad-rings bring support to bear on the strongest section of the glass detector envelope rather than complete support as provided by the potting compound. With utilization of the quad-ring mounting, a Sun sensor assembly can survive an extreme temperature range from −100 to +125°C without failure.

d. Sun sensor testing and Sun simulation. There are many difficulties inherent in the problem of simulating an extremely bright, collimated light source. Therefore, most of the Sun sensor testing has been done with the Sun as the source. A temporary test site was constructed at Chilao, California (Fig. E-3). The facility uses a two-mirror coelostat system to provide a collimated Sun bundle at a constant position. This bundle is directed through a tube into a trailer to a Leitz optical dividing head which rests on a stable tripod. The system includes a bore sighting telescope and motors to drive the coelostat

Fig. E-3. Chilao test site

mirrors. The over-all accuracy of the pointing system is better than 10 sec of arc. The sensors are tested by mounting them on the dividing head and positioning to known angles, while monitoring the outputs.

2. Earth Sensor

Earth sensor optical mechanization is much the same as the Sun sensor in that a variable aperture shadowing technique is used. The detectors in this case are three ¾-in.-D end-on photomultiplier tubes arranged so that their current outputs can be resolved into two-axis error signals. The expected variation of Earth-light intensity is in the range of 0.06–40 ft-candles.

The *Ranger* Earth sensor, previously described in JPL *SPS 37-16*, Vol. 1, has been modified for missions of Block III. A very large field of view (40 × 60 deg) had been incorporated into the earlier units so that changes in acquisition preset hinge angle would not be necessary during any launch period. The large field of view, however, presented many constraints to the *Ranger* terminal maneuver and picture-taking mission. In order to circumvent these constraints, the field of view was reduced to ±5 deg in roll and to ±10 deg in hinge for the *Ranger* 6 and all subsequent missions (*RA* 7 through 9). An eight-position antenna preset-hinge-angle update system has also been incorporated to make the small field of view possible.

Linear range extends only several degrees on either axis from null, at which points the output error signals saturate and remain saturated to the field of view limits. A typical plot around a null is shown in Fig. E-4 and E-5.

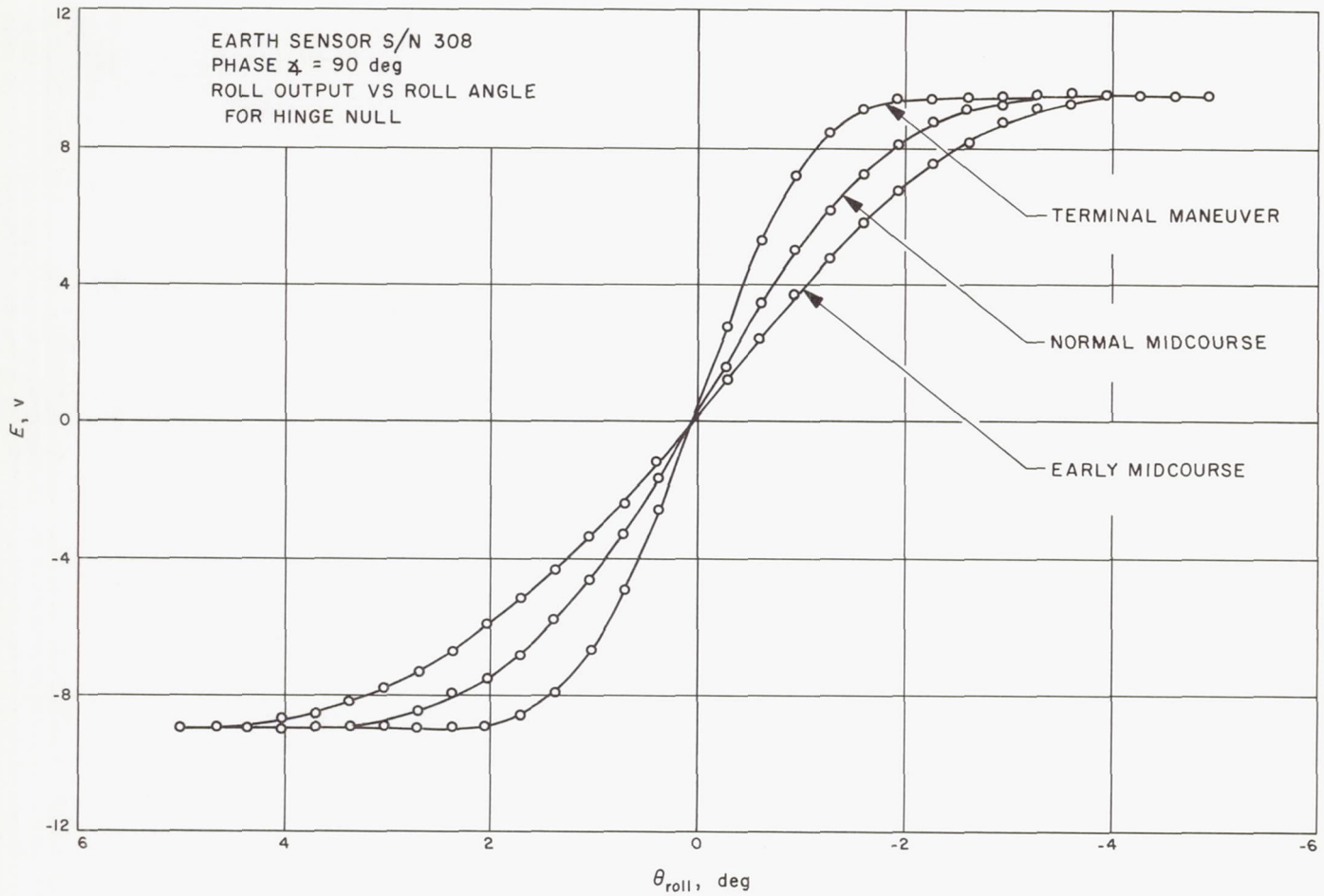

Fig. E-4. Earth sensor roll-axis characteristics

The long range Earth simulator (discussed below under Section a. Performance) was used to simulate the Earth at (1) its approximate color temperature, (2) a Sun-Earth-probe angle of 90 deg as shown in the sketch on the plots of the above two figures, (3) the corresponding light intensities during the respective maneuvers, and (4) the approximate Earth diameters. The rounding of the curves near the saturation points is due to the finite size of the Earth. If the Earth were a point of source of light, the curves would be a straight line saturating at 1.25 deg for roll and 2.5 deg at hinge. The finite size of the Earth causes these intersecting lines to curve in a region of plus and minus the radius of the Earth from the saturation points of the point source. This is readily seen in Fig. E-4. Because there is only a half-illuminated Earth in the hinge direction in Fig. E-5, this effect is very much diminished. If the Earth moves away from null on a line not along either axis, the performance becomes truly two dimensional. Note from Fig. E-6 that as the Earth moves in the positive θ roll direction, the hinge error signal weakens because less of the cathodes' A and B photomultipliers is exposed. For motion in θ hinge direction, however, the gain on the roll axis remains essentially constant. In reality, neither of these conditions will be precisely true due to variations in sensitivity over the photomultiplier cathode surfaces. The actual experimental situation is illustrated in Fig. E-7. The coordinate axes are roll and hinge dc error signals. The vertical lines are lines of constant hinge angle θ_H, and the horizontal ones are constant roll angle θ_R. The nonsymmetry of the actual two-axis output plot cannot be entirely justified by variations in cathode sensitivity and remains unexplained at this time.

Figure E-8 is a photograph of the redesigned narrow field-of-view Earth sensor. A series of evaluation tests was performed on the redesigned Earth sensor to verify the modification. The evaluation tests consisted of a dynamic offset response curve, null-axis response data at light intensities which correspond to Earth-sensor *first* turn-on,

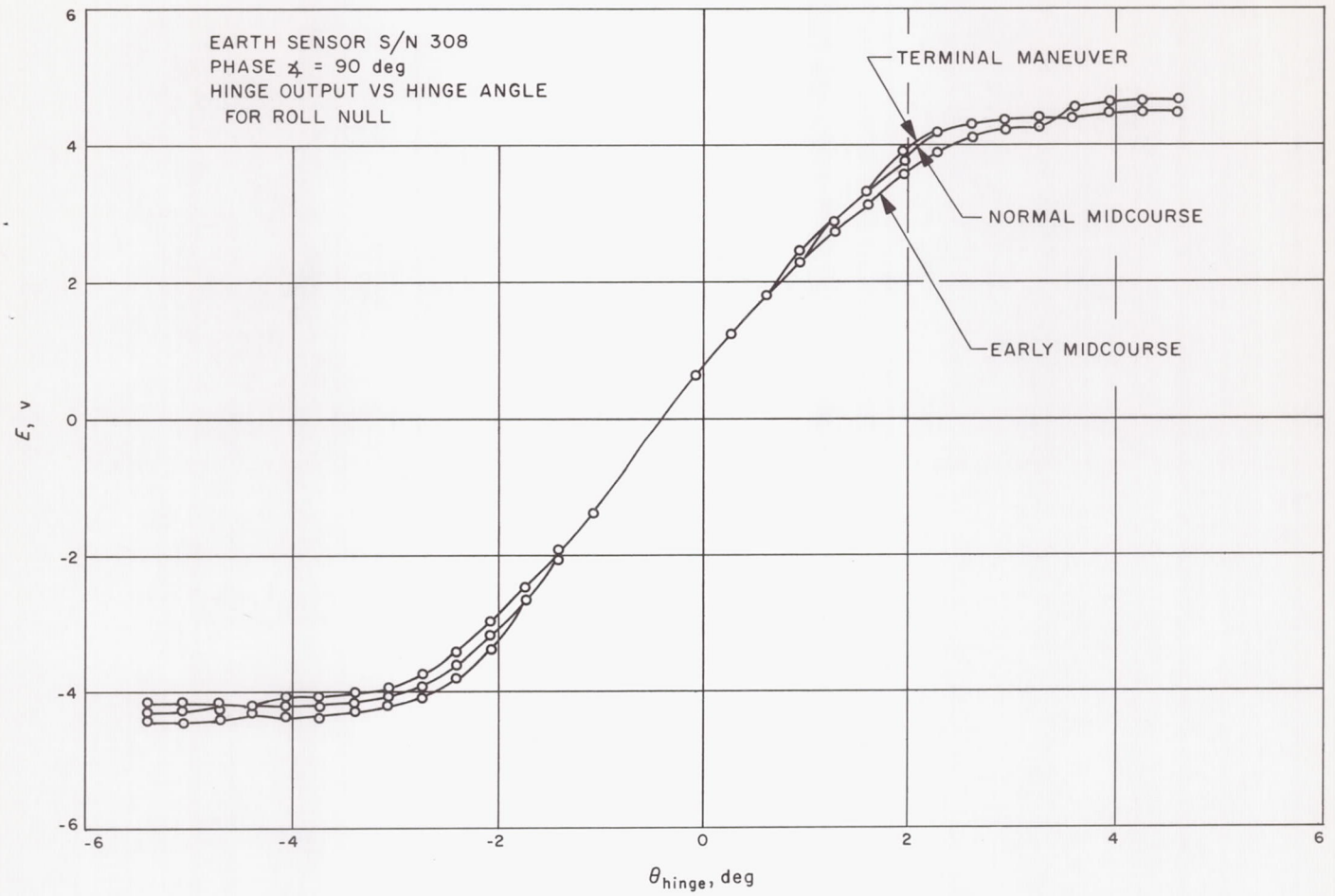

Fig. E-5. Earth sensor hinge-axis characteristics

midcourse maneuver and terminal maneuver, Earth-probe-Sun angle measurements, light reflection tests from the spacecraft into the Earth sensor, and type-approval environmental tests.

Figure E-9 shows the effect of roll-axis angular offsets at a null hinge angle; it includes roll-error voltages, Earth-sensor light intensity voltage outputs, and acquisition threshold points of the reduced field-of-view Earth sensor. The redesigned Earth sensor can operate safely within tolerance at an Earth-probe-Sun angle during terminal maneuver of 47 deg or larger. Previously, modification on the Earth-probe-Sun angle constraint during terminal maneuver was 73 deg or larger. The reflection measurements indicate that the maximum antenna angle during Earth search is 135 deg; previously, it had been 126 deg.

Figure E-10 shows the effects of light reflection into the 40 × 60 deg field-of-view design and into the reduced field-of-view Earth sensors that are intense enough to produce an acquisition signal in the Earth sensors.

In summary, Earth-sensor performance in the presence of off-axis disturbances has been greatly enhanced by reduction of field of view.

a. Performance. The following discussion is a look at the *Ranger* Earth sensor, noting, in particular, performance of *Rangers* 1 through 6.

The characteristics of each Earth sensor are calibrated just prior to launch. A short range Earth simulator simulates the Earth at its color temperature, various sizes, and light intensities of the Earth at midcourse and terminal maneuvers. The long-range Earth simulator has the added feature of providing various phase angles of the Earth. The short-range Earth sensor is mounted on top of a mechanical alignment fixture and a T-2 theodolite. The Earth sensor can be rotated to any desired angle with

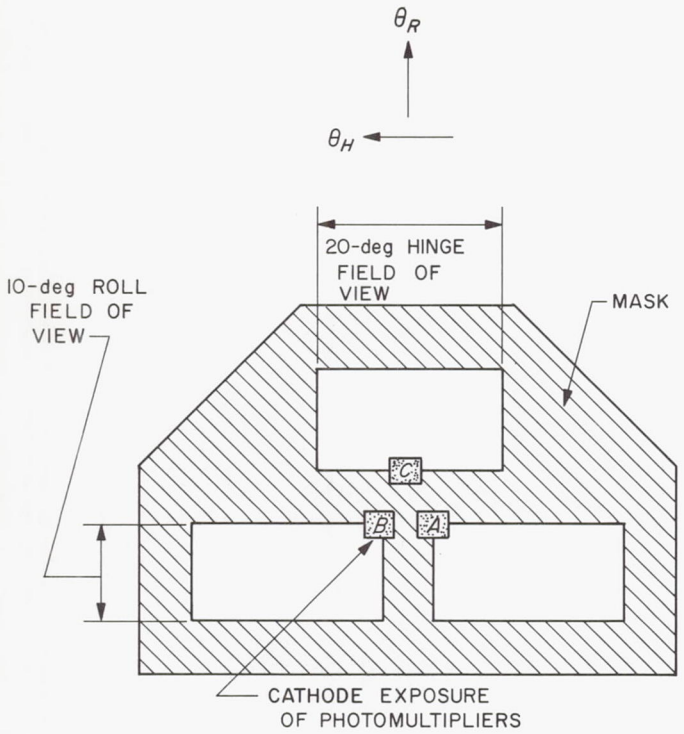

Fig. E-6. Earth sensor shadow box

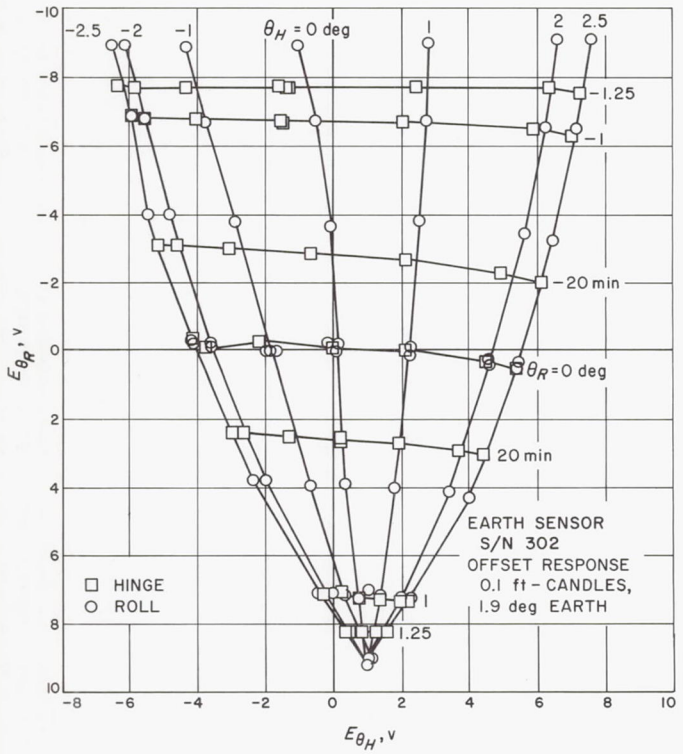

Fig. E-7. Earth sensor sensitivity characteristics

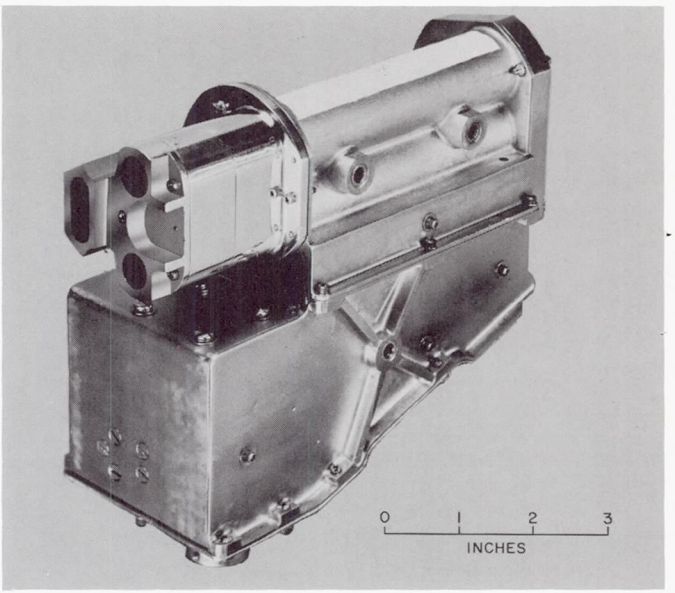

Fig. E-8. Redesigned Earth sensor

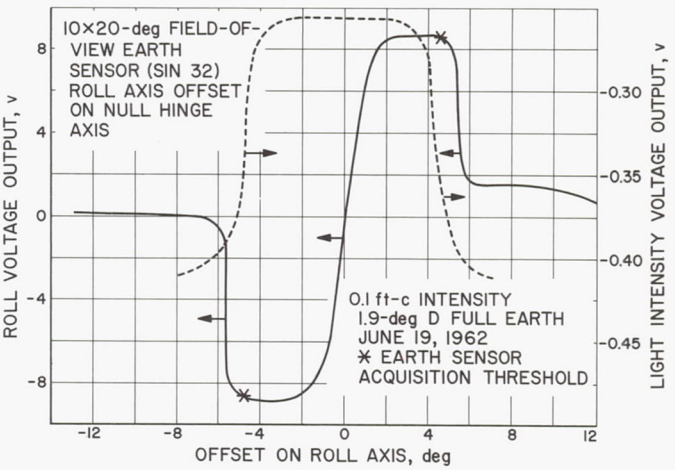

Fig. E-9. Error signal and light intensity vs roll angle

respect to the Earth by means of the theodolite, and the mechanical null position of the Earth sensor with respect to the Earth can be determined with the mechanical alignment fixture. The small telescope on the mechanical alignment fixture is adjusted parallel to the mounting reference surfaces on the Earth sensor using autocollimation techniques.

Voltage outputs of the Earth sensor are read out of the dynamics meters after the signal has passed through demodulators and simulated loads, as would be the case in the attitude control subsystem.

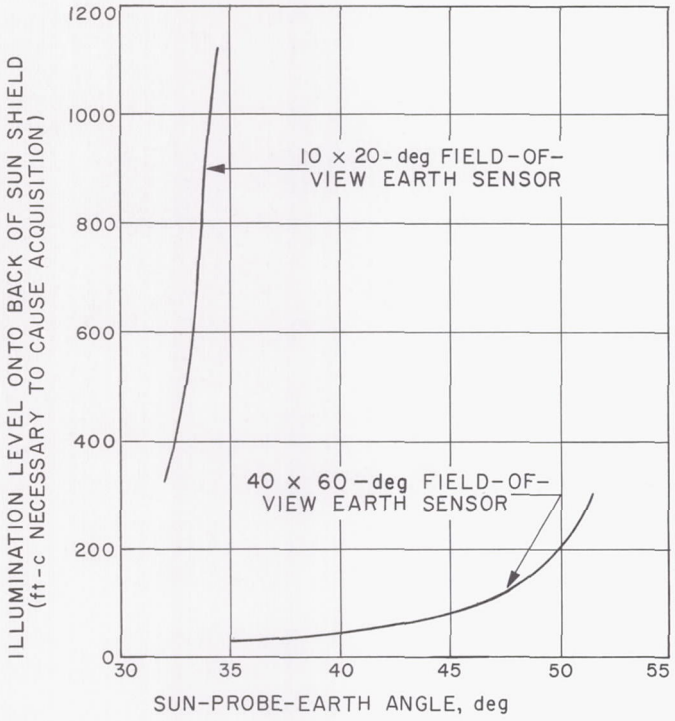

Fig. E-10. Sun-shield back-side-illumination Earth-sensor disturbance vs hinge angle

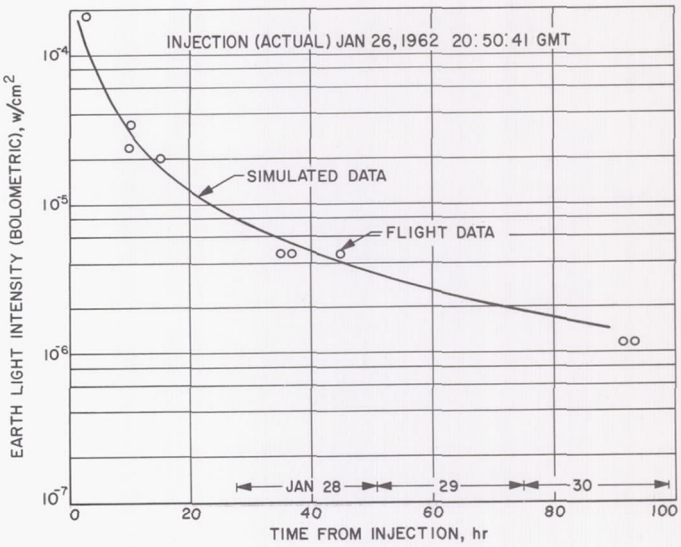

Fig. E-11. Simulated and flight data of Earth-light intensity for *Ranger* 3

The Earth sensor functioned in *Rangers* 1, 2, 3, 5, and 6. On *Ranger* 4, the Earth sensor was never energized. *Rangers* 1 and 2 operated in a low Earth orbit, and the Earth sensors indicated acquisition on lighted objects with *Ranger* 1 giving more information, in general. The Earth sensor appeared to be operating correctly even though its temperature was close to the maximum allowable Earth sensor temperature, and the intensity of the Earth was 10 times brighter than expected on normal *Ranger* trajectories.

Ranger 3 provided the first good in-flight evaluation of Earth sensor performance. This evaluation indicated that the sensor performed as intended during flight. A spurious pitch command at terminal (Moon distance) caused the spacecraft to pitch in the direction of Earth, eventually bringing the Sun shade between Earth sensor and Earth; this caused a loss of Earth acquisition. From this point on, the spacecraft performance became quite confused, and further Earth sensor performance cannot be adequately stated.

Figure E-11 is a plot of simulated Earth sensor light-intensity data calculated for the *Ranger* 3 flight and light intensity telemetered back from the *Ranger* 3 Earth sensor during flight. The correlation between the two sets of data is good. The simulated data was calculated, considering the Earth to be a perfectly diffuse (Lambert) reflector with an Earth albedo of 0.4.

Asymmetrical snow and cloud cover, coupled with finite size of the Earth, will cause the Earth sensor to have a roll-axis error (hinge errors are unimportant to guidance). An estimate of these errors indicates them to be approximately 5% of the Earth's apparent diameter (approximately 0.1 deg at terminal and 0.25 deg at midcourse).

APPENDIX F

Inertial Sensors

The control of the *Ranger* spacecraft requires that both angular rate and displacement be sensed about the principal axes. To do so, requires the use of gyroscopes. During the midcourse thrust phase, the measurement of the desired acceleration must be sensed; an accelerometer was designed to meet this requirement.

1. Gyroscopes—Background Information

The original requirements for the *Ranger* mission provided that only rate information for the stabilization of the spacecraft during initial acquisition and cruise was required. However, the additional requirement of providing a reference for the angular displacement of the spacecraft during the midcourse and terminal maneuvering dictated the need for sensing the position also.

During the Block I (*Ranger* 1 and 2) period, the design of an instrumentation-rate gyro package was initiated to measure the angular rates about either the roll or pitch axis of the spacecraft during the period after separation and prior to Sun acquisition. Due to a weight problem concerning *RA*-3, the instrumentation-rate gyro module was deemed unnecessary for the satisfactory completion of the *Ranger* mission.

a. Control gyros. The *RA* 1 and 2 flyby missions employed three single-axis floated gyros, a modification of the Minneapolis-Honeywell miniature integrating gyro model *GG*49-*E*2. The modified gyro, designated *GG*49-*E*5, was filled with a low-viscosity high-density fluid which provided 100% flotation at a nominal temperature of 115°F. The flotation fluid used in the *E*5 model was *MO*-10, which, when accompanied by an increased damping gap, provided a coefficient of viscous restraint of approximately 258 dyne-cm-sec/rad, as compared to a nominal value of approximately 17,000 in the *E*2 model used for the *Sergeant* missile. This configuration of the *MIG* gyro lowers the operating temperature to 115°F, thereby eliminating the need for heater power required to maintain the normal 190°F operating temperature of the *GG*49 gyro. The low-viscosity flotation fluid provides very low damping of the gyro gimbal, thus making handling of the instrument extremely delicate when the gyro is not being operated in the rebalanced mode.

Performance requirements for the low-damped version of the *MIG* remain essentially the same as the *Sergeant* requirements, except where the increased torquer pattern field excitation level had required an increase in the allowable reaction-torque drift rate. This increase in the *g* insensitive drift rate made it necessary to bias the torquer control field from a precision constant current source, during normal system operation.

The succeeding *Ranger* missions imposed the additional requirement that the gyro be able to provide a reference for measuring the angular deviation of the spacecraft during the midcourse and terminal maneuvers.

The gyro subassembly derived this information by a unique application of three, single-degree-of-freedom, floated integrating gyros. This gyro, the model *GG*49-*E*12, was filled with a low-viscosity, high-density fluid which provided full flotation at 115°F, similar to the *GG*49-*E*5 gyro. A low-viscosity fluid was again selected which would permit the operation of the gyro without the use of heaters. The damping and precession axis restraint are accomplished by a torque feedback loop. The restraint provided by this electronic loop remains relatively constant, independent of changes of fluid viscosity due to the temperature.

Included in the gyro subassembly was the gyro module containing three gyros, switching relays, a bank of capacitors which provided the passive integrators for the derivation of the angle information required by the system, and an electronic control module which provided the three servo-amplifiers and command current regulators.

b. Control gyro module failure analysis. Fabrication of the control modules was delayed due to a number of difficulties uncovered in the GG49-E12 gyro. Paramount of these problems was the weakness due to insulation breakdown in the signal-generator, torquer Dualsyn windings. The failures occurred after both thermal sterilization and temperature testing. It was found that the Dualsyn winding was a marginal choice for high-temperature application and was changed from double Formvar to Nyleze insulated wire.

A second difficulty, although it did not produce any discrete gyro failures, resulted in the rejection of several gyros from system usage. These particular gyros caused an approximate 10-cps oscillation in the attitude control system. An intensive investigation uncovered a number

of minor damping differences between the *E*-12 and *E*-5 gyros which were corrected by increasing the fluid viscosity. This was accomplished by changing the fluid from *MO*-10 to *SW*-30.

Another interesting problem was created by the gyro pivot and jewel clearance. The gimbal of the gyro is supported by pivots and jewels, and there is some amount of clearance between the pivot and jewel. It was noticed that before the gyro torqued around its normal output axis, it moved laterally, then torqued. There is barely any movement in terms of normal rotation before the gimbal moved laterally across the gap. The actual problem was solved by a thorough study of the gyro model on the analog computer. A 3-deg of freedom analysis was first studied where the normal rotation about the output axis, one axis of rotation sideways, and the ability for lateral motion were simulated. Ultimately, a 5-deg of freedom study was made with two-dimensional constraints on the pivot and jewel, corresponding to the ability to move in both directions. A very close correspondence between the actual gyro and the model was obtained. The model was then extended by including Dualsyn loading effects to the torquers, signal generators, and the end to end buoyancy effects. As soon as the 5-deg of freedom study was made, additional problems such as damping around the normal axis, translational damping, and two rotational damping terms were of concern.

The results of this analysis led to the modification of the gyro by closing down the jewel and pivot clearance. The maximum allowable tolerance previously had been approximately 200–500 μin.; it was closed down to less than 100 μin. This correspondingly shortened the response time of the gimbal to a step torque input of less than 100 msec.

2. Analysis of the Gyroscope

The spacecraft attitude about each axis is measured by the gyro loop. The term gyro loop is applied to the entire gyro subsystem, which consists of the gyro, preamplifier, demodulator, gyro amplifier, and gyro control network, as shown in a block diagram, Fig. F-1.

a. Description of the gyro model. The gyro is of the single-degree-of-freedom type, the gimbal being suspended in a fluid with very low viscosity. The approximate values of the known parameters are given below:

H = moment of momentum of rotor = 100,000 dyne-cm-sec/rad

I = moment of inertia of the gimbal = 100 dyne-cm-sec^2/rad

D = viscosity of the fluid (maximum) = 9400 dyne-cm-sec^2/rad

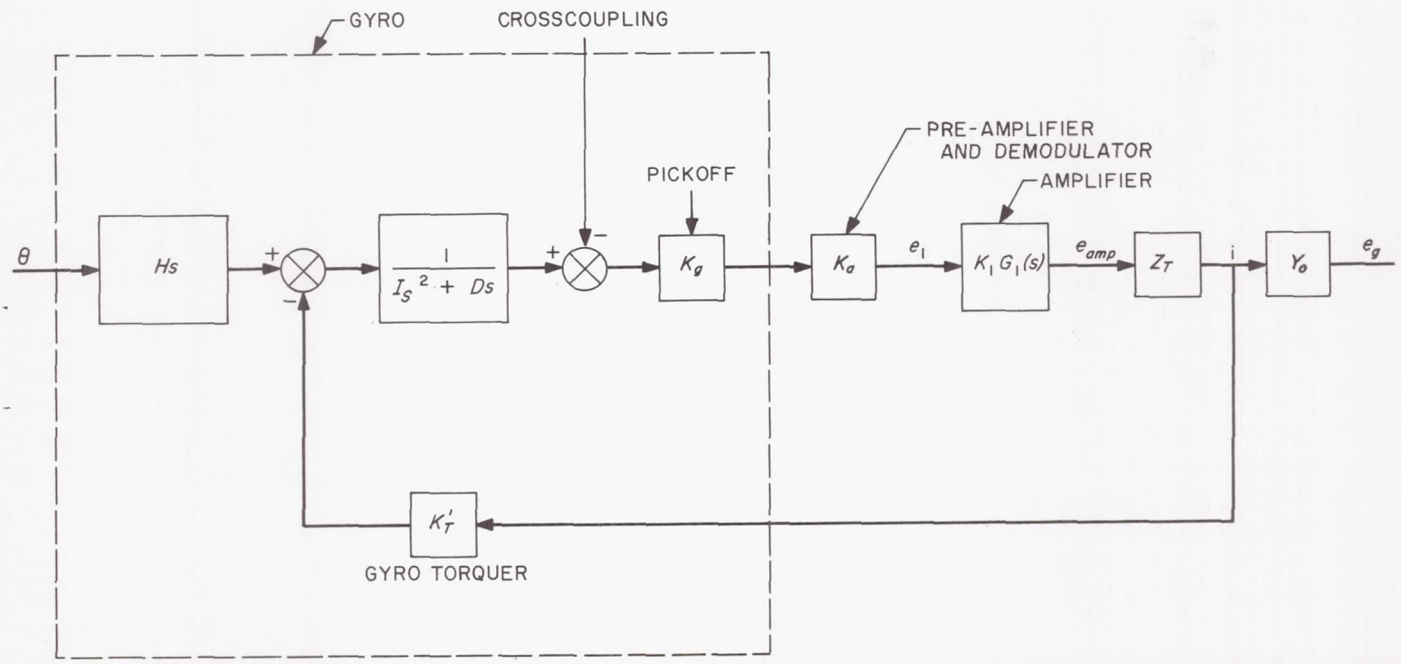

Fig. F-1. Block diagram, gyro loop

k_g = output voltage scale = 5 v/rad gimbal angle factor

$k_{T'}$ = torquer scale factor = Hk_T = 50 dyne-cm/ma

k_T = torquer scale factor equivalent to input angular rate = 105 deg/hr/ma = 0.509 rad/sec/amp

The transfer function of the gyro is given by

$$\frac{e_g}{\theta_i} = \frac{\left(\frac{K_g K_a K_1 G_1(s)\, Z_o(s)\, H}{Z_T(s)}\right) s}{Is^2 + Ds + \frac{HK_T K_g K_a K_1 G_1(s)}{Z_T(s)}} \qquad \text{(F-1)}$$

Similarly, the transfer function relating the gyro output to the disturbance (crosscoupling) input is given by

$$\frac{e_g}{\theta_j} = \frac{\left(\frac{K_g K_a K_1 G_1(s)\, Z_o(s)}{Z_T}\right)(Is^2 + Ds)}{Is^2 + Ds + \frac{HK_T K_g K_a K_1 G_1(s)}{Z_T}} \qquad \text{(F-2)}$$

The two transfer functions are related by the equation

$$\frac{e_g}{e_{\theta_j}} = \left(\frac{Is + D}{H}\right)\frac{e_g}{\theta_i} \qquad \text{(F-3)}$$

Several of the constants associated with the block diagram and with the above equations were given above in this section of Appendix F; the additional unknowns are now derived.

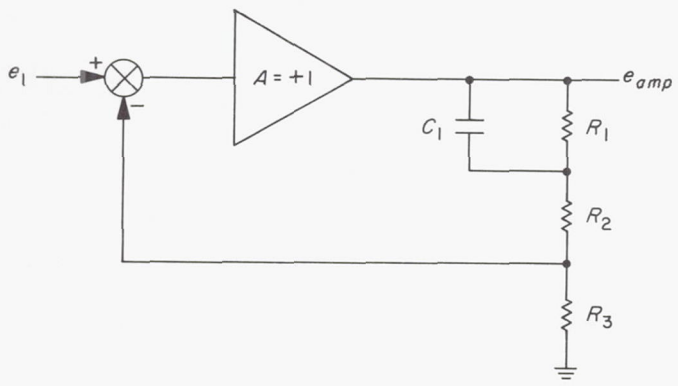

Fig. F-2. Simplified gyro amplifier

Gyro amplifier. A diagram showing a simplified version of the gyro amplifier is given below in Fig. F-2.

The amplifier acts as the output stage of the gyro loop and provides feedback compensation for loop stability. The transfer function of the amplifier is given as

$$\frac{e_{amp}}{e_1} = k_1 G_1(s) \qquad \text{(F-4)}$$

Based upon the diagram in Fig. F-2, the transfer function is given by a unit gain in the forward loop and has a feedback loop given by

$$\frac{e_f}{e_a} = \frac{R_3(sC_1R_1 + 1)}{(R_1 + R_2 + R_3)\left(\frac{sC_1R_1(R_2 + R_3)}{R_1 + R_2 + R_3} + 1\right)} \qquad \text{(F-5)}$$

Closing the gyro amplifier loop, we obtain the following transfer function:

$$\frac{e_{amp}}{e_1} = \frac{(R_1 + R_2 + R_3)}{(R_1 + R_2)} \frac{\left(\frac{R_1(R_2 + R_3)}{(R_1 + R_2 + R_3)} C_1 s + 1\right)}{\left(\frac{R_1 R_2}{(R_1 + R_2)} C_1 s + 1\right)} \qquad \text{(F-6)}$$

Upon substitution of the following parameter values, Eq. (F-6) reduces to

$R_1 = 22\ k\Omega$

$R_2 = 3.6\ k\Omega$

$R_3 = 30\ k\Omega$

$C_1 = 7.5\ \mu f$

Equation (F-6) reduces to

$$\frac{e_{amp}}{e_1} = K_1 G_1(s) = 2.17 \frac{\left(\frac{s}{9.95} + 1\right)}{\left(\frac{s}{43.1} + 1\right)} \qquad \text{(F-7)}$$

Amplifier gain. The voltage gain through the preamplifier, the demodulator, and the gyro amplifier is such that 1 mv rms input provides for 1 v dc output. Therefore, the gain for a modulated gyro signal is given by

$$K_a = ac \text{ gain} \times 2.17$$

$$= 1085 \tag{F-8}$$

Gyro control network. The gyro control network consists of passive circuit components in series with the gyro torquer coil, as shown below in Fig. F-3. Assuming that the torquer inductance is negligible, the total impedance is given by the expression

$$Z_T = \frac{1}{C_1 s} + R_1 + R_2 + R_3 + R_T \tag{F-9}$$

The circuit values are

$$R_1 = 845\,\Omega$$

$$R_2 = 5\,\Omega$$

$$R_3 = 90\,\Omega$$

$$R_T = 400\,\Omega$$

$$C_1 = 4\,(1020\,\mu f) = 4080\mu f$$

The total impedance is therefore given by the equation

$$Z_T = \left[\frac{\left(\frac{s}{0.183} + 1\right)}{4.08 \times 10^{-3} s}\right]\Omega \tag{F-10}$$

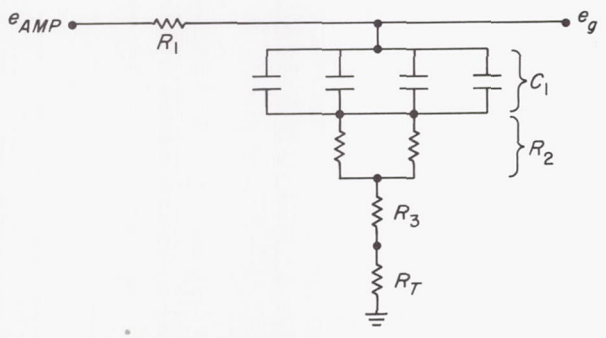

Fig. F-3. Gyro control network

The output impedance is described by

$$Z_o = \frac{1}{C_1 s} + R_2 + R_3 + R_T$$

$$Z_o = \left[\frac{\left(\frac{s}{0.495} + 1\right)}{4.08 \times 10^{-3} s}\right]\Omega \tag{F-11}$$

b. Transfer function. The transfer function for the gyro can now be written. Substituting Eq. (F-7), (F-8), (F-10), and (F-11) into (F-1), we have

$$\frac{e_g}{\theta_i} = \frac{K_g \sigma_g \omega_g^2 (s + 0.495)(s + 9.95)}{0.495 (s + \sigma_g)(s^2 + 2\zeta_g \omega_g s + \omega_g{}^2)}$$

$$= \frac{K_g \omega_g{}^2 (s + 0.495)}{0.495 (s^2 + 2\zeta_g \omega_g s + \omega_g^2)}$$

where

$$K_g = 505 \text{ v/rad}$$

$$\zeta_g = 0.3$$

$$\omega_g = 94.5 \text{ rad/sec}$$

and therefore

$$\frac{e_g}{\theta_i} = K_g G(s) = \frac{505\left(\frac{s}{0.495} + 1\right)}{\left(\frac{s^2}{94.5^2} + \frac{0.6}{94.5} s + 1\right)} \tag{F-12}$$

For purposes of the autopilot analysis, Eq. (F-12) may be further simplified by assuming that the poles in the denominator of the expression are sufficiently far away from the other system poles and zeroes under investigation, that the following gyro model may be assumed:

$$\frac{e_g}{\theta_i} = 505\,(2.02\,s + 1) \tag{F-13}$$

Equation (F-3) may therefore be approximated by

$$\frac{e_g}{\theta_j} = 0.005\,(0.1s + 1)\,(2.02s + 1) \tag{F-14}$$

where

$$I = 100 \text{ dyne-cm-sec}^2/\text{rad}$$

$$D = 1000 \text{ dyne-cm-sec/rad}$$

and

$$\frac{D}{I} = 10 \text{ rad/sec}$$

$$\frac{D}{H} = 0.01$$

Root locus analysis. The root locus of the gyro is plotted, based upon Eq. (F-12), in Fig. F-4 below.

Since the viscosity of the gyro fluid varies considerably depending on its temperature, the root loci are plotted for several values of D/I. The theoretical locations of the closed loop poles are also indicated for the gain settings described above. The actual locations of these poles cannot be determined, due to not only the uncertainty in the fluid viscosity but also due to other nonlinearities inherent in the gyro. Empirical data indicate these poles are confined to the region hashed in Fig. F-4. The limits of the region are

$$\text{frequency: } \omega_g = 10\text{-}13 \text{ cps}$$

$$\text{damping ratio: } \zeta = 0.3\text{-}0.8$$

The linear analysis indicates that the ratio of $D/I = 10$ corresponds to the least damped case.

Gyro crosscoupling. The gyro signal is generated by a pickoff, which senses the angular position of the gyro gimbal with respect to the case. This indicates that a signal is generated by rotating the gyro about either its input or output axis. The gyro axes are orientated in the system as shown in Fig. F-5. When the gyro loops are open, the input-output relationships can be summarized in matrix form as described by the equations below.

$$\begin{bmatrix} e_{1_x} \\ e_{1_y} \\ e_{1_z} \end{bmatrix} = \begin{bmatrix} \dfrac{k_g H}{(Is + D)} & -k_g & 0 \\ -k_g & \dfrac{k_g H}{(Is + D)} & 0 \\ 0 & -k_g & \dfrac{k_g H}{(Is + D)} \end{bmatrix} \begin{bmatrix} \theta_x \\ \theta_y \\ \theta_z \end{bmatrix} \qquad \text{(F-15)}$$

When the gyro-loops are closed, the outputs of the gyro loops are

$$\begin{bmatrix} e_{gx} \\ e_{gy} \\ e_{gz} \end{bmatrix} = \begin{bmatrix} G_1(s) & -G_2(s) & 0 \\ -G_2(s) & G_1(s) & 0 \\ 0 & -G_2(s) & G_1(s) \end{bmatrix} \begin{bmatrix} \theta_x \\ \theta_y \\ \theta_z \end{bmatrix} \qquad \text{(F-16)}$$

where

$$G_1(s) = \frac{505 \text{ v/rad} \left(\dfrac{s}{0.495} + 1\right)}{\left(\dfrac{s^2}{94.5^2}\right) + \left(\dfrac{0.6s}{94.5}\right) + 1} \qquad \text{(F-17)}$$

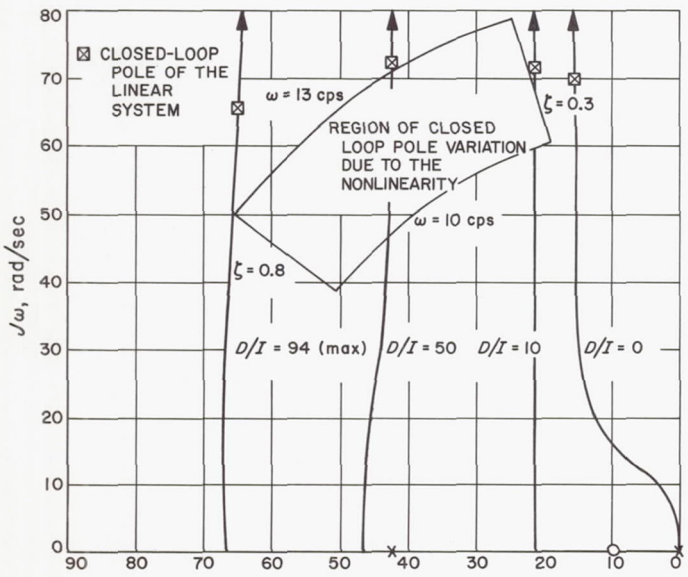

Fig. F-4. Root loci, gyro loop

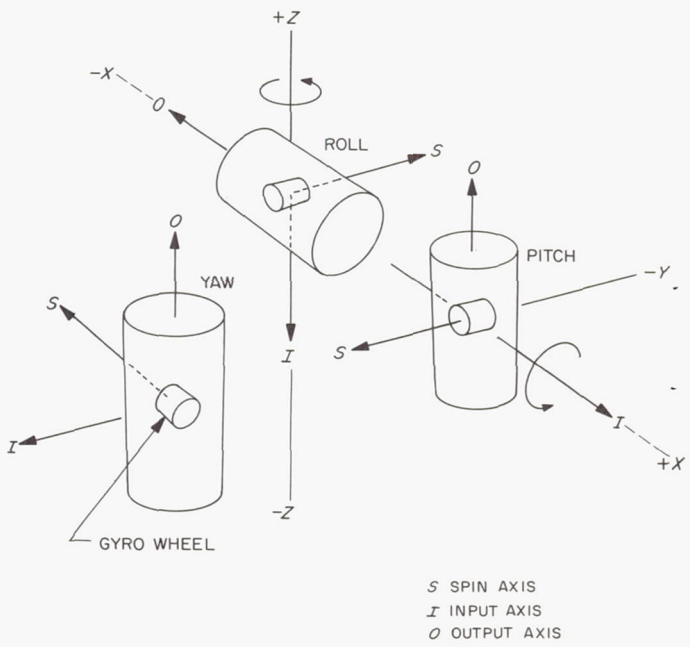

Fig. F-5. Gyro reference-axis orientations

$$G_2(s) = \frac{505 \text{ v/rad}\left(\frac{s}{0.495}+1\right)\left(\frac{s}{10}+1\right)}{\left(\frac{s^2}{94.5^2}\right)+\left(\frac{0.6s}{94.5}\right)+1} \qquad \text{(F-18)}$$

$G_1(s)$ and $G_2(s)$ vs frequency are plotted in Fig. F-6. Equation (F-16) shows that there exists a crosscoupling between x and y (pitch and yaw) axes of the autopilot. However, the matter is not investigated further, since the gyro output voltage due to crosscoupling is considerably smaller than that due to input and no positive feedback signal is generated through gyro crosscoupling (Fig. F-7).

3. Accelerometer

The magnitude of the velocity increment added to the Block II and III series of spacecraft during the midcourse correction maneuver is measured by means of a linear accelerometer and integrator combination. Since a digital computer is an integral part of the CC&S unit and the magnitude of the corrective velocity increment is transmitted digitally from the Earth, a digital accelerometer system was required and developed. The system is also used for midcourse-motor shutoff.

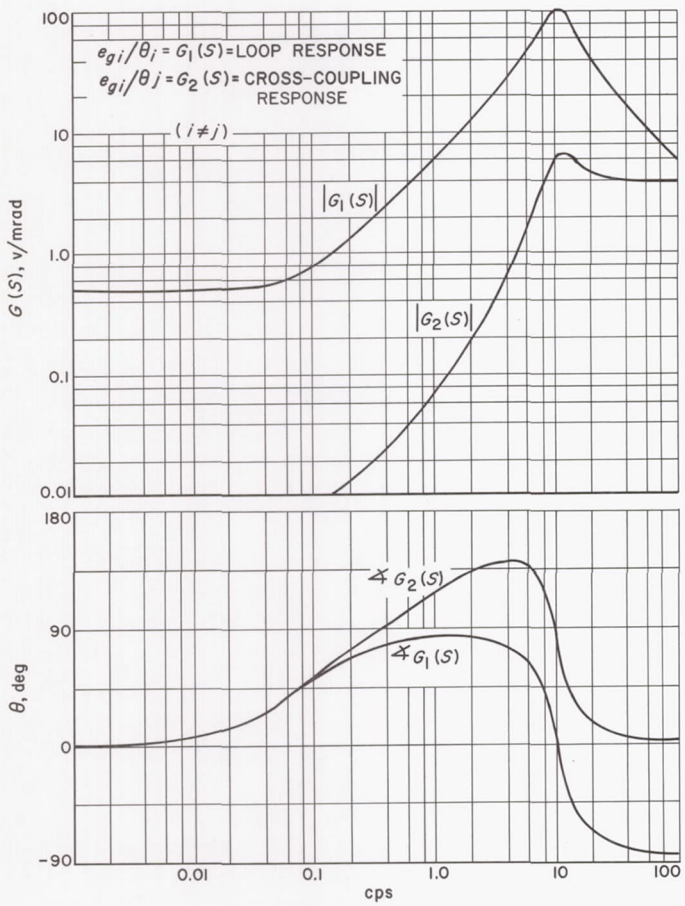

Fig. F-6. Gyro-loop frequency response

The accelerometer selected for this application was the Bell Aerospace Corporation Type III-B. The unit is basically a pendulous force balance with a pulse-torqued rebalance loop to provide capture current to the proof mass. In this method of operation, the pulsing rate is directly proportional to the applied acceleration, and each pulse produced represents a constant value of velocity increase (or decrease, depending on the direction of the acceleration). It is noted that this accelerometer is a miniature version of the type used in the *Sergeant* guidance system. It was also selected for use in the *Vega* platform. Several changes are incorporated in this unit to make it more compatible with the digital torquing requirements of the *Ranger* system. The major difference is in the pickoff circuit, which was changed from 8.4 kc to 200 kc, thus giving a wider bandwidth and resulting in less information delay from the pickoff to the electronic package. The scale factor of the proof mass torquer was changed from 260 $\mu a/g$ of acceleration to a higher value of 2.2 ma/g in order to take fullest advantage of presently available transistor switches.

a. Accelerometer null stability. In the previous applications of this accelerometer, the reliability was proven except for one major area of uncertainty—the stability of the null offset (bias error). Null offset is defined as the output of the instrument when subjected to a zero-g input. Efforts at both JPL and Bell Aerospace solved the problem which was creating an uncertainty of about

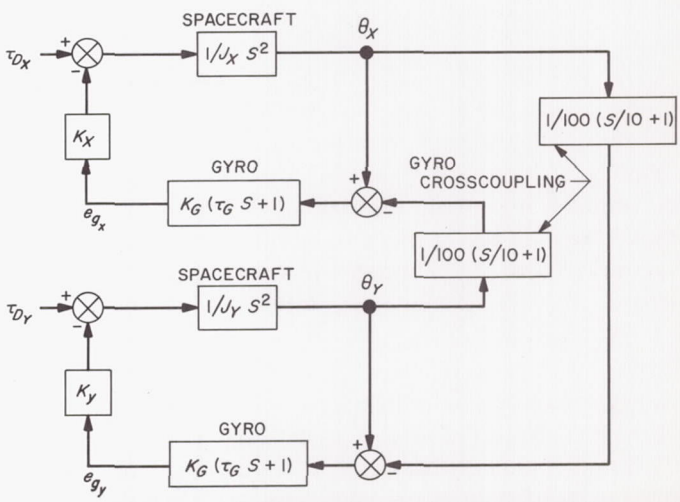

Fig. F-7. Block Diagram, pitch/yaw crosscoupling

4×10^{-4} over several months of testing at varying temperatures. The improved accelerometers have a 3σ null offset stability of approximately 1.0×10^{-4} g. The most important point noted was the absence of drift trends or bias in the data. This further demonstrated that adjustments and calibrations will hold over extended periods of time. Any shift of null offset is serious because the digital system cannot differentiate between g inputs, due to actual acceleration, and the apparent inputs due to a null offset. A null offset shift of 1×10^{-4} g will cause a scale factor shift of 0.14% at the expected 0.07-g acceleration produced by the midcourse-motor thrust. The 1σ limits for the accelerometer system are $\pm 0.25\%$ applied; therefore, the null torque changes must be kept to a minimum.

b. Experimental analysis. The calibration deviation is a composite error caused by the effects of null offset, accelerometer torquer scale factor, and errors within the electronic package. The electronic problems are largely due to changes in the *zener* reference diode voltage, changes of the switching transistor leakage current or saturation resistance, and changes of leakage in the damping feedback capacitor. Shifts of actual scale-factor adjusting resistors are possible, but are much less probable than the others mentioned.

c. The digital accelerometer mechanization. The accuracy in the digital accelerometer is determined to a large extent by how accurately the current pulses to the torquer can be generated. The method for developing this pulse in the *Ranger* system is referred to as the open-loop system. Basically, this system uses an accurate frequency from the computer clock to control the pulse width and an accurate voltage, controlled from a precision *zener* diode, to determine the pulse height.

The accelerometer pickoff is a capacitive type which is excited with 200 kc from an oscillator in the electronic package. This pickoff produces an error signal to the ac amplifier which has a gain of 200. The output of the ac amplifier is coupled through a 3:1 step-up transformer to a double bridge or ring demodulator. The demodulator reference signal is obtained from the same 200 kc oscillator as the accelerometer excitation.

The demodulated error signal is applied to a decision device which is a Schmitt trigger circuit. This circuit will detect displacement of the proof mass which, for a predetermined amount of acceleration, will develop a rebalance pulse. When the Schmitt circuit changes state, the logic circuit will then allow the precision clock pulses to pass through to the flip-flop. In this circuit, the flip-flop is actually a trigistor. The first positive clock pulse will cause the trigistor to conduct; 1250 μsec later, a negative clock pulse turns the trigistor back to the nonconducting state. This *on-off* action of the trigistor is transformer coupled to a low-leakage, high-speed transistor switch. The switch is supplied with 8.4 v from a precision *zener* diode. This diode voltage is stable to $\pm 0.01\%$ over 100°F temperature range.

A current-limiting resistor is placed in series with the switch and *zener* diode. The value of this resistor is varied as a function of the accelerometer temperature to compensate for the change in accelerometer permanent-magnet torquer characteristic. This type of torquer has a gain function which changes rapidly with temperature.

It will be noted that pulses of only one polarity can be generated. This provides capture in only one direction as the *Ranger* spacecraft can only accelerate in one direction. Each pulse provides for a velocity increase of 0.1 ft/sec. The accelerometer has a built-in eddy current damper associated with the proof mass. This damping is not sufficient to restrain the pendulum against vibration, so an additional rate feedback loop is applied around the accelerometer. This loop uses the same demodulated signal as the decision device. This signal is amplified by a low-gain dc amplifier. The output is capacitor-coupled back to the torquer to produce a current which is proportional to the proof mass rate of motion. This circuit provides a damping increase of five.

Laboratory testing under constant temperature and no vibration conditions has shown that the accelerometer system is stable to a 3σ accuracy of 0.03% of applied acceleration. The system can retain capture up to 1 g of acceleration while the expected acceleration of the *Ranger* midcourse maneuver is 0.07 g.

d. Accelerometer acceptance tests and results. One unexpected area of difficulty was encountered during the acceptance tests. Early in the evaluation of the accelerometer transducer, it was discovered that the seismic proof mass within the instrument was subject to random static charge effects. These static charges would produce error torques of large and variable magnitudes. To eliminate these errors, a fix consisting of a radioactive static discharger was installed at the vendor's facility. No system design constraints existed with regard to small radioactive sources on board the spacecraft at this time. During the final testing of *Ranger* 4 at the Atlantic Missile Range (AMR), a radioactivity mapping operation, using the

gamma-ray experiment from the spacecraft, disclosed that enough gamma radiation was coming from the accelerometer to create a detrimental effect in the gamma-ray measurement system. Due to the fact that insufficient time remained prior to launch of *Ranger* 4, no reduction of this spurious radiation was possible.

Testing at JPL disclosed that it was possible to change from the existing radium isotope source to a polonium source without impairing the accelerometer's performance. The advantage of the polonium static discharger is that it emits mostly alpha particles, and that the gamma radiation present was below the interference level with respect to the gamma-ray experiment. The alpha particles do not pass through the accelerometer case at all.

All available accelerometer modules for *Ranger* 5, 6, and 7 (and spares) were converted to the polonium source. Re-testing of these modules proved that no degrading of performance or accuracy was produced by the change.

Accelerometer transducers purchased for the Block III series of spacecraft did not use any form of radioactive dischargers. The problem was overcome by developing a form of grounded torquer and pendulum assembly, to replace the former insulated design.

APPENDIX G
Gas System

Twelve miniature jet valves, connected to a dual gas source, are employed on the *Ranger* spacecraft to control the attitude (Fig. G-1). Four valves each are used to control the yaw and roll axes providing couples, and the remaining four valves control the pitch axis. On *Ranger*, the center of mass is expected to shift significantly along the roll axis. Therefore, utilization of a pure couple for roll control permits the roll valve positions to be frozen for the spacecraft.

The axis of each valve is oriented to prevent gas from impinging onto the structure during valve actuations. Investigations have shown conclusively that the bias or coupling effects of impinging gas are significant. This influence established the requirement that the yaw control valves be moved from their earlier position on the pitch axis to a position giving a clear field of view (i.e., the solar panel actuator arm was obstructing one of the valves on the pitch axis). This off-axis condition gave rise to the requirement for the two additional valves in controlling yaw, thus providing pure couple control. The pitch control valves have been oriented 25 deg with their axes.

1. Gas Actuator

In a spacecraft system employing mass expulsion actuators, a tight pressure circuit having low losses due to leakage is paramount. The permissible (total system) leakage-rate out of the seals, welds, and fittings of the *Ranger* system has been set at 60 standard cc/hr. This figure is consistent with the considerations of flight time and the amount of gas stored for the mission.

The *Ranger* gas actuator system is a two-part, unitized, strap-on gas system. Each half section is capable of providing the required control torques autonomously, in the event of a component failure in a half section. Each half-system is made up of a 7-in. pressure vessel, one pneumatic regulator (inlet pressure 100 to 3650 psi, outlet 15 ± 1.2 psi), and six reaction control valves (thrust level 0.0092 to 0.038 lb)—two valves on each axis providing plus and minus torque control. The gas system is an all welded stainless-steel system, except for special *B* nut fittings at valve manifolds, *O*-ring seals between the valve and manifold, and crush seals between the plumbing and tank. The solar-panel bays serve as the packaging area for the vessel, regulator subassembly, associated plumbing, and the yaw jet assemblies. The yaw valves are mounted approximately 2 in. off the pitch axis, adjacent to the solar panel actuator, to reduce crosscoupling when a half section is operating. The flight weight of each assembly is 14.3 lb, including a thermal control shield (0.9 lb) and nitrogen gas. The angular acceleration requirement of 0.3 mrad/sec^2 is provided by each section,

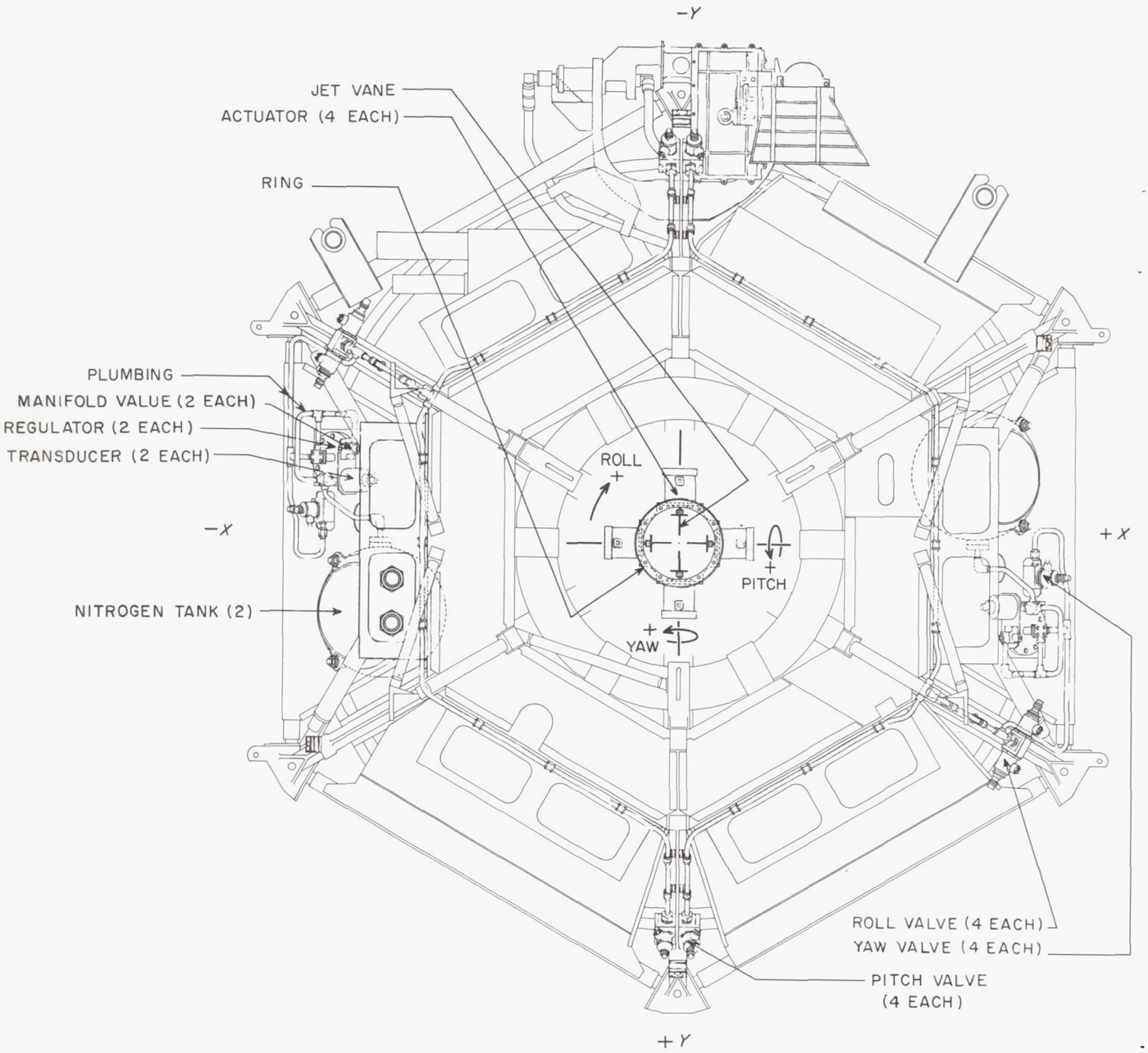

Fig. G-1. *Ranger* gas system

thereby being compatible for commanded turn acceleration requirements in the event the spacecraft is operating on a half system. A diagram of the attitude control system semiredundant gas actuator system is shown in Fig. G-2. The total fuel capacity for this system is 4.18 lb. In the event that a gas jet fails to open during launch, the remaining half system would be left with 1.39 lb of N_2. This figure is based on reasoning that 1½ units of gas flow from the half system, which has failed (i.e., worst case), until the gas supply is exhausted (see Section 5, Gas Consumption Analysis, further on in this Appendix G). During this period, one-half unit is given up by the second half system. A review of *Ranger* gas-system flight performance indicates that 1.39 lb of N_2 would be sufficient to complete the mission. The weight penalty for using the dual gas system over the original system is approximately 7 lb. The total gas system weight including gas weight is approximately 30.5 lb.

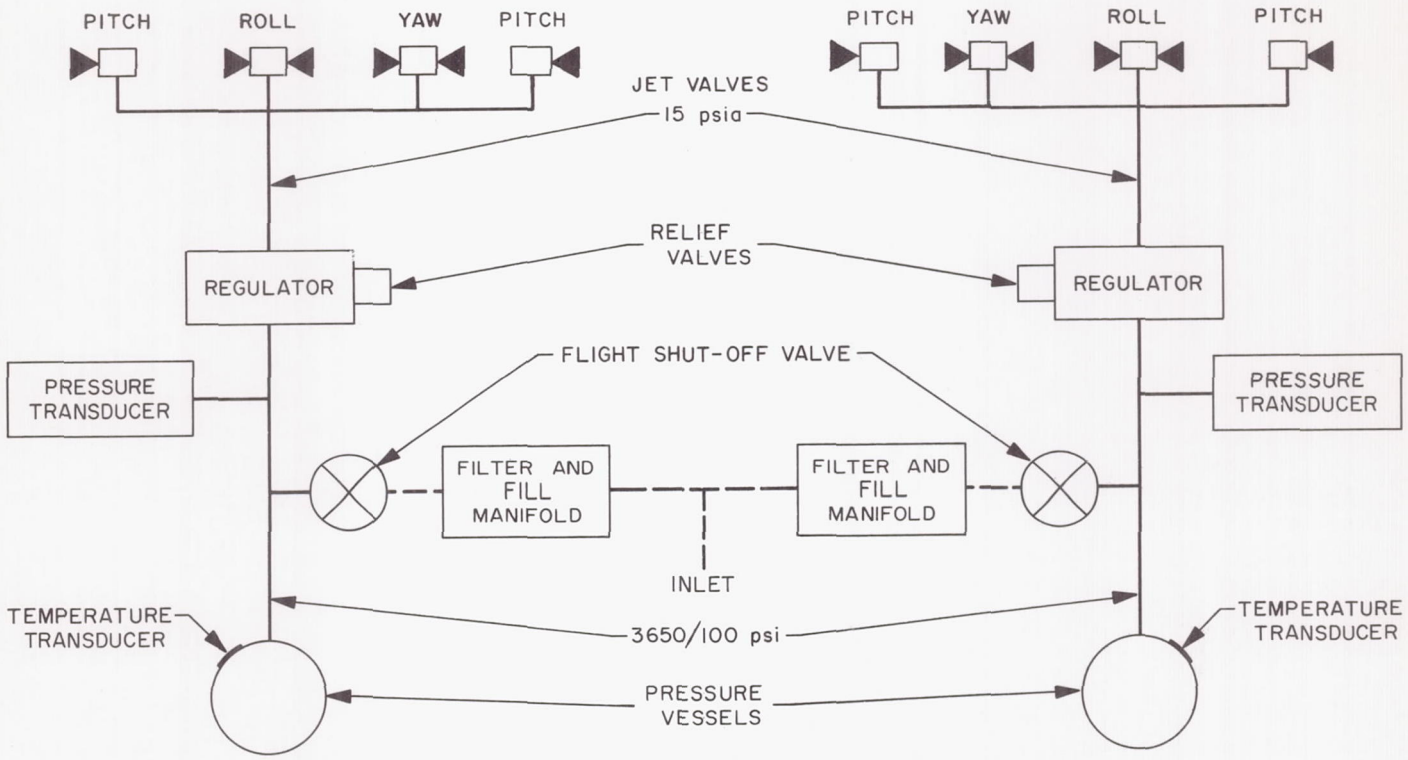

Fig. G-2. Attitude control semi-redundant gas-actuator system

a. Jet valve description. The redundant gas system was first used on the *Ranger* 6. The valves utilize metal-to-metal primary seals which have leak characteristics of 0 to 3 cc/hr. With a valve containing a metal-to-metal seal, clean contamination-free systems are paramount for low leakage.

The criteria for metal-to-metal valves presently require clean levels below 5 μ metallic and 25 μ non-metallic. The units perform with exceptionally fast response times. The smaller coil and lower winding inductance provide for opening and closing times of 15 and 7 msec when excited with the normal voltage.

b. Fill manifold and filter. The *Ranger* gas subsystems utilize conditioned nitrogen gas as the working fluid. The inlet manifolding to the gas system has included a bacteria filter rated at 0.22 μ absolute to meet sterilization requirements formerly imposed. Included also in the fill manifold assembly are one shutoff valve, a check valve, a pressure port for calibration and leak testing and associated plumbing. A new compact fill manifold assembly was designed to improve this subassembly.

The compact filter assembly provides all of the basic utilities of the old system, in addition to fail-safe protection. A check valve in parallel with the filter limits the reverse flow pressure drop which would otherwise puncture the filter membrane. One needle-point ball shut-off valve replaces the previous two. The fill assembly is removed from the spacecraft after the final flight charging operation.

c. Gas valve solenoid improvement. In the gas attitude control used on the *Ranger* spacecraft, a source of impulse error in correcting the position of the spacecraft is the slow and variable closing time of the solenoids used on the gas valves. Because of this error, gas wastage results and more gas must be stored aboard the spacecraft for any particular mission. This is a problem inherent in solenoid coils, as the holding current level is well below pull-in current level, and the associated switching circuitry must be protected from the high voltages that can be induced by the solenoid upon disconnecting the circuit. The commonly used circuit protection is shown in Fig. G-3.

In the relationship $L\,(di/dt) + iR = 0$ (which is the equation that describes what happens in an inductive circuit when the outside energy is removed), R is the coil resistance and the forward resistance of the protective diode in Fig. G-3a. The voltage developed across the coil in this circuit is less than 1 v.

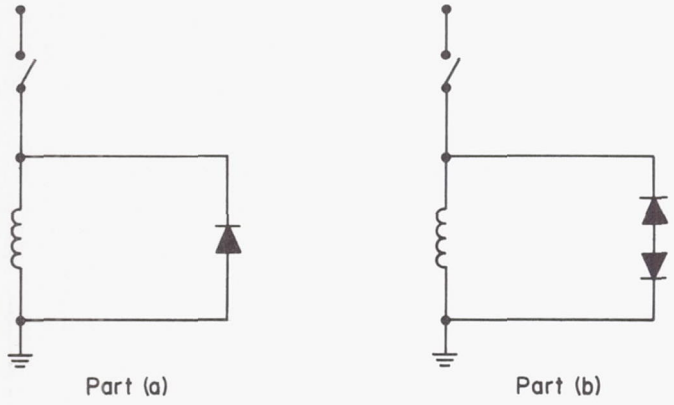

Fig. G-3. Solenoid switch-circuit protection

To speed the current drop, more resistance is needed in the diode circuit. This results in higher voltages being induced across the coil. The limit is the voltage level that the controlling switch can stand. In the *Ranger* attitude control, this is a transistor switch and little real aid can be obtained in adding resistance to the diode circuit. A more promising means of speed current drop and solenoid closing time is the addition of a *zener* diode, as shown in the circuit of Fig. G-3b. This increases the resistance in the circuit and places a limit on the induced voltage, protecting the control switch.

Experimental results show the following:

1. Solenoid valve with protective diode: 40 to 95 msec.

2. Solenoid valve with *zener* protection: 8 msec.

The reason for the large variation in solenoid drop-out time for the circuit of Fig. G-3a is that it takes in excess of five time constants of the circuit for the solenoid valve to close. The case for the circuit of Fig. G-3b is that the solenoid valve closes in less than one time constant of the circuit.

In the gas attitude control system used aboard the spacecraft, the addition of the *zener* diode allows a much more accurate prediction of gas consumption, a better prediction of impulse imparted to the spacecraft, and less gas required for any particular mission.

Further investigation is in progress to establish the relationship of *zener* dynamic resistance to valve closing time, as well as a reliability of higher order for this use of a *zener* diode.

2. Pressure Regulators

The attitude control pressure regulator reduces the source pressure, carried by a pressure vessel, of nominally 3650 psi down to 15 psig for use by the jet valves.

In early tests at cold environmental temperatures of approximately 32°F and with the dew point of the inlet gas at −60°F, the regulator slowly cut off its flow. Further investigations have indicated that the regulator is unaffected up to 2100 psi inlet pressure when the inlet gas is dryer (−70°F dew point). Apparently the moisture content of −60°F dew point gas is sufficient to cause the small area downstream of the poppet to be clogged with ice during regulation. After heating, the regulator again operates normally until it ices-up again. To eliminate this problem, the dew point of the charged gas is carefully controlled on the spacecraft.

For charging of the pressure vessel aboard the spacecraft, the Lo-Boy nitrogen booster is used. This system is a completely self-contained charging station requiring neither electrical power nor driving air for its operation. Two commercial *K*-bottles charged with nitrogen up to 2100 psi are housed within the cabinet. A gas-operated pump boosts the pressure to that required for system charging. A dehydration system within the unit is installed in the high-pressure line to provide delivery of approximately −70°F dew-point gas. Particle filters and hydrocarbon filters are also included in the system.

3. Leakage Detection

Impulse conservation of the gas actuator system during flight is essential because a specific amount of gas is stored at launch to comply with mission requirements. Potentially, loss of impulse accountable to system leakage can be significantly greater than all other causes (e.g., combating solar torque, meteor impacts, etc.). After assembly of the actuator system to the spacecraft, quantitative leakage checks of the system must be run periodically to determine if the over-all leakage is within acceptable limits. Results using a mass-spectrometer helium sniffer to detect leakage proved to be inadequate. Also, the usual approach for pinpointing leakage by using special bubble solutions was misleading. Two new approaches have been taken to quantitatively determine over-all leakage of the entire system: one utilizes a test console to test the gas system; the other uses a bag and mass-spectrometer technique to determine the over-all leak rate of the half system and is still in development. This latter approach will be used prior to assembly of the gas system on the spacecraft.

The spacecraft is pressurized through the charging valve common to the leak-test console. During the charging operation, the shutoff valves are in the open position allowing the reference supply to be pressurized to the same pressure as the spacecraft. The spacecraft temperature sensor is taped to the spacecraft pressure vessel and, after the temperatures have stabilized, a temperature balance pot is adjusted to yield a bridge null. The bypass shutoff valve is then closed, and monitoring of the differential pressure gauge and the bridge output is initiated. After sufficient time has elapsed, the differential pressure and temperature indications are recorded. Equation (G-1) is then applied to determine the rate of leakage. This formula is accurate within 1% for temperature variations of less than 5°F.

$$L = \frac{V}{R\rho T_1 t}\left[\frac{P_1}{T_1}\Delta T - \Delta P\right] \qquad \text{(G-1)}$$

where

L = leakage

V = volume of spacecraft supply

R = gas constant

T_1 = initial temperature

t = elapsed time of the test

P_1 = initial pressure

ρ = density at standard conditions

ΔT = differential temperature

ΔP = differential pressure

Three parameters change during the test: time, differential pressure, and differential temperature. For high resolution, it is apparent that a relatively long test time (i.e., 1 to 3 days for a leakage rate of 60 cc/hr) is required. The console is used to determine the leakage rate after assembly, after shake testing, and after shipment of the spacecraft to the launch site.

4. Gas Jet Nozzle Calculations

The specifications of the gas jets are based on the acceleration requirement of $\alpha = 0.6$ mrad/sec² for the normal gas system or $\alpha_{1/2} = 0.3$ mrad/sec² for the half-gas system. The gas jets must provide the above acceleration during the midcourse and terminal maneuvers.

The moments of inertia used for the nozzle specifications were computed analytically and are given below in Table G-1.

Table G-1. Spacecraft moments of inertia

Phase	I_{xx}, slug-ft²	I_{yy}, slug-ft²	I_{zz}, slug-ft²
I. Launch	82.15 84.70*	84.74 85.87*	32.23
II. Cruise	93.10	120.94	62.40
III. Midcourse	92.05 97.67*	114.60 117.98*	67.68
IV. Cruise	92.99	120.83	62.38
V. Terminal	92.52	116.39	66.35

$g = 32.14$ ft/sec²
*Experimental measurements

The force imparted by each of the jets is found by writing the torque equations as

$$\tau = I\alpha \qquad \text{(G-2)}$$

and

$$\tau = Fd \qquad \text{(G-3)}$$

where

α = acceleration

I = moment of inertia

F = thrust

d = jet moment-arm length

and equating so that

$$F = \frac{I\alpha}{d} \qquad \text{(G-4)}$$

Table G-2, below, presents the moment arms for the jets shown in Fig. G-1.

Table G-2. Gas jet moment arms

Moment arm		Jet moment arm length (d), in.	
Pitch	$+x$ torque	29.85	29.85
	$-x$ torque	28.08	28.08
Yaw	$+y$ torque	32.30	11.21
	$-y$ torque	32.51	11.47
Roll	$+z$ torque	25.97	26.39
	$-z$ torque	25.97	26.39

The force exerted by the gas of the plus pitch jet during the maneuver sequence is therefore

$$F_{+x} = \frac{(97.67 \text{ slug-ft}^2)\,(0.3 \text{ mrad}/s^2)}{29.85 \text{ in.}}\,(12 \text{ in./ft}) \tag{G-5}$$

$$F_{+x} = 0.0118 \text{ lb}$$

Table G-3 summarizes the force needed by each of the gas jets in order to maintain the required acceleration.

Table G-3. Thrust required by each gas jet

Axis		Thrust required (lb)		Nozzle D (in.)	
Pitch	$+x$	0.01180	0.01180	0.0256	0.0256
	$-x$	0.01252	0.01252	0.0263	0.0263
Yaw	$+y$	0.01316	0.0379	0.0269	0.0467
	$-y$	0.01308	0.0371	0.0269	0.0460
Roll	$+z$	0.00936	0.00922	0.0227	0.0225
	$-z$	0.00936	0.00922	0.0227	0.0225

The nozzle diameters that are required to produce the desired thrust levels are determined from the graph in Fig. G-4 and are also given in Table G-3.

For the levels of thrust in the range of 0.037 lb and for a supply pressure of $P_s = 14.8$ psi, Fig. G-4 is used.

The thrust is given as

$$F = AP_cK_c \tag{G-6}$$

where

A = area of the nozzle

K_c = dimension factor depending on the chamber pressure

P_c = chamber pressure

Equation (G-6) is then rewritten as

$$K_c = \frac{F}{AP_c} \tag{G-7}$$

Therefore, from Fig. G-5, the knowledge of the nozzle diameter desired provides information as to the magnitude of the dimensionless factor K_c, by giving the chamber pressure. Figure G-6 is used to verify the choice of P_c and K_c since they are plotted as a function of the nozzle throat diameter (D).

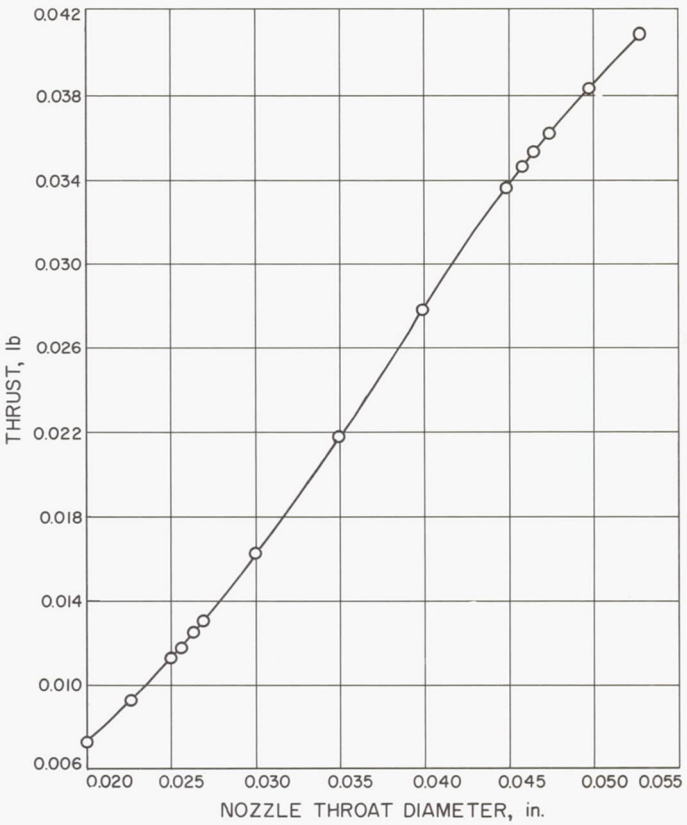

Fig. G-4. Thrust vs orifice diameter for a supply pressure of 14.8 psi

Table G-4, below, describes the nozzle characteristics.

Table G-4. Jet nozzle thrust required

Diameter (in.)	(P_c/P_s)	Area 10^{-3} (in.^{2})	P_c (psi)	(F/AP_c) (10^{-1})	Force (lb)
0.055	0.79	2.375	11.7	15.27	0.0424
0.053	0.819	2.205	12.12	15.34	0.0410
0.050	0.856	1.962	12.68	15.42	0.0384
0.0475	0.890	1.772	13.18	15.51	0.0362
0.045	0.920	1.590	13.61	15.59	0.0337
0.040	0.956	1.256	14.15	15.67	0.0279
0.035	0.975	0.961	14.42	15.72	0.0218
0.030	0.987	0.707	14.60	15.75	0.0163
0.025	0.994	0.419	14.70	15.79	0.0114
0.020	0.997	0.314	14.76	15.70	0.0073

For large thrust levels, the empirical data displayed in Fig. G-6 was assumed for an exit diameter of 0.200 in. The efficiency can be improved over that which is seen

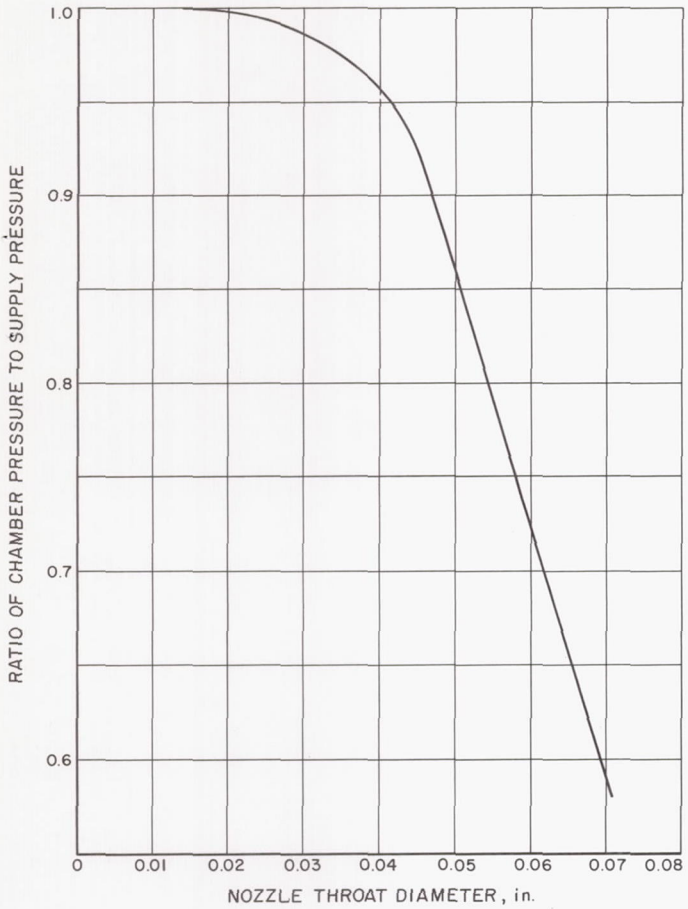

Fig. G-5. Steady-state chamber pressure, effective solenoid valve-flow diameter, 0.063 in.

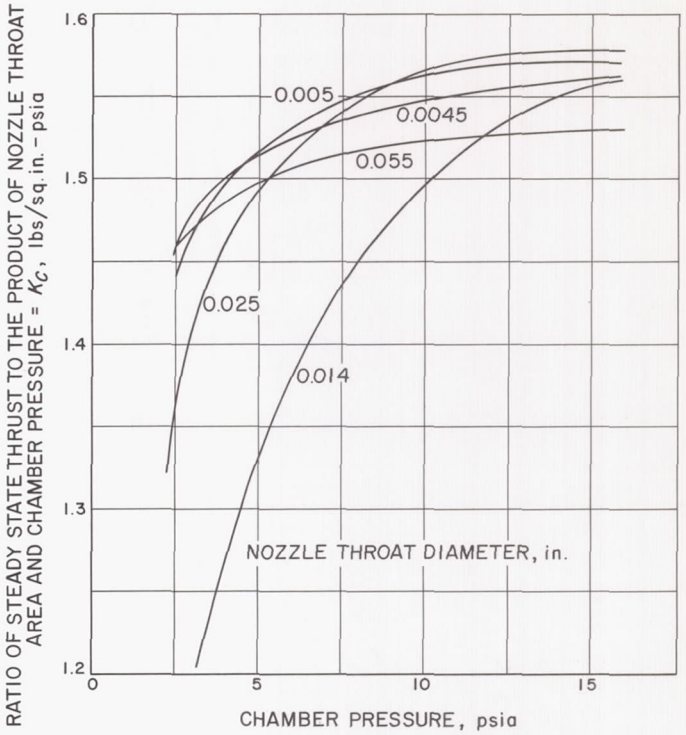

Fig. G-6. Nozzle steady-state thrust, nozzle exit diameter = 0.1982 in. (20° half angle)

in Fig. G-6 by 7% with an area ratio of 100:1. Therefore, the thrusts are divided by 1.07 to compensate; this yields

$$F_{+y} = 0.0354 \text{ lb}$$

$$F_{-y} = 0.0347 \text{ lb}$$

The nozzle diameters shown make this allowance. Thrust levels other than those noted are not benefitted as greatly.

Table G-5, showing the relationship between the C.G. location and control valve, is given below.

A picture of the jet nozzles is shown in Fig. G-7.

5. Gas Consumption Analysis

The attitude control gas is stored in two independent reservoirs to provide redundancy for reliability. If a valve should fail to close, one reservoir will be entirely depleted, but only one-third of the other will be used to balance the torque from the failed valve. The dual gas system is shown in Fig. G-8.

The failure mode of interest occurs when one of the valves from reservoir *A* remains open. Assuming that the gas supplies in *A* and *B* are equal, then the control

Table G-5. Relationship between C.G. location and control valve

Control valve rotation	C.G. offset (center of mass)	Roll axis C.G. location			
		Cruise I 473.82	Midcourse 473.36	Cruise II 473.74	Terminal 473.46
Pitch (−x)	−0.66 yaw	28.15		28.19	
	−0.93 yaw				28.07
	−0.98 yaw		28.08		
Pitch (+x)	−0.66 yaw	29.36		29.41	
	−0.93 yaw				29.76
	−0.98 yaw		29.85		
Yaw (−y)	+0.13x	32.08	32.37	32.12	32.30
		11.62	11.44	11.58	11.47
Yaw (+y)	+0.13x	32.30	32.58	32.34	32.51
		11.34	11.17	11.32	11.21

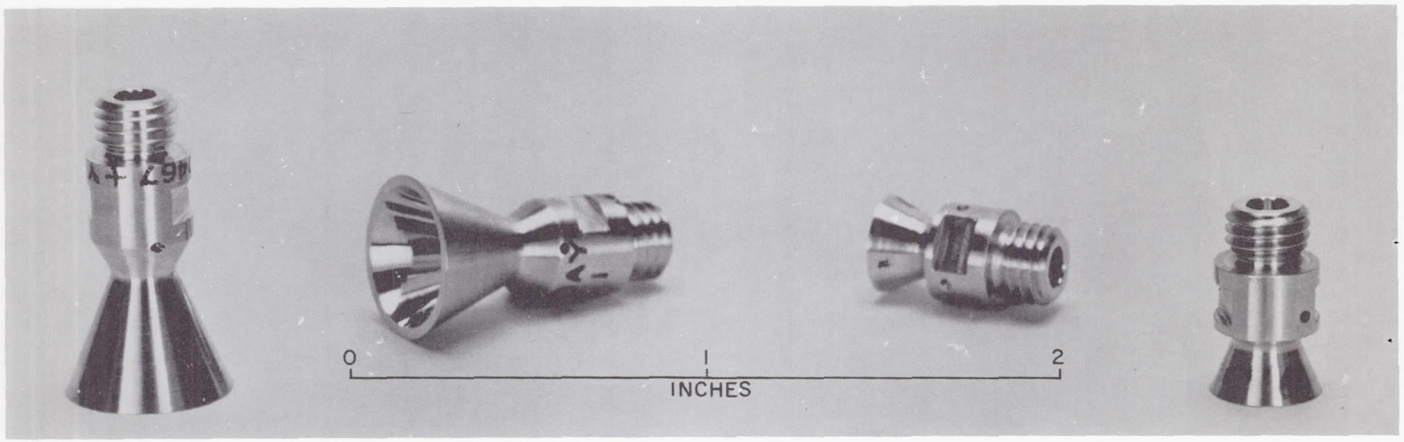

Fig. G-7. *Ranger* gas-jet nozzles

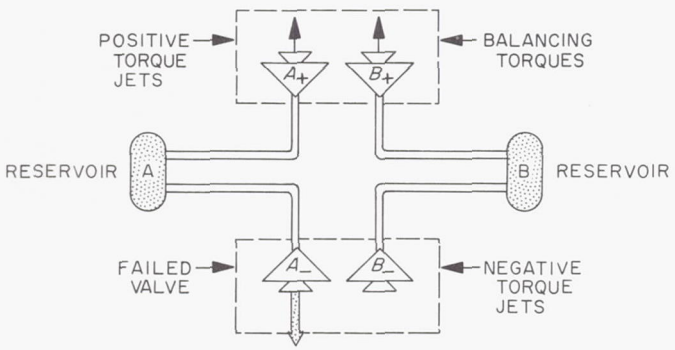

Fig. G-8. Dual gas system, one axis

moment needed to equal the torque created by the stuck valve A_- is proportional to the gas flow rates, as

$$Q_{A_+} + Q_{B_+} = Q_{A_-} \tag{G-8}$$

where Q = mass flow rate of the gas. Since

$$Q_{A_+} = Q_{B_+} \tag{G-9}$$

Eq. (G-9) may be rewritten as

$$Q_{A_+} = \frac{1}{2} Q_{A_-} \tag{G-10}$$

Therefore, each valve must provide one-half the torque needed to equalize that created by the stuck valve.

Now the gas consumed is given by

$$W = Q\Delta T \tag{G-11}$$

where

W = gas weight

ΔT = duration that valves are open

For reservoir A, the gas expulsion is a function of the stuck valve flow rate and also the valve providing the righting torque, so that

$$W_A = (Q_{A'_-} + Q_{A_+})\,\Delta T \tag{G-12}$$

Substituting Eq. (G-10) into (G-12)

$$W_A = (Q_{A_-} + \tfrac{1}{2}Q_{A_-})\,\Delta T$$

and

$$W_A = (\tfrac{3}{2}Q_{A_-})\,\Delta T \tag{G-13}$$

The additional gas that reservoir B must contain in the event of a failure of this nature is then

$$\Delta W_B = Q_B \Delta T \tag{G-14}$$

where, from Eq. (G-9) and (G-10),

$$Q_B = \tfrac{1}{2}Q_{A_-} \tag{G-15}$$

Then, Eq. (G-14) is rewritten as

$$\Delta W_B = \tfrac{1}{2}Q_{A_-}\Delta T \tag{G-16}$$

The ratio of the gas consumed in reservoir B to that in A gives

$$\frac{\Delta W_B}{W_A} = \frac{1}{3} \tag{G-17}$$

or

$$\Delta W_B = \tfrac{1}{3} W_A \qquad \text{(G-18)}$$

so that a failure depletes all of the gas stored in reservoir A and one-third of B, leaving only two-thirds of the initial gas stored in B. Therefore, there will be a reserve equal to one-third of the total original amount stored just prior to failure. Assuming that a failure may occur at the start of the mission, the total gas storage requirement is then equal to three times the amount necessary for attitude control operation.

In the event a failure does deplete one reservoir, the control system acceleration will be reduced by one-half. This will affect the gas consumption in some maneuvers. As a consequence, separate analyses have been made for a normal and a failed (half-gas) system.

The system parameters and environment affect the rate of gas consumption. Therefore, a nominal and *worst* case calculation is made for both the normal and half-gas systems. Since some parameters are difficult to evaluate, they have been selected in the direction of a *worst* case, and thereby cause both the nominal and *worst* cases to be on the pessimistic side.

6. Gas Requirement Summary

The following summary, in Table G-6 below, compiles the results of the gas requirements computed in the main body of this Report for the *Ranger* Block III attitude control system.

Table G-6. Gas requirement summary

Mode	Gas system			
	Normal (no valve failure)		Half (valve failure at mission)	
	Nominal (lb)	Worst case (lb)	Nominal (lb)	Worst case (lb)
Initial rate reduction	8.93×10^{-2}	10.6×10^{-2}	8.93×10^{-2}	10.6×10^{-2}
Acquisition transients	5.3×10^{-2}	6.9×10^{-2}	11.0×10^{-2}	14.3×10^{-2}
Cruise	20.0×10^{-2}	67.0×10^{-2}	20.0×10^{-2}	67.0×10^{-2}
Commanded turns	9.5×10^{-2}	11.9×10^{-2}	12.2×10^{-2}	16.8×10^{-2}
Midcourse motor firing	9.8×10^{-2}	12.2×10^{-2}	4.9×10^{-2}	6.1×10^{-2}
Leakage	1.0×10^{-2}	1.5×10^{-2}	0.5×10^{-2}	0.7×10^{-2}
Total	54.5×10^{-2}	110.0×10^{-2}	57.5×10^{-2}	115.5×10^{-2}

The total gas storage at launch is

$$W = 4.18 \text{ lb}$$

The amount of gas available if a valve failure occurs at launch is, therefore,

$$W_f = \tfrac{1}{3} W = 1.39 \text{ lb}$$

The gas reserve at encounter is given in Table G-7 below.

Table G-7. Gas reserve at encounter

System			
Normal		Half	
Nominal (lb)	Worst case (lb)	Nominal (lb)	Worst case (lb)
3.64	3.08	0.82	0.23

The most significant number is the reserve available for the system that has a valve failure at launch, and flies with parameters in the *worst* direction. In this case, there is a 0.23-lb reserve. *Worst* case modifications are presented below.

a. Worst case modifications.

(1) *Initial rate reduction.* The only major change assumed is due to a variation in the specific impulse of $\pm 20\%$.

(2) *Acquisition transients.* Several parameters affect the acquisition gas consumption. The specific-impulse acceleration constant and torque, for example, contribute to a total variation of approximately 30%.

(3) *Commanded turns.* The gas consumed in the turns is mostly changed by an increase in the *on* time due to changes in system parameters and I_{sp}. The full system is changed by $\pm 25\%$; the half-system by $\pm 37\tfrac{1}{2}\%$.

(4) *Midcourse motor firing.* A total change of approximately 25% is due to I_{sp} and the acceleration constant α.

APPENDIX H

Attitude Control Schematics

The circuit diagrams provided in this appendix are included to extend the depth of the analyses conducted in this Report. Each of the attitude control subsystems are listed below, and shown in schematic form on the following pages in Fig. H-1 through H-12.

Figure	*Attitude Control Subsystem*
H-1.	Sensors, Sun; primary and secondary
H-2.	Earth sensor
H-3.	Gyro control
H-4.	Gyro and capacitor
H-5.	Switching amplifier
H-6.	Derived-rate switching amplifier
H-7.	Antenna control electronics
H-8.	Actuator, antenna
H-9.	Command switching and logic
H-10.	Autopilot electronics
H-11.	Accelerometer
H-12.	Actuator, jet vane

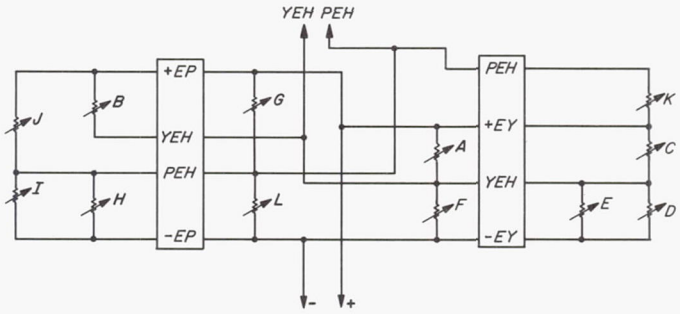

Fig. H-1. Sensors, Sun; primary and secondary

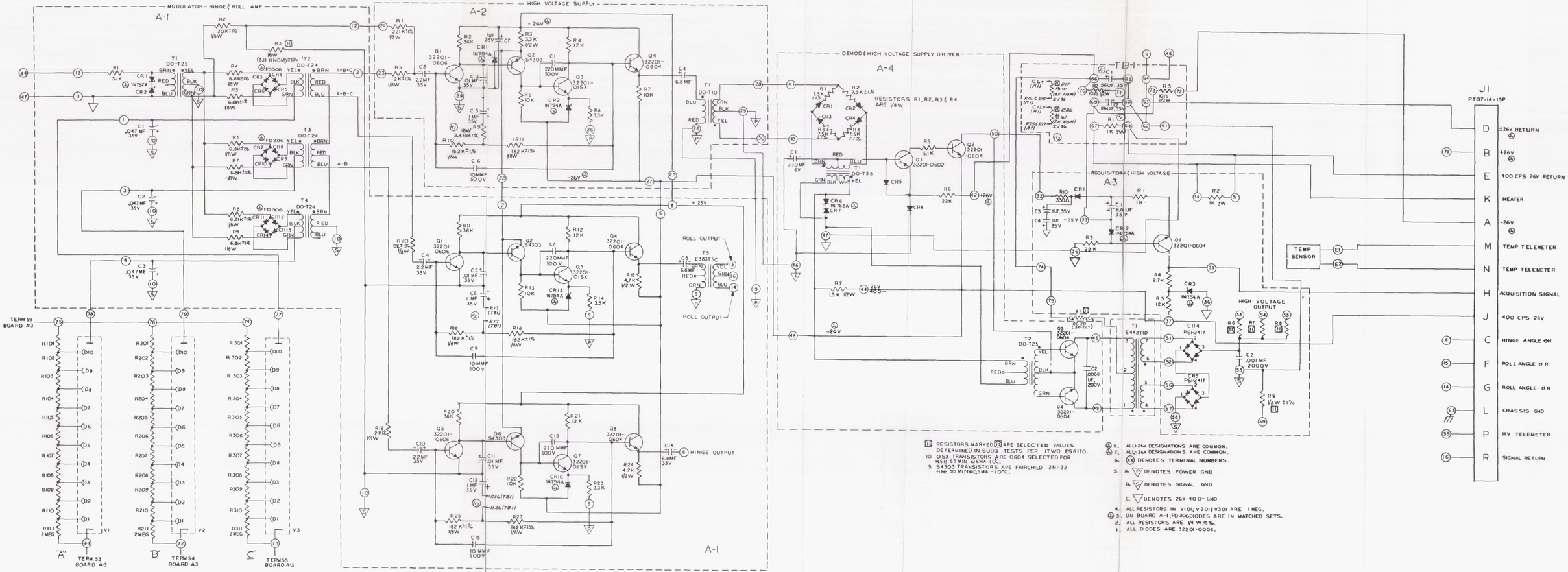

Fig. H-2. Earth sensor

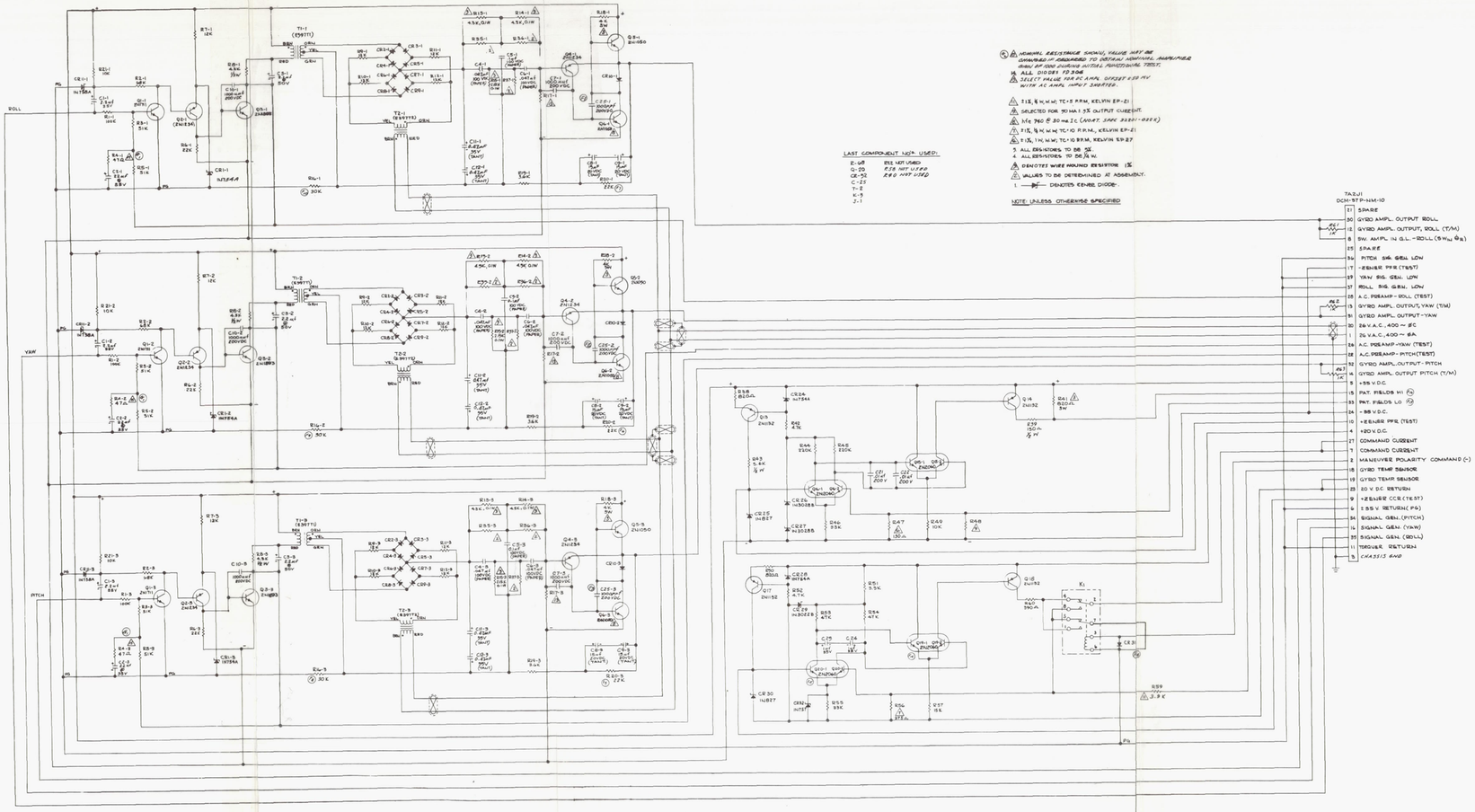

Fig. H-3. Gyro control

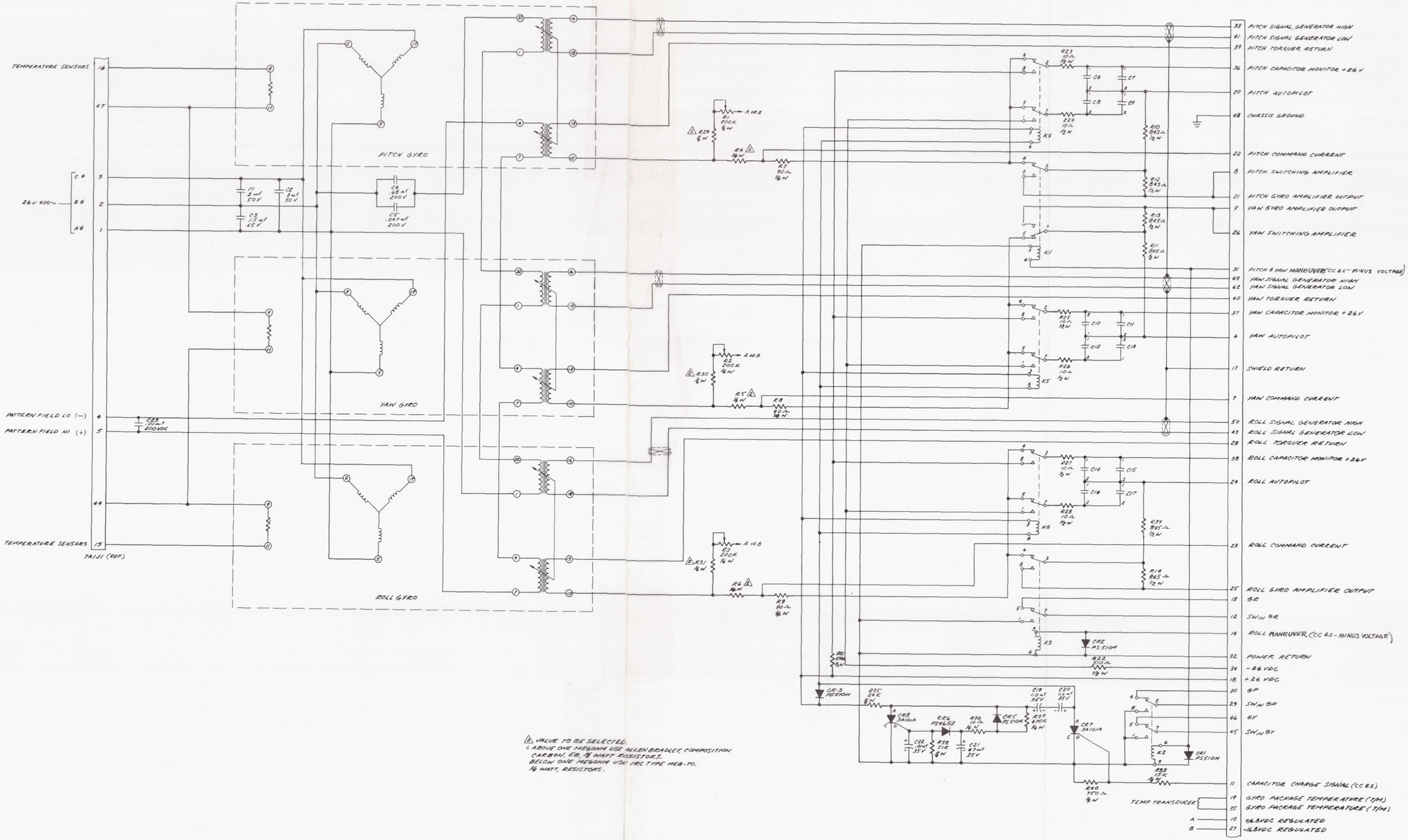

△ VALUE TO BE SELECTED.
1. ABOVE ONE MEGOHM USE ALLEN BRADLEY, COMPOSITION CARBON, ±2%, ½ WATT RESISTORS.
BELOW ONE MEGOHM USE: IRC TYPE MEB-TO, ½ WATT, RESISTORS.

Fig. H-4 Gyro and capacitor

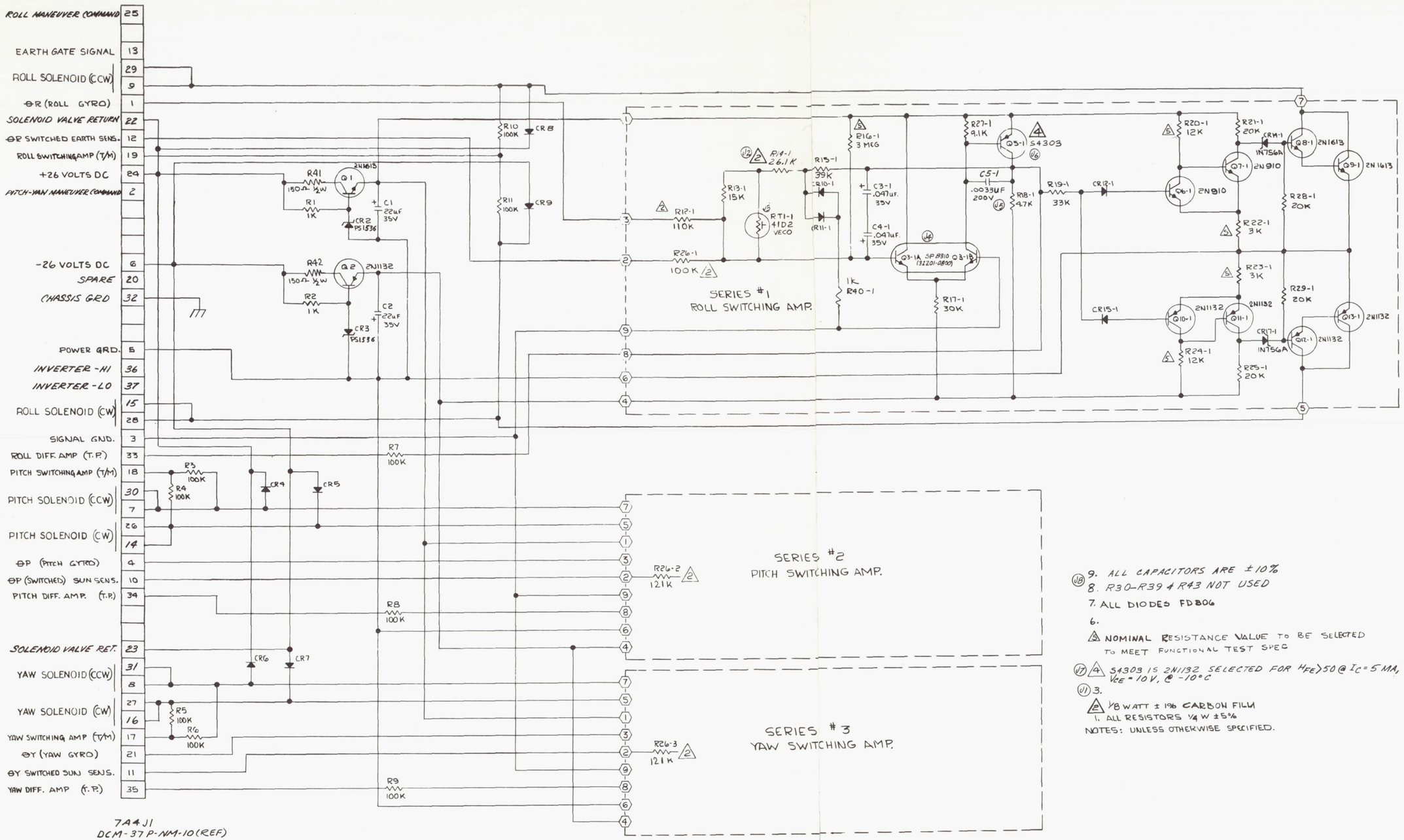

(J8) 9. ALL CAPACITORS ARE ±10%
8. R30–R39 & R43 NOT USED
7. ALL DIODES FD806
6.
△5 NOMINAL RESISTANCE VALUE TO BE SELECTED TO MEET FUNCTIONAL TEST SPEC
(J7) △4 S4303 IS 2N1132 SELECTED FOR H_{FE} > 50 @ I_C = 5 MA, V_{CE} = 10 V, @ -10°C
(J1) 3.
△2 ⅛ WATT ± 1% CARBON FILM
1. ALL RESISTORS ¼ W ±5%
NOTES: UNLESS OTHERWISE SPECIFIED.

Fig. H-5. Switching amplifier

2. 150

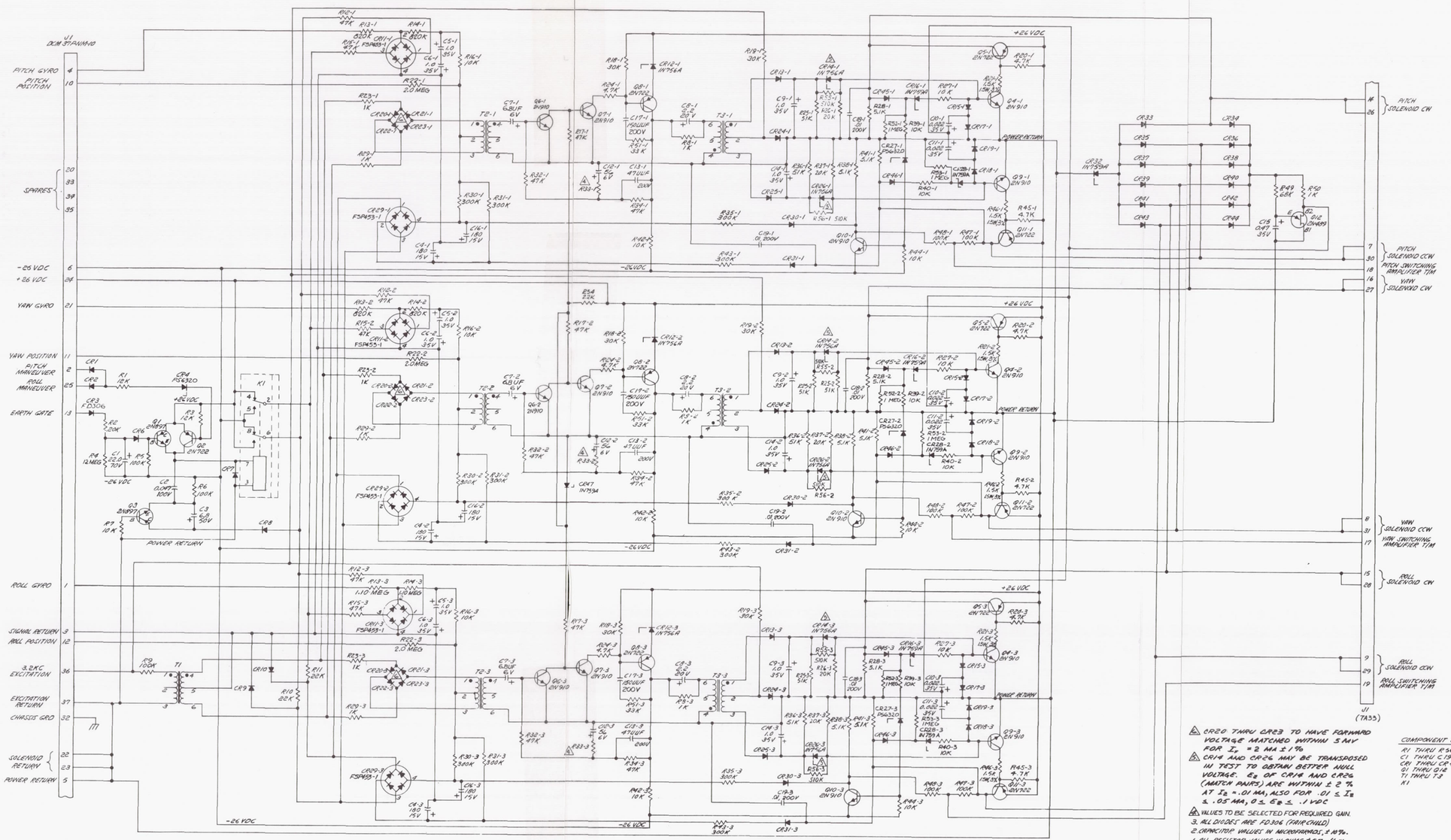

△ CR20 THRU CR23 TO HAVE FORWARD VOLTAGE MATCHED WITHIN 5 MV FOR I_F = 2 MA ± 1%

△ CR14 AND CR26 MAY BE TRANSPOSED IN TEST TO OBTAIN BETTER NULL VOLTAGE. E_R OF CR14 AND CR26 (MATCH PAIRS) ARE WITHIN ± 2 % AT I_R = .01 MA, ALSO FOR .01 ≤ I_R ≤ .05 MA, 0 ≤ E_R ≤ .1 VDC

△ VALUES TO BE SELECTED FOR REQUIRED GAIN.

3. ALL DIODES ARE FD 306 (FAIRCHILD)
2. CAPACITOR VALUES IN MICROFARADS, ± 10%.
1. ALL RESISTOR VALUES IN OHMS ± 5%, ¼W.

NOTES: UNLESS OTHERWISE SPECIFIED

COMPONENT DESIGNATIONS USED

R1 THRU R56-3
C1 THRU C19
CR1 THRU CR49 (NOT USED: CR5)
Q1 THRU Q12
T1 THRU T3
K1

Fig. H-6. Derived-rate switching amplifier

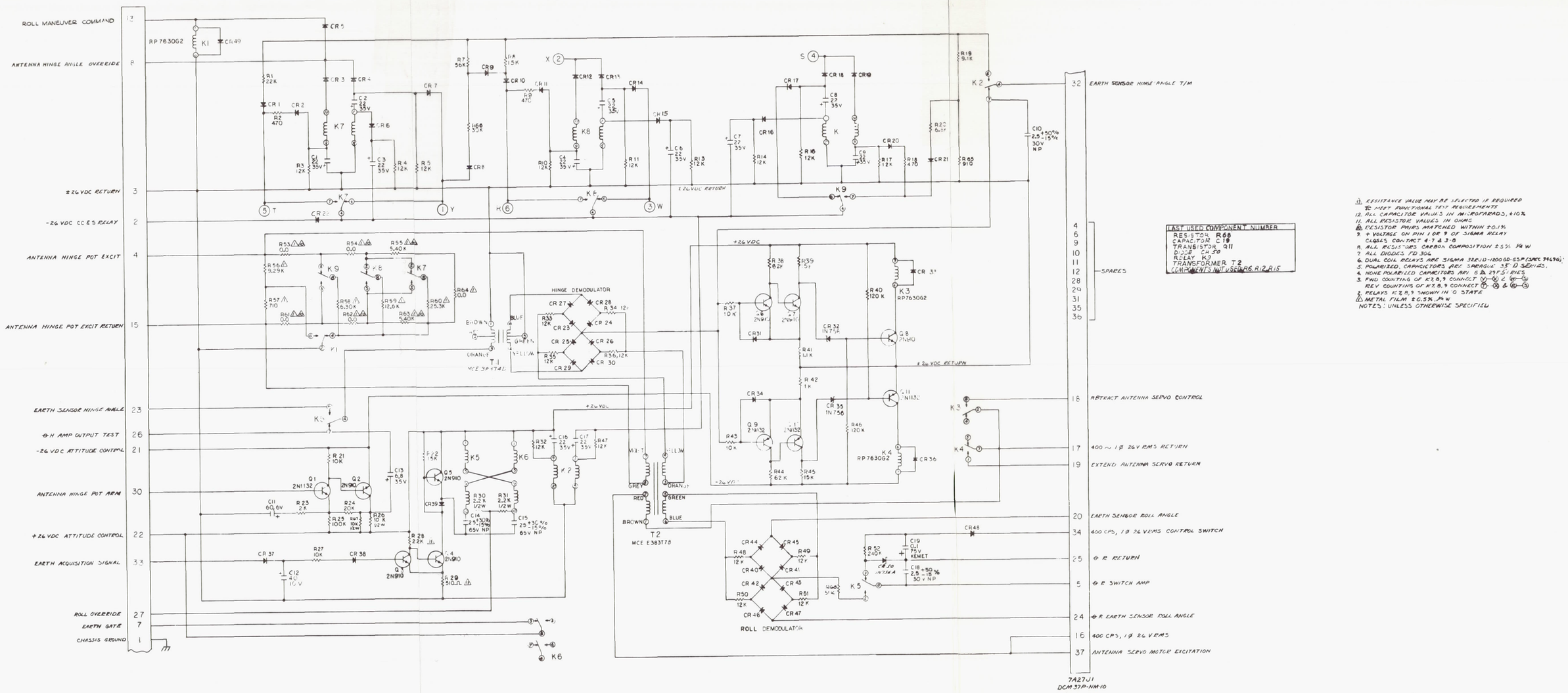

Fig. H-7. Antenna-control electronics

1. 152 2 152 3

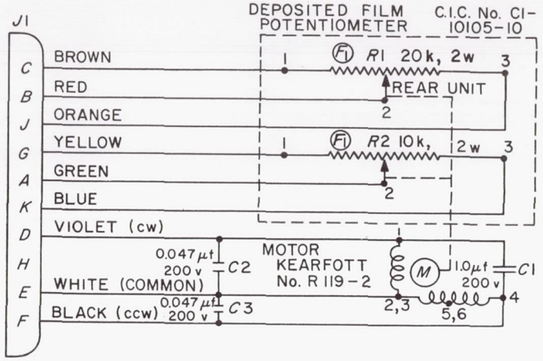

BENDIX CONNECTOR
PT07H-12-10 P

WARNING:
LIMIT CURRENT IN POTENTIOMETER WIPERS TO LESS THAN 0.1 ma TO PREVENT DAMAGE TO THE POTENTIOMETERS

Fig. H-8. Actuator, antenna

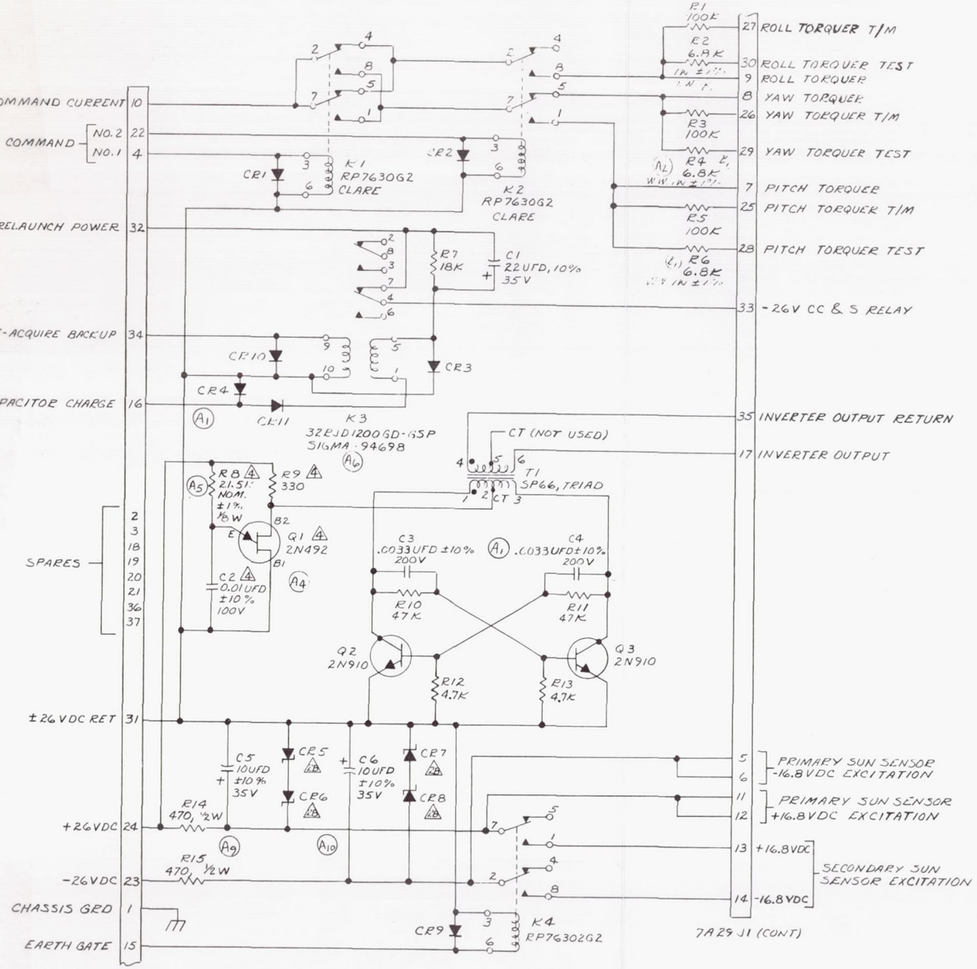

(A3) ⚠4 BEFORE TEST, COMPONENTS SHALL BE SELECTED TO TUNE INVERTER TO 3000 ± 200 CPS

3. CAPACITORS
   A. C1, C5 & C6 ARE SPRAGUE TYPE 350D.
   (A7) B. C2 IS WES-CAP TYPE A98K_____-3
   C. C3 & C4 ARE VITRAMON TYPE VK

⚠2 DIODES
   A. CR1, CR2, CR3, CR4, CR9, CR10, CR11 ARE FD306
   (A11) B. CR5 & CR6; CR7 & CR8 ARE DICKSON ELECTRONICS DIODES, CT3053 WILL BE SUPPLIED IN MATCHED PAIR. (A12) SELECTED FOR 16.8VDC ± 0.5%

1. ALL RESISTORS ARE ±5%, 1/4 W

NOTES: UNLESS OTHERWISE SPECIFIED

Fig. H-9. Command switching and logic

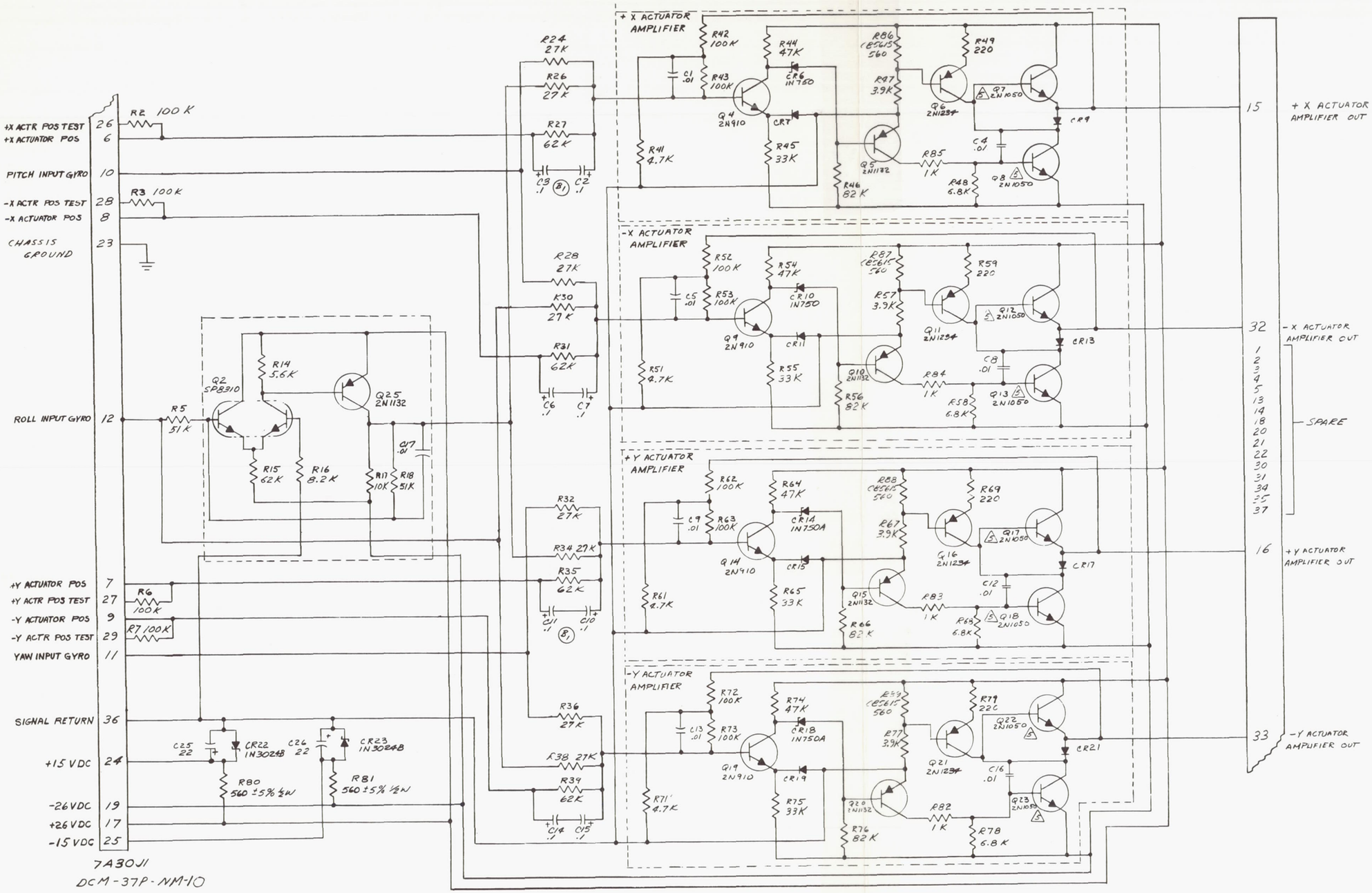

9. COMPONENTS NOT USED:
R1, R4, R8 THRU R13, R19 THRU R23, R25, R29, R33, R37, R40, R50, R60, R70. CR1 THRU CR5, CR8, CR12, CR16 & CR20. C18 THRU C24. Q1, Q3, Q24.

8. LAST COMPONENTS USED:
R89
CR23
C26
Q25

7. ALL POLARIZED CAPACITORS ARE SPRAGUE TYPE 350D 10% 35V.

6. ALL NON-POLARIZED CAPACITORS ARE VITRAMON TYPE VK 10% 200V.

△ SELECTED FOR H_{FE} 790 @ I_C = 30 ma

4. NONE

3. CAPACITANCE IN μF

2. RESISTANCE IN OHMS ±5%, 1/4W

1. ALL DIODES ARE FD300.

NOTES-UNLESS OTHERWISE SPECIFIED

Fig. H-10. Autopilot electronics

154

1.

2.

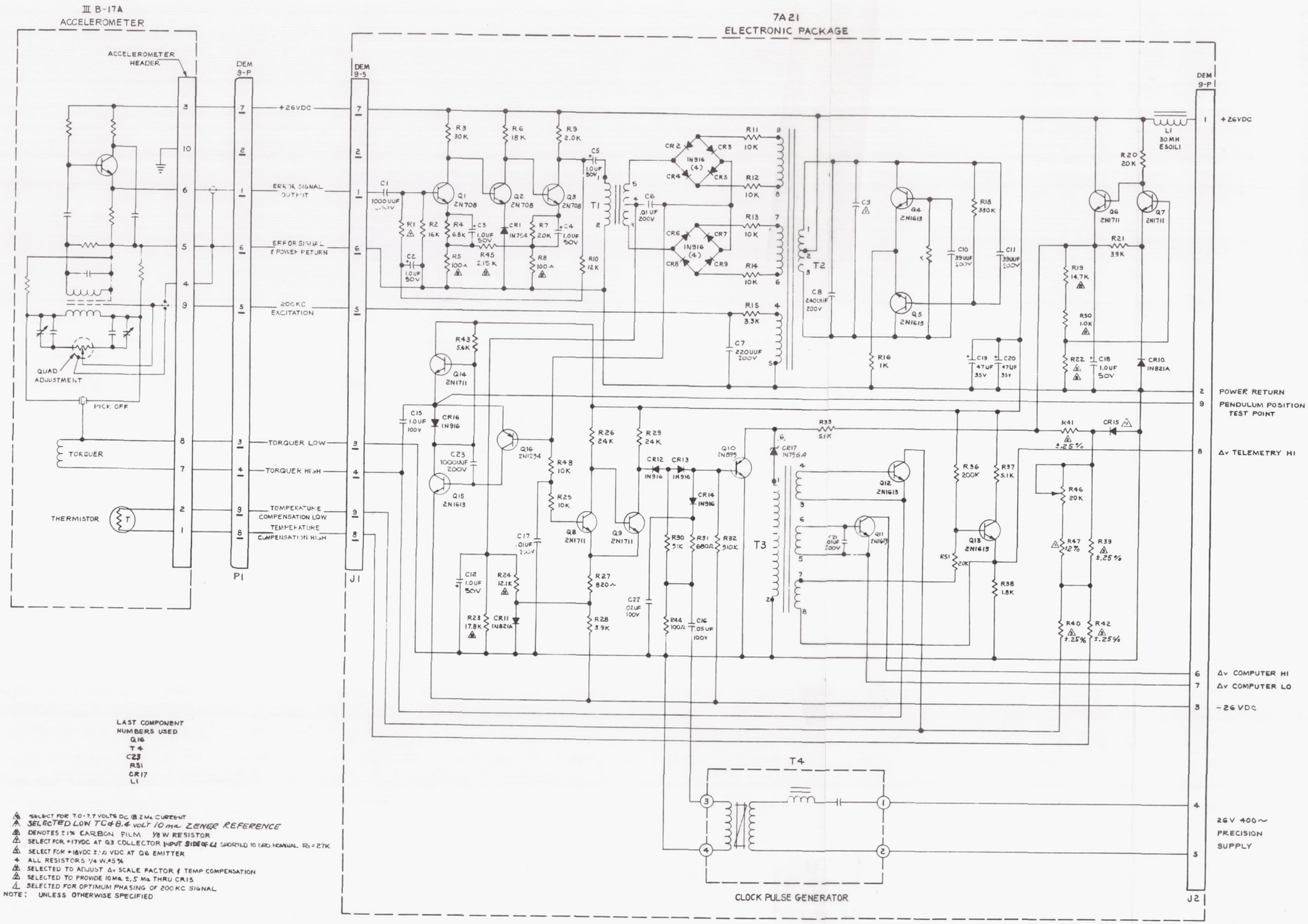

LAST COMPONENT NUMBERS USED
Q16
T4
C23
R51
CR17
L1

NOTE: UNLESS OTHERWISE SPECIFIED
- SELECT FOR 7.0-7.7 VOLTS DC @ 2 Ma CURRENT
- SELECTED LOW TC 8.4 VOLT 10 ma ZENER REFERENCE
- DENOTES ±1% CARBON FILM 1/8 W RESISTOR
- SELECT FOR +17VDC AT Q3 COLLECTOR INPUT SIDE OF L1 SHORTED TO GRD NOMINAL RL = 27K
- SELECT FOR +18VDC ±1.0 VDC AT Q6 EMITTER
- ALL RESISTORS 1/4 W, ±5%
- SELECTED TO ADJUST Δv SCALE FACTOR & TEMP COMPENSATION
- SELECTED TO PROVIDE 10 Ma ±.5 Ma THRU CR15
- SELECTED FOR OPTIMUM PHASING OF 200 KC SIGNAL

Fig. H-11. Accelerometer

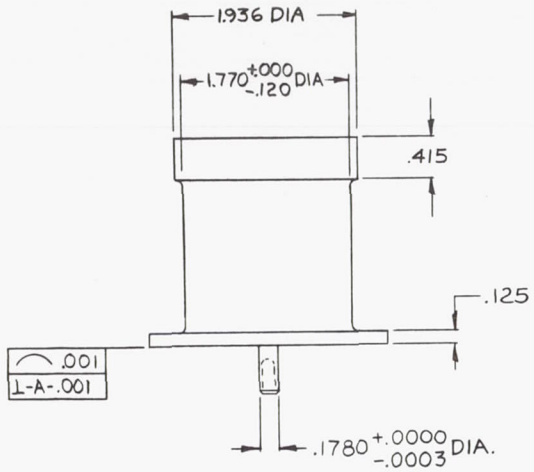

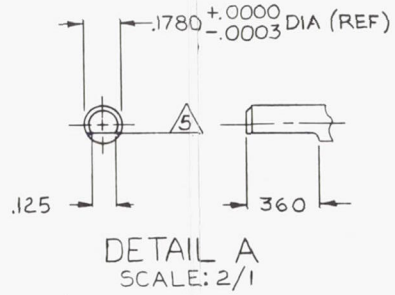

DETAIL A
SCALE: 2/1

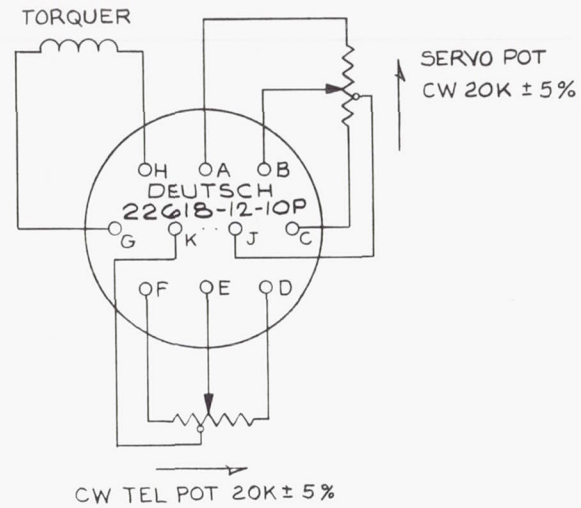

CONNECTOR SCHEMATIC 8 9 10

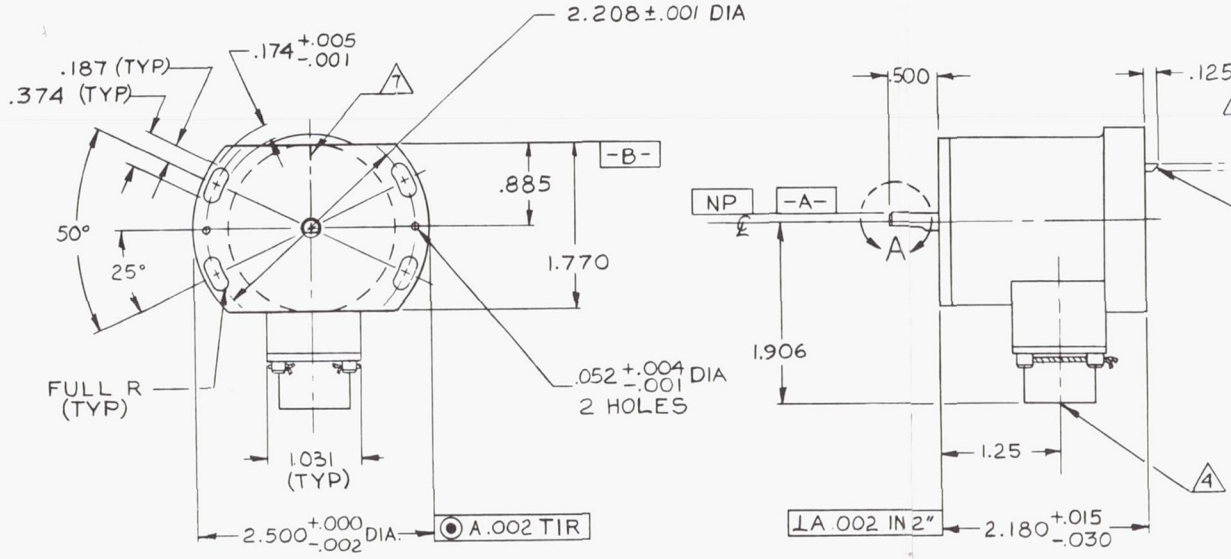

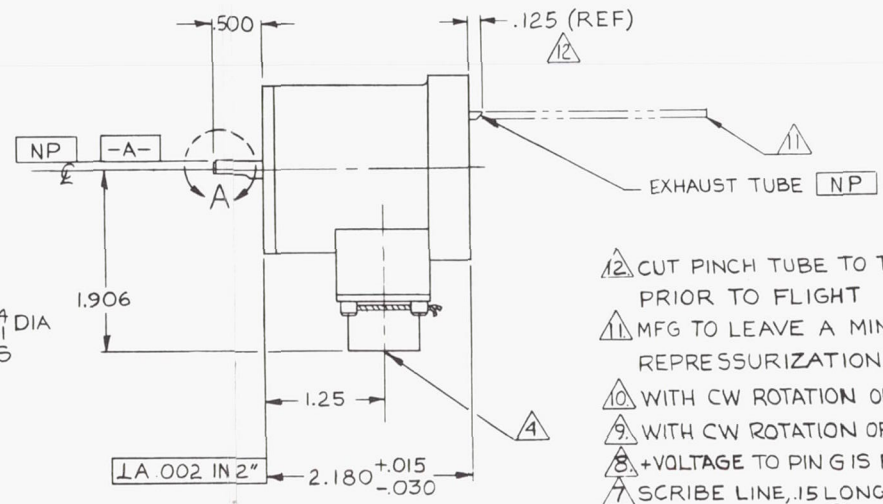

12 CUT PINCH TUBE TO THIS DIMENSION AFTER FINAL PRESSURIZATION PRIOR TO FLIGHT
11 MFG TO LEAVE A MIN. OF 2.5 LENGTH OF PINCH TUBE FOR REPRESSURIZATION PURPOSE
10 WITH CW ROTATION OF OUTPUT SHAFT, TELEMETERING POT SLIDER APPROACHES PIN 'D'
9 WITH CW ROTATION OF OUTPUT SHAFT, SERVO POT SLIDER APPROACHES PIN 'A'
8 +VOLTAGE TO PIN G IS PRODUCED BY CW ROTATION (LOOKING AT TORQUER) OF OUTPUT SHAFT
7 SCRIBE LINE, .15 LONG, .005 +.005 -.000 WIDE LOCATED WITHIN .010 OF TRUE POSITION AS SHOWN
6. POLISH PER (3) EXCEPT SURFACE MARKED NP
5 FLAT TO BE PARALLEL TO -B- ± ½° AT ELECTRICAL NULL
4 CONNECTOR TO BE DEUTSCH 22618-12-10P OR EQUIVALENT
3. MACHINE FILLET RAD. .030 MAX.
2. REMOVE ALL BURRS AND SHARP EDGES
1. MACHINE FINISH 125

NOTES: UNLESS OTHERWISE SPECIFIED

Fig. H-12. Actuator, jet vane

2 156

APPENDIX I

Supplemental Documents

The subject matter prepared in this appendix may be said to contain some very essential contributions which made this extensive Report possible. From the inception of the *Ranger* program in 1959 to the present, many engineering reports, memos, design workbooks, and engineering notes have been meticulously written and documented, for the most part. However, no matter how these documents were finally assembled, they originated in the minds of many exceptionally talented and dedicated engineers at JPL. The following list of supplemental documents is presented, therefore, in this appendix since most of these documents are not distributed off-Lab as are, for example, the Technical Reports, Technical Memoranda, and Space Programs Summary (SPS). However, the bulk of this material originated in the Guidance and Control Division and may possibly be available upon request from Mr. R. G. Forney, Chief of Section 344.

These supplemental documents are divided into several sections in order to present information pertaining (1) to a particular phase of the flight or (2) to one of the subsystems. Also included is a list of supplemental documents related to the *Mariner* spacecraft; this is done simply because many of the *Ranger* studies are neatly related to the *Mariner* program. All of these pertinent and significant supplemental documents are listed on the following pages.

The supplemental documents are listed chronologically, for the most part, and originated from Division 34 and/or Section 344, unless otherwise noted. Pertinent abbreviations used in the listed documents include the following, in their order where first mentioned:

1. IOM = Internal Office Memorandum
2. G&C = Guidance and Control
3. TM = Technical Memo
4. SPS = Space Programs Summary
5. ARS = American Rocket Society
6. Conf. = Conference
7. AIAA = American Institute of Aeronautics and Astronautics
8. DER = Design Evaluation Review
9. Spec. = Specification
10. FR = Functional *Ranger*
11. RFP = Request for Proposal
12. RL = Revised List
13. RTM = *Ranger* Technical Memo
14. TR = Technical Report
15. Mar. = *Mariner*
16. RA = *Ranger*

1. Attitude Control

	Document	Title	Author
1.	IOM (10/23/59)	Sun Oriented Attitude Control System	H. Vivian, D. Acord
2.	G&C #2 (1/19/60)	Tumbling Rate Reduction for a Vehicle with a Simplified Gas Type Attitude Control System	A. Klumpp
3.	G&C #4 (2/10/60)	Three-Dimensional Study of Spacecraft Attitude Control	P. Eckman
4.	IOM (3/7/60)	Specifications of Sun-line Attitude Control Parameters for *RA*-1 and *RA*-2 Spacecraft	T. Barber
5.	IOM (3/9/60)	*RA*-3 Spacecraft Guidance and Control Program	J. Stearns
6.	IOM (3/16/60)	Specifications of Earth-Line Attitude Control Parameters for *RA*-1 & 2 Spacecraft	W. Breckenridge
7.	G&C #6 (3/30/60)	Torque Crosscoupling Arising from Jet Axis Misalignment & Center of Gravity Motion for a Single Jet per Axis System	T. Barber
8.	IOM (4/14/60)	Engineering Review *RA*-3 Attitude Control and Power System	J. Stearns
9.	IOM (7/15/60)	Preliminary *RA*-3 Functional Description	A. Klumpp
10.	IOM (8/5/60)	Definition of Spacecraft Coordinate System for *RA*-3, 4, 5	A. Forsythe, A. Klumpp

	Document	Title	Author
11.	IOM (10/5/60)	*RA*-3, 4, 5, Bi-Weekly Reports, Sept. 19, 1960–Jan. 23, 1962	E. Linderman
12.	IOM (12/5/60)	*RA*-3, 4, 5 Attitude Control Problem Items	A. Klumpp
13.	G&C TM #12 (5/2/61)	Analysis of a Roll, Pitch Maneuver Using Optical Pitch & Yaw Control and Inertial Roll during the Roll Turn & All Inertial Control during the Pitch Turn	A. Klumpp
14.	SPS 37-9, Vol. II (6/1/61) (Confidential)	*Ranger* Attitude Control System	JPL, Sect. 344
15.	Design Workbook (8/3/61)	*Ranger* 3, 4, 5 Attitude Control Sun Acquisition Design	A. Klumpp
16.	Aerospace Corp., ARS G&C Conf. (8/7/61)	Limit Cycles in Reaction Jet Attitude Control Systems, Subject to External Torques	P. R. Dahl, G. T. Aldrich, L. K. Herman
17.	IOM (5/31/62)	Attitude Control Design Criteria	V. Anthony, E. Linderman
18.	IOM (4/2/63)	Attitude Control Interface Changes	A. Cohee, R. Hill
19.	AIAA G&C Conf. #63-327 (8/12-14/63)	Theoretical & Practical Aspect of Solar Pressure Attitude Control for Interplanetary Spacecraft	J. D. Acord, J. Nicklas
20.	NASA/JPL Re-order #63-425 (9/63)	Attitude Control—*Ranger* Program Documentation Data	Northrop Space Laboratories
21.	Northrop Space Labs, DER #0069 (10/4/63)	Design Evaluation Recommendation, Attitude Control Subsystem	D. McLain
22.	Spec. #FR3-4-420 (10/21/63)	Functional Specification *Ranger* Block III Attitude Control and Autopilot Subsystems	JPL, Sect. 344
23.	IOM (11/12/63)	*Ranger* Block III Information	R. G. Forney
24.	IOM (5/7/64)	Functional Changes between *Ranger* 6 & 7	P. Meyer
25.	IOM (5/28/64)	*Ranger* Block III Guidance and Control Subsystem Functional Description	JPL, Sect. 344

2. Midcourse Analysis

26.	IOM (4/14/60)	Attitude Control Requirements of the Midcourse Motor for *RA*-3	A. Klumpp
27.	IOM (4/14/60)	Current Estimates of Guidance and Subsystems Errors for *RA*-3	D. Morris
28.	IOM (4/18/60)	Summary of Assumption and Calculations of Midcourse Pointing and Guidance Errors for *RA*-3	W. Breckenridge
29.	IOM (7/14/60)	*RA*-3, 4, 5 Midcourse Maneuver	E. Linderman
30.	IOM (7/14/60)	*RA*-3 Midcourse Guidance System Function Specification	W. Breckenridge
31.	IOM (7/20/60)	*RA*-3 Midcourse Autopilot	T. Casad
32.	IOM (8/8/60)	Attitude Control Requirements on Spacecraft Dynamic Characteristics, Midcourse Motor Calibration, & Midcourse Motor Mounting	A. Klumpp, T. Casad
33.	G&C TM #8 (8/12/60)	Midcourse-Maneuver Error Analysis	W. Breckenridge
34.	IOM (8/19/60)	*RA*-3 Midcourse Autopilot (Revised)	T. Casad
35.	IOM (8/20/60)	*RA*-3 Midcourse-Roll Control System	W. Breckenridge,
36.	IOM (8/23/60)	*RA*-3 Midcourse & Terminal Error Analysis	A. Klumpp
37.	IOM (10/6/60)	*RA*-3, 4, 5 Midcourse Motor Vibration Measurements at the Accelerometer	E. Linderman
38.	IOM (11/9/60)	*RA*-3 Autopilot Roll Control	T. Casad

	Document	Title	Author
39.	Engr. Notes (12/5/60)	Midcourse Maneuver Constraints	W. Breckenridge
40.	Sec. 312 RFP #3 (2/11/61)	Error Analysis of Midcourse Guidance System	J. O. Maloy
41.	Sec. 312 RFP #3, Addendum #1 (5/8/61)	Change in Midcourse Error Analysis Program	J. O. Maloy
42.	IOM (3/14/61)	Command Turn Analysis (Analog Computer)	A. Klumpp
43.	IOM (3/23/61)	Mandatory Autopilot Change	E. Linderman
44.	IOM (4/5/61)	Electrical Limiting in the Autopilot Roll Channel for *Ranger* 3 and *Mariner* A	A. Klumpp
45.	Sec. 312 RFP #2, Addendum #2 (5/22/61)	Error Analysis of Midcourse Guidance System	J. O. Maloy
46.	Design Workbook (7/31/61)	Commanded Turn Analysis	A. Klumpp
47.	IOM (9/20/61)	Effect of Structural Resonances on Autopilot Stability	J. Smith
48.	IOM (12/1/61)	*RA*-3 Midcourse Maneuver Error Analysis	E. Suggs
49.	Engr. Notes (1/12/62)	Commanded Turn Analysis	K. Bouvier
50.	Engr. Notes (1/15/62)	Roll, Pitch Turns	A. Klumpp
51.	Spec. #RL-4-460 (1/22/62)	Functional Specification Spacecraft, *Ranger* 6, 7, 8, 9 Flight Equipment, Midcourse Autopilot System	JPL, Sect. 344
52.	IOM (1/31/63)	Request for Midcourse Guidance Program	E. Suggs
53.	IOM 312-281 (2/25/63)	Effect of Some Midcourse Mechanization Tolerances on the Precision of Lunar Impact	L. Bronstein, D. Curkendall
54.	IOM (5/3/63)	Meeting on C.G. Documentations: Autopilot Stability and Midcourse Correction Accuracies	A. Kidd
55.	IOM (5/16/63)	Thrust-Vector Errors in Midcourse	A. Kidd
56.	Nortronics Memo 1-T4403/63/9 (9/9/63)	Comparison of Modified Jet-Vane Actuator with Old One	H. Nakano
57.	Nortronics Memo 1-T4403/63/8 (9/9/63)	Transverse Velocity Error during Midcourse Maneuver	H. Nakano
58.	Nortronics Memo 1-T4403/63/7 (9/9/63)	Jet-Vane Actuator Loop Analysis	H. Nakano
59.	IOM (10/10/63)	*RA* Block III Midcourse Maneuver Execution Capabilities	G. D. Pace
60.	IOM (10/11/63)	Midcourse Maneuver Error Analysis Block III	W. Turk
61.	IOM (12/8/63)	*RA* Block III Midcourse Maneuver Execution Capabilities	G. D. Pace
62.	SPS 37-4, Vol. II (1/1/60) (Confidential)	*RA*-3 Midcourse Guidance System	JPL, Sect. 344
63.	IOM (1/31/64)	*Ranger* Autopilot Analysis	H. Nakano

3. Terminal Analysis

64.	G&C TM #11 (4/20/61)	Error Analysis for Pitch-Yaw-Pitch Maneuver Using Optical Roll Control and Inertial Pitch and Yaw Control	A. Klumpp
65.	IOM (10/3/61)	*Ranger* 3 Terminal Maneuver Error Analysis	E. Suggs
66.	IOM (9/24/63)	*Ranger* Block II Terminal Maneuver Error	H. K. Bouvier

	Document	Title	Author
67.	Northrop Space Labs, RTM-E-004 (12/63)	Earth-Probe-Sun Angle Constraints Imposed by Attitude Control System	M. Smith
68.	Engr. Notes (12/63)	*Ranger* Pitch-Yaw-Pitch Turns	W. Kirhofer
4. Gas System			
69.	IOM (4/22/60)	Cold-Gas Midcourse Attitude Control for *RA*-3	J. Stearns
70.	IOM (7/5/60)	Addition of Yaw-Gas Jet Actuators to the *RA*-1, 2 Attitude Control Subsystem	V. Anthony
71.	Engr. Notes (9/19/60)	Gas Calculations	A. Klumpp
72.	IOM (9/26/60)	*RA*-3 Gas Consumption	A. Klumpp
73.	IOM (10/17/60)	Acceleration Tolerances *RA*-1, 2	T. Barber
74.	IOM (11/7/60)	Acceleration Tolerances *RA*-1, 2	T. Barber
75.	IOM (11/23/60)	Redesign of N_2 Pressure Vessel	E. Linderman
76.	IOM (4/10/61)	*RA*-3 Gas Consumption	E. Suggs
77.	IOM (5/8/61)	*RA*-3, 4, 5 N_2 Gas Allowance	E. Linderman
78.	IOM (7/21/61)	Effects of Short-Pulse Duration, Multiple Switching, & Noise on *RA*-3 Gas Consumption & Proposed Action	J. Dahlgren
79.	IOM (8/15/61)	Detailed Report *RA*-1 Attitude Control Gas Leakage	J. Dahlgren
80.	IOM (9/12/61)	*RA*-3 Jet Valve Nozzle Specs.	J. Dahlgren
81.	IOM (11/7/61)	*RA*-3, 4, 5 Attitude Control Gas System	W. Atkinson
82.	IOM (11/9/61)	*RA*-3 Jet Valve Nozzles	J. Dahlgren
83.	IOM (11/13/61)	*RA*-3 Flight Gas Analysis	J. Dahlgren
84.	IOM (11/17/61)	*RA*-3 and *RA*-4 Spacecraft Gas Subsystem Updating & Evaluation	J. Dahlgren
85.	IOM (11/30/61)	*RA*-3 Flight Analysis (Revised)	J. Dahlgren
86.	IOM (4/20/62)	Attitude Control Gas Actuator Bibliography	J. Dahlgren
87.	IOM (1/5/63)	Actuator Group Reliability Estimation	J. Nicklas
88.	JPL RA Spec. (1/30/63)	Attitude Control Gas Actuator System	G. Courville
89.	SPS 37-22, Vol. I (7/31/63)(Confidential)	*Ranger* Gas Actuator Development	E. Koch, J. Dahlgren
90.	IOM (9/20/63)	*Ranger* Block III Gas Storage	K. Bouvier
91.	Engr. Notes (10/63)	Commanded-Turn Transient On Time for Gas Computation	A. E. Cherniack
92.	IOM (10/16/63)	*Ranger* Gas System Acceleration Constant	R. E. Hill
93.	IOM (11/14/63)	Pressure Transducer Safety, & *Ranger* 6, 7 & PTM Regulator Checks	R. Summers
94.	Engr. Notes (1/10/64)	Nozzle Calculations, *Ranger* 6	J. Dahlgren
5. Center of Gravity and Dynamic Problems			
95.	IOM (9/7/60)	Change of C.G. for *RA*-1	J. Stearns
96.	IOM (11/7/60)	Analysis of Disturbance to Spacecraft Due to Motion of On-Board Apparatus	E. Suggs, J. Nicklas
97.	Engr. Notes (1/16/62)	Criteria for Stability for Structural Resonances in the *Forbidden Region*	A. Klumpp
98.	Engr. Notes (4/16/63)	*Ranger* Spacecraft Dynamics	J. South
99.	IOM (7/22/63)	Out-Position Latches for *Ranger* Solar Panel Actuators	W. W. Hough, W. J. Carley

	Document	Title	Author
100.	IOM (8/30/63)	Determination & Control of *Ranger* C.G.	R. G. Forney
101.	IOM (9/17/63)	Recommendations for *Ranger* Block III Structural Design Verification Tests	R. Hill, J. South

6. Celestial Sensors

102.	IOM (1/23/61)	Sensor Short-Term Null Stability vs Null Absolute Values	G. Meisenholder
103.	IOM 344-11 (2/27/61)	Affect of Asymmetrical Albedo on *Ranger* Earth Sensor Accuracy	G. Meisenholder
104.	IOM (3/15/61)	*Ranger* 3 Experimental Sun Sensor Data	G. Meisenholder
105.	IOM (5/15/61)	Asymmetrical Earth Albedo & the *RA*-3, 4, 5 Earth Sensor Pointing Accuracy	G. Meisenholder
106.	IOM (8/17/61)	*RA*-3 and *Mariner A*, Short *Ranger* Earth Sensor Operation	T. Baxter
107.	IOM (10/16/61)	*RA*-2 Earth Sensor	G. Meisenholder
108.	IOM (10/24/61)	Earth Sensor Operation During *RA*-3 PTM Shake Test	T. Baxter
109.	IOM (11/6/61)	Sun Sensors	B. Stultz
110.	IOM (11/7/61)	Reflections from the Spacecraft that Could Produce an Acquisition Signal in the Earth Sensor	T. Baxter
111.	IOM (11/1/61)	Sun Sensors	B. Stultz
112.	IOM (11/20/61)	*RA*-3 Earth Sensor Reflected-Light Discussion	G. Meisenholder
113.	IOM (1/18/62)	Some Inputs Toward the Solution of the *RA*-1 Dilemma	G. Meisenholder
114.	IOM (3/28/62)	Minimum Earth-Probe-Sun Angle for the Present Earth-Sensor Sun Shade	T. Baxter
115.	IOM (5/23/62)	EPS Angle Constraints on *Ranger*	A. Wolfe
116.	IOM (5/29/62)	Present Status of Earth-Sensor-Light Hoods	T. Baxter
117.	TR 32-274 (5/31/62)	Application of Optical Sensors for Lunar and Planetary Space Vehicle	J. Scull
118.	IOM (6/8/62)	*Ranger* Earth Sensor Mechanical Null Measurement	T. Baxter
119.	IOM (6/11/62)	Earth-Sensor-Light Hood with a Decreased Field of View	T. Baxter
120.	Engr. Memo 344-28 (6/19/62)	Relating Detector Response from One Radiant Source to Another Through an Intermediary Calibration such as Foot Candle	G. Meisenholder
121.	IOM (6/22/62)	Additional Power Consumption of the *RA*-6 Primary Sun Sensors	T. Baxter
122.	IOM (6/29/62)	Minimum EPS Data for *Ranger* 8, 9	T. Baxter, V. Anthony
123.	Engr. Notes (7/26/62)	Light-Hood Summary	T. Baxter
124.	IOM (9/6/62)	Revised *Ranger* Earth Sensor & Primary Sun Sensor Temperature Ranges	T. Baxter
125.	IOM (1/14/63)	*Ranger* Celestial-Sensor Talk Outline	JPL, Sect. 344
126.	Engr. Memo 344-29 (3/6/63)	Correction Factors for Converting Present Attitude Reference Bolometric Intensity Readout for the Planets to True Bolometric and also True Times Canopus for an Arbitrary Sensor Response	G. Meisenholder
127.	IOM (3/20/63)	Increased Input Voltages to the *Ranger* 3 Sun Sensors	T. Baxter
128.	IOM (4/4/63)	Summary of Celestial Sensor Activities	G. Meisenholder
129.	IOM (9/5/63)	Proposals for Development of Gas Earth Sensor for *Ranger* Block V	G. Hooper

	Document	Title	Author
130.	IOM (10/22/63)	Accuracy of E-P-Near Limit Mean-Angle Measurement, Using T_2 Optics, and Earth Sensor Test Fixture	W. Berg
131.	IOM (11/1/63)	Attitude Control Design Specification	K. Bouvier
132.	IOM (11/14/63)	Pressure Transducer Safety and *Ranger* 6, 7 and PTM Regulator Checks	R. Summers
133.	IOM (11/14/63)	*Ranger* Earth Sensor Trajectory Constraints	T. Baxter
134.	IOM (11/14/63)	Acceptable *Ranger* Block III Primary Sun Sensor & Earth Sensor Temperature Limits	T. Baxter
135.	IOM (12/27/63)	Earth-Probe-Near Limb-Lit Moon-Angle Test on Earth Sensor S/N 32, 302 [*RA*-6 Flight and 304 (*RA* Spare #1)]	T. Baxter
136.	IOM 344-75 (3/4/64)	Variance between Observed and Produced Earth Light Intensity During the *RA*-6 Flight	T. Baxter
137.	IOM (7/6/64)	Earth and Sun Sensor Calibration Curves to Support the *RA*-7 Flight	T. Baxter
7. Inertial Sensors			
138.	IOM (12/7/60)	*RA*-3, 4, 5 Gyro Factors	R. Hill
139.	IOM (10/25/61)	Gyro Failures, *RA*-3, 4, 5	R. Forney
140.	IOM (3/22/62)	Proposed Scale-Factor Change for *Ranger* Digital Accelerometers	P. Hand
141.	IOM (4/18/62)	*Ranger* 4 Control Gyro-Command Calibration	W. Bachman
142.	IOM (3/11/63)	Calculation of Parameters for the *Ranger* Gyro-Loop Integrators	R. Hill
143.	Engr. Notes (8/17/63)	Gyro & Associated Electronics	M. Laub
144.	Engr. Notes (1/64)	Proposed *Ranger* Block III Gyro Selection	G. Starks
8. Antenna Control Problems			
145.	IOM (4/20/60)	Antenna Hinge Angle for *RA*-3	A. Klumpp
146.	IOM (9/12/60)	Antenna Pointing Control Functional Description	A. Klumpp
147.	IOM (10/17/60)	Angular Velocity of Spacecraft Due to Deployment of High-Gain Antenna *RA*-3	E. Suggs
148.	IOM (10/27/60)	Counterbalancing of High-Gain Antenna Rotational Disturbances, *Ranger*	E. Suggs
149.	IOM (11/3/60)	Counterbalancing of High-Gain Antenna Rotational Disturbances, *Ranger*	J. Nicklas E. Suggs
150.	IOM (2/6/61)	Disturbances to *RA*-3 Attitude Control Resulting from ADF Altimeter and OMNI Support from Motion	E. Suggs
151.	Design Workbook (8/14/61)	Determination of *RA*-3, 4 Preset Antenna Hinge Angles	E. Suggs
152.	IOM (9/27/61)	*RA*-3 Preset Antenna Angles	E. Suggs
153.	IOM (7/3/62)	Antenna Angle While Tracking the Earth on all *Ranger* Missions	T. Baxter
9. Noise Studies			
154.	IOM (6/11/61)	Attitude Control Noise Study	D. Griep
10. Derived Rate			
155.	IOM (2/19/63)	Derived Rate on *Ranger*	E. Cherniack

	Document	Title	Author
156.	IOM (9/13/63)	Flight Acceptance Testing of Derived Rate Switching Amplifiers for *Ranger* Block III	R. E. Hill, T. A. Almaguer
157.	IOM (9/13/63)	System Tests Required from the Derived Rate System	R. E. Hill
11. Reliability			
158.	Table, *RA* (7/1/63)	*Ranger* Attitude Control Reliability Summary, Sun Acquired Cruise	JPL, Sect. 344
12. Flight Analysis			
159.	IOM (4/2/62)	*Ranger* 3 Attitude Control Flight Data Analysis	A. Cherniack, D. Griep, R. Hill
160.	IOM (12/7/62)	*RA*-5 Report to SDAT	E. Linderman
161.	TM 312-269 (1/30/63)	*RA*-6 Study: Some Preliminary Results	D. Curkendall
162.	IOM (11/12/63)	*Ranger* Block III Information	R. G. Forney
163.	IOM (11/14/63)	*Ranger* Block III Flights	R. G. Forney
164.	IOM 344-79 (3/4/64)	*Ranger* 6 Attitude Control Flight Performance	R. E. Hill
165.	IOM (5/8/64)	*RA*-6 Report	F. L. Hattersley
13. Circuit Analysis			
166.	IOM (3/19/63)	*Ranger* Circuit Analysis Program	H. Vivian
14. *Mariner*			
167.	IOM (5/25/61)	Selection of Derived Rate Parameters *Mariner A*, A/C System	K. Bouvier
168.	IOM (5/25/61)	Selection of Derived Rate Parameters *Mariner A*, Attitude Control System	K. Bouvier, D. Griep
169.	*Mar. A*, Design Workbook (6/12/61)	A/C Effect of Possible Transient at Start of Roll Maneuver	D. Griep
170.	*Mar. A*, Design Workbook (6/21/61)	A/C, Definition of Derived Rate Parameters	D. Griep
171.	*Mar. A*, Design Workbook (6/26/61)	Attitude Control, Definition of Rate of Position Constants	A. Cherniack, D. Griep
172.	IOM (7/11/61)	Estimated Gas Requirements, *Mariner A* Attitude Control System	J. Dahlgren, G. S. Perkins
173.	IOM (8/15/61)	*Mariner B*, Roll Autopilot	A. Smith
174.	IOM (8/30/61)	*Mariner B* Roll A/P Using Jet-Vane Control	A. Smith
175.	*Mar. A*, Design Workbook (9/8/61)	A/C, Phase Plane Trajectories for the Roll-Axis Control System Using Derived Rate	D. Moore
176.	*Mar. R*, Notes (9/12/61)	Antenna Slewing Rate Considerations	A. Klumpp
177.	Design Workbook (9/19/61)	Jet-Vane Simulation	A. Smith
178.	IOM (11/22/61)	*Mariner R* Attitude Control System Phasing and T/M Phasing	D. Griep
179.	IOM (1/30/62)	Midcourse Maneuver Error Estimate, *Mariner R*	K. Bouvier
180.	IOM (3/1/62)	*Mariner* Attitude Control Gas System	R. Forney
181.	IOM (3/22/62)	*Mariner R*, Gas Requirements	G. Perkins
182.	IOM (5/28/62)	*Mariner B*, Pitch, Yaw, & Roll Acquisition	K. Bouvier

	Document	Title	Author
183.	IOM (1/18/63)	*Mariner R* Attitude Control Flight Analysis	D. Griep
184.	IOM (8/63)	*Mariner R*, Autopilot	A. Smith
185.	*Mar. R*, Design Workbook (9/63)	Optical Coupling of Yaw Limit Cycle Motion into the Roll Error Channel when High-Gain Antenna Hingle Angle Is Different from 90 Deg	K. Bouvier
186.	IOM (10/28/63)	The Effect of the Derived Rate Signal in Roll Acquisition	C. W. Howard
187.	IOM (10/29/63)	Commanded-Turn Dynamics	C. W. Howard
188.	IOM (10/31/63)	Roll-Axis Cruise-Mode Operation	C. W. Howard
189.	TM 343-39 (11/15/63)	Midcourse Guidance *Mariner C* Accuracy Analysis	D. R. Thomas
190.	IOM 344-45 (2/6/64)	An Analysis of the *Mariner C* Roll Search Transient During Gyro Spin-up	E. Cherniack

15. Space Programs Summary (SPS)—Guidance and Control

	Document	Topics
191.	SPS 37-5, Vol. II, pp.13–23 (10/1/60) (Confidential)	1. Attitude Control a. Sun Sensor b. Earth Sensor c. Jet Valves d. Pressure Regulators e. Nitrogen Charging System f. Gyro Module 2. Midcourse Maneuver
192.	SPS 37-6, Vol. II, pp. 12–33 (12/1/60) (Confidential)	1. *RA*-1, 2 a. Sun Sensor b. Earth Sensor c. Control Gyros d. Instrumentation Gyros e. Controller Timer f. Attitude Control Electronics g. Evaluation 2. *RA*-3, 4, 5 a. Autopilot 1) Mechanization 2) Electronic Design b. Velocity Shutoff System c. System Disturbance 1) Counterbalancing Rotational Disturbances d. Guidance-Error Analysis
193.	SPS 37-8, Vol. II, pp.14–18 (4/1/61) (Confidential)	1. Instrumentation Rate Gyro Module 2. Control Gyro Module 3. Velocity Shutoff Subassembly
194.	SPS 37-9, Vol. II, pp. 4–11 (6/1/61) (Confidential)	1. Analytical Design a. *RA*-1, 2 b. *RA*-3, 4, 5 2. Attitude Control System a. Subsystem Studies b. Electronic Development c. Actuator Development d. Leakage Detection 3. Velocity Shutoff Subsystem 4. Earth Sensor

	Document	Topics
195.	SPS 37-10, Vol. II, pp. 5–9 (10/1/61) (Confidential)	1. Control Gyro Module 2. Midcourse Guidance Velocity Shutoff System 3. Ground Support a. Central Computer & Sequencer GSE b. Attitude Control GSE
196.	SPS 37-11, Vol. II, pp. 7–9 (10/1/61) (Confidential)	1. Central Computer & Sequencer a. Fabrication b. Status 2. Velocity Shutoff Subsystem
197.	SPS 37-12, Vol. II, pp. 17–22 (12/1/61) (Confidential)	1. A/P Analysis
198.	SPS 37-14, Vol. II, pp. 11–13 (4/1/62) (Confidential)	1. Single-Axis Autopilot Simulator
199.	SPS 37-15, Vol. I, pp. 7–15 (5/31/62) (Confidential)	1. Secondary Power 2. Attitude Control a. Earth Sensor b. Gyro Control Module & Electronics c. Velocity d. Celestial Simulation
200.	SPS 37-18, Vol. I, pp. 12–16 (11/30/62) (Confidential)	1. *Ranger* Earth Sensor 2. *RA*-6-9 Attitude Control 3. Secondary Power
201.	SPS 37-19, Vol. I, pp. 7–15 (1/31/63) (Confidential)	1. Secondary Power a. *RA*-5 Flight Analysis b. *RA*-6-9 c. *RA*-6-8 2. Terminal Turns for TV Picture Nesting a. Introduction b. Methods of Solution 3. Gas Actuator System Development a. System b. Jet Valve Development c. Fill Manifold & Filter 4. Gas Valve Solenoid Improvement 5. Electronic Component Reliability a. Space-Parts Working Groups b. Spacecraft Multipin Connection
202.	SPS 37-20, Vol. I, pp. 7–15 (3/31/63) (Confidential)	1. Secondary Power a. *Ranger* 3 Solar Panels 2. Component Part Sterilization Studies
203.	SPS 37-21, Vol. I, pp. 7–12 (5/31/63) (Confidential)	1. Secondary Power a. Block III Solar Panels b. Batteries c. Electrical Conversions 2. Control-Circuit Analysis Programs
204.	SPS 37-22, Vol. I, pp. 2–3 (7/31/63) (Confidential)	1. Block III Gas-Actuator Development
205.	SPS 37-23, Vol. I, pp. 5–7 (9/30/63) (Confidential)	1. Jet-Vane Actuator Development a. Block III Actuator Configuration b. Quality Control c. Hot Firing Tests d. Space Vacuum Tests
206.	SPS 37-24, Vol. I, pp. 7–8 (11/30/63) (Confidential)	1. Analysis of *Ranger* Block III Midcourse Execution Errors a. Introduction b. Maneuver Sequence c. Relationship of Error Sources to the Maneuver Errors d. Limiting Assumptions and Conclusions